Superionic Conduction of Next-Generation Mobile Ions in Solids Enabled by Coordinating Ligands

Thesis by
Zachery William Benjamin Iton

In Partial Fulfillment of the Requirements for the
Degree of
Doctor of Philosophy

CALIFORNIA INSTITUTE OF TECHNOLOGY
Pasadena, California

2024
Defended May 8th, 2024

Zachery William Benjamin Iton
ORCID: [0000-0002-2226-9006]

ACKNOWLEDGEMENTS

I was one of the lucky ones who truly enjoyed my PhD — I will always look back on these years as not just some of the most enjoyable of my life, but as a period of significant personal and professional growth.. This was entirely due to the people who I was blessed to meet, work, and laugh alongside during my time at Caltech and in LA. I will forever cherish the impact they've had on me.

I could not have asked for a better PhD advisor than Prof. Kimberly See. Thank you for teaching me how to approach solving hard problems, for truly emphasizing the importance of scientific presentation, for showing us the most obscure songs as if they should be universally known, and for fostering a collaborative, enjoyable dynamic in the group. Having an advisor who prioritizes your well-being, and who advocates for you and is investigated in your future goals makes a huge difference. Your guidance and friendship over the years have been crucial in making me the scientist and person I have grown into.

To my other gradschool mentors, Dr. Andy Martinolich, who was my postdoc mentor when i joined the group, and Dr. Forrest Laskowski, who was my adopted mentor in the middle of my Caltech journey, thank you both. Andy taught me the foundation of everything I know about materials chemistry and solid state synthesis. Forrest always had a clever electrochemical method up his sleeve to probe a hypothesis that I had no idea how to approach. He also ignited my love for scientific illustration. Andy and Forrest are two of the most brilliant scientists I know and I'm also lucky to call them friends outside of the lab. Whether it be playing pool with them or wine nights, I will always cherish those memories.

I also had the honor of being a mentor myself, Abby it has been inspiring to watch you grow, win all of the the awards and do great science while passionately advocating for the causes that are important to you. Thank you for your camaraderie and friendship. And Zion, thank you for diving into the rigors of a final-year PhD project without complaint, and adding creative ideas. You are both talented and passionate scientists and I have no doubt you'll do amazing things in the future. It was an honor to work with both of you.

My coworkers in the See Group made me look forward to working on challenging chemistry problems every day. It has been a pleasure to get to know all of you over the years. I spent the majority of my time in the See Group sharing an office

with Steven, Christopher, and Wendy. Thank you for answering my most random questions and putting up with me and Eshaan's constant scientific and nonsensical conversations. Also, my sincere thanks to the past and present members of the ionics subgroup: Forrest, Andy, Xiaotong, Kim Pham, Dan, Jadon, Zion, and Brian who were a critical pillar of support in troubleshooting projects and coming up with new ideas. The See Group is filled with talented scientists and passionate people, I look forward to seeing the amazing work that comes out of the group in the future.

I want to thank a few of my lab mates in particular. Steve was my first friend in the group; he really helped me find my footing, and I'm honored to have made it to the end of this journey together and thankful that I can still call you one of my closest friends. Brian was in the trenches with me in the early days of the $ZnPS_3$ project, I wouldn't have made it through it without you. Kim Pham for spearheading DEI efforts in the lab and on campus, for her friendship, for always being there and for the boba trips. Dan for being a constant sounding board for ideas, a wonderful teammate and opponent in several inter-mural sports, and also a great friend. Michelle, one of the kindest, most thoughtful people I've met, thank you for the constant, unwavering support and spontaneous adventures, for your company on the unnecessary walks to Red Door to clear my mind, and for brightening everyday in the lab. And to Eshaan, you are one of the most thorough people I know, in all walks of life. Thank you for teaching me how to slow down and appreciate the finer things, and for the exercise in patience, waiting for you as you were late for everything. Thank you for building me up scientifically and personally and listening attentively to my problems inside and outside of lab. Thank you for the surprise birthday parties, which I disliked at first but have become some of my most cherished memories, and for treating me like a member of your family. I feel like I've gained another brother in addition to a PhD.

Outside of the See Group, I met countless other incredible people at Caltech, who I have no doubt will also be some of my lifelong friends. Jordan and Dan, thank you both for always being ready to go to Caribbean parties, helping me to feel home away from home. Prithvi, thank you for the memories, from you cooking amazing food, to the unforgettable nights out. I appreciate you all more than you know. Everyone else who has shared part of this journey with me; especially Neehar, Brandon, John, Tarun, Ben, Tomi, Ien, Magel, Josh, Nabha, Ana Karen, Gema, Clara, Anukta, and Arisa, thank you as well.

To my Caribbean friends in LA, outside of Caltech: T-Ray, Danny, Halia, Kaia, and Nkese, thank you for helping me reset and keeping me grounded. To my friends back in Barbados who have been with me for the last ~ 20 years, thank you for cheering me on and being a consistent source of comedic relief and support. I want to especially thank Yohance, who has been like a brother to me over the last decade.

I am very fortunate to have a large family that we make feel like a small family. Thank you all for your undying support and love. In particular, thank you Linda and Billy for welcoming me into your family in LA and making me feel at home. To my sister, Alex, thank you for always being very loudly proud of me. To my dad, William, and step dad, Richard, thank you for your encouragement and support. To my loving mother, Karen, thank you for all the sacrifices you made for us, for being my rock and always pushing me to achieve more than I could have dreamed of. I wouldn't be half the man I am today if not for you.

Finally, to my Grandmother, Anita Jean, who did not have a chance see the end of my PhD journey, thank you for being my biggest supporter always, thank you for everything.

ABSTRACT

Advancements in battery technologies are a critical step towards meeting the growing demand for sustainable energy storage solutions. The development of next-generation battery technologies using "beyond-Li" ions, like Na^+, K^+, Mg^{2+}, Ca^{2+}, Zn^{2+}, and Al^{3+}, could potentially offer improved performance, safety, and cost-effectiveness over traditional lithium-ion systems. However, the realization of next-generation battery technology based on "beyond-Li" mobile ions is limited, in part, due to a lack of understanding of solid state conduction of next-generation ions, which governs ion transport in electrodes, interphases, and solid electrolytes. “Beyond-Li” ions tend to have relatively low mobility in solids due to: (1) the larger ionic radii (Na^+, K^+, Ca^{2+}), which limit the accessible migration pathways, or (2) higher charge densities (Mg^{2+}, Zn^{2+}, Al^{3+}), which results in strong electrostatic interactions within the solid.

This work discusses several structure-property relationships and structural modifications that are hypothesized to lead to facile conduction of next-generation working ions. A notable discovery is the superionic conductivity of $ZnPS_3$ after exposure to humid environments. Water is introduced into the grain boundaries, thereby enabling Zn^{2+} ions from the material to migrate and conduct freely in the network of adsorbed water. The introduction of water leads to potential H^+, therefore a methodology for decoupling the contributions of Zn^{2+} and H^+ in mixed ionic conducting solids using ion-selective EIS, transference number measurements, and deposition experiments is established.

Further extending this approach, superionic conductivity of other next-generation ions in electronically-insulating inorganic solids is achieved by leveraging the established ion exchange/intercalation mechanism of MPS_3 (M = Cd, Mn) materials. The mobile cations that are introduced are coordinated with H_2O ligands which simultaneously increase the size of the bottlenecks within the migration pathway and screen the charge-dense ions resulting in high mobilities. Potential applications can be extended to water-incompatible systems by replacing the water ligands with aprotic molecules.

These insights contribute significantly to the understanding and development of next-generation battery technologies, representing an important step toward the development of more sustainable and efficient energy storage solutions.

PUBLISHED CONTENT AND CONTRIBUTIONS

(1) **Iton, Zachery W. B.**; Irving-Singh, Z.; Hwang, S.-J.; Bhattacharya, A.; Das, T.; Shaker, S.; Clément, R. J.; Goddard III, W. A.; See, K. A. Modular *M*PS_3-Based Frameworks for Superionic Conduction of Monovalent and Multivalent Ions. *Manuscript submitted*.
Contributions: Z. W. B. Iton conceived, designed, and performed experiments, and wrote the manuscript.

(2) **Iton, Zachery W. B.**; Kim, S. S.; Patheria, E. S.; Qian, M. D.; Ware, S. D.; See, K. A. In *Comprehensive Inorganic Chemistry III*; Elsevier: 2023, 308–363. 10.1016/B978-0-12-823144-9.00110-2,
Contributions: Z. W. B. Iton participated in the conception of the project, wrote the sections contained within 3.1.1 and 3.1.2, and edited and compiled the entire chapter.

(3) **Iton, Zachery W. B.**; Lee, B. C.; Jiang, A. Y.; Kim, S. S.; Brady, M. J.; Shaker, S.; See, K. A. Water Vapor Induced Superionic Conductivity in $ZnPS_3$. *J. Am. Chem. Soc.* **2023**, *145*, 13312–13325. 10.1021/jacs.3c03368,
Contributions: Z. W. B. Iton conceived, designed, and performed experiments, and wrote the manuscript.

(4) **Iton, Zachery W. B.**; See, K. A. Multivalent Ion Conduction in Inorganic Solids. *Chem. Mater.* **2022**, *34*, 881–898. 10.1021/acs.chemmater.1c04178,
Contributions: Z. W. B. Iton conducted the literature review, structured and wrote the manuscript.

TABLE OF CONTENTS

LIST OF ILLUSTRATIONS

LIST OF TABLES

Chapter 1

INTRODUCTION

1.1 Motivation

The escalating number of the global population and technological advances have led to a surge in energy demand. Traditionally, this demand has been met predominantly through fossil fuels. However, the use of fossil fuels results in the emission of greenhouse gases, thereby accelerating climate change and threatening human and ecological well-being.[1, 2] Therefore, transitioning from fossil fuels to more sustainable energy sources, like solar, wind, nuclear, and geothermal, has become a critical challenge of modern society.[3] By the late 2010s, renewable technologies, such as solar and onshore wind, had become cost competitive with the least expensive fossil fuel options.[4] However, the broad adoption of these renewable energy sources is hindered by the need for affordable and effective energy storage solutions to manage their intermittent output.[4, 5]

Key to this transition are advanced energy storage technologies, particularly versatile solutions such as batteries. Among these, Lithium-ion batteries (LIBs) are predominant and have facilitated the proliferation of electric vehicles and portable electronics. However, their high cost, particularly for grid-scale applications, and reliance on limited resources like lithium and cobalt, pose significant challenges.[6, 7] The price trends of LIBs and the compound annual growth rate (CAGR) of Li production, as well as target values for complete electrification, are shown in Figure 1.1. Projections indicate that achieving a battery cost of $20/kWh is essential for competing with fossil fuels in some regions.[8] Moreover, the recent "Future of Energy Storage" study by MIT underscores the need for a dramatic increase in lithium production in order for LIBs to meet future energy storage demands for achieving net zero emissions by 2050, suggesting a required CAGR roughly triple that of historical rates.

In order to realize sufficient energy storage to facilitate the transition from fossil fuels to renewable technologies, and thus achieve a net zero emission society, the development of novel battery chemistries that leverage more abundant and less expensive materials is necessary. Promising alternatives include batteries based on other monovalent ions, such as Na^+ or K^+, or multivalent ions, such as Mg^{2+},

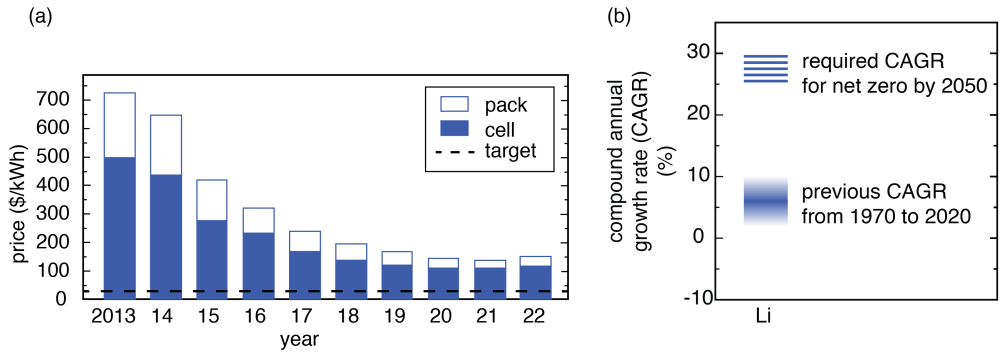

Figure 1.1: (a) the price trend of LIBs over the last decade, and (b) the CAGR of Li production for the last 50 years and target amounts to reach net zero by 2050.

Ca^{2+}, Zn^{2+}, or Al^{3+}. These alternatives are more abundant than Li and potentially enable the use of metal anodes with higher capacities than the graphite anodes used in LIBs. Developing next-generation battery technologies will require a profound understanding of the fundamental processes governing "beyond-Li" devices. This includes the transport of next-generation mobile cations in the solid state, which is critical for various aspects of battery operation such as intercalation into and movement within electrodes, across interfaces and interphases, and in solid state electrolytes (SSEs). Solid state ionic conduction of next-generation mobile ions, particularly multivalent ions, will be the primary focus of this thesis.

1.2 Thesis Overview

This thesis focuses on understanding the structure-property relationships that govern solid state conduction primarily of multivalent ions, like Mg^{2+}, Ca^{2+}, Zn^{2+}, or Al^{3+}, in addition to alternative monovalent ions like Na^{+} and K^{+}, in electronically-insulating inorganic materials.

In order to set the stage for the work presented in this thesis, Chapter 2 delves into the fundamentals of solid state ionic conduction in general, including a mathematical basis for conceptualizing solid state ionics, various established mechanisms, and commonly used characterization techniques. An emphasis is placed on the challenges in achieving high ionic conduction of multivalent ions. Then, a perspective on structural features or modifications that may enable mobility of multivalent ions at ambient temperature is provided. The structural characteristics hypothesized to

enable facile multivalent ionic conduction are explored throughout the rest of this thesis.

Chapter 3 presents a brief summary of computational, structural and electrochemical studies of several promising materials families pre- and post defect engineering. The compounds selected exhibited several properties that were hypothesized to enable ambient temperature multivalent ionic mobility, however attempts to realize high conductivity were largely unsuccessful.

Chapter 4 highlights the successful application of one of these design principles, using ligand molecules to screen of charge dense ions, to achieve superionic Zn^{2+} conductivity in $ZnPS_3$. We utilize impedance spectroscopy with ion selective electrodes, ionic transference number measurements, and deposition and stripping of Zn metal, to confirm that both Zn^{2+} and H^+ act as mobile ions in hydrated $ZnPS_3$. To our knowledge, the novel ionic conduction mechanism exhibited in hydrated $ZnPS_3$ results in the highest Zn^{2+} conductivity reported when using an inorganic solid electrolyte.

Chapter 5 extends the methodology to other mobile ions by leveraging the ion-exchange properties of $CdPS_3$ and $MnPS_3$ to introduce hydrated ions into the van der Waals gap. The coordinated water widens the diffusion bottleneck and screens the charge dense mobile ions paving the way for high-mobility of various ions. This rich set of materials allows us to develop structure-property relationships for ligand-assisted ionic conduction in electronically-insulating inorganic solids. Additionally, the water can be exchanged for nonaqueous, aprotic ligands which extends the potential application of these materials to water-incompatible systems.

Chapter 5 reflects on the findings and implications of these studies, discussing the broader impact of ligand-assisted ionic conduction in solids and the potential for advancing multivalent ionic conduction without ligands.

Chapter 2

THE FUNDAMENTALS OF AND A PERSPECTIVE ON SOLID STATE MULTIVALENT ION CONDUCTION

This chapter has been adapted from:

(1) **Iton, Zachery W. B.**; See, K. A. Multivalent Ion Conduction in Inorganic Solids. *Chem. Mater.* **2022**, *34*, 881–898. 10.1021/acs.chemmater.1c04178,

2.1 Abstract

Multivalent ion-based batteries are the subject of substantial research interest as beyond Li-ion batteries due to the potential for superior performance at a lower cost. A key fundamental process to their operation is the conduction of the multivalent ion in the solid state, which controls the charge storage processes at the electrode materials, conductivity and stability of metal-electrolyte interfaces, and conductivity of potential solid state electrolytes. However, multivalent ionic conduction in inorganic solids has struggled to keep pace with the monovalent analogues because of the challenges posed by the high charge density. In this perspective, we discuss why it is difficult to conduct multivalent ions and include electronic and structural considerations. Using literature reports, we highlight the specific challenges that emanate from the high charge density of multivalent ions, and factors that can mitigate the detrimental impact. Factors including charge screening by electrons and water, the geometry of conduction pathways, the polarizability of the anions, coordination environment, and structural flexibility are discussed. We also highlight the difficulty in characterizing the conductivity of these unconventional working ions and emphasize the need for new characterization techniques to advance the field. Ultimately, we provide suggestions for structural factors that are likely to facilitate multivalent ion diffusion.

2.2 Introduction

It has long been understood that ions can undergo long-range conduction through rigid solid lattices. However, the underlying mechanism as well as the ease with which ions conduct in solids vary immensely across different materials. The first identification of ionic conduction in the solid state was reported by Faraday with Ag^+ conduction in Ag_2S in 1833 and F^- conduction in PbF_2 in 1838.[9–11] Less than a

century later, fast Ag^+ and Cu^+ ionic conduction was identified in the corresponding metal halides by Carl Tubandt and coworkers[12]. The silver and copper halides showed "liquid-like" conduction of Ag^+ and Cu^+ ions above a transition temperature. The lowest superionic transition temperature occurred in AgI (~150 °C),[13] though subsequent studies would evidence superionic conductivities at even lower temperatures using derivatives of AgI (e.g. Ag_3SI and Ag_4RbI_5).[14, 15] Interest in the field surged drastically following the discovery of Na^+ (followed swiftly by Li^+, Ag^+ and H^+) conduction in β-alumina ($M_{1+x}Al_{11}O_{17}$), which represented the advent of solid materials that could conduct other cations besides Ag^+ and Cu^+.[16]

In the decades following the demonstration of ionic conduction in β-alumina, solid state ionics has enabled several practical technologies including batteries, solid oxide fuel cells (SOFCs), and sensors. Notably, the growing understanding of solid state ionics was pivotal in the development of rechargeable Li-ion batteries (LIBs), which have enabled the global adoption of portable electronics. In LIBs, Li^+ ions intercalate into and out of both the graphite anode and the $LiCoO_2$-based cathode material. The reversible nature of the intercalation mechanism facilitated by facile Li^+ diffusion in both materials enables long-term cycling of LIBs. Recently, substantial efforts to realize an all-solid-state battery that promises to improve on the safety, power density and energy density of LIBs has spurred interest in electronically insulating ionic conductors that can operate at room temperature.[17–21] Accordingly, several materials that exhibit room temperature superionic conductivity ($\sigma \geq 1$ mS cm^{-1}) of Li^+ or Na^+ that could potentially serve as solid state electrolytes (SSE) have recently been discovered and characterized. The reported Li^+ and Na^+ conductors with the most promise are discussed at length in several reviews.[22–24]

In addition to the development of all-solid-state cells, next generation batteries that utilize multivalent working ions have also garnered significant interest.[25–27] The focus has primarily included investigations of Mg^{2+}, Ca^{2+}, Zn^{2+}, and Al^{3+}, due to the high abundance (and thus, low cost) and the high volumetric capacities afforded by the utilization of the respective metal anodes. Figure 2.1 shows the size, charge density, gravimetric and volumetric capacities, and standard reduction potentials of the multivalent ions of interest compared with Li^+ and Na^+.

Assuming a coordination number (CN) of six, the ionic radii of Mg^{2+} and Zn^{2+} are 0.72 Å and 0.74 Å, respectively, which are similar to that of Li^+ (0.76 Å). The obvious difference between the ions of similar size is the magnitude of the charge, and thus the charge density. Fast diffusion of multivalent ions in solids has proven

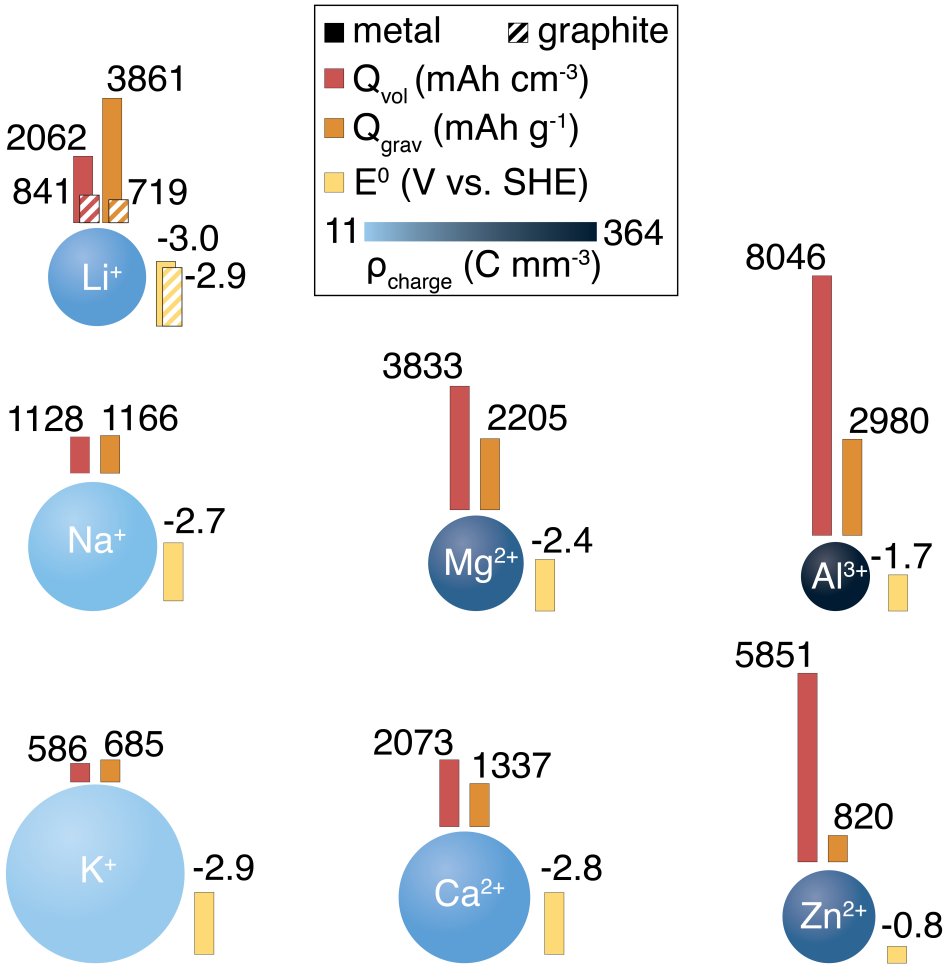

Figure 2.1: A comparison of the size, charge density (ρ_{charge}), volumetric and gravimetric capacities (Q_{vol} & Q_{grav}), and standard reduction potentials E^0 of the relevant multivalent ions with Li^+ and Na^+.

to be much more difficult to achieve than that of monovalent counterparts. The sluggish diffusion may be in large part a consequence of the higher charge density, as ions of high charge density invoke stronger coulombic interactions with the anion sublattice. Additionally, the ionic radius of Ca^{2+} is similar to that of Na^+ (1.0 Å and 1.02 Å, respectfully), whereas the radius of Al^{3+} is significantly smaller (0.54 Å). Conduction of the more polarizable Ca^{2+} may be easier than Mg^{2+} and Zn^{2+} but experimental results have yet to reflect this. Achieving high Al^{3+} mobility is more challenging because the even higher charge density exasperates the complications

of conducting divalent ions. In fact, several computational approaches suggest that existence of SSEs with high Al^{3+} mobility near ambient temperature is unlikely.[28, 29]

Despite the inherent challenges associated with multivalent ion diffusion in solids, there are a handful of reported examples that we can reflect on to gain a better understanding of the factors that are most important in the governance of solid state multivalent ionics. These reports include both intercalation cathode materials and conduction in electronically insulating solids as potential solid state electrolyte candidates. As ions migrate in cathodes, the charge neutrality of the material is maintained through compensation by mobile electrons, whereas in solid electrolytes the charge neutrality is maintained by vacancies that effectively possess opposite charge to the mobile cations. Analyzing both cathodes and electronic insulators will provide valuable information regarding multivalent ionics in different circumstances. The majority of reports to date have focused on Mg^{2+} conduction, and thus Mg^{2+} mobility in solids will largely be the focus of this perspective. However, other multivalent ions will be discussed when appropriate. Additionally, although there have been reports of multivalent ion conductivity on the order of 10^{-4} S cm^{-1} for Mg^{2+} in metal-organic framework (MOF) materials,[30] and between 10^{-7} – 10^{-5} S cm^{-1} for salts of the relevant multivalent ions in polymer matrices,[31] this perspective will focus solely on inorganic solids.

The most promising reported intercalation cathodes are the seminal Chevrel phase Mo_6S_8 and cubic Ti_2S_4 (c-Ti_2S_4), both of which exhibit high Mg^{2+} ion kinetics at room temperature (RT). The Mg^{2+} intercalation cathode materials will be discussed in detail. We will also discuss claims of multivalent intercalation and conduction in transition metal oxides, and water-facilitated multivalent diffusion.

Early reports of multivalent cation conduction (Mg^{2+}, Zn^{2+}, Ca^{2+}) in electronically insulating solids were largely limited to high temperature measurements on crystal structures based on successful monovalent ion conductors. Early reports include attempts to facilitate multivalent ion conduction in β-alumina structure (e.g., $M_{0.6}Al_{11}O_{17.1}$) known to conduct Na^+, Li^+, Ag^+ and H^+. These studies showed sluggish kinetics even at high temperatures (up to 400 °C), and the bulk conductivity was below the detection limit of the instrument 10^{-7} S cm^{-1}. However, in β''-alumina structures (e.g., $M_{0.84}Mg_{0.67}Al_{10.33}O_{17}$, M= Zn, Ca Sr, Ba, Pb) divalent ion conductivity was reported with conductivities of 10^{-6} S cm^{-1} at 40 °C and 10^{-1} S cm^{-1} at 400 °C.[32, 33]

multivalent ion systems based on the β-$Fe_2(SO_4)_3$-type structure ($M_{0.5}Zr_2(PO_4)_3$, M= Mg or Zn) and NASICON (Na super ionic conductor) structure (M= Ca) were investigated.[34, 35] The β-$Fe_2(SO_4)_3$ structure, is related to the well-known NASICON structure in that it contains corner sharing ZrO_6 and PO_4 polyhedra in a "lantern unit" configuration, but the lantern units in the β-$Fe_2(SO_4)_3$-type structure are disordered, whereas in the NASICON-type structure the lantern units are ordered. The β-$Fe_2(SO_4)_3$-type and NASICON-type structures were of particular interest due to the open structure (i.e. wide bottlenecks) and large interstitial voids that are connected by a 3D network and can be occupied by a variety of guest species.[36] The β-$Fe_2(SO_4)_3$-type materials were shown to display significant conduction only at high temperatures (10^{-5} S cm^{-1} at 400 °C, 10^{-3} S cm^{-1} at 800 °C), that of the NASICON Ca analogue was even lower. [34, 35, 37, 38] Several derivatives of these materials have been investigated, and display significant conductivity exclusively at elevated temperatures.[39–42]

In addition to discussing multivalent cation SSEs, it is useful to examine solid state multivalent anion conductors, i.e. O^{2-} conductors. O^{2-} conductors have been investigated extensively for decades primarily due to their application in solid oxide fuel cells and oxygen separation membranes. O^{2-} has a larger radius than the multivalent cations of interest (~1.40 Å) and is thus bulkier but less charge-dense. Similar to the early multivalent cation conductors, fast O^{2-} conduction has been demonstrated at elevated temperatures (500-1000 °C) in a few materials. Many of the predominant O^{2-} ion conductors crystallize in the cubic fluorite structure (AO_2). Such materials include ceria (CeO_2) and yttria-stabilized zirconia (YSZ, $Zr_{1-x}Y_xO_{2-y}$). Perovskites (AB O_3, A = larger cation 12-CN and B = smaller cation 8-CN) have also been extensively investigated and display effective O^{2-} conduction. The most established perovskite material are based on $LaGaO_3$. $La_{1-x}Sr_xGa_{1-y}Mg_yO_{3-\delta}$ (LSGM) was demonstrated to be an effective O^{2-} conductor and found to have higher conductivity than fluorite materials at intermediate temperatures (650-800 °C).[43, 44]

Recently, the search for potential SSE for multivalent ion batteries, with ionic conductivities on par with liquid electrolytes and the best performing superionic Li^+ conductors ($\geq$ 10^{-2} S cm^{-1}) has reinvigorated research efforts to find novel electronically insulating solids that are capable of conducting multivalent ions at RT. To date, a limited number of materials with multivalent ion conductivity near ambient temperatures have been reported including the spinel $MgSc_2Se_4$,[45] several derivations of $Mg(BH_4)(NH_2)$,[46–52] $MgAl_2X_8$ (X= Cl, Br),[53] and $ZnPS_3$.[54]

The properties that enable ambient temperature multivalent conductivity in these materials will be dissected and discussed in detail later. However, superionic conduction of multivalent ions at ambient temperature has yet to be observed. Figure 2.2

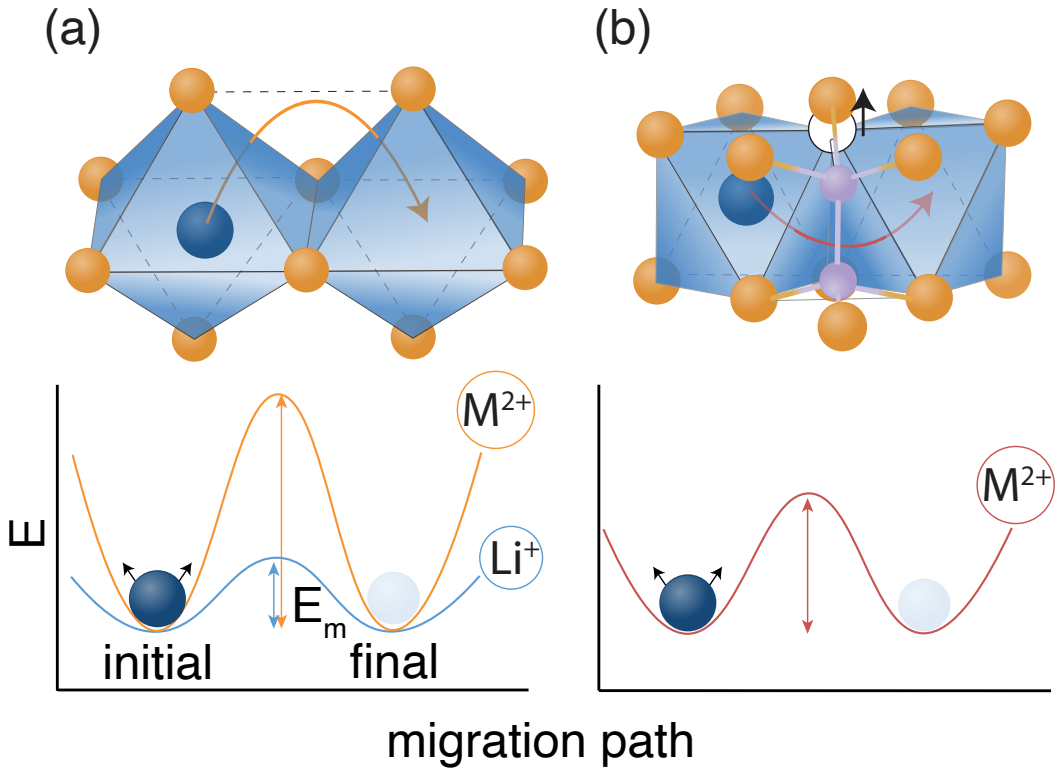

Figure 2.2: A comparative illustration of potential energy landscapes along the migration pathway of (a) multivalent ions (orange) vs. Li^+ ions (blue) in established Li^+ conducting structures, and (b) multivalent ions in structures optimized to diminish the strong electrostatic interactions between multivalent cations and the anion sublattice (red) – e.g. through widening of the bottleneck using flexible polyanions.

illustrates that even in structure types that display superionic Li^+ conductivity, multivalent ions are subject to high migration barriers due to the stronger electrostatic interactions with neighboring ions. Instead of imposing design rules for superionic Li^+ conductions, the identification or development of superionic multivalent conductors will require structures to be optimized for facile multivalent ion conduction through the mitigation of the strong interactions. Such an optimization of the structure will lead to significantly reduced migration energy, E_m, for multivalent ionic conduction (Figure 2.2b). Therefore, in this perspective we aim to tackle the challenge of achieving fast solid state multivalent ion conduction by establishing a clear, fundamental understanding of the factors that play a crucial role in solid state multivalent conduction, and how those factors can be leveraged to create an

optimized environment for multivalent conduction. We will begin by reviewing the principles of solid state ionic conduction with a focus on multivalent ions. We then evaluate the suitability and highlight the shortcomings of extending common characterization techniques that are used to understand ionics in monovalent systems to novel multivalent ion systems. Following this, we analyze and compare factors that enable multivalent ion conduction in reported cathodes, high temperature multivalent anion and cation conductors, and novel SSE candidates. We first highlight the impact of screening the dense charge of multivalent ions, via electrons or molecules like H_2O. Then, we detail relevant structural effects on multivalent ionics, such as preferable structure types, polarizability of the anion sublattice, coordination environment, and structural flexibility (in the form of medium–long range disorder or flexible sublattice components). The discussion will conclude by outlining several potential structural pitfalls that can decrease the efficiency of multivalent mobility in solids. The ultimate goal is to provide a concise outlook to guide the discovery and analysis of solids with high multivalent ionic conductivity.

2.3 Fundamentals of Solid State Ionic Conduction

To gain insight into ionic conduction and diffusion of multivalent ions in solids, it is essential to review the fundamentals of solid state ionics. The principles of solid state ionics can then be extended to account for the specific characteristics of multivalent ions vs. monovalent ions.

In general, the conductivity of a material is defined as:

$$\sigma = \sum_i n_i q_i \mu_i \tag{2.1}$$

where σ is the conductivity, n_i is the concentration of a given charge carrier, q_i is the charge of that carrier, and μ_i is the mobility of the charge carrier in the material, which describes the ability of the ion to move through the solid. Right away we encounter the first instance of q_i. In this case, divalent charge carriers have an advantage over their monovalent equivalents because they produce double the current for each ion.

For ionic conduction, the Einstein relation relates the mobility, μ, to the diffusivity, D_σ, of the charge carrying species:

$$\mu = \frac{qD_\sigma}{kT} \tag{2.2}$$

where k is the Boltzmann constant and T is temperature. D_σ is the macroscopic long-range diffusivity, often called the diffusion coefficient.

It is important to note that diffusion refers to transport of particles due to a concentration gradient. Another mass transport mechanism at play in a solid state electrolyte is migration, which refers to the transport of charged particles in an electric field. The kinetics of the net migration of charged particles under an applied potential gradient is described by D_σ. In that way, it can be understood as the diffusivity of the entire collection of mobile ions, as if that collection was a single particle. Thus, D_σ is different than diffusion coefficients which describe diffusion that occurs at equilibrium. The first such diffusion coefficient, D_r is the random diffusion coefficient, which can appropriately model microscopic ionic diffusion at the dilute concentration limit. D_r can be calculated using a random walk approach:

$$D_r = \frac{\langle R_n^2 \rangle}{bt_n} = \frac{\alpha^2 \nu}{b} \tag{2.3}$$

where R_n^2 is the total displacement in n steps, b is a geometric factor to quantify the number of available neighboring sites (2, 4, 6 for 1D, 2D, 3D respectively), t_n is the time taken to complete n steps, α is the jump distance and ν is the successful jump frequency. The second relevant equilibrium diffusion coefficient, D^* is the tracer or self-diffusion coefficient. D^* is a measure of the diffusivity of an ion in a chemically homogeneous material with no chemical potential gradient, and is the diffusivity used as the constant of proportionality in Fick's First Law.[55, 56]

Often it can be difficult to experimentally measure D_σ due to a lack of precise knowledge of the charge carrier concentration, n, although decent estimates can be made.[57] However, D_σ can be related to D_r and D^* which are more easily measurable quantities. The relationship between the different diffusion coefficients will be explained in the following discussion focusing on vacancy mediated diffusion.

The vacancy mediated diffusion model is the most general solid state diffusion mechanism that is simple enough to be quantitatively modeled. In the vacancy mediated mechanism, charge is conducted across the material by the charge carrier

(ions) exchanging positions with an adjacent vacancy. Every solid state material contains some amount of intrinsic vacancies because the inclusion of such vacancies decreases the free energy of a perfect vacancy-free crystal.

The diffusivity, D^* within the vacancy–mediated diffusion model can be defined as follows;[56, 58]

$$D^* = f\alpha_0^2 x_V^o \nu = f\alpha_0^2 \nu_0 exp\left(\frac{-\Delta G_M}{kT}\right) exp\left(\frac{-\Delta G_V}{kT}\right) \tag{2.4}$$

where f (≤ 1) is a correlation coefficient, which accounts for the correlation between successive jumps, i. e. the measure of randomness of successive jumps. The inclusion of f differentiates D^* from D_r, and they are related by the equation $f = \frac{D^*}{D_r}$. When diffusion is completely random and uncorrelated, f =1. α_0 is the jump distance in the assumed direction of migration. ν is the successful jump rate or rate of exchange of the atom and the adjacent vacancy. ν can be expanded in terms of the attempt frequency ν_0 and the statistical description for the portion of atoms with enough energy to successfully move from its lattice site to the adjacent vacancy, given by $exp\left(\frac{-\Delta G_M}{kT}\right)$ where ΔG_M is the free energy associated with the formation of an activated complex (transition state). Finally, x_V^0 is the equilibrium concentration of vacancies, which represents the probability that an adjacent vacant site is available. As such, the concentration of vacancies in the material, as opposed to the charge carrying ion, limits long-range percolation, and is functionally the carrier concentration. It can be shown that x_V^0 is given by $exp\left(\frac{-\Delta G_V}{kT}\right)$ where ΔG_V is the free energy change per vacancy.

Furthermore, D^* can then be related to D_σ through the Haven ratio H_R ($H_R = \frac{D^*}{D_\sigma}$). H_R, like f, serves as an indication of correlated effects. Many factors affect H_R, and there is a lack of a general straightforward physical meaning.[56] However, ionic interactions were not considered in the derivation of the Einstein relation (equation 2.2), thus H_R can be associated with deviations from the assumption that multi-ion interactions can be ignored.[56, 59] Additionally, H_R can be used to obtain information about the mechanism of diffusion.[57, 60–62] Combining equations 2.1–2.4 and using the relationship between the various diffusivities, one can obtain an expression for vacancy mediated conductivity in a lattice:

$$\sigma = \frac{f}{H_R}\left(\frac{\alpha_0^2 \nu_0 n q^2}{kT}\right) exp\left(\frac{\Delta S_M + \Delta S_V}{k}\right) exp\left(-\frac{\Delta H_M + \Delta H_V}{kT}\right) = \frac{\sigma_0}{T} exp\left(-\frac{E_a}{kT}\right). \tag{2.5}$$

In which the free energies are expanded into the respective entropic (ΔS) and enthalpic (ΔH) terms using $\Delta G = \Delta H - T\Delta S$. The enthalpic terms are collectively represented as the activation energy, E_a. From equation 2.5, it is clear that the vacancy mediated conductivity of a solid material follows an Arrhenius relationship, the prefactor σ_0 is used for simplicity.

This analysis elucidates some of the general requirements for a material to exhibit high ionic conductivity:

- The activation energy, E_a should be low. This is especially important for multivalent ionics, as the high charge density of the mobile ion results in an increased electrostatic interaction with the anion sublattice and consequently, a high E_a. Computational studies from Rong *et al.* suggest that for adequate battery operation E_a for intercalation cathodes should be at most ~525 meV for micron sized particles and ~650 meV for nanosized particles.[28] Additionally, the activation energy of several fast Li-conductors such as LISICON (~200-500 meV) and garnets (~400-500 meV) reside in this range, thus an $E_a \leq 500$ meV is likely promising for multivalent solid state electrolyte candidates. [22, 63] In superionic conductors the free energy of defect formation (ΔG_V) is often negligible and therefore the measured activation energy corresponds solely to the ΔH_M (=E_m).[64–66] However, the contribution of the vacancy formation energy to the E_a can have a significant effect, especially in materials without extrinsic defects.[23, 65, 67, 68]
- The concentration of carriers must be high. In a vacancy mediated conduction mechanism, the charge carriers are functionally the vacancies. Although multivalent ions can supply equivalent charge to monovalent ions with a fraction of the charge carriers, since the successful jump rate of multivalent ions is lower due to the stronger electrostatic interactions and the higher E_m that results, maximizing the number of available sites for multivalent ions to jump into will be essential for significant long-range conduction. Intrinsic vacancies are formed as Frenkel or Schottkey defects, the concentration of

which are temperature dependent, and may be too low at ambient temperature to elicit meaningful bulk conduction.[69] Aliovalent substitution is generally used to create a stoichiometric amount of vacancies. This extrinsic carrier concentration is much greater than the intrinsic value at ambient temperatures and has been shown in Li conductors to increase the conductivity by several orders of magnitude (up to 7 in extreme cases).[68]

- The prefactor, σ_0 should be high. In addition to the carrier concentration, this is most easily affected by the attempt frequency (ν_0) and the migration entropy (ΔS_M). ν_0 and (ΔS_M) are both associated with the vibrational frequencies of the ion in the lattice site.[23, 65, 70] Notably, σ_0 and E_a are related by the Meyer–Nedel (MN) law, which states that for an Arrhenius relationship (like equation 2.5) as E_a varies, σ_0 responds in accordance with the relation, $ln\sigma_0 = a + bE_a$. Therefore, attempts to reduce the E_a– such as using a softer, more polarizable anion lattice (discussed later in detail)– also result in a decrease in σ_0.[68, 71–73] Thus, when trying to increase multivalent ionic conduction, one must ensure that the benefit of the decrease in E_a is greater than the cost of the decrease in σ_0, which is often assumed to be the case, but is not guaranteed.[71, 74, 75] A recent study by Gao *et al.* discusses in detail how the MN energy (Δ_0, the reciprocal of a in the MN law) can be determined and used to predict if increasing or decreasing E_a will result in an increase in conductivity of a material at a given temperature. This appears to be a more considerate approach compared to simply seeking low activation energy, but the authors highlight that understanding the physical meaning of Δ_0 is key to advancing design principles developed through this approach.[76]

In addition to vacancy mediated diffusion, other more complex mechanisms have been proposed to be responsible for transport of ions through a solid. The transport mechanisms are shown pictorially in Figure 2.3. These include:

- The interstitial mechanism in which atoms that occupy interstitial positions in the lattice can diffuse normally without occupying lattice sites. Thus, the vacancy concentration does not limit the charge carrier concentration.
- The interstitialcy mechanism in which atoms that initially occupy interstitial sites diffuse into an occupied lattice site and push the atom from that lattice site into another interstitial position. β-Alumina is an example of a material in which diffusion occurs through an interstitalcy mechanism. The interstitialcy

mechanism is an example of concerted ion migration model in which multiple ions hop simultaneously along neighboring occupied sites triggering jumps in a series of ions. The concerted mechanism has been suggested to be at the origin of fast ionic diffusion in many superionic conductors. [77]

- The paddlewheel mechanism in which correlated polyanion rotation is suggested to facilitate high cationic conductivity. The paddlewheel mechanism has generally been observed especially in high volume crystalline phases that are stabilized at high temperatures, or in glassy, disordered materials. [78]

2.4 Complications with Established Characterization Techniques

Combining multiple characterization techniques has been evinced to overcome their individual limitations and time scale sensitivities, and thus enables the determination of the magnitude and and governing mechanisms of ionic conductivity and diffusivity in solids. In electronically insulating solids, electrochemical impedance spectroscopy (EIS) is often used to determine σ and E_a, while pulse field gradient (PFG) nuclear magnetic resonance (NMR) is used to directly measure D^*. Techniques that probe microscopic physical characteristics of diffusion, such as variable temperature (VT) NMR (capable of spanning a large range of time scales 100ps – 100s) and NMR relaxometry (most readily probes fast local motion in 100 – 1 ns range), provide insight into the jump rate and thus enable the calculation of D_r. Additionally, muon spin relaxation (μSR) spectroscopy and Quasielastic Neutron Scattering (QENS) (probe 100μs–ps and 10 ns–ps range, respectively) have also been utilized to determine hopping rates and estimate D_r in Li^+ and Na^+ solid state conductors.[79, 80] In electronically conducting materials that serve as intercalation cathodes, galvanostatic (or potentiostatic) intermittent titration technique (GITT) has been used to determine D_σ. The fundamentals of these techniques are discussed at length in other reviews.[56, 60, 81–84] This perspective will briefly discuss some of the limitations associated with these techniques and challenges related to extending them to multivalent ionic systems.

Although EIS is widely used to determine the ionic conductivity and E_a of long-range diffusion in solids, EIS-derived conductivity values are known to be highly dependent on processing and measurement conditions. A recent inter-laboratory study highlighted the effect of stack pressure, pellet density, pelletizing pressure, contacting material and deposition method, measurement temperature, and frequency ranges on the resulting conductivity and showed that conductivity values

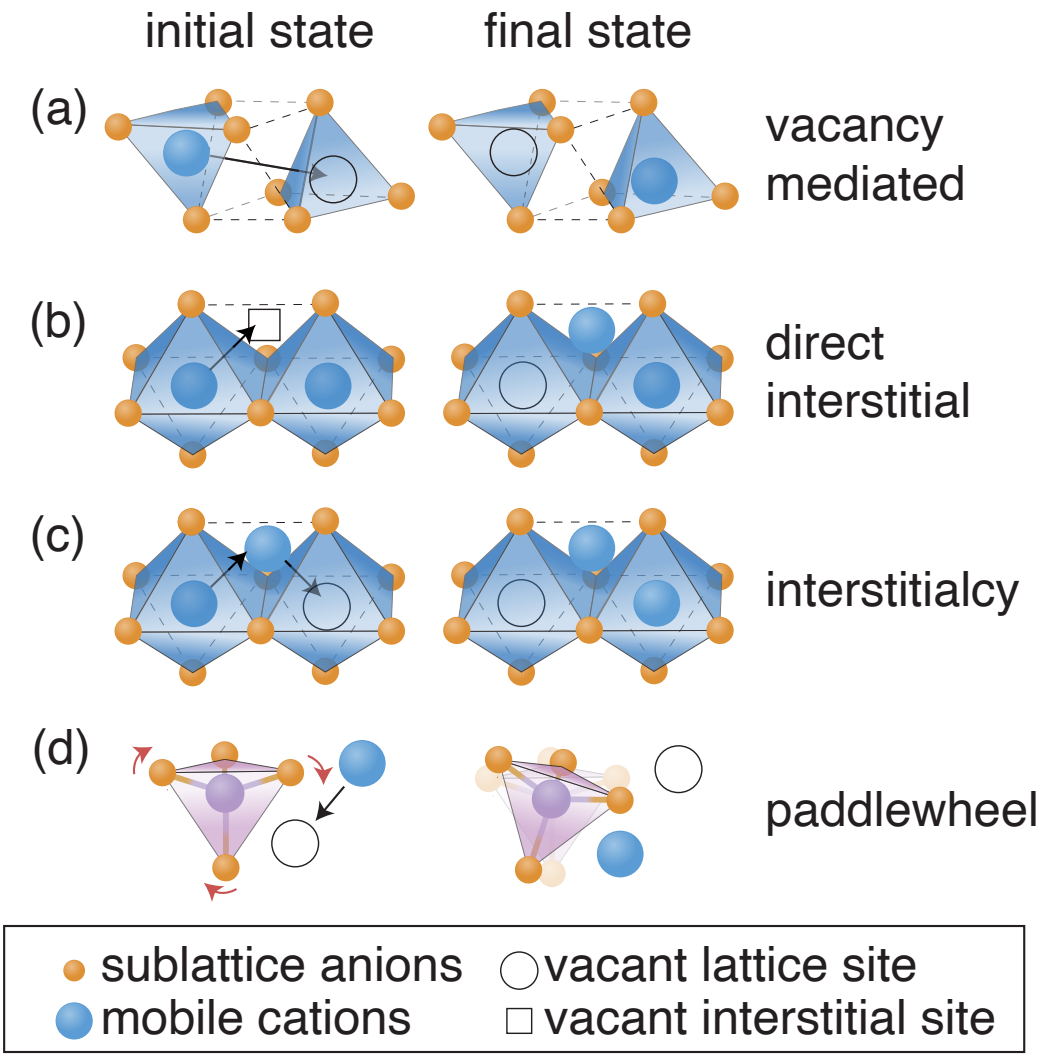

Figure 2.3: Illustrations of solid state ionic diffusion mechanisms: (a) vacancy mediated — the ion jumps from a lattice site to a neighboring, unoccupied lattice site, (b) direct interstitial — the ion jumps from a lattice site to an unoccupied neighboring interstitial, (c) interstitialcy — a concerted mechanism in which an ion jumps from a lattice site into an interstitial site which was previously occupied pushing the interstitial ion into a neighboring vacant lattice site, and (d) the paddlewheel mechanism — the rotation of polyanion species facilitates the jump of an ion from a lattice site to a vacant neighboring site.

for the same material vary up to an order of magnitude and E_a up to $\sim$ 100 meV among different research groups.[85] Other variables that significantly impact experimentally measured conductivity include pre-measurement sintering time and temperature, measurement atmosphere, grain size, and induced disorder (controlled by ball milling).[57, 86–88] Therefore, it is imperative that material preparation

and measurement conditions are meticulously reported to enable meaningful comparisons across materials and research groups. This is especially crucial as more multivalent ion conductors are explored, given the scarcity of literature in the field.

Additionally, quantitative analysis of EIS entails fitting the obtained data to an equivalent circuit. The application of different equivalent circuit models to the same system is possible and results in different interpretations of the ionics. For instance, the studies on $MgSc_2Se_4$ have assigned both ionic and electronic contributions to the observed Nyquist plots.[45, 89] Fundamentally, features in the Nyquist plot can be attributed to corresponding processes in a material through the consideration of the capacitance value of a given feature.[81] Several reports attribute the high frequency intercept in the Nyquist plot to the bulk conductivity in multivalent systems. Although the intercept of the high frequency feature can fundamentally be associated with bulk conductivity in materials with high conductivity, it should not be assumed to correspond to the bulk conductivity without evidence. Low temperature measurements or variation of cell constant should be performed to resolve the high frequency feature to provide more confidence about its origin.

Due to the susceptibility of EIS results to measurement or interpretation error, NMR techniques are often used to corroborate the E_a and obtain information about the relevant diffusivity for Li^+ SSEs. Unfortunately, the multivalent ions of interest are all both quadrupolar and have relatively low relative abundances (besides Al) — the NMR active nuclei ^{25}Mg ^{27}Al ^{43}Ca and ^{67}Zn have abundances of 10.13, 100, 0.135, and 4.1, respectively. The quadrupolar interactions cause potentially rapid spin-lattice (T1) and spin-spin (T2) relaxation and significant quadrupolar broadening of the peaks. The quadrupolar broadening can easily convolute motional narrowing studies. Therefore, NMR spectroscopy of such nuclei is significantly more difficult to perform than that of nuclei with spin 1/2. Additional challenges associated with low signal due to the low abundance of the relevant isotopes, often necessitate make expensive isotopic enrichment. Although ^6Li and ^7Li are also quadrupolar, they exhibit small quadrupolar coupling and can be treated as fictitious spin 1/2 systems. Thus, before information about diffusivity or E_a can be inferred from NMR studies on multivalent ions, it is vital to understand the quadrupolar effects in a given material especially if the line width and relaxations are being investigated. Mathematical models that can extract mobility information from NMR measurements of quadrupolar nuclei exist. However, significantly lower signal sensitivity of multivalent nuclei renders it difficult to obtain data of sufficient quality

Element	incoherent neutron scattering cross-section (barns)
^{1}H	80.27
^{6}Li	0.46
^{7}Li	0.78
^{23}Na	1.610
^{25}Mg	0.28
^{27}Al	0.0082
^{43}Ca	0.31
^{67}Zn	7.18

Table 2.1: A comparison of the incoherent neutron scattering cross-section of relevant elements.

to apply such models without the use of magnetic fields higher than those commonly present in most laboratories. Similarly, PFG techniques are in principle possible in suitable materials, but have yet to be employed and require a very high field magnet, a strong field gradient probe, and isotopic enrichment.

The potential effectiveness of μSR, is similar to that of NMR techniques as it requires the nuclei of the ion of interest to have both a magnetic moment and high abundance. However, advantages of μSR over NMR techniques are the ease of separating the effect of paramagnetic ions, and the smaller consequence of studying quadrupolar nuclei. Of the multivalent ions of interest, Mg^{2+} can be studied using μSR but the signal may be hard to resolve. Ca^{2+} and Zn^{2+} conductors would need to be isotopically enriched to enable the potential of μSR studies.[84] QENS has been most successfully employed to study diffusion in H^{+} conductors. Incoherent neutron scattering is essential to the collection of QENS spectra, and the incoherent neutron scattering cross-section of H is significantly larger than that of other relevant elements. The incoherent neutron scattering cross-section of relevant elements is shown in Table 2.1.[90]

Due to the low incoherent scattering cross-section and high neutron absorptivity of ^{6}Li, ^{7}Li enrichment is needed to obtain high quality QENS measurements. These measurements require significant data collection times and several grams of sample. Application of QENS to multivalent ion systems is likely hindered by the need for expensive enrichment, large sample size, and experimental time requirements.

GITT has been used to investigate the ionic diffusivity in electronically conductive materials that have been studied as intercalation cathodes. GITT probes a chemical diffusion coefficient akin to $D\sigma$ as the ions are diffusing in the cathode material

under the application of an external potential. In GITT experiments, the characteristic diffusion time is directly probed, and then $D\sigma$ is calculated with knowledge of the 1D diffusion length. [83] Studies have suggested that extension of this theory to 3D particles produces erroneous results, due to the lack of consideration for finite heterogeneous kinetics in the initial derivation,[91] and incorrect analytical assumptions. The commonly applied analysis of GITT is based on ideal diffusion (i.e., Fick's Laws) when it should be based upon transport driven by potential gradients instead of concentration gradients.[92] Additionally, GITT is usually measured on a composite electrode containing conductive carbon additives and binders. The relaxation dynamics measured pertain to the entire system, and thus could include relaxation dynamics associated with the tortuous network imposed by the composite electrode. Nonetheless, the use of GITT to determine D is commonplace in the field. It should be noted that calculation of D requires numerous assumptions, and the results for Li^+ diffusivity have been shown to vary by orders of magnitudes for identical materials.[92, 93] In these studies, the large variation in results is likely due to the underestimation of surface area of the electrode particles, which can drastically inflate the calculated D value. Therefore, careful determination of the surface area is critical to facilitate comparison across different materials.[94] Additionally, care must be taken to ensure that there are no other processes in the cell that could be contributing to the overpotential and convoluting the calculation of the diffusivity.[93] Importantly, the complications and limitations of GITT-derived diffusivity analysis extend to multivalent systems.

In light of the difficulty associated with extending the common techniques used to study solid state ionics to multivalent systems, it is clear that new characterization techniques tailored to multivalent ions need to be developed as the field matures. Currently, since GITT cannot be applied to electronically insulating materials, EIS is the only technique that is particularly suitable for routine investigation of electronically insulating multivalent ionic conductors. NMR techniques that investigate microscopic diffusion may be applied to Mg^{2+} systems relatively effectively if the quadrupolar interactions are understood and accounted for. The development and implementation of PFG techniques to probe long-range dynamics would be invaluable for characterization of multivalent ionic conductors. In Zn^{2+} and Ca^{2+} systems, the isolation of EIS as the sole conductivity characterization method not only leaves a cloud of doubt over the findings, but also precludes the ability to elucidate the conduction mechanism. Computational methods, such as nudged elastic band (NEB)

calculations, can be used to hypothesize the mechanism, though experimental verification would be ideal.

2.5 The Effect of Screening Charge-Dense Multivalent Ions

The charge density of multivalent ions is frequently cited as a critical factor responsible for the observed sluggish solid state diffusion. Therefore, one method to increase the mobility of multivalent ions in solids is through screening the charge of the ions, to weaken the Coulombic interactions with the host lattice and with other immobile ions.

Electronic Screening

Screening of the charge-dense multivalent ion by mobile electrons likely contributes to the successful demonstration of ambient temperature multivalent ion intercalation (mostly Mg^{2+} and Zn^{2+}) in some cathode materials with high electronic conductivity. Many reports of multivalent ion intercalation into cathode materials (especially transition metal oxides) are over-reliant on observed capacity as the indication of intercalated Mg^{2+}, when the capacity can often be accounted for by parasitic side reactions or proton intercalation. We direct interested readers to the following critical reviews which discuss reports that have sufficiently proven Mg^{2+} intercalation in metal oxide cathodes, and the experimental procedures necessary to do so.[26, 95]. Concrete examples of reversible, electrochemical insertion of multivalent ion into solid lattices are limited. Thus, analyzing successful demonstrations of intercalation cathode materials can afford us valuable insight into solid state multivalent ion diffusion.

The seminal example of multivalent intercalation is the Chevrel phase (Mo_6S_8) reported in 2000 by Aurbach *et al.* [96] Reversible intercalation of up to two equivalents of Mg^{2+} was achieved in Mo_6S_8 at slightly elevated temperatures (60 °C).[96] Unlike the close-packed anion sublattice in commercialized Li-ion battery cathodes, the structure of the Chevrel phase is comprised of clusters. It contains Mo_6T_8 blocks (T = S, Se, Te) with the eight T atoms forming a cube in which the six Mo, one on each of the cube faces, form an octahedron. The first equivalent of intercalated ions occupies one of six of the "inner-sites" located farthest away from the Mo atoms, in cavities at the corner of the Mo_6S_8 cubes. The second equivalent occupies one of six of the "outer-sites," which are located within the cavity along the edges of the Mo_6T_8 cubes.

The high Mg^{2+} mobility in the Chevrel phase is attributed to its unique ability to redistribute the ions' charge, which can successfully mitigate the strong Mg-anion attraction or Mg-cation repulsion that is normally associated with charge-dense multivalent ions.[97] The electrostatic charge of the mobile ions in cathodes during intercalation is compensated by a change in oxidation state of the host cations. An obvious barrier to facile multivalent ion intercalation stems from the inability of many transition metals to undergo electrochemical processes that involve multiple electron transfers without drastic local structure changes. Levi *et al.* proposed that the Chevrel phase is able to facilitate fast Mg^{2+} (and other multivalent ion) insertion and diffusion because the Mo_6S_8 clusters act as a single entity in which the Mo_6 octahedron can accommodate, and share, up to four additional electrons. Follow-up computational work by Thole *et al.* and subsequent experimental verification using *ex situ* X-ray absorption near edge spectroscopy (XANES) by Wan *et al.* suggest that the Mo_6 clusters do not actually change their formal oxidation state, but rather that the S atoms closest to the Mg^{2+} ions are the redox center and become electron enriched.[98, 99] Additionally, the calculations suggest that pristine Mo_6S_8 displays metallic behavior, until it undergoes a metal-semiconductor transition upon intercalation of two eq. of Mg^{2+}. Recently a study by Yu *et al.*, debated the interpretation of the XANES results but agreed that there is redistribution of the charge on the S atoms during initial intercalation.[100] Regardless, these studies suggest that the metallic nature of the pristine material, and the delocalization of electron density across the neighboring S enable highly localized electronic screening of the charge-dense multivalent ions, facilitating the uniquely high multivalent ion mobility in the Chevrel phase.

The other notable material in which reversible Mg^{2+} intercalation has been achieved is the spinel phase c$-Ti_2S_4$. c$-Ti_2S_4$ can reversibly intercalate ~0.84 equivalents of Mg^{2+} into the lattice at 60 °C. Energy-dispersive X-ray spectroscopy (EDS) and Rietveld refinement of the X-ray diffraction (XRD) data were used to confirm Mg^{2+} intercalation was responsible for the observed capacity.[101] The important role of electronic screening was elucidated by a subsequent study by Bonnick *et al.*, in which c$-Zr_2S_4$ was shown to only support intercalation of up to 0.6 Mg^{2+} at 60 °C. Intercalation was confirmed by XRD, EDS, electron energy loss spectroscopy (EELS), and scanning transmission electron microscopy (STEM).[102] Despite the larger lattice dimensions of Zr_2S_4 vs. Ti_2S_4 (a = 10.356 vs. 9.776), D_{Mg} is ~one order of magnitude lower in Zr_2S_4 across the entire intercalation composition range. The lower mobility of Mg^{2+} in c$-Zr_2S_4$ was a consequence of less electronic

shielding in c$-Zr_2S_4$, as conductivity of c$-Zr_2S_4$ four orders of magnitude lower than that of c$-Ti_2S_4$.

Additionally, Mg^{2+} intercalation and diffusion into layered TiS_2 at 60 °C has also been demonstrated, again confirmed by XRD and EDS.[103] Computational results suggest that E_m in the layered TiS_2 is 1.16 eV, whereas it is 0.86 eV in c$-Ti_2S_4$. The difference in E_m has been attributed to the ability of the spinel phase to better redistribute the electron density over more Ti–S bonds than in the layered material.[104] Thus, the ability to screen the high charge of the multivalent ions with mobile electrons may be beneficial for high mobility in these systems, though its absence may not preclude conductivity. However, so far the realization multivalent ionic conductivity in electronically insulating solids has be limited. The thiospinel $MgSc_2Se_4$ has shown the highest reported electrochemical impedance spectroscopy (EIS)-derived Mg^{2+} conductivity at RT of any SSE candidate (10^{-4} S cm^{-1}), accompanied by a low E_a (200 ± 40 (EIS) 380 ± 90 (^{25}Mg MAS NMR)). However, $MgSc_2Se_4$ also has a significant electronic conductivity($\sim 10^{-6}$ S cm^{-1}) which convolutes the EIS results. Although the fast ionic mobility in $MgSc_2Se_4$ has been largely attributed to structural factors, which will be discussed later in detail, the role of charge screening by the significant electronic conductivity cannot be ignored.

Solvent Screening

It has also been hypothesized that charge screening can be accomplished by molecules like water, either structural water coordinated to the material or water that is directly solvating the multivalent cation. Most instances of water-screened multivalent ion intercalation have been reported in layered transition metal oxides, in which multivalent ion kinetics have been notoriously sluggish. Critically, having even a minuscule amount of water in the system can produce H^+ that diffuse much easier than multivalent ions and could be responsible for the electrochemical measurements observed. Therefore, it is essential to either prove that multivalent ions are intercalated and/or diffusing in the solid, or decouple the contribution of the multivalent ions from that of H^+. The studies with sufficient evidence to corroborate multivalent ion intercalation pertain to various phases of MnO_2. Structural water and additive water to the non-aqueous electrolyte in δ-MnO_2 (birnessite) were shown to successfully facilitate the intercalation of Mg^{2+}. The presence of water decreases the desolvation energy via intercalation of hydrated Mg^{2+} ions, enhances the structural stability, and screens strong coulombic interactions.[105] Another study reports that adding water to $Mg(ClO_4)_2$ in propylene carbonate (PC) electrolytes appeared to help the

intercalation of Mg^{2+} in MnO_2 (phase not given) from 0.18 to 0.69 equivalents.[106] Reports have also suggested the possibility of H_2O-supported Ca^{2+} intercalation into $K_{0.31}MnO_2 \cdot 0.25\,H_2O$, although Ca^{2+} can only account for 60% of the capacity.[107] The studies of H_2O supported intercalation of multivalent ions into vanadium oxides are plentiful, but often lacking sufficient evidence to prove multivalent ion insertion. Several reports have shown that the capacity is most likely due to H^+ intercalation.[108, 109]

Notably, recent studies have provided conclusive evidence for increased Li^+ mobility in a $Li_2Sn_2S_5$ SSE as a result of charge screening by added water.[110] In a similar vein, investigations by our group, which is in preparation, suggest that Zn^{2+} conduction can potentially be significantly improved by hydration of $ZnPS_3$. Therefore, screening coulombic interactions of charge-dense multivalent ions with H_2O, or potentially other solvents in a non-aqueous environment, is a promising pathway to enhance ambient temperature multivalent ion conduction in electronically insulating solid. In lieu of applicable NMR techniques, data to support that hydration enhances multivalent ion conduction in hydrated solids could be found in the form of transference number measurements,[111–114] and metal deposition and stripping experiments, although neither is flawless or conclusive. Therefore, the development of simple methods to conclusively decouple multivalent ion conduction from H^+ conduction in systems with added water will be crucial to understand and develop water-assisted multivalent ion conducting electronically insulating solids.

2.6 Structural Effects on Multivalent Ion Conduction

In addition to enabling high mobility through screening of the multivalent ion charge, several structural factors can mitigate the strong coulombic interactions experienced by multivalent ions. In the following sections we will detail the benefits of certain crystal structures, the effect of polarizability of the anion sublattice, the coordination site preference of multivalent ions, and structural flexibility.

Favorable Structural Types

Open Structures with Large Bottlenecks

Certain crystal structures and structural motifs tend to reoccur consistently in materials that exhibit high ionic conductivity. In general, a material with an extensive interconnected 3D conduction pathways is better equipped to support long-range ionic diffusion. 2D or 1D pathways are more easily blocked by impurity atoms or antisite defects which can greatly impede long-range migration.[115] Addition-

ally, the bottleneck size in the diffusion channel directly influences the strength of coulombic interactions and thus the diffusion of the mobile ion.[24]. For example, "open" structures like the NASICON compounds contain a subarray of corner sharing (rather than edge sharing) ZrO_6 and PO_4 polyhedra, which facilitates 3D conduction channels with wide bottlenecks. Widening of the bottleneck has been shown to improve multivalent ion conductivity. Figure 2.4 illustrates the conduction pathway in a stereotypical NASICON structure, as well as how substitution of the immobile cations in the lattice for a larger cation can widen the bottleneck and decrease the E_m.

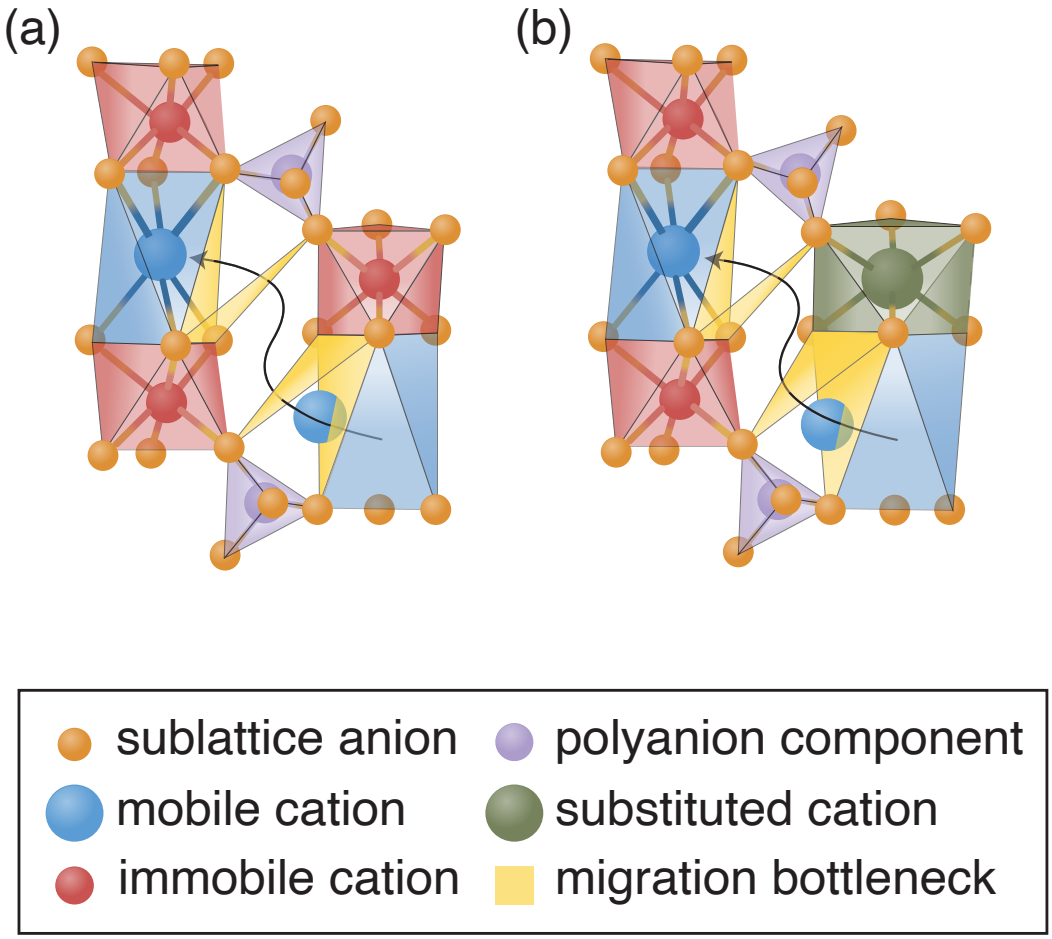

Figure 2.4: (a) An illustration of the diffusion pathway in NASICON materials with the triangular bottlenecks highlighted. (b) Widening of the migration bottleneck after substitution of an immobile cation for a larger cation.

In the fluorite O^{2-} conductors, the larger ionic radius of Ce^{4+} (0.97 Å) than that of Zr^{4+} (0.84 Å) results in a more open structure of ceria vs. YSZ and a larger bottleneck. This culminates in ~one order of magnitude higher ionic conductivity of ceria than YSZ under similar dopant and temperature conditions.[116] Similarly Mg^{2+} conduction in the NASICON derivatives is higher in a $HfNb(PO_4)_3$ based material than in a $Zr_2(PO_4)_3$ based material, at least in part due to the expansion of the conduction pathway.[117]

Layered vs. Spinel Structures – Mitigation of Cation-Cation Repulsion

Although layered structures are prominent Li^+ conductors, they do not appear to support facile multivalent ion transport in the interlayer as previously discussed in regards to TiS_2. Calculations have suggested that widening the layer spacing will significantly reduce the migration barriers of multivalent intercalation in layered TiS_2 by ~ 50%, due to the widening of the triangular face of the diffusion pathway.[104] Similarly, poly(ethylene oxide) (PEO) was inserted in layered MoS_2 to increase the interlayer spacing from 0.615 nm to 1.45 nm. The substantial increase in layer spacing was hypothesized to allow the Mg^{2+} to coordinate strongly to just one side of the interlayer, effectively acting as an ion on a monolayer sheet of MoS_2. Calculations suggest such an increase in layer spacing would result in the decrease of E_m from 2.61 eV in bulk MoS_2,[118] to 0.48-0.22 eV (not verified experimentally).[118, 119] The authors experimentally realized a dramatic 200% increase in capacity in the material with widened layers.[119] However, conclusive evidence that the capacity was a result of solely Mg^{2+} intercalation was not provided. Nonetheless, this remains a viable avenue to decrease the migration barriers of multivalent ions in layered materials. Interestingly, even though $ZnPS_3$ is a layered material, conduction of Zn_2^+ occurs within the metal layer and not through conduction of interstitial defects in the 0.31 nm van der Waals gap.[54] The formation energy of an interstitial defect is high, over 1 eV, likely preventing interstitial stabilization and interlayer conduction.[54]

Unlike layered materials, spinel structures appear among the limited reports of multivalent ion conduction.[45, 101, 120] The spinel structure lends itself towards the potential of high mobility of multivalent ions due to the 3D conduction channels and the relatively large distance between the cation in the transition state and the neighboring cations compared to other crystal structures.[97]. Figure 2.5 illustrates the distance between the mobile ion in the activated state and the nearest immobile

cation in a layered structure (~2.0 Å) vs. that of a spinel structure (~2.85 Å) – based on the distances of layered $LiCoO_2$ and spinel $LiCo_2O_4$. Thus, utilizing structure types that inherently mitigate cation-cation repulsion may be crucial to enabling ambient temperature multivalent conduction.

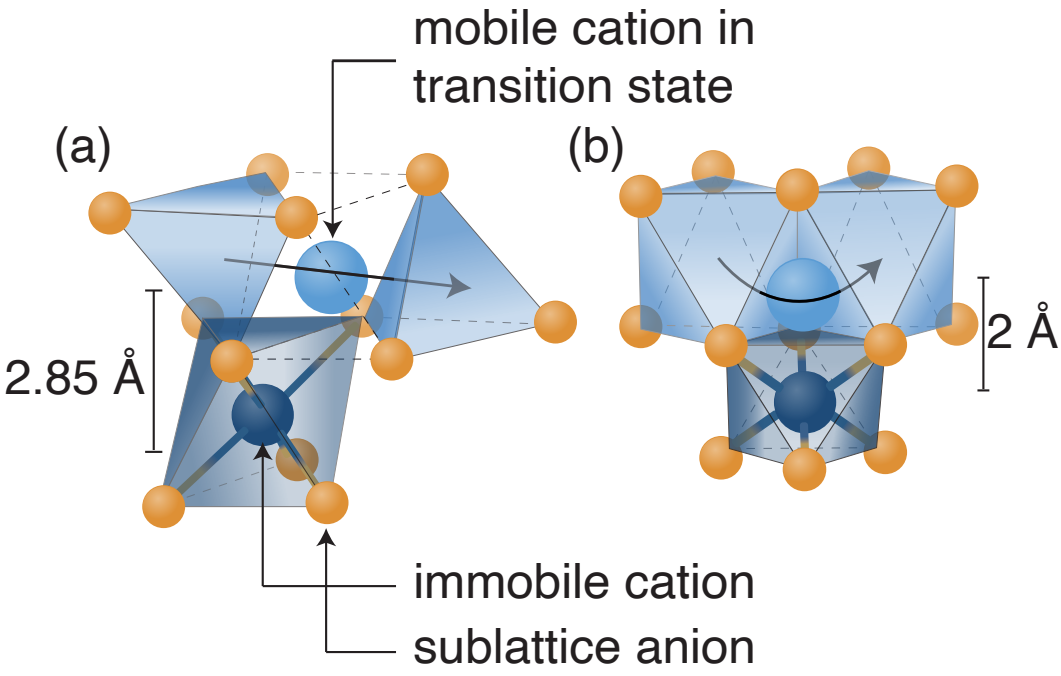

Figure 2.5: An illustration of the distance between the mobile ion in the activated state and the nearest immobile cation in (a) a spinel structure (~2.85 Å) vs. that of an activated mobile ion in (b) a layered structure (~2.0 Å) in which case the mobile ion experiences a greater electrostatic repulsion.

A study by Bonnick *et al.*, highlights the significant impact of cation-cation repulsion on multivalent ion conduction by comparing the diffusion of Li^+ and Mg^{2+} in c−Ti_2S_4. This study demonstrated that initially D_{Li} and D_{Mg} were very similar at ~10^{-8} cm^2s^{-1}. D_{Li} remains relatively constant until ~1.6 Li^+ equivalents are intercalated. However, after ~0.2 equivalents of Mg^{2+} are intercalated, D_{Mg} decreases by ~one order of magnitude. After ~0.55 equivalents of Mg^{2+} are intercalated, D_{Mg} decreases further until it reaches ~10^{-12} cm^2s^{-1} at the end of discharge (E_m increases from ≤550 meV to ~ 850 meV).[101, 121] It should be noted that these diffusion coefficients were calculated by GITT measurements and, as previously discussed, it is known that lack of accurate measurement of surface area of the electrode particles can inflate these values.[94] Nonetheless, analysis of the trends is useful. The initial parity of D_{Li} and D_{Mg} followed by the difference of several orders of

magnitude of D_{Mg} at higher intercalation values highlight the considerable impact of cation-cation repulsion in multivalent ion diffusion. The coulombic repulsion is more detrimental to multivalent ions due to the stronger electrostatic interactions between them, resulting in large increases in D_{Mg}, while D_{Li} remains largely unaffected. The decrease in D_{Mg} has been primarily attributed to the lack of available triple vacancy jumps, in which the octahedral sites surrounding the tetrahedral transition site are both vacant.[122] Triple vacancy jumps have lower E_m than double or single vacancy jumps.[122] As the amount of intercalated cations increases, the chances that the site adjacent to the transition state are occupied increases. Kinetic Monte Carlo simulations conducted by Kolli and Van der Ven suggest that the sharp decrease in D_{Mg} around $x = 0.5$ is correlated with the concentration at which triple vacancy sites are no longer above the percolation threshold.[94] They note that at $\sim x = 0.5$ the diffusion correlation factor, f (see equation 2.4), decreases by approximately four orders of magnitude. The decrease in f signifies the onset of highly correlated diffusion, where Mg^{2+} ions are diffusing back and forth in the disconnected triple vacancy chains. The simulations also show that this effect scales with the repulsion between cations in nearest-neighbor sites.[94] Therefore, due to the stronger coulombic repulsion in multivalent ion systems, the occupancy of too many neighboring sites by charge-dense ions can more readily result in the increase of D by several orders of magnitude, and ultimately the shut-down of the diffusion process, even in structures that are better equipped to mitigate this repulsion. This concept can be applied to other structure types, for instance in the NASICON family, which is amenable to a large variety of substitutions,[36] replacing Zn^{4+} with a 3+ cation like Sc^{3+} may result in weaker cation-cation repulsion in the activated state and thus a lower E_m and a higher σ.

In addition to the sluggish kinetics caused by strong interactions, structural reorganization can block diffusion channels. For instance, in c$-Ti_2S_4$, intercalated Mg^{2+} initially occupies the vacant octahedral sites (16c) until ~0.50 equivalents, after which the coulombic repulsion favors distribution across both tetrahedral and octahedral sites. Conversely, intercalated Li^+ only occupies octahedral sites throughout the entire composition range. The reduction of total possible diffusion pathways and available sites due to tetrahedral site occupation by Mg^{2+} may play a significant role in the decrease of D_{Mg} at high intercalation contents. The occupation of tetrahedral sites by Mg^{2+} blocks six possible diffusion pathways between neighboring octahedral sites, whereas the occupation of octahedral sites only blocks one diffusion pathway between nearest-neighbor tetrahedral sites.[121]

Borohydride Derivatives

To conclude the discussion of favorable structure types, we analyze Mg borohydrides, one of the few reported families of electronically insulating materials which exhibit promising Mg^{2+} conductivity near RT. The parent material $Mg(BH_4)_2$ is a poor Mg^{2+} conductor ($\sim 10^{-12}$ S cm^{-1} at 50 °C, 10^{-9} S cm^{-1} at 150 °C).[46, 52] Whereas, the conductivity of $Mg(BH_4)(NH_2)$ is 3 orders of magnitude higher at comparable conditions (10^{-6} S cm^{-1} at 150 °C), despite having a high activation energy (E_a = 1.31eV). The low conductivity of $Mg(BH_4)_2$ was attributed to the strong covalent bonds between the Mg^{2+} and the four BH_4^- units that form a tetrahedral cage that is difficult for Mg^{2+} to escape from. Conversely, in $Mg(BH_4)(NH_2)$ — two of the B in the tetrahedral cage are replaced by N — the nearest neighbor distance between Mg^{2+} ions is 3.59 Å vs. 4.32 Å, and the introduction of the NH_2 groups provides a zig-zag chain, tunnel framework which is hypothesized to be favorable for Mg^{2+} diffusion. The introduction of other neutral molecules into $Mg(BH_4)_2$, such as ethylenediamine (en) or diglyme has also resulted in similar conductivity increases (10^{-8} and 10^{-9} S cm^{-1} at RT, respectively).[49, 123] Addition of ammonia borane resulted in a more substantial increase in conductivity (10^{-5} S cm^{-1} at RT).[49] The activation energies remain significantly high, consistently at values comparable to Higashi's initial report (E_a between 1-1.5 eV). The improved conductivity after addition of en or diglyme (and partially for ammonia borane) was attributed to the increase of the Mg–B bond distance, the volume, and the distortion of the tetrahedra, the latter two of which have been suggested to increase the number of Mg^{2+} conduction pathways and sites.[49] It is interesting that these structural changes are not accompanied by a significant decrease in E_a, which would logically follow if Mg^{2+} were more easily liberated from the tetrahedra. Moreover, in the case of the "en" substituted borohydrides, the MN energy is such that the compounds with higher E_a exhibit greater conductivity due to an increase in σ_0.[76, 123] Additional studies are likely necessary to confirm the fundamental origin of the increased conductivity. Nonetheless, the addition of the neutral molecules to change the bonding/coordination environments in Mg borohydrides and similar materials does appear to significantly improve the conductivity.

The Polarizability of the Anion Sublattice

Since the motion of the charge-dense multivalent ions has a strong polarizing affect on the anion sublattice, increasing the polarizability of the anions can weaken the bonding interactions, and as a result, lower the E_m. This is evidenced by the fact

that sulfide ionic conductors display higher conductivity and lower E_m than their oxide counterparts,[124] and that the most promising multivalent ion intercalation cathodes and SSEs are sulfide based.

The realization of high multivalent ion mobility in oxides would represent an important discovery in multivalent ionics. It would prove that multivalent ions can display significant conductivity in less polarizable lattices under the right conditions. In this section we will discuss several reports of multivalent ion migration in oxides, highlighting reports with conclusive evidence.

Recent studies have suggested that multivalent ion intercalation into metal oxides can be achieved by overcoming the sluggish multivalent ion kinetics at elevated temperatures (~100 °C). multivalent ion conduction in layered transition metal oxides have been largely focused on vanadium oxides. Mg^{2+} intercalation into α-V_2O_5 in a dry electrolyte was not achieved at RT, but successfully conducted at 110 °C.[125] Additionally, similar papers regarding the tungsten bronze framework $V_4Nb_{18}O_{55}$, and ζ-V_2O_5, indicate promising Mg^{2+} intercalation in dry conditions.[126, 127] In such studies, care must be taken to eliminate contributions from protons produced by thermal decomposition of the organic electrolyte that can convolute high temperature multivalent insertion.[128]

Oxide-based spinel-type Mn_2O_4 compounds have been extensively studied in the recent years. Solid state ^{25}Mg NMR spectroscopy in conjunction with theoretical calculations and μSR were used to determine the Mg^{2+} mobility in $(Mg)_{tet}(Mg_{0.15}Cr_{1.85})_{oct}O_4$, $(Mg)_{tet}(Mn_2)_{oct}O_4$and the partially inverted spinel, $(Mg_{0.41}Mn_{0.59})_{tet}(Mg_{0.41}Mn_{1.59})_{oct}O_4$. Based on the VT NMR motional narrowing, the calculated E_m values were 510 ± 190, 690 ± 90 and 1100 ± 140 meV respectively. [129] Figure 2.6c shows that the E_m values from VT NMR are in good agreement with theoretical calculations and μSR measurements, except for the partially inverted spinel. In the case of the inverted spinel the negligible observed ionic motion resulted in poor spectral resolution.

Interestingly, the partially inverted material displays the highest migration energy even though it has the highest electronic conductivity, providing the greatest capability for electronic shielding. The results indicate that the Mg^{2+} migration in these structures is more strongly affected by the occupation of the octahedral sites by Mg^{2+} than by the electronics. This is in contrast to the previously discussed mechanism for the c$-Ti_2S_4$. However, in the oxide spinels Mg^{2+} preferably occupies the tetrahedral sites, therefore the diffusion pathway is different than in c$-Ti_2S_4$ (tet -> oct -> tet, as illustrated in Figure 2.6a, vs. oct -> tet -> oct, respectively). The

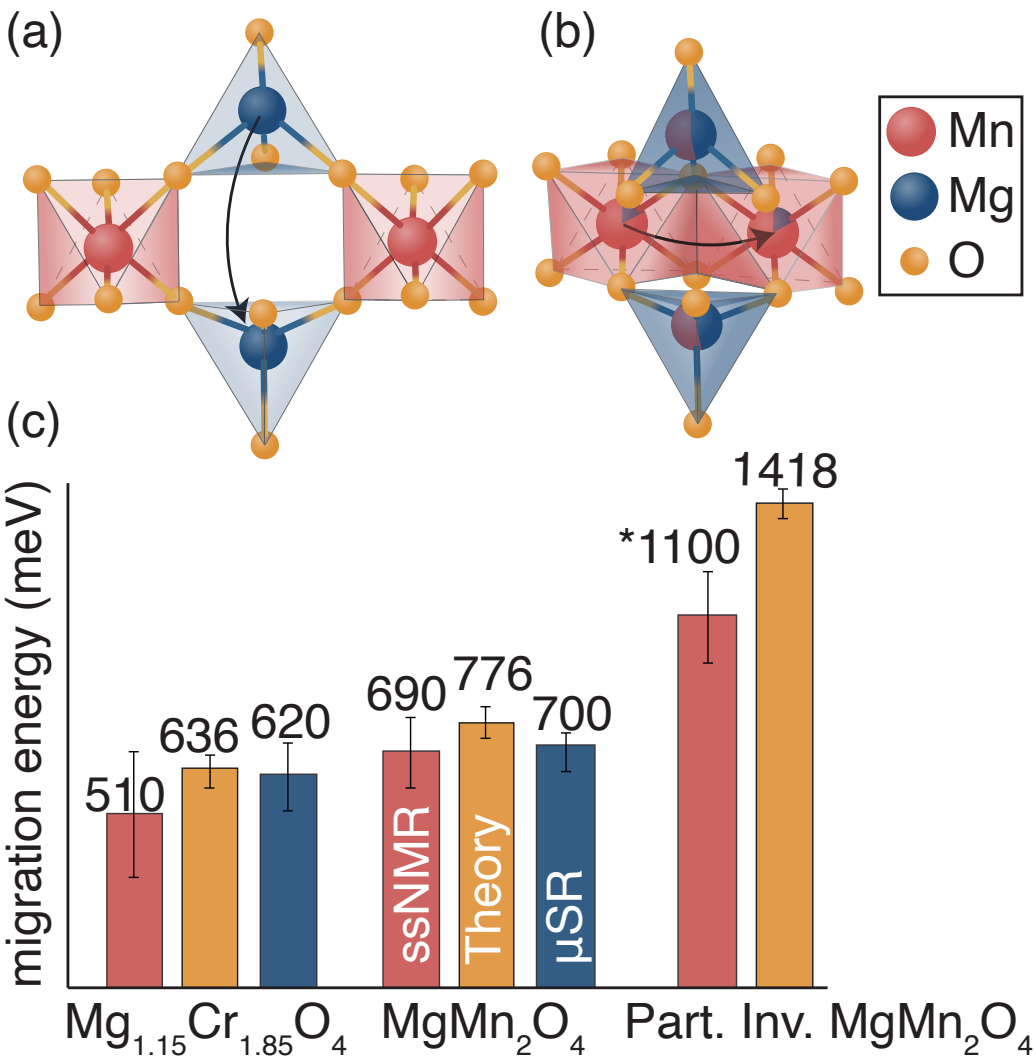

Figure 2.6: Local cation arrangement in (a) normal and (b) inverted spinels, showing the nearest cations to the mobile ion transition state in each case. Arrows highlight Mg migration pathways. (c) Experimentally (ssNMR – red, μSR – blue) and theoretically (orange) calculated activation energies for ion migration in the three spinels. * indicates a semiquantitative estimate due to poor spectral resolution. Reproduced from ref[129] . Copyright 2020 American Chemical Society.

authors suggest that the increased barrier occurs as a result of the octahedral (16d) Mg^{2+} having to move through vacant intermediate tetrahedral sites (46f), which are in close proximity to already occupied tetrahedral sites (8a) (Figure 2.6b).[129] A study by Kwon *et al.* supports this hypothesis by demonstrating that decreasing the Mn–Mg site inversion increased the Mg^{2+} mobility in $MgCrMnO_4$.[130]

An operando synchrotron XRD study by Yin *et al.* was able to elucidate the complex mechanisms of Mg^{2+} insertion and removal from $MgCrMnO_4$ with 18%

Mg–Mn inversion.[120] This structural study showed that up to 0.12 mol of Mg^{2+} per $MgCrMnO_4$ could be reversibly removed from the sample at 90 °C. A further 0.08 mol of Mg^{2+} migrated from the tetrahedral 8a site to the octahedral 16c site due to the stabilization of the octahedral sites by the vacancies created in the neighboring 8a sites after Mg^{2+} extraction. The reversibility of the intercalation was compromised upon insertion of excess Mg^{2+} into the structure. Additionally, the initially inverted Mg^{2+} (occupying the 16d site) was completely uninvolved in the extraction. Only the Mg^{2+} on the 8a tetrahedral site was mobile. The lack of mobility of the 16d Mg^{2+} is attributed to the small triangular faces in the 16d-8a-16d diffusion channel which are ~30% smaller than those in the 8a-16d-8a diffusion channel.[120] Particularly in less polarizable oxide lattices, the smaller migration channel is enough to render Mg^{2+} immobile. Furthermore, although the majority of the observed capacity was revealed to be a result of electrolyte decomposition, it is encouraging that some reversible multivalent intercalation can occur in spinel oxides. Ultimately, this study provides us with new insight into the mechanisms of multivalent ion diffusion in spinel oxides and highlights that the extent of intercalation can be falsely exaggerated by capacity values measured at elevated temperatures.

Unlike that of oxides, the sublattice polarizability of selenides exceeds that of sulides. Thus, selenide-based materials can display even higher multivalent ion mobility than sulfides, at the expense of electrochemical stability. The Se analogue of the Chevrel phase (Mo_6Se_8) can also reversibly intercalate Mg^{2+} with high mobility. Interestingly, Mo_6Se_8 exhibits both complete magnesiation and demagnesiation at RT, whereas about 20–25% of the Mg in the inner sites remains trapped after charging with Mo_6S_8. Complete demagnesiation of Mo_6S_8 is only observed at 60 °C.[131] The different Mg^{2+} extraction behavior of the S and Se analogues is partially attributed to the higher mobility of Mg^{2+} ions afforded by the more polarizable Se framework, and partially due to counterproductive structural factors which will be discussed in the section on local minima traps.[132]

Coordination Environment

The coordination environments of both the original and activated state lattice sites have been suggested to have a meaningful impact on the E_m. A computational study by Rong *et al.* suggests that multivalent ions in a lattice site with an "unfavorable" coordination environment and an activation state with a "favorable" coordination environment result in a significantly lower E_m.[28]

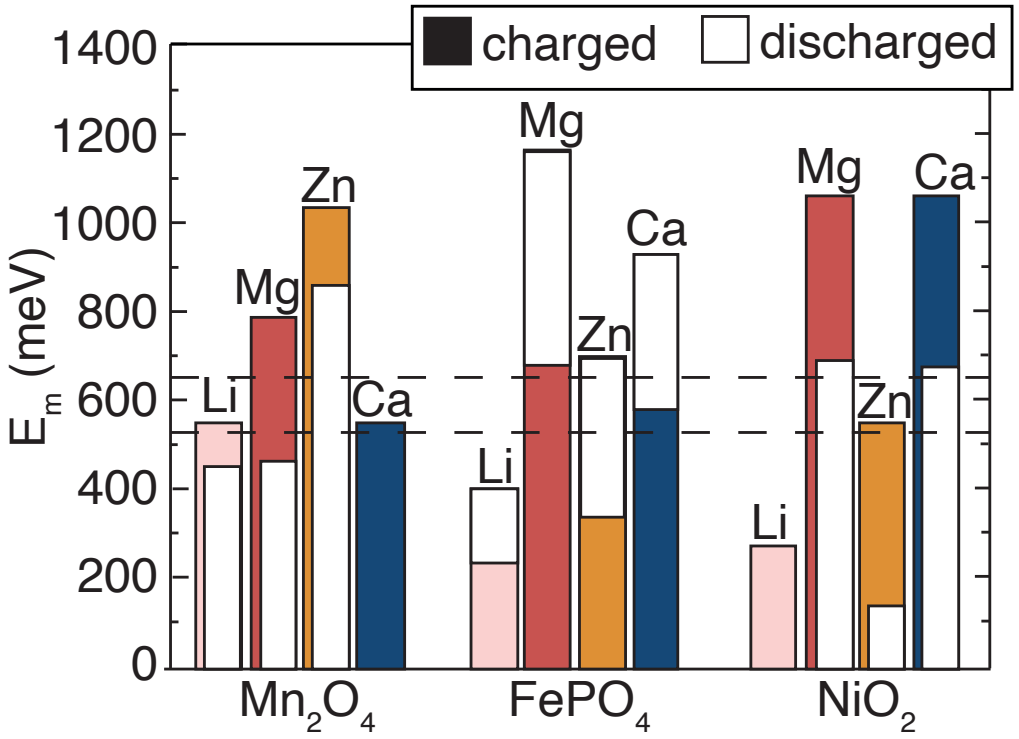

Figure 2.7: A summary of First-principles (NEB) results for migration energies E_m of Li^+ and multivalent ions (Mg^{2+}, Zn^{2+}, and Ca^{2+}) in the spinel Mn_2O_4, olivine $FePO_4$, and NiO_2 structures. The E_m values are compared to the prescribed ~525–650 meV threshold (dashed) for practical application. Reproduced from ref[28] . Copyright 2015 American Chemical Society.

The definition of a "favorable" coordination environment was determined by analysis of structures reported in the Inorganic Crystal Structural Database (ICSD), which showed that in oxides and sulfides Mg^{2+}, Zn^{2+}, and Ca^{2+} are most often found in octahedral, tetrahedral, and 8-coordinate sites, respectively.[133] Therefore, using NEB calculations (summarized in Figure 2.7), Rong *et al.* showed that Mg^{2+} (Zn^{2+}) is likely to have a lower E_m in material wherein the stable lattice site has tetrahedral (octahedral) coordination and the activated state has octahedral (tetrahedral) coordination, e.g., spinel structures (layered NiO_2).[28] This hypothesis has been supported by further calculations by Canepa *et al.* on Mg/Zn sulfide and selenide spinels, in which the Mg and Zn occupied the tetrahedral sites. The results demonstrate that the Mg compounds consistently had lower E_m, and initial experimental evidence was provided in the form of $MgSc_2Se_4$.[45] In addition, minimizing the change in coordination environments along the path by flattening the potential energy landscape over the diffusion channel has been hypothesized to facilitate ionic

conduction.[134] Thus, materials in which the migration path consists of sites with equivalent energies have been suggested to be ideal.[134]. Materials with multivalent ions in "unfavorable" coordination environments seem to consistently have low E_m in NEB calculations. In reality, if a more favorable intermediate coordination site is available, then the material is likely to form antisite defects which could block conduction pathways. Ultimately, more experimental evidence is needed to confirm the proposed hypothesis.

Structural Flexibility

Medium-long range disorder

Amorphous/disordered structures may offer enhanced mobility of multivalent ions by providing a network capable of absorbing considerable deformations. Additionally, the structural flexibility and accommodation of free spaces in the structure allows for smooth diffusion pathways of multivalent ions.[135] Despite the difficulty of achieve multivalent ionic intercalation in ordered oxide materials, a recent study suggested that between 0.22-0.33 equivalents of Mg^{2+} can be inserted into 10 nm particles of chemically delithiated, defective $FePO_4$ at RT.[135] Although no explicit mobility studies were reported, the possibility of significant reversible intercalation was attributed to the medium and long-range structural disorder afforded by the defective structure.

Amorphous structures may achieve high ionic conductivity at low temperatures by leveraging the paddlewheel mechanism, (Figure 2.3d) which is typically observed in high temperature crystalline polymorphs. Smith and Seigel suggest that the paddlewheel mechanism contributes to Li^+ mobility in glassy Li^+ ion conductors that contain polyanions.[78] The rationale presented was that the lower density afforded by the amorphous structure vs. the crystalline analogue provides additional free volume to enable anion rotations. Additionally, the lack of a long-ranged covalent polyanion network, engineered by limiting the polyanion content of the glass, enables the more isolated polyanion entities to rotate more readily.[78] Similar structures could also prove to be effective for conducting multivalent ions via the paddlewheel effect.

A few attempts to develop multivalent SSEs utilizing glassy compounds have been reported. An amorphous mixture of MgS-P_2S_5-MgI_2 was obtained by ball milling and showed increasing conductivity with MgI_2 content, reaching a max of 10^{-8} S cm^{-1} at 200°C.[136] The crystallized glass ceramic was shown to have a conductivity

one order of magnitude higher than the glass. The conductivity increase of the glassy ceramic was attributed to the presence of $MgPS_3$. Preliminary results in our group suggest that ordered $MgPS_3$ is not an effective solid state Mg^{2+} conductor but perhaps the $MgPS_3$ embedded in the glass ceramic has a high concentration of defects that facilitate ion conduction.

Moreover, careful study of $Mg(BH_4)(NH_2)$ suggests that an increase in amorphous product increases conductivity. Optimization of the synthesis conditions ensured that impurities were not contributing to the initially reported Mg^{2+} conduction in $Mg(BH_4)(NH_2)$. No crystalline impurities were observed, but ^{11}B NMR revealed an amorphous impurity phase which formed a glass-ceramic like composite.[47] The glass-ceramic composite material displayed a conductivity of 10^{-6} S cm^{-1} at 100 °C – three orders of magnitude higher than Higashi's initial report. The increased conductivity (and slightly reduced E_a – 1000-1300 meV) was attributed to the presence of the amorphous phase. Notably, crystallizing the impurity phase decreased the conductivity of the material. Similarly, the stabilization of an amorphous form of $Mg(BH_4)_2{\cdot}2NH_3$ by combination with 75 wt% MgO nanoparticles resulted in an increase in the conductivity at RT by three orders of magnitude, and a significant reduction in E_a over the crystalline phase.[51]

Flexible Covalent Components

In structures with long-range order, especially electronic insulators in which there is no screening of the charge-dense multivalent ions, flexible components that can distort or rotate in response to multivalent ionic conduction to facilitate lower energy activated states may be important to realize high conductivity. For instance, $ZnPS_3$ is a rare example of multivalent ion conductivity with low E_a in an electronic insulator. The E_a of $ZnPS_3$ was measured experimentally to be 350 meV, agreeing with NEB calculations.[54] The NEB calculations suggest that the flexibility of the $[P_2S_6]^{4-}$ polyanion is responsible for the strikingly low activation energy for solid state divalent ion conduction in $ZnPS_3$, which is comparable to many superionic Li^+ conductors.[23]

In $ZnPS_3$, Zn^{2+} conducts through a vacancy-hopping mechanism. As illustrated in Figure 2.8, the activated state is stabilized by a distortion of the $P_2S_6{}^{4-}$ polyanion into the van der Waals gap, which widens the diffusion bottleneck (triangular face of the octahedra), decreasing coulombic interactions and ultimately enabling facile multivalent ion conduction.[54]

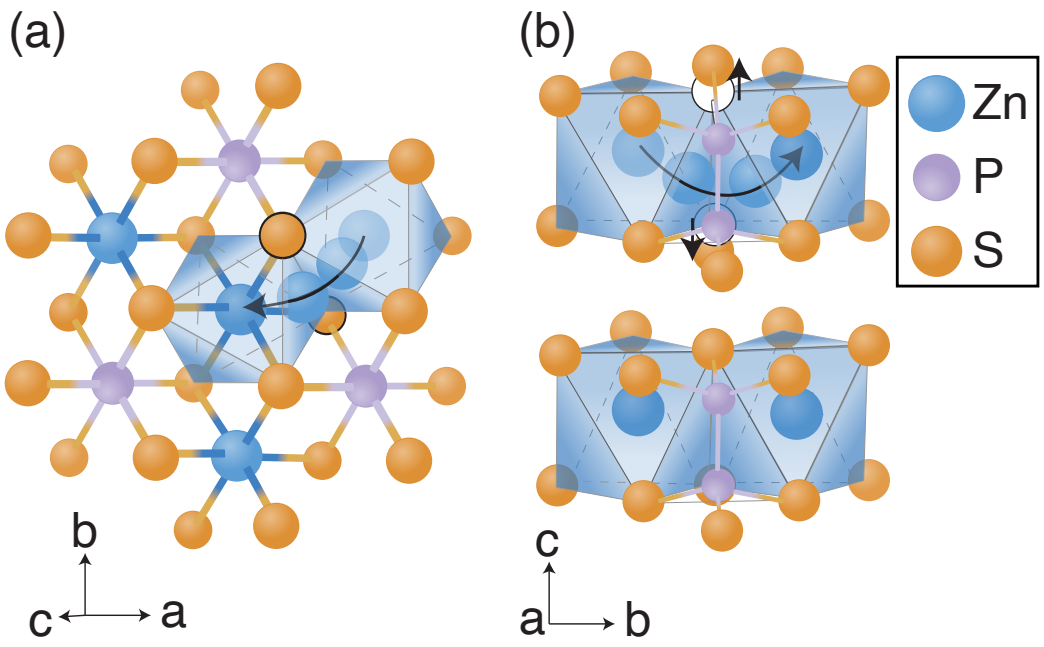

Figure 2.8: An illustration of the lowest energy diffusion pathway in $ZnPS_3$ (a) top down view, and (b) viewing along the *a* axis. The Zn^{2+} ions migrate through the octahedral faces into the neighboring site, the S atoms along the shared edge (highlighted) distort into the van der Waals gap to facilitate the low E_m.

Conductivity enhancements in some $Mg(BH_4)_2$ derivatives have also been attributed to the flexible nature of the added neutral molecule. $Mg(BH_4)_2(NH_3BH_3)_2$, as previously discussed, experiences a significant increase in conductivity over $Mg(BH_4)_2$. In addition to the tetrahedral expansion and distortion, the flexibility of the NH_3BH_3 molecules, which can be displaced or can rotate slightly to accommodate migrating Mg^{2+} ions, is suggested to be a major factor in the increased conductivity.[49] This hypothesis is pending confirmation through future studies. Using QENS, Burnakova *et al.* demonstrated that in $Mg(BH_4)_2$-$diglyme_{0.5}$, the diglyme molecules coordinated to the Mg are flexible and likely help to facilitate the high conductivity of 2 x 10^{-5} S cm^{-1} at 70 °C (E_a is not reported). Additionally, the high conductivity of $Mg(BH_4)_2NH_3$ (3.3 x 10^{-4} S cm^{-1}at 80 °C, ~eight orders of magnitude higher than $Mg(BH_4)_2$) is attributed to the high structural flexibility of $Mg(BH_4)_2NH_3$ due to the dihydrogen bond network between the terminal BH_4^- and the NH_3 molecule which links the –BH_4–Mg–BH_4–Mg– chains, in addition to the versatile BH_4^- coordination.[51] The flexible nature of this bonding network is capable of stabilizing the mobile ion in a wide range of coordination environments.

2.7 Potential Structural Pitfalls

During the investigation of solid state multivalent ion diffusion, several instances of other structural effects that hinder or arrest multivalent ionic conduction besides strong coulombic interactions have been identified. Highlighting these circumstances and the structural motifs that enable them is equally as important as focusing on the factors that enable multivalent ion diffusion in solids. This section will discuss ionic trapping in local minima, vacancy ordering, and vacancy-dopant ion pair binding. A superionic multivalent ion conductor will need to overcome these structural pitfalls.

Local Minima Traps

To facilitate long-range ionic conduction, excessive trapping of ions in local minima must be avoided. Although the last ~25% of Mg^{2+} ions in Mo_6S_8 seem to be trapped at RT, Levi *et al.* showed that the Mg^{2+} diffusivity in Mo_6S_8 varied several orders of magnitude depending on the intercalated Mg^{2+} content. At high Mg^{2+} concentrations, D_{Mg} was $\sim 10^{-13}$ cm^2s^{-1} but was below the detection limit at low Mg^{2+} concentrations.[137] In a later study, it was estimated to be $\sim 10^{-15}$ cm^2s^{-1}.[138] NEB and *ab initio* molecular dynamics (AIMD) calculations suggest that the E_m only changes by ±50 meV across the whole range of Mg^{2+} intercalation from $x = 0$ to 2.[138] Thus, the experimentally observed change in diffusivity in Mo_6S_8 at low Mg^{2+} content is seemingly not kinetic in origin. Structural studies combining X-ray and neutron diffraction of both the S and Se Chevrel phases determined that in Mo_6S_8, intra-ring jumps (both inner–inner and outer–outer) are much easier than inter-ring jumps (inner–outer) due to the shorter jump distance of ~0.9 Å vs. ~2.0 Å, respectively.[139, 140] Whereas in Mo_6Se_8, and $Mo_6S_{8-y}Se_y$, $y \leq 2$,[141] intercalation causes a structural distortion from rhombohaedral to triclinic leading to a widening of the inner ring and an elongation of the intra-ring jumps to 1.3 Å. The widening of the inner ring levels causes congruence of the energy manifolds associated with inter vs. intra-ring jumps and thus enables long-range transport in the Se analogue without significant thermal agitation.[97, 139, 140] It is hypothesized that during extraction of the first equivalent of Mg^{2+} from Mo_6S_8, the coulombic repulsion between Mg^{2+} ions in neighboring outer and inner sites promotes inter-ring jumps, resulting in long-range diffusion. This hypothesis is supported by the fact that using $Cu_xMo_6S_8$, the precursor for Mo_6S_8, as the cathode material avoids the stage of total cation extraction and results in complete demagnesiation at RT. The mobile Cu^+ ions push Mg^{2+} from the inner to outer

sites at low levels of magnesiation, when the Mg^{2+}–Mg^{2+} interactions are no longer prevalent.[142] These results support that concerted mechanisms help to promote fast long-range diffusion in structures with complex cation sites.

Vacancy Ordering

The energetic benefit of vacancy ordering at intermediate compositions during intercalation can cause an increase in the barrier to continued ionic conduction. Again examining the Chevrel phase Mo_6S_8, recently, Ling *et al.* suggested that the low diffusivity and trapping at low Mg^{2+} content is a result of long-range vacancy ordering along the <001> direction. Such vacancy ordering stabilizes the structure by decreasing the repulsive interactions between Mg^{2+} sites. Calculations suggest that the stabilization results in the formation of several intermediate phases throughout deintercalation, with energies up to 300 meV lower than the disordered alternative. The formation of these predicted intermediate phases has not yet been proved or disproved by structural studies. Nonetheless, the formation of long-range ordered vacancy super structures must be highlighted as a pitfall to multivalent ion diffusion in solids specifically due to the stronger coulombic interactions that are mitigated by such a transformation.[138]

Vacancy Pair Binding

A high concentration of carriers is essential to high ionic conductivity (equation 2.5). The concentration of vacancies is generally the limiting factor to long-range percolation in multivalent conductors, and thus, the vacancy concentration can be effectively considered as the carrier concentration. Aliovalent substitution is a common method utilized to drastically increase the carrier concentration in solid state conductors through the introduction of extrinsic vacancies. For example, the aliovalent substitution of a 4+ cation with a 3+ or 2+ cation in the case of YSZ and ceria-gadolinia (CGO) is needed to obtain high conductivities vs. the pristine material. In this case, a maximum in conductivity occurs at relatively low dopant concentrations ($\leq$ 10%). Further increasing the vacancy concentration leads to a decrease in conductivity.[143] This has been attributed to: (1) the coulombic binding energy between the effectively negative dopant and the positive oxygen vacancy, and (2) the interaction between the vacancy and the substituent ion due to the ability of the localized vacancy to relieve the elastic stain imposed on the lattice resulting from the size difference between the original and the substituent cation.[143, 144] The second effect is illustrated in Figure 2.9 and was hypothesized to be the more

important interaction because not all substituent ions of the same charge affect the conductivity in the same way.

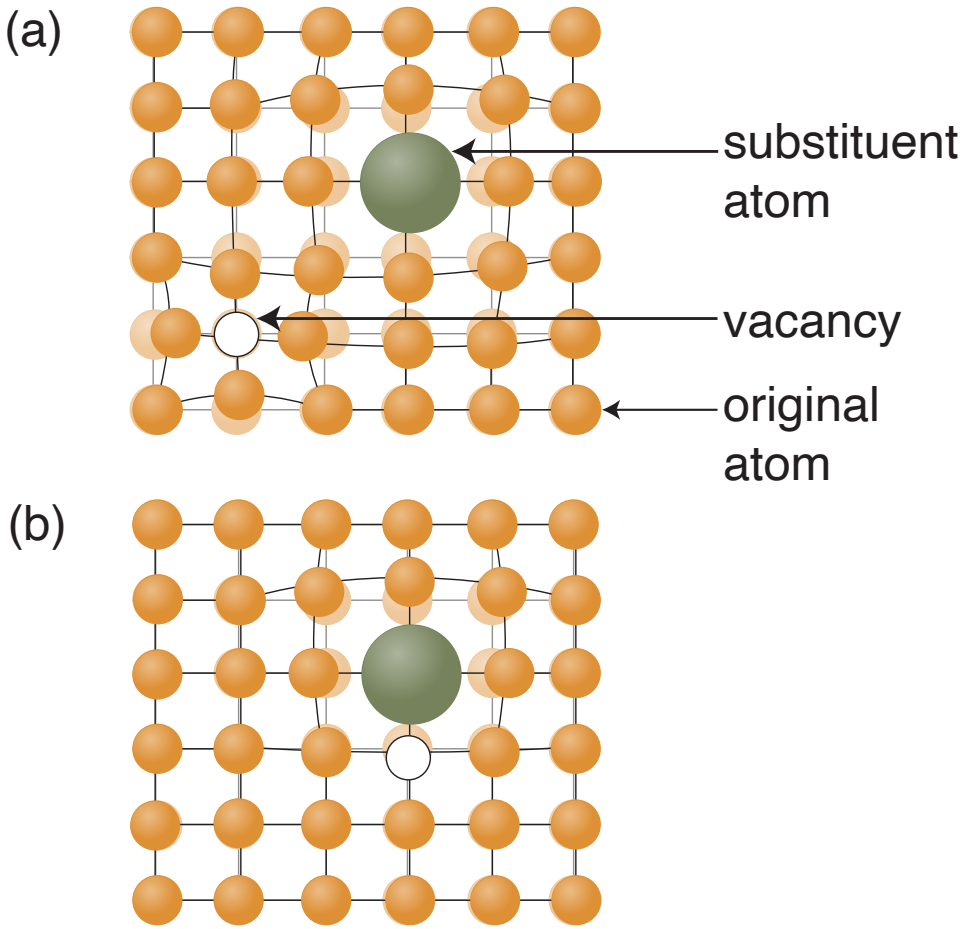

Figure 2.9: Illustration of introduction of a vacancy through aliovalent substitution with a large substituent atom. Both the vacancy and the substituent atom impose strain on the lattice. The induced lattice stain is greater when (a) the vacancy and the substituent atom are separated than (b) when the vacancy is adjacent to the substituent.

The pair binding energy of the vacancy and the substituent ion is minimized when the substituent is similar in size to the original ion, thus the lattice distortions are minimized. It follows that Sc (8.70 Å in 8-CN environment) stabilized Zr has a higher conductivity than YSZ, due to the more comparable size of Sc and Zr than Y and Zr. Similarly, Gd (1.05 Å in 8-CN) substituted ceria is also one of the best O^{2-} conductor. In higher dopant concentrations the complex defect pair of bound dopant cations and vacancies are increased. Since the bound pairs are not easily

separated, the available sites for multivalent ion hopping are decreased, resulting in both lower mobilities and decreased conductivity.

2.8 Summary

This chapter provides an in-depth analysis of solid-state multivalent ion conduction, a fundamental aspect critical for developing advanced battery technologies beyond traditional Li-ion systems. It examines the unique challenges associated with the conduction of multivalent ions due to their high charge densities or large size and how these challenges can be mitigated through structural properties or modifications. Additionally. the inadequacies of current characterization techniques for selectively capturing the mobility of multivalent ions are highlighted.

The key factors that can facilitate solid state multivalent conduction are charge screening — with mobile electrons or ligand molecules, the geometry and size of conduction pathways, the polarizability of the anion framework, the coordination environment of the mobile ion and structural flexibility.

Chapter 3

ATTEMPTED SOLID STATE MULTIVALENT ION CONDUCTORS

3.1 Abstract

This chapter investigates the development of multivalent ion conductors with the aim of achieving high ionic conductivity through a variety of approaches, including aliovalent substitution of both cations or anions, introduction of defects or amorphization through ball milling, and the synthesis of novel materials. Drawing inspiration from efficient Li^+ conductors in combination with chemical intuition about properties that may lead to high multivalent mobility, we targeted a range of materials, such as, Ca thioolivines, multivalent argyrodites, $ZnLa_6Si_2S_{14}$, $CaIn_2S_4$ thiospinel, and NASICON-like phases, to evaluate their divalent ion conduction properties. Despite containing promising characteristics, many of the targeted materials did not exhibit significant ionic conductivity at ambient temperatures. Further, we explored amorphous divalent ion-containing phases and mechanochemical synthesis methods. Challenges encountered include phase purity, the presence of immobile cations that block conduction pathways, and sample pellet density. The results indicate that while progress has been made in developing design rules that may enable room temperature multivalent ionic conduction, further optimization and exploration are needed to realize useful multivalent ion conductors.

3.2 Introduction

To develop a fundamental understanding of divalent ion diffusion in the solid state, we aimed to prepare electronically insulating materials devoid of redox centers, that could be used both for fundamental studies of divalent ion diffusion and as a divalent ion solid state electrolyte. Based on the structure-property relationships hypothesized to impact solid state ionics of multivalent ions, as discussed in Chapter 1, we identified, synthesized, and characterized several materials both computationally and experimentally. In some cases, the materials were pre-screened computationally using the SoftBV package,[145] an adaptation of bond valence site energy (BSVE) analysis.[146] BVSE has previously been applied to Mg^{2+} conduction in inorganic oxides and was shown to produce comparable estimates to E_a as DFT calculations at a fraction of the cost.[147] The successfully synthesized materials underwent ex-

perimental investigations, including structural and electrochemical characterization. Promising materials were further subjected to chemical or structural modifications, like aliovalent substitution or ball milling, to increase the defect concentration and potentially enhance the ionic conductivity.

3.3 Attempted Materials and Modifications to Achieve Enhanced Mobility of Multivalent Ions

Increasing Zn^{2+} Conduction in $ZnPS_3$

Earlier work in the See group investigated $ZnPS_3$ as a potential Zn^{2+} conductor.[54] $ZnPS_3$ crystallizes in 2D sheets of octahedrally coordinated Zn^{2+} and $[P_2S_6]^{4-}$ polyanions. The sheets are separated by a van der Waals gap of approximately 3.3 Å. In the initial study, we demonstrated that $ZnPS_3$ exhibited high Zn^{2+} mobility, with an E_a of 351 ± 99 meV, which is comparable to superionic Li^+ conductors.[54] DFT calculations by our collaborator suggest that conduction occurs in the metal layer and that facile Zn^{2+} diffusion is enabled by the flexible, polarizable $[P_2S_6]^{4-}$ polyanion, which can distort into the van der Waals gap to widen the conduction pathway. However, despite the low E_a, the ionic conductivity of $ZnPS_3$ is also low, ranging from 10^{-8} to 10^{-6} mS cm^{-1}. Therefore, we attempted to increase the conductivity of $ZnPS_3$ with a variety post-synthetic modifications that are discussed below.

Aliovalent Metal Substitution

Initially, to increase the Zn^{2+} conductivity of $ZnPS_3$ we employed aliovalent substitution. This method involves introducing a higher valent metal in place of Zn^{2+}, creating metal-site vacancies to maintain charge neutrality. Since we hypothesize that Zn^{2+} conduction in $ZnPS_3$ occurs through a vacancy-hopping mechanism, by introducing vacancies in a controllable fashion at much higher concentrations, the ionic conductivity of the material can be increased.

We successfully substituted various closed-shell higher valent cations (Al, Ga, In, or Ge) into the $ZnPS_3$ lattice in place of Zn through stoichiometric reaction of Zn, the metal substituent, P_2S_5, and S. The reactions targeted a stoichiometry of $Zn_{1-1.5x}M^{3+}_xPS_3$, where M = Al, Ga, or In, and $0 < x < 0.25$, or $Zn_{1-2y}Ge^{4+}_yPS_3$ where $0 < y < 0.1$. XRD analysis of the products indicated that the same crystal structure was maintained at the targeted substitution levels (Figure 3.1b). Additionally, no new vibrational modes appeared in the Raman spectroscopy (Figure 3.1a), supporting

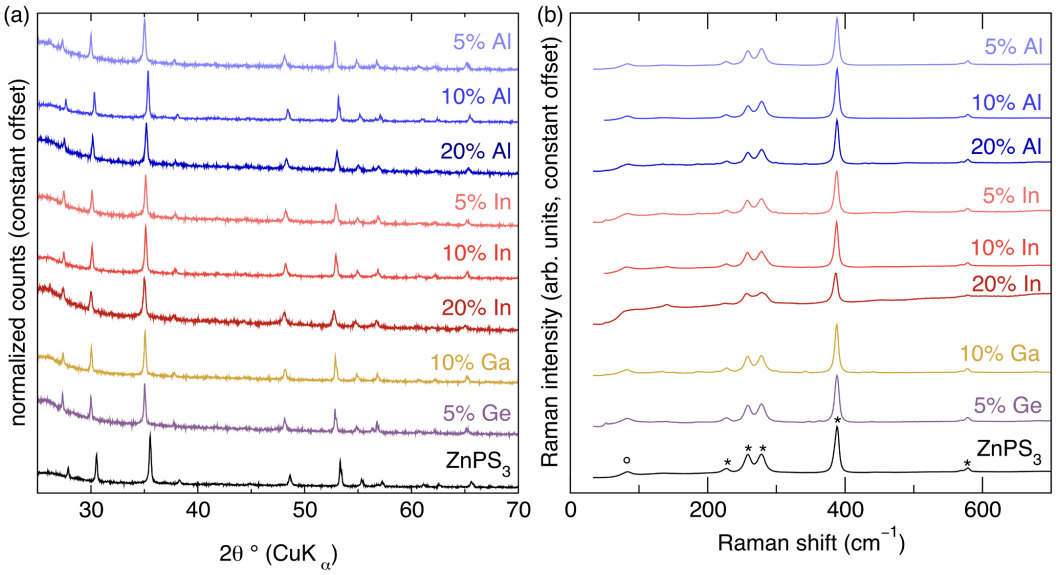

Figure 3.1: (a) XRD and (b) Raman spectroscopy of aliovalent substituted $ZnPS_3$: $Zn_{1-1.5x}M^{3+}{}_xPS_3$. No new reflections or vibrational modes are observed in the data upon aliovalent substitution, indicating that a single isostructural phase forms in all cases. The circle and asterisks in (b) indicate the Zn translational and $[P_2S_6]^{4-}$ vibrational modes, respectively.

the fact that the aliovalent substitution onto the $ZnPS_3$ lattice is achieved without major changes to the structural dynamics of the $[P_2S_6]^{4-}$ polyanion and precluding any microscopic phase separation that is not observable via XRD.

The substitution of Al^{3+}, Ga^{3+}, In^{3+}, or Ge^{4+} for Zn^{2+} and the creation of vacancies does not drastically change the electronic structure of the material due to the closed-shell electronic configuration of the substituents. No obvious color changes were observed at low concentrations of aliovalent substitution, contrasting to the substitution of open-shell transition metals for Zn or Mg. The Nyquist plot of $Zn_{0.95}Al_{0.1}PS_3$, which is representative of all high impedance samples discussed in this chapter unless otherwise noted, is shown in Figure 3.2. The high-frequency region is highlighted in the inset of Figure 3.2 showing no x-intercept at frequencies that could be correlated with bulk conductivity. The low-frequency region solely contains a "blocking" or capacitive feature, likely because the low ionic and electronic conductivity of this material results in capacitive-like behavior between the Au electrodes. Therefore, we found that the introduction of stoichiometric vacancies did not meaningfully change the ionic conductivity of $ZnPS_3$. This could be due to the introduction of more charge-dense, immobile cations that may block the 2D conduction pathways in the lattice and inhibit Zn^{2+} mobility.

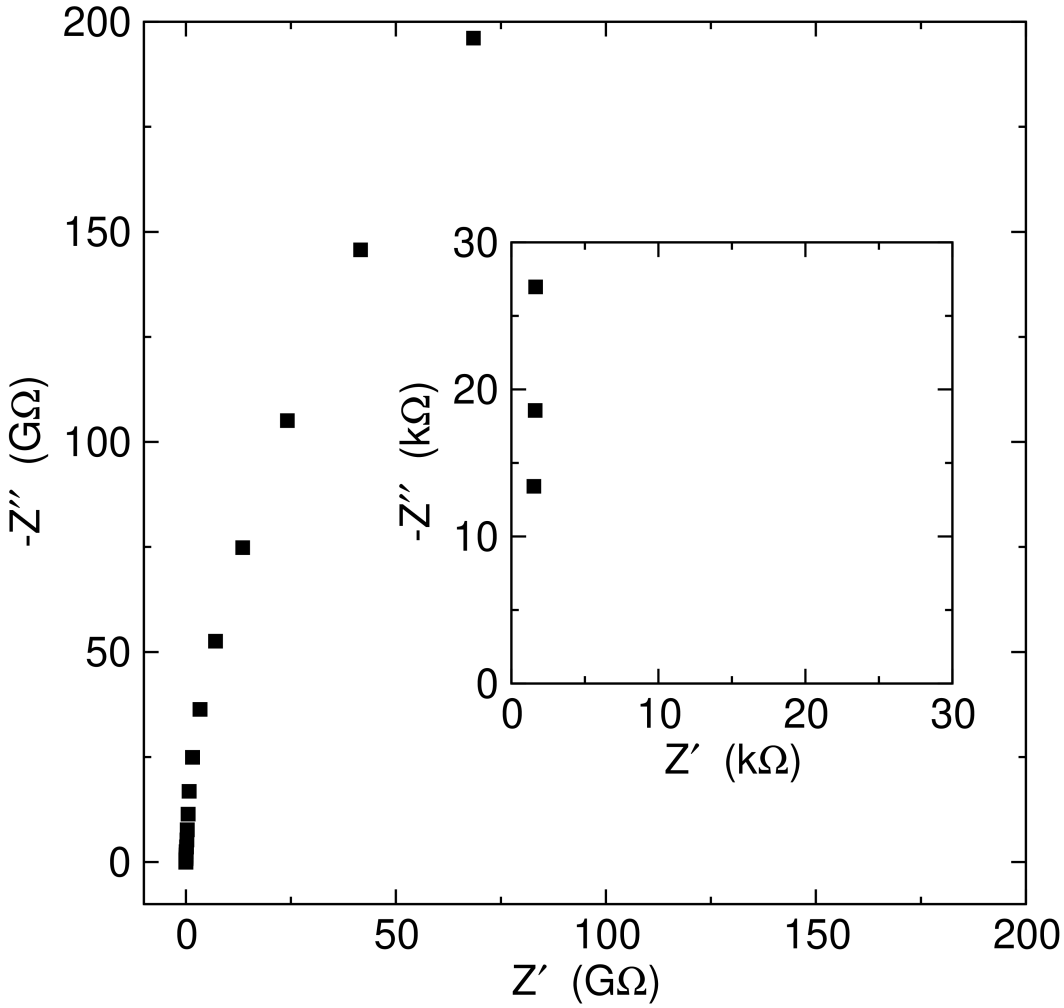

Figure 3.2: Nyquist plot of $Zn_{0.95}Al_{0.1}PS_3$ in a spring-loaded Swagelok cell with symmetric sputtered Au electrodes at ambient temperature. The inset shows the high frequency region of the Nyquist plot to highlight that there is no x-intercept at high frequency in these high impedance samples as there is in low impedance samples.

Aliovalent Anion Substitution

Since the introduction of vacancies through metal substitution did not result in a significant increase in conductivity, we attempted to avoid the detrimental immobile substituent cations blocking the migration pathway by introducing vacancies through anion substitution. We substituted Cl into the $ZnPS_3$ lattice in place of S, using a stoichiometric reaction of Zn, $ZnCl_2$, P_2S_5, and S. The reactions targeted a stoichiometry of $Zn_{1-0.5x}PS_{3-x}Cl_x$, $0 < x < 0.2$. Although there is less precedent for anion substitution in MPS_3 materials compared to cation substitution, the XRD results indicated that the structure was maintained and no crystalline impurities were

present. The resulting powder was a pale green instead of the off-white color of pristine $ZnPS_3$. However, similarly to the metal substitution, no significant increase in conductivity was observed. This could be explained by a lack of Cl integration into the lattice — further characterization, including Raman spectroscopy, SEM or ^{35}Cl MAS NMR should be conducted to determine if Cl is integrating into the $ZnPS_3$ structure or forming amorphous impurities. If no amorphous impurities are identified, elemental analysis should be conducted to ensure the intended vacancy concentration is present in the material.

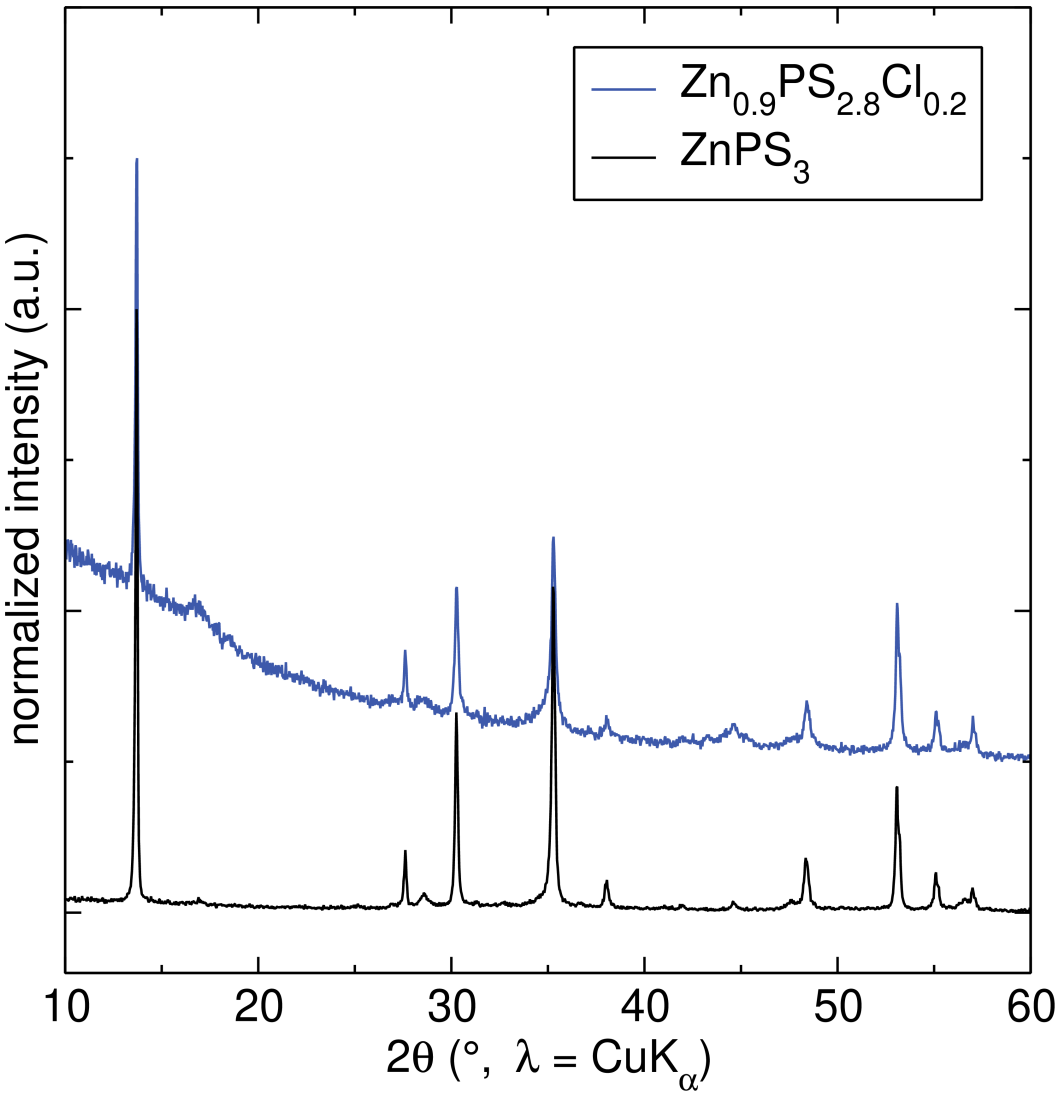

Figure 3.3: XRD of aliovalent anion substituted $ZnPS_3$: $Zn_{1-0.5x}PS_{3-x}Cl_x$,. No new reflections are observed in the data upon aliovalent substitution, and no remnant crystalline $ZnCl_2$ is present, suggesting that a single isostructural phase forms in all cases.

Despite the inability to enhance the Zn^{2+} conductivity of $ZnPS_3$ through aliovalent substitution, ultimately this is achieved via the introduction of water molecules to leverage solvent-assisted ionic conduction mechanisms. This is discussed extensively in Chapter IV.

Calcium Containing Thioolivine Phases, Ca_2MS_4

Taking inspiration from phases that are efficient Li^+ conductors, like the Li-ion cathode $LiFePO_4$ — which has relatively poor electronic conductivity but good Li^+ (de)insertion kinetics — we investigated isostructural Ca thioolivines, Ca_2MS_4 (M = Si, Ge, Sn). This phase displays characteristics that have been hypothesized to lead to high ionic mobility: it contains a polarizable anion framework, which decreases the strength of the electrostatic interactions, and edge-sharing Ca octahedra, which provide clear diffusion pathways around the MS_4 polyanions. Ca_2MS_4 compounds were synthesized by mixing stoichiometric amounts of CaS, M, and S, and heating in an evacuated ampuole at 900 °C for 24 h.

Figure 3.4 shows the XRD patterns, Rietveld refinements — to determine phase purity — and colors of the resulting product powders. A pure phase of Ca_2GeS_4 readily formed, however EIS measurements suggested there was no meaningful ionic conductivity at or near ambient temperature. We increased the vacancy concentration through aliovalent substitution by substituting Ge for Ca. $Ca_{1.9}Ge_{0.8}P_{0.2}S_4$ was successfully synthesized based on XRD analysis, but did not exhibit increased conductivity. Retrospective SoftBV calculations suggested that the E_a for Ca^{2+} conduction in any direction was > 2 eV, as such, despite the clear 3D diffusion pathways and the sulfide framework, the electrostatic interactions in Ca_2MS_4 are likely too strong for ambient temperature conduction.

Multivalent Argyrodites, $M_{3.5}PS_{5.5}I_{0.5}$

We again drew inspiration from Li^+ conductors. Superionic conductors like cubic $Li_7La_3Zr_2O_{12}$ (LLZO), $Li_{10}GeP_2S_{12}$ (LGPS), and Li_6PS_5X (Li argyrodites) all have a connected network of partially occupied Li sites. This structural motif is not often observed in multivalent ion containing compounds. However, a material with an argyrodite-like structure with a partially occupied network of Cd^2+, $Cd_{3.25}PS_{5.5}I_{0.5}$, was previously reported,[148] leading us to hypothesize that this compound may exhibit Cd^{2+} conductivity and that we could potentially synthesize analogues containing more energy-relevant multivalent ions.

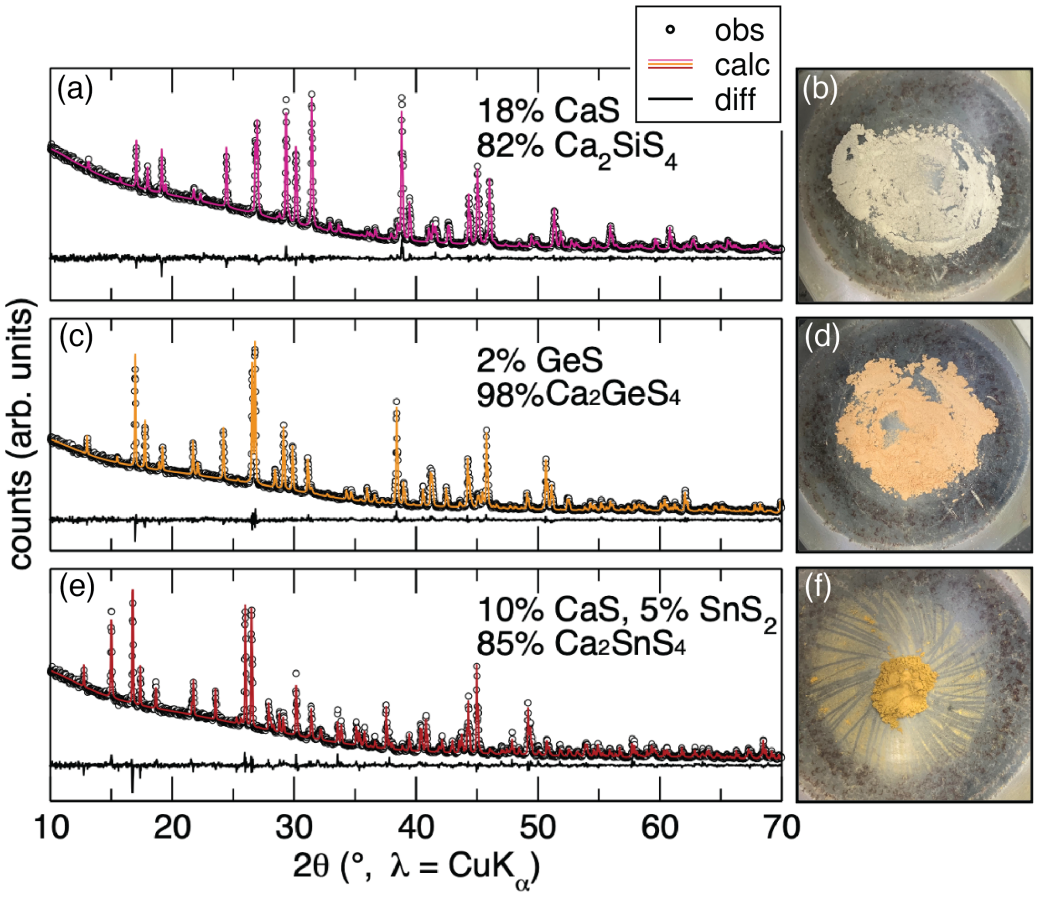

Figure 3.4: The XRD patterns and Rietveld refinement of attempted synthesis of Ca_2MS_4 (M = Si, Ge, Sn) compounds and the resulting powders.(a), (c), and (e) show XRD of synthesis attempts of M = Si, Ge, and Sn, respectively, and (b), (d), (f) show off-white, pale orange, and yellow powder resulting from M = Si, Ge, and Sn synthesis attempts, respectively.

Figure 3.5 shows the structures, XRD patterns and Rietveld refinements synthesized Cd argyrodite phases. We successfully synthesized $Cd_{3.25}PS_{5.5}I_{0.5}$ by traditional solid state synthesis, as opposed to the chemical vapor transport method in the report, and also synthesized Cd_3PS_5I and Cd_3PS_5Cl, which were not previously reported. These materials were synthesized by mixing stoichiometric amounts of CdS, CdI_2 and P_2S_5 and heating in an evacuated ampule for 1 week at 550 °C.

Although the partially ordered network of Cd^{2+} ions were hypothesized to facilitate high mobility, none of these phases exhibit long range Cd^{2+} conduction. This is potentially due to a lack of connectivity between the more isolated "cages" of Cd^{2+} ions than in the Li argyrodite structures, potentially leading to local mobility but not

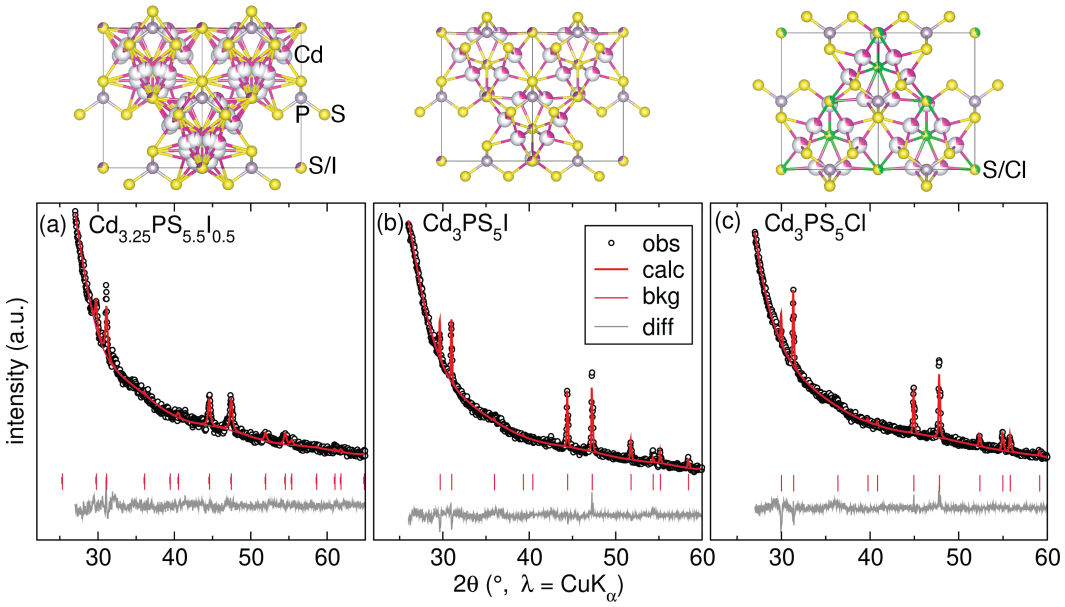

Figure 3.5: The structures, XRD patterns and Rietveld refinements synthesized Cd argyrodite phases, (a) $Cd_{3.25}PS_{5.5}I_{0.5}$, (b) Cd_3PS_5I, and (c) Cd_3PS_5Cl. To the best of our knowledge Cd_3PS_5I and Cd_3PS_5Cl have not been previously reported.

bulk transport as measured in EIS. Alternatively, the large size of the Cd^{2+} cations might hinder intercage jumps and long-range mobility.

Additionally, analogous Zn, Mg, and Ca argyrodyte phases were inaccessible through traditional solid state synthetic routes, likely due to the stability of the binary sulfide. Initial attempts to access these phases through mechanochemical synthesis were unsuccessful but could be further explored. The mechanochemical attempts were based on synthesis of some Li argyrodites that could not be accessed through solid state synthesis, like Li_7GeS_5Br,[149]. Typically, a stoichiometric amount of the metal sulfide, the metal chloride and P_2S_5 in batches of about 1 g in a planetary ball mill with YSZ containers and balls for 20 hours at 380 rpm, followed by an annealing step at 500, 600, or 700 °C for six hours.

$ZnLa_6Si_2S_{14}$

We targeted $ZnLa_6Si_2S_{14}$ because it contains "unfavorable" octahedral Zn^{2+} connected in a 1D chain of face-sharing octahedra with half of the Zn sites vacant in the pristine material. Additionally, $ZnLa_6Si_2S_{14}$ contains a polarizable anion framework, a combination of factors that seem ideal for ionic conduction via a vacancy-mediated ion hopping mechanism. $ZnLa_6Si_2S_{14}$ can be synthesized by a solid-state reaction of ZnS, *M*, La_2S_3,and S.[150] Using SoftBV, we computationally

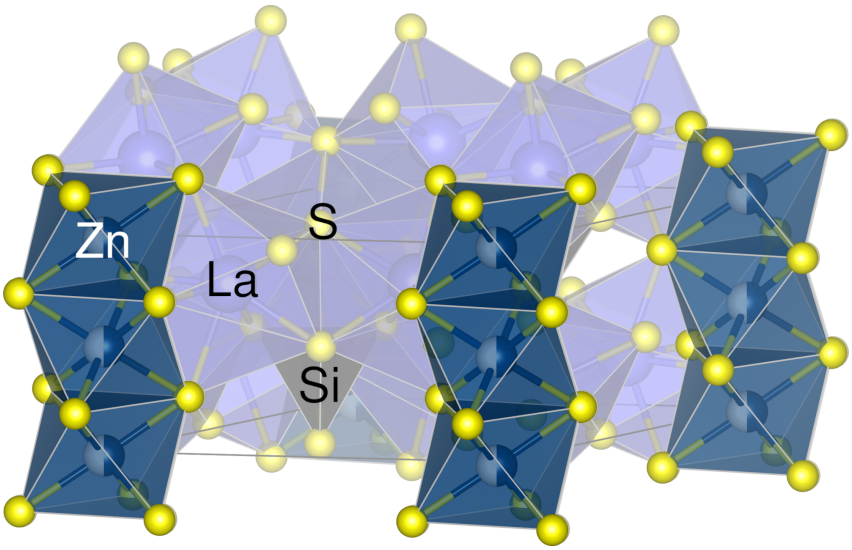

Figure 3.6: $ZnLa_6Si_2S_{14}$ has a network of partially occupied O_h Zn sites along the corners of the unit cell. Inherent partial occupancy in the structure may facilitate enhanced vacancy-mediated ion diffusion.

estimated the E_a of Zn^{2+} migration to be 680 meV for migration in the 1D channels (along the *c*-axis) but 2.72 eV within the *ab*-plane.

However, again we were unable to measure any bulk ionic conductivity. Since the conduction of Zn^{2+} in directions perpendicular to the 1D channels is very energetically expensive, it is unlikely to occur. Moreover, as previously discussed 1D diffusion pathways are prone to blocking by anti-site defects,[115] which could inhibit Zn^{2+} conduction in the channels and be the reason for the lack of measurable long range conduction. A recent computational study also identified $ZnLa_6Si_2S_{14}$ as a candidate for room temperature Zn^{2+} ion conduction,[151] so it may be worth further exploring this compound, or other analogues in the material family.

Calcium Indium Thiospinel, $CaIn_2S_4$

We targeted $CaIn_2S_4$ because it is a rare example of a compound that contains "unfavorable" tetrahedrally coordinated Ca^{2+}, has a polarizable S-based anionic framework, and, as a spinel material, contains interconnected 3D conduction pathways.[28, 45] Computationally, we determined that the E_a for Ca^{2+} migration in $CaIn_2S_4$ is isotropic and has a value of 550 meV. $CaIn_2S_4$ can be synthesized through a hydrothermal reaction of $Ca(NO_3)_2 \cdot 4\ H_2O$, $In(NO_3)_3 \cdot 4.5\ H_2O$, and CH_3CSNH_2, heated at 160 °C for 16 h in a Teflon-lined stainless steel autoclave, followed by 3 h of calcination at 600 °C.[152] However, we were unable to detect

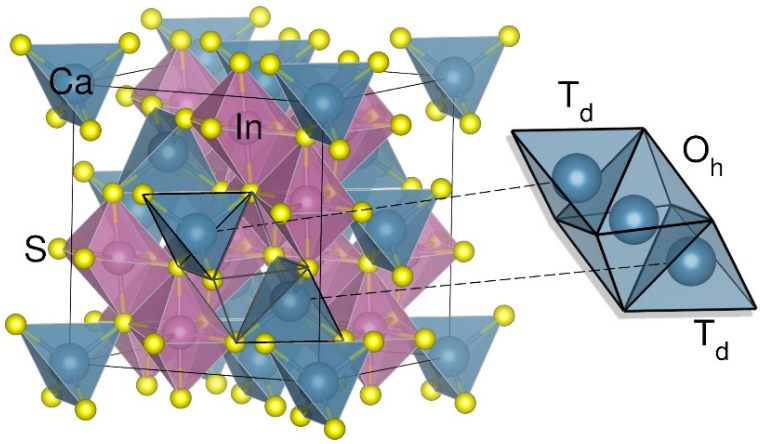

Figure 3.7: $CaIn_2S_4$ thiospinel phase with tetrahedral Ca. A possible ionic diffusion pathway is shown to the right with an octahedral Ca intermediate site that is vacant in the ground state.

significant bulk ionic conductivity within a densified pellet using EIS. Figure 3.8 shows the lab XRD patterns and Rietveld refinement of hydrothermally synthesized $CaIn_2S_4$, indicating a phase pure product. The best fit is achieved when that there is about 40% inversion, i.e. mixing of Ca on In sites, which has been shown to decrease conductivity in similar phases due to blocking of conduction pathways.[63] Preliminary attempts to alter the synthesis procedure to decrease invention, such as slow cooling, were unsuccessful. Initial attempts to do aliovalent substitution of Ge or Sn for Ca, through the introduction of soluble Ge/Sn salts to the hydrothermal reaction, to introduce stoichiometric vacancies seemed to be successful based on XRD analysis. $Ca_{0.8}Ge_{0.1}In_2S_4$ and $Ca_{0.8}Sn_{0.1}In_2S_4$ were red and dark green, respectively. However, elemental analysis was not conducted. It is possible that amorphous impurity phases formed instead of substitution, or that the inverted octahedral Ca were preferentially removed to form the vacancies, which would not enhance the ionic conduction.

Multivalent NASICON-Like Materials

Additionally, we aimed to develop divalent ion conductors that leverage a concerted migration mechanism to achieve high conductivity, similar to several superionic Li^+ conductors.[77, 153] In a concerted migration mechanism, an ion in a lattice site migrates to a neighboring, occupied interstitial site, and the ion from that interstitial site is pushed into the adjacent vacant lattice site. For instance, NASICON phases that

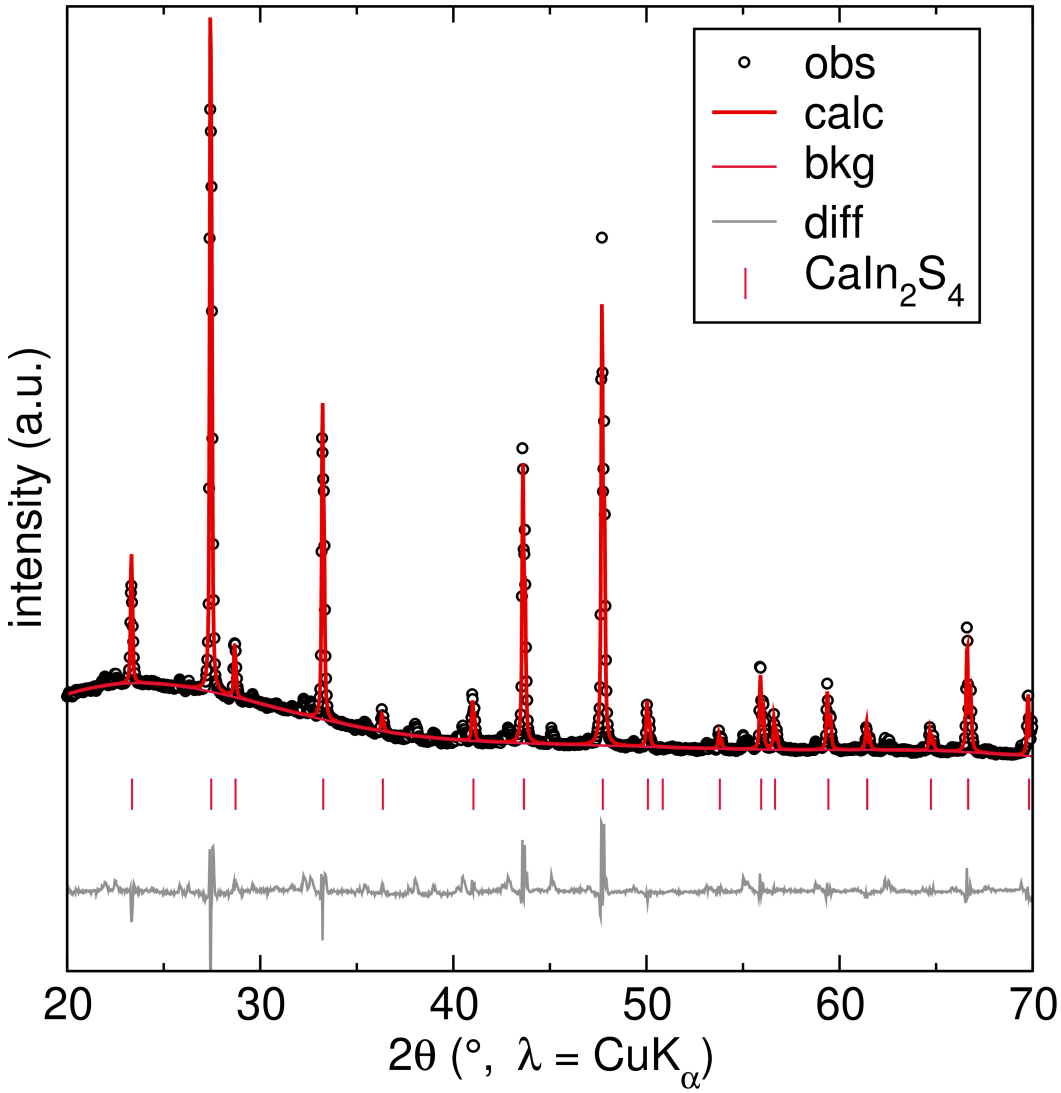

Figure 3.8: XRD pattern and Rietveld refinement of $CaIn_2S_4$ with Ca/In site inversion.

contain mobile ions in interstitial sites can exploit a concerted mechanism, showing significantly decreased E_a for Na^+ migration and increased conductivity.[36, 154]

It is challenging to stabilize charge-dense divalent ions in interstitial sites due to the electrostatic repulsion exerted by and on neighboring cations. However, this strong repulsion could also make concerted migration mechanisms especially effective at facilitating divalent ion conduction if such phases can be realized. Thus, we targeted phases with open frameworks with large interstitial sites where we could potentially stabilize excess divalent ions. We attempted to prepare NASICON-like phases in which Mg, Zn or Ca occupy interstitial sites along the migration pathway.

The endmembers $M_{0.5}Zr(PO_4)_3$ have been reported to conduct divalent cations at elevated temperatures (> 500 °C).[155]

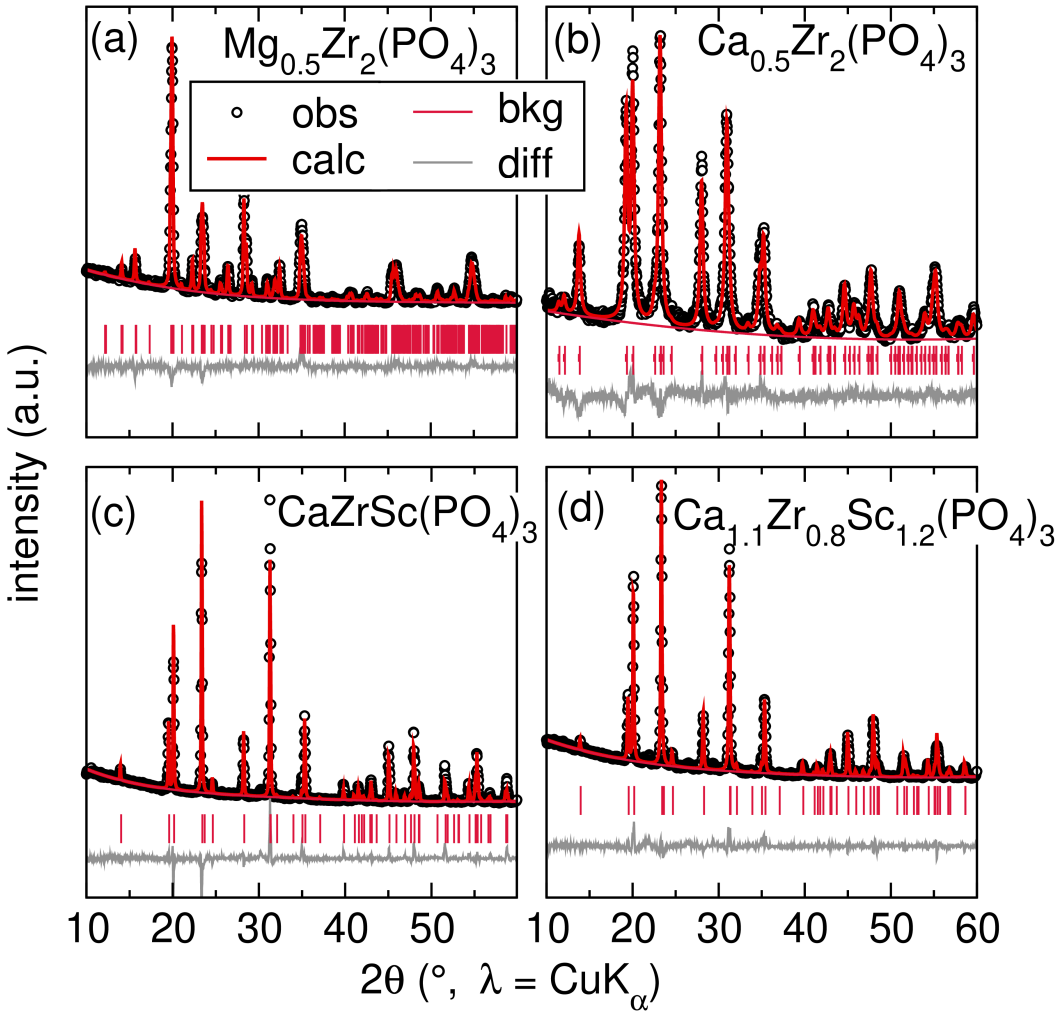

Figure 3.9: XRD and Rietveld refinement of (a) $Mg_{0.5}Zr_2(PO_4)_3$, (b) $Ca_{0.5}Zr_2(PO_4)_3$, (c) $CaZrSc(PO_4)_3$, and (d) $Ca_{1.1}Zr_{0.8}Sc_{1.2}(PO_4)_3$ showing phase purity.

We successfully synthesized the endmembers, $M_{0.5}Zr_2(PO_4)_3$ (M = Mg, Ca), the fully occupied Ca phase, $CaZrSc(PO_4)_3$ and a slightly stuffed Ca phase, $Ca_{1.1}Zr_{0.8}Sc_{1.2}(PO_4)_3$. Figure 3.9 shows the XRD patterns and Rietveld refinement of $Mg_{0.5}Zr_2(PO_4)_3$, $Ca_{0.5}Zr_2(PO_4)_3$, $CaZrSc(PO_4)_3$, and $Ca_{1.1}Zr_{0.8}Sc_{1.2}(PO_4)_3$, confirming phase purity. Pure phases of these materials were synthesized using a sol-gel method, where $M(NO_3)_2$ (5- 10 % excess was needed if product was not pure), $ZrOCl_2$, $NH_4H_2PO_4$, and $Sc(NO_3)_3$, if necessary, were dissolved separately in 20 ml of DI water and then combined. The solutions were heated at 60 °C overnight while stirring at 300 rpm.

The resulting powders were heated in an alumina crucible at 600 °C for 24 hour to remove the volatiles, then pelletized and annealed at 900 °C for 24 hours. A pure phase of the Mg compounds, besides the endmember, could not synthesized reliably. More success may be had using a smaller metal like Ti instead of Zr in this case. The structures of the endmember and the stuffed material are shown in Figure 3.10, as well as an illustration of the concerted migration mechanism. Ten percent interstitial Ca should be enough to observe the hypothesized decrease in E_a associated with concerted migration.

The pure materials were pelletized with a hydraulic press and then sintered at 1100 °C or 1300 °C. The $Ca_{0.5}Zr_2(PO_4)_3$ material reached 90% density, but the stuffed material, $Ca_{1.1}Zr_{0.8}Sc_{1.2}(PO_4)_3$, could not be densified more than 60% under these conditions. Initial results suggest the stuffed phases, like the endmembers, do not have high enough ionic conductivity to resolve at ambient temperature. However, it may be worth optimizing the densification procedure of the stuffed compound or studying these materials at elevated temperature to see if the concerted mechanism decreases the E_a significantly. Note that under ambient humidity conditions, some ionic conduction was observed ($\sim 10^{-7}$ S cm^{-1}); however, this decreased significantly upon drying, suggesting that this low conductivity may be a result of H^+ conduction on the surface of the material from adsorbed water. Additionally, more characterization including elemental analysis and synchrotron XRD should be employed to confirm that the extra Ca is incorporated into the lattice and occupies the interstitial sites. The lab diffraction is not conclusive since the concentration of occupied interstitials is low.

Mechanochemical Attempts to Make Amorphous Conductors

We briefly explored amorphous divalent ion-containing phases as potential divalent ion conductors. Amorphous Li_2S-P_2S_5 mixtures of different stoichiometries show high Li^+ conductivity.[156] Amorphous mixtures containing divalent ions could potentially support conduction of divalent ions due to the lack of long rage order and flatter energy landscape.[78] The Li-containing amorphous phases are generally formed after about several hours of high-energy ball milling of the respective reagents. We attempted to synthesize divalent analogues of these phases, including 7:3 mixtures of ZnS-P_2S_5 and CaS-P_2S_5, and Ca_3N_2-P-Ca, targeting a stoichiometry of Ca_3NP. However, no significant conductivity was observed in the ZnS-P_2S_5 and CaS-P_2S_5 mixtures. Although, we note that XRD studies of the mileld mixtures suggest that there were still crystalline domains present. Further attempts to amor-

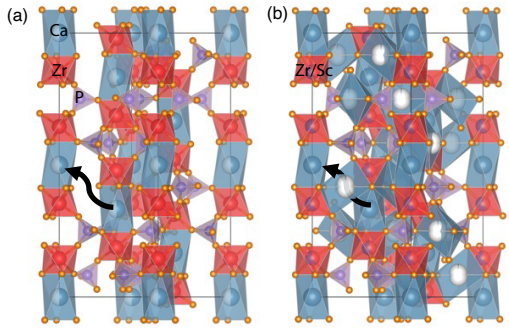

Figure 3.10: Crystal structures viewed down the [110] direction of (a) $Ca_{0.5}Zr_2(PO_4)_3$, illustrating the open network, and (b) the stuffed phase $Ca_{1.1}Zr_{0.8}Sc_{1.2}(PO_4)_3$ in which some Ca ions sit in the interstitial site. The diffusion pathway between lattice sites is shown with a black arrow.

phous the mixture, such as high-energy milling instead of planetary milling could be attempted. The Ca_3N_2-P-Ca mixture resulted in a brown powder which displayed some electronic conductivity (10^{-6} mS cm^{-1}), based on EIS measurements and DC polarization.

Additionally, we amorphized crystalline materials of interest, like $ZnPS_3$ and $CaIn_2S_4$, to determine if reducing long-range order in these structures wpould enhance the ionic conductivity. After about 24 hours of planetary milling, there were no identifiable reflections corresponding to any crystalline species in lab XRD. However, these compounds also did not show meaningful ionic conductivity at or around ambient temperature.

Other Materials of Interest

Other phases that were briefly investigated include antiperovskites, of the form M_3NP (M = Mg, Ca), which were recently highlighted in a computational study, which suggested that the antiperovskite structure may facilitate a low E_a,[69] and the sodalite phase $Ca_8Al_{12}O_{24}T_2$ (T = S, Se, Te, SO_4),[157] which is another phase that contains "unfavorable" tetrahedral Ca. However, obtaining a pure phase was synthetically challenging and we did not obtain a sufficiently pure sample to accurately characterize electrochemically.

3.4 Conclusion

In this chapter, we undertook a thorough exploration of various materials and strategies to enhance multivalent ion conductivity. Our efforts included the synthesis and characterization of $ZnPS_3$ with aliovalent metal and anion substitutions, Ca_2MS_4 thio-olivines, multivalent argyrodites, $ZnLa_6Si_2S_{14}$, $CaIn_2S_4$ thiospinel, and Mg or Ca contiaining NASICON-like materials. Despite the promising characteristics and some computational predictions, our experimental results showed limited success in achieving high ionic conductivity at ambient temperatures.

Aliovalent metal substitution in $ZnPS_3$ introduced vacancies but did not significantly enhance conductivity, likely due to the presence of immobile cations within the diffusion pathway. Anion substitution with Cl also maintained structural integrity but failed to increase conductivity, possibly due to inadequate integration of Cl into the lattice and creation of vacancies. The exploration of Ca thioolivines revealed that the thioolivine phase may not be suited for room temperature conduction of multivalent ions. Additionally, Ionic conduction in the thiospinel $CaIn_2S_4$ was not realized, despite the unfavorable tetrahedral Ca and S-based framework, likely due to Ca/In inversion causing blockages in the diffusion pathway.

Our attempt to leverage concerted migration mechanisms in NASICON-like materials may have potential, yet practical implementation and densification issues hindered significant conductivity improvements. The exploration of amorphous phases through mechanochemical methods did not yield the desired conductivity, suggesting the need for further refinement of preparation techniques and the need to explore a larger phase space.

Finally, we briefly examined other materials of interest, such as antiperovskites and sodalite phases, but faced challenges in obtaining pure phases suitable for electrochemical characterization.

Overall, while the studies outlined here lay a solid foundation and identifies critical challenges in the development of divalent ion conductors, further research and innovative approaches are required to achieve the desired high ionic conductivities.

Chapter 4

WATER VAPOR INDUCED SUPERIONIC CONDUCTIVITY IN $ZNPS_3$

This chapter has been adapted from:

(1) **Iton, Zachery W. B.**; Lee, B. C.; Jiang, A. Y.; Kim, S. S.; Brady, M. J.; Shaker, S.; See, K. A. Water Vapor Induced Superionic Conductivity in $ZnPS_3$. *J. Am. Chem. Soc.* **2023**, *145*, 13312–13325. 10.1021/jacs.3c03368,

4.1 Abstract

Next-generation batteries based on sustainable multivalent working ions, such as Mg^{2+}, Ca^{2+}, or Zn^{2+}, have the potential to improve the performance, safety, and capacity of current battery systems. Development of such multivalent ion batteries is hindered by a lack of understanding of multivalent ionics in solids, which is crucial for many aspects of battery operation. For instance, multivalent ionic transport was assumed to be correlated with electronic transport, however, we have previously shown that Zn^{2+} can conduct in electronically insulating $ZnPS_3$ with a low activation energy of 350 meV, albeit with low ionic conductivity. Here, we show that exposure of $ZnPS_3$ to environments with water vapor at different relative humidities results in room temperature (RT) conductivity increases of several orders of magnitude, reaching as high as 1.44 mS cm^{-1} without decomposition or structural changes. We utilize impedance spectroscopy with ion selective electrodes, ionic transference number measurements, and deposition and stripping of Zn metal, to confirm that both Zn^{2+} and H^+ act as mobile ions. The contribution from Zn^{2+} to the ionic conductivity in water vapor exposed $ZnPS_3$ is high — representing superionic Zn^{2+} conduction. The present study demonstrates that it is possible to enhance multivalent ion conduction of electronically-insulating solids as a result of water adsorption, and highlights the importance of ensuring that increased conductivity in water vapor exposed multivalent ion systems is in fact due to mobile multivalent ions and not solely H^+.

4.2 Introduction

Interest in multivalent ion batteries (MIBs) as next-generation energy storage technology has increased significantly in recent years.[25, 158, 159] The excitement is in

part due to limitations in state-of-the-art Li-ion batteries (LIBs), which are approaching theoretically achievable energy densities. Additionally, LIBs are relatively expensive, have safety concerns associated with the flammable liquid electrolyte, and rely on metals with supply chain and abundance concerns. [6, 7, 160]

Batteries based on multivalent working ions such as Mg^{2+}, Ca^{2+}, and Zn^{2+} use less expensive metals and promise improved metrics related to both performance and safety over current LIBs.[25, 158] Specifically, the volumetric capacities of multivalent metal anodes (3833, 2073, and 5851 mAh cm^{-3} for Mg, Ca, and Zn respectively) are much higher than that of the commercialized graphite anode in LIBs (720 mAh cm^{-3}), and even next-generation Li metal anodes (2062 mAh cm^{-3}). A major obstacle in the development of MIBs is insufficient understanding of multivalent ion conduction in solids. Solid state ionic conduction is critical for many aspects of batteries including intercalation electrodes, solid state electrolytes (SSEs), and electrode-electrolyte interfaces. The charge density of multivalent ions is generally higher than Li^+, making diffusion in solids inherently more challenging.[95, 158] To date, there have been limited reports of multivalent ion conduction in inorganic solids around RT. Notable materials include the seminal Chevrel phase Mo_6S_8 and thiospinel Ti_2S_4, both of which were shown to reversibly intercalate Mg^{2+} at slightly elevated temperatures (60 °C).[96, 103] The electronic conductivity in both Mo_6S_8 and Ti_2S_4 is hypothesized to screen the ionic charge, allowing for high Mg^{2+} mobility.[97, 102] Indeed, we have found that the identification of electronically-insulating solids capable of multivalent ion conduction is challenging. Previous reports are limited to derivatives of Mg borohydrides[46, 48, 49, 51, 52, 123] and $ZnPS_3$ at slightly elevated temperatures.[54] $ZnPS_3$ was reported as the first electronically-insulating solid state Zn^{2+} conductor near ambient temperature.[54] $ZnPS_3$ boasts a low activation energy (E_a) comparable to Li garnets of 351 ± 99 meV; however, the ionic conductivity at 60 °C is low at $\sim 10^{-7}$ S cm^{-1}.

Besides charge screening with electrons, it has been suggested that solvent molecules, like water, can screen charge to affect the conduction and intercalation of multivalent ions in cathodes.[161] Several reports have claimed that structural water in a host lattice can facilitate multivalent ion conduction in various compounds like MnO_2 and V_2O_5 by increasing diffusion kinetics through either (1) shielding of the charge-dense multivalent ions,[105, 106, 161, 162] or (2) solvating the ions in the electrolyte to decrease the impedance at the electrolyte-cathode interface.[162, 163] In addition to the previous reports of water-assisted multivalent ion diffusion

that focused on cathodes, enhanced Li^+ mobility was achieved via hydration in the electronically-insulating $Li_2Sn_2S_5$ SSE.[110]

Here we aim to determine if water can increase the ionic conductivity in electronically-insulating $ZnPS_3$. Several layered MPS_3 (M = Mn, Cd, Zn) phases are stable in humid environments and in water for extended periods of time, and are likely to intercalate water or guest molecules into the van der Waals gap.[113, 164–168] Therefore, $ZnPS_3$ is an ideal candidate for an initial study of enhancement of Zn^{2+} ionic conduction in inorganic solids via water exposure.

Water-containing solids capable of conducting Zn^{2+} could additionally be applicable in aqueous Zn-ion batteries (ZIBs). Aqueous ZIBs have re-emerged as promising candidates for grid-scale energy storage and wearable technology within the last decade because of the high abundance of Zn, established manufacturing processes, safety benefits offered by the low potential (-0.76 vs. SHE), and low toxicity.[169–173] However, current limitations of aqueous ZIBs include (1) cathode dissolution, (2) Zn dendrite formation upon deposition, (3) formation of unexpected byproducts, (4) poorly-understood operation mechanisms, and (5) corrosion and passivation of the Zn surface.[169, 174] Replacing the aqueous electrolyte with a water-containing SSE would reduce the amount of active water in the system, and therefore could potentially mitigate the majority of the issues that arise from the interactions between excess water and ZIB components. [171–175]

We note, however, that incorporation of water can also introduce a new ionic charge carrier: H^+. In fact, the observed capacity in many reported multivalent cathodes with water present could be explained by H^+ intercalation[26, 108, 109, 176] or co-intercalation.[107] Park *et al.* highlighted examples in which the observed electrochemical behavior was misassigned to the insertion of multivalent ions instead of H^+. The authors emphasized the necessity of using multiple characterization techniques to confirm the identity of the charge carriers in systems containing water.[95] Taking into account the lessons from water-containing cathodes systems, here we study the effect of water vapor exposure on the ionic conductivity of $ZnPS_3$ and carefully characterize the charge carriers.

The structure of $ZnPS_3$ and proposed Zn^{2+} conduction pathway in the pristine material are shown in Figure 4.1.[54] $ZnPS_3$ forms as a layered compound with a slightly distorted hexagonal network of edge-sharing Zn^{2+} octahedra. The Zn^{2+} are coordinated by $[P_2S_6]^{4-}$ polyanions. The layers stack along the c-axis separated by a van der Waals gap of 3.38 Å. We hypothesize based on experimental and theoretical data

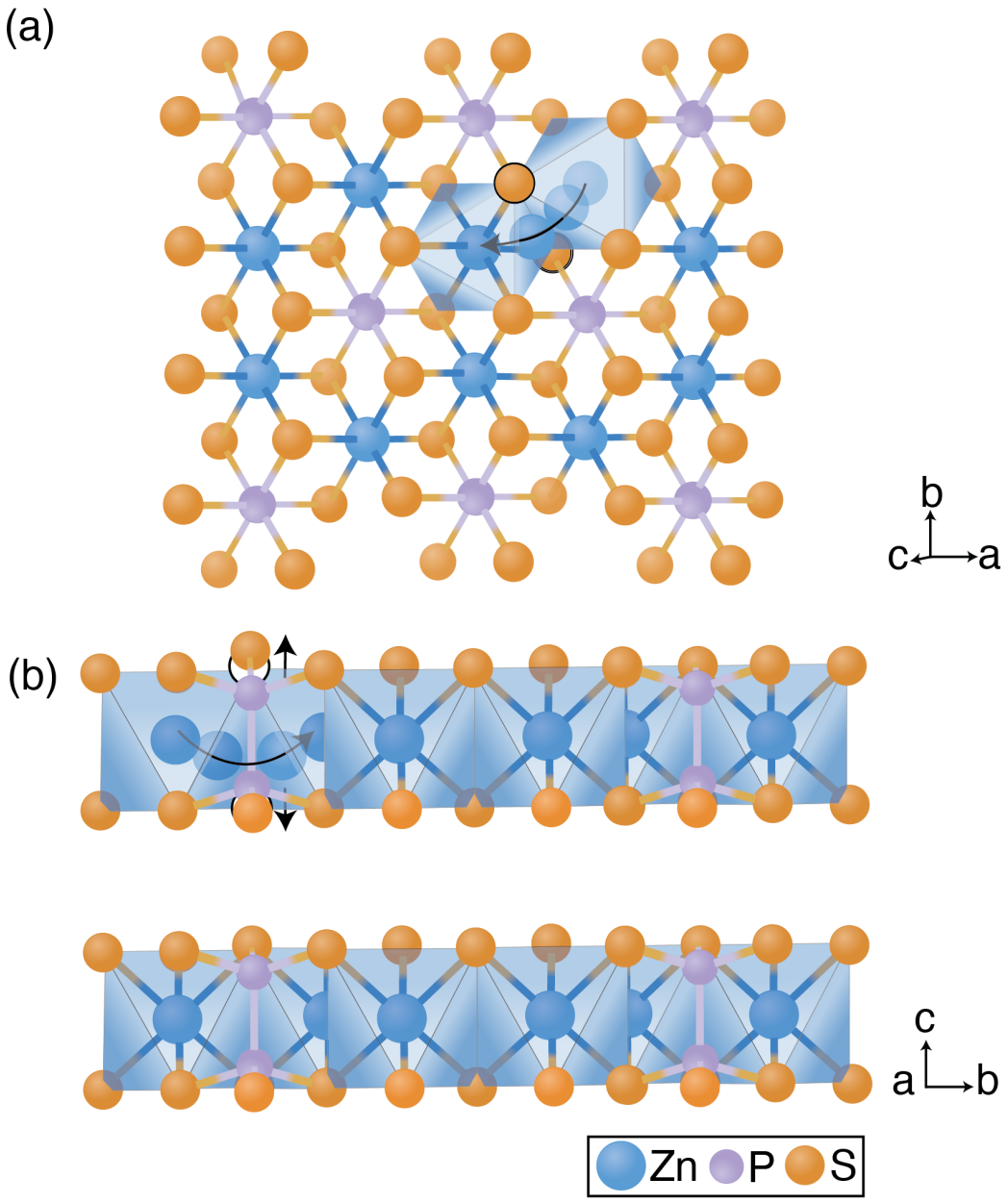

Figure 4.1: The crystal structure of pristine $ZnPS_3$ including an illustration of the lowest energy diffusion pathway predicted by NEB in $ZnPS_3$ from Martinolich *et al.*[54] (a) looking down the *c* axis and (b) along the *a* axis. The Zn^{2+} ions migrate through the octahedral faces into a neighboring vacancy in the Zn layer. The S atoms along the shared edge (highlighted) distort into the van der Waals gap facilitating low activation energy.

that Zn^{2+} conducts within the metal layer via a vacancy-mediated mechanism (Figure 4.1). Here, we show that $ZnPS_3$ readily takes up water after exposure to humid

air (*vide infra*). We name the water-containing materials x $H_2O/ZnPS_3$ where x indicates the moles of water adsorbed per mole of $ZnPS_3$. After exposure, a combination of ^1H and ^{31}P solid state magic angle spinning nuclear magnetic resonance (MAS ssNMR), X-ray diffraction (XRD), Raman spectroscopy, thermogravimetric analysis (TGA), differential scanning calorimetry (DSC), and Fourier transform infrared (FTIR) spectroscopy are used to investigate the incorporation of water and resulting structural changes. Subsequently, electrochemical impedance spectroscopy (EIS) is employed to determine the bulk conductivity of $ZnPS_3$ exposed to different relative humidities (RHs). The identity of the mobile ion is probed using ionically selective electrodes, ionic transference number measurements, deposition, and stripping of Zn metal. The deposited Zn metal is characterized with scanning electron microscopy (SEM), energy dispersive X-ray spectroscopy (EDS), and X-ray photoelectron spectroscopy (XPS). The 0.52 $H_2O/ZnPS_3$ material exhibits superionic conduction (> 0.1 mS cm^{-1}). The enhanced ionic conduction stems from both increased Zn^{2+} conduction and the introduction of mobile H^+. When decoupling the two charge carriers, we find that Zn^{2+} conduction is superionic. Ultimately, the present study illustrates the utilization of adsorbed water to aid charge-dense ion conduction in electronically-insulating compounds, and provides a novel approach for the development of multivalent SSEs. Additionally, we demonstrate experimental methods to qualitatively decouple H^+ and multivalent ion conduction.

4.3 Results And Discussion

Ionic Conductivity of Water Vapor Exposed $ZnPS_3$

First, we discuss the effect of water vapor exposure on the ionic conductivity of $ZnPS_3$. To control the degree of water uptake, pellets of $ZnPS_3$ are placed in a chamber with controlled RH for 2 days. The pellets expand significantly upon exposure to humid air (Figure A.1), suggesting water adsorption. The mass change after exposing $ZnPS_3$ to humid air for two days is the same whether $ZnPS_3$ is a pellet or a powder, suggesting that the $ZnPS_3$ pellet takes up water homogeneously. The amount of water adsorbed is quantified later; however, we will now refer to the materials by the average amount of adsorbed water, x in x $H_2O/ZnPS_3$, measured by TGA (*vide infra*).

We utilize EIS to probe the ionic conductivity and activation energy at various water contents. Figure 4.2a shows Nyquist plots of a representative Au symmetric cell with a 0.52 $H_2O/ZnPS_3$ electrolyte from room temperature to 50 °C in 10 °C increments. Nyquist plots of x = 0.02, 0.09 and 2.38 are shown in Figure A.3.

In cases where the high frequency semicircle could be resolved (x = 0.02 & 0.09), the Nyquist plots are fit with an equivalent circuit consisting of a resistor (R_c) in series with a RQ circuit (resistor, R_b, in parallel with a constant phase element, Q_b) in series with an additional Q_{int}. R_c is the circuit resistance, and R_b and Q_b are associated with the electrolyte, and Q_{int} represents the capacitive charge buildup at the blocking electrode surface. The high frequency semicircle is attributed to total ionic conduction through x $H_2O/ZnPS_3$, since the capacitance values extracted from the equivalent circuit (10^{-10}–10^{-9} F) match those expected for solid state ionic conduction, and are similar to the high frequency feature of the non-blocking symmetric cell (Zn|$ZnPS_3$|Zn) in our initial report.[49, 54, 81] The high frequency semicircle could not be resolved for 0.52 $H_2O/ZnPS_3$ above room temperature or 2.38 $H_2O/ZnPS_3$ at any temperature. In these cases, the x intercept value is taken as a "worst case" approximation for the total impedance, which we conservatively approximate as the electrolyte impedance.

The ionic conductivity of x $H_2O/ZnPS_3$ can thus be extracted by converting the R_b values from the fits of the Nyquist plots at various temperatures. Figure 4.2b shows the ionic conductivity of x $H_2O/ZnPS_3$ as a function of RH at room temperature (approx. 23 °C). The ionic conductivity of $ZnPS_3$ increases with adsorbed water content reaching a room temperature conductivity on the order of 1 mS cm^{-1}. Therefore, the ionic conductivity of water vapor exposed $ZnPS_3$ at room temperature is up to four orders of magnitude higher than that of pristine $ZnPS_3$ at 60 °C and two orders of magnitude greater than hydrated $CdPS_3$ reported under comparable conditions [113]. We note that the charge carriers in $CdPS_3$ are most likely H^+.[113]

The E_a is determined using the Arrhenius-type relationship that governs the thermally activated ionic conduction process.[70, 158] Figure 4.2c shows the plot of $\ln(\sigma T)$ vs. T^{-1} for cells exposed to various RH environments. The resulting E_a along with the room temperature conductivities are listed in Table A.1. In the humidity exposed samples, the E_a decreases as the amount of adsorbed water increases. The lower E_a may result from either more water in the system leading to greater solvation of Zn^{2+} ions or greater contributions of mobile H^+ to the ionic conductivity. Exceedingly high H^+ conduction was recently reported in the isostructural $CdPS_3$ phase after a complicated ion exchange to introduce H^+.[113] The H^+ conduction is reported to have an E_a of 170-200 meV (depending on the extent of hydration).[113] Therefore, we are cognizant that H^+ conduction very likely contributes to the en-

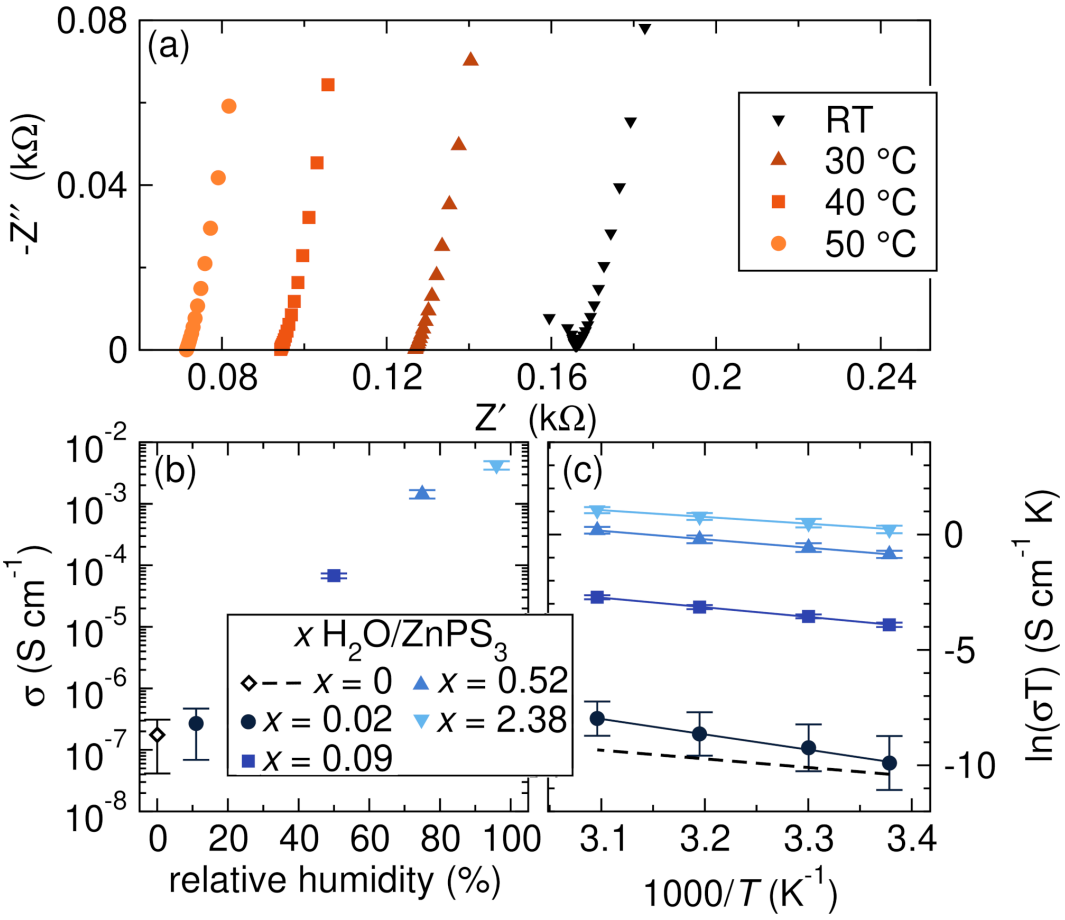

Figure 4.2: (a) Representative Nyquist plots of 0.52 $H_2O/ZnPS_3$ from 3 MHz to 100 mHz and from room temperature to 50 °C. (b) the ionic conductivity of x $H_2O/ZnPS_3$ vs. RH at RT. (c) Arrhenius-type plots of x $H_2O/ZnPS_3$ at different RHs. Error bars in both (b) and (c) represent errors from at least three replicate cells. The conductivity and Arrhenius data for $x = 0$ was obtained through extrapolation to RT of the five replicate cells measured in the previous study of $ZnPS_3$ from our group. In that study, EIS was measured from 60 to 90 °C.[54]

hanced ionic conductivity of hydrated $ZnPS_3$ over the pristine material since H^+ are able to conduct more easily than multivalent ions.

Due to the substantial increase in total ionic conductivity of $ZnPS_3$ after exposure to humid environments, structural, chemical, and electrochemical characterization are used to understand the origin of conductivity enhancement and determine if Zn^{2+} contributes to the observed superionic conductivity.

RH (%)	H_2O adsorbed (mol/f.u.)	σ_{RT} (mS cm^{-1})	E_a (meV)
0	0	$(1.75 \pm 1.34) \times 10^{-4}$*	351 ± 99
11	0.02 ± 0.01	$(2.69 \pm 3.05) \times 10^{-4}$	573 ± 147
45-55	0.09 ± 0.04	$(6.78 \pm 0.61) \times 10^{-2}$	360 ± 2
75	0.52 ± 0.25	1.44 ± 0.26	314 ± 15
96	2.38 ± 0.21	4.25 ± 0.67	252 ± 23

Table 4.1: H_2O content measured by TGA and conductivity metrics of $ZnPS_3$ exposed to various RH environments. * the conductivity of the $x = 0$ material was obtained through extrapolation of EIS measurements from 60 – 90 °C to RT.

Characterization of Water Vapor Exposed $ZnPS_3$

Next, we discuss in-depth characterization of the water vapor exposed $ZnPS_3$ materials. Techniques including TGA, DSC, and FTIR are used to confirm and characterize water adsorption in x $H_2O/ZnPS_3$ after equilibration at the selected RHs. Figure 4.3a shows TGA results of x $H_2O/ZnPS_3$ up to 250 °C. The DSC results (Figure A.4) show that mass loss occurs through an endothermic process at T ≤ 150 °C. The endothermic region is attributed to loss of adsorbed water from the samples.[166] At T > 150 °C the mass loss occurs through an exothermic process, which could be due to minor decomposition or hydrolysis at elevated temperatures. Therefore, the adsorbed water contents are determined by considering the mass after heating to 150 °C. By the end of the endothermic process, the samples exposed to 11% RH, ambient air (45-55% RH), 75% RH, and 96% RH experience mass loss corresponding to 0.02 ± 0.01, 0.09 ± 0.04, 0.52 ± 0.25 and 2.38 ± 0.21 moles of H_2O per mole of $ZnPS_3$, respectively. The error bars reflect the standard deviation of three replicate measurements. The TGA is magnified in Figure A.5 to illustrate the difference between the pristine, x = 0.02 and 0.09 samples. Additionally, a comparison of adsorbed water content from TGA measurements and measurements of sample mass change using a bench top balance is shown in Table S1. As in previous reports of water-containing $MnPS_3$ and $CdPS_3$,[166] the mass loss begins slightly above room temperature, suggesting that the adsorbed water is weakly bound to $ZnPS_3$. A second endothermic weight loss event at higher temperatures is not observed. The absence of mass loss at higher temperature indicates the absence of tightly bound

"crystalline" water. Additionally, the DSC contains only one peak, suggesting that the removal of adsorbed water requires similar energy.

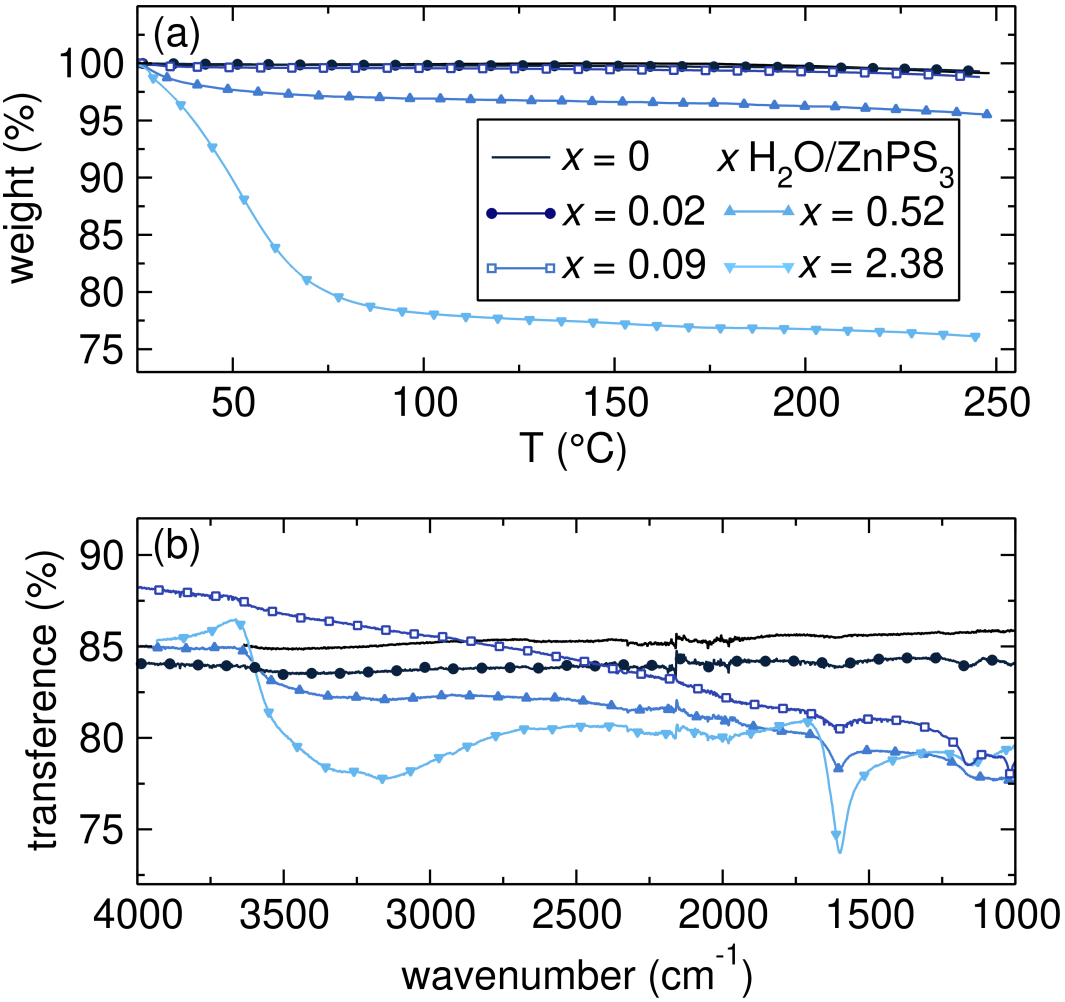

Figure 4.3: (a) TGA of x $H_2O/ZnPS_3$ showing that samples exposed to higher RH environments uptake more water. (b) ATR FTIR of pristine and water vapor exposed $ZnPS_3$ illustrating the presence of adsorbed water in the water vapor exposed samples and not in the pristine sample.

Figure 4.3b shows FTIR spectra of x $H_2O/ZnPS_3$. The spectra of the water vapor exposed samples contain a sharp peak at 1600 cm^{-1} and a broad feature around 3300 cm^{-2}, which correspond to well-established IR active bending and stretching modes of water molecules, respectively. The bands related to water are much easier to observe in the materials with higher water content due to the concentration dependence of the absorption intensity. However, a small feature at 1600 cm^{-1} is observed even in the x = 0.02 material, confirming the presence of water. The FTIR is shown magnified in Figure A.6 to more easily evaluate this feature. Additionally,

these features match previously observed FTIR spectra of H_2O containing $MnPS_3$. [166]

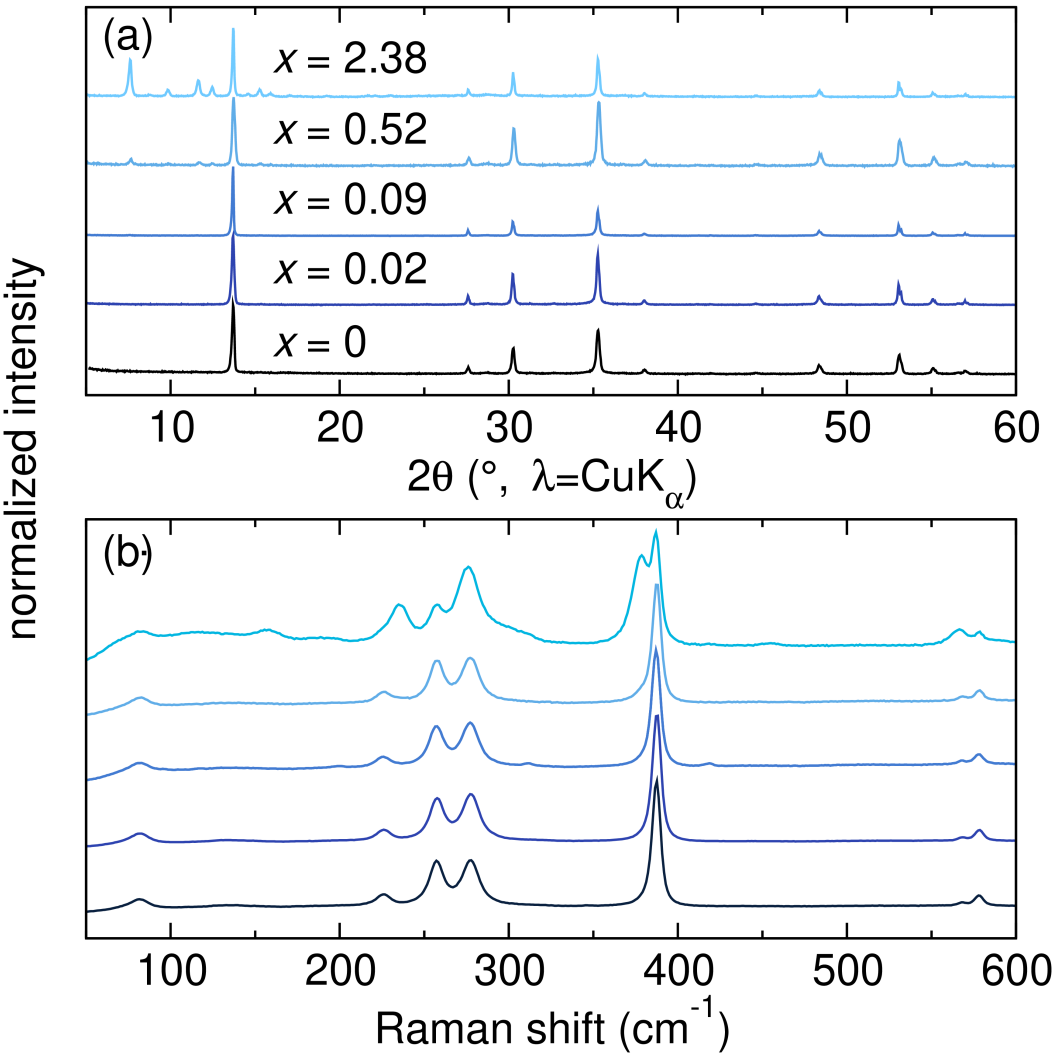

Figure 4.4: (a) XRD patterns of x $H_2O/ZnPS_3$ normalized to the (001) reflection of $ZnPS_3$ at 13.6 ° 2θ, showing that no major crystalline decomposition products form after water vapor exposure until x = 2.38. (b) Raman spectra of x $H_2O/ZnPS_3$ showing that the modes associated with $ZnPS_3$ are unchanged until x = 2.38, at which point modes associated with the hydrated crystalline phase appear.

XRD and Raman spectroscopy are used to investigate changes to the crystal structure of $ZnPS_3$ after water vapor exposure. Figure 4.4a compares the XRD patterns of x $H_2O/ZnPS_3$. Water uptake in layered materials commonly leads to an expansion of the interlayer spacing when the water is accommodated in the van der Waals gap.[113, 166, 177, 178] However, Figure 4.4a shows that the (001) reflection does not shift from 13.6° 2θ to lower 2θ values, as would be expected for lattice expansion,

which indicates that there is no increase in the layer spacing after water uptake. Therefore, the XRD and TGA results suggest that the water is weakly adsorbed to the surface and does not reside in the van der Waals gap. When $x \geq 0.52$, an unidentified impurity phase is formed, evidenced by the emergence of several reflections between 5 - 15 ° 2θ. None of the emergent reflections could be fit to any likely hydrolysis or decomposition products of $ZnPS_3$. These reflections possibly indicate the formation of a new crystalline phase that incorporates excess adsorbed water into the crystal structure. The reflections of the new crystalline phase are weakly present in the XRD pattern of 0.52 $H_2O/ZnPS_3$, and 0.52 $H_2O/ZnPS_3$ experiences no further significant change to the XRD pattern after one month of exposure (Figure A.7). However, exposure at high RH (96 %) after a few weeks allows the transformation proceeds to completion, and the characteristic reflections of $ZnPS_3$ vanish and only those of the unknown phase are present (Figure A.7). Additionally, the reflections associated with the unknown phase disappear after briefly drying at 100 °C or exposure to moderate vacuum in a glovebox antechamber for 30 minutes (Figure A.9a) further suggesting that the unidentified phase is related to the adsorbed water, and that the incorporated water is also weekly bound.

The Raman spectra in Figure 4.4b shows that the characteristic Raman modes of $ZnPS_3$ remain unchanged after water adsorption until excess adsorption at $x = 2.38$. At $x \leq 0.52$, the modes at 227, 259, 279, 389 and 579 cm^{-1} that are related to the $[P_2S_6]^{4-}$ polyanion remain unchanged.[179, 180] Therefore, the bulk $ZnPS_3$ lattice does not undergo significant structural changes at $x \leq 0.52$. At $x = 2.38$ additional modes are observed at 159, 235, 274, 378, and 566 ppm in some regions of the sample. These modes correspond to the Raman active modes of the new unidentified crystalline phase discussed in the section pertaining to XRD results. A Raman spectrum of the unidentified crystalline phase after complete transformation is shown in Figure A.8. In some areas of the $x = 2.38$ sample the Raman spectra looks identical to that of $ZnPS_3$, suggesting that the formation of the new crystalline phase is localized to certain areas of the powder as water adsorption progresses.

^1H MAS ssNMR is used to confirm the presence of H^+ containing species and probe their local chemical environments, and ^{31}P MAS ssNMR is used to gain further insight into potential changes in local structure of $ZnPS_3$ after water adsorption. Figure 4.5a shows the ^1H NMR spectra of x $H_2O/ZnPS_3$. There are no resonances present for $x = 0$, whereas $x \geq 0.02$ spectra exhibit a resonance, suggesting H^+ containing species are present in all of the water vapor exposed samples. Generally,

water incorporated into or adsorbed on inorganic solids shows a resonance anywhere between 4 ppm and 8 ppm, depending on the interaction between the adsorbed water and the solid.[181–184] Neutral, liquid water would show a very sharp resonance around 4.7 ppm.[185] For x = 0.02 the resonance is broad and centered around 6.5 ppm. When the water content is low all of the water is likely interacting with $ZnPS_3$. As x increases the ^1H peak shifts upfield closer to a liquid water-type position, suggesting that there is more free water as excess water is adsorbed. The resonances also sharpen with higher water contents, indicating faster ^1H mobility. The disappearance of the resonance after mild heating or evacuation at room temperature indicates that it likely arises from loosely held physisorbed water (Figure A.9b).[186] The resonance for all x $H_2O/ZnPS_3$ are best fit with two pseudo-Voigts, suggesting two distinct environments, which have two different spin lattice (T1) relaxation times (Figure A.11). One could envision many different environments including surface-confined water, "bulk"-like water, and Zn^{2+} coordinated water, to name a few. The ^1H MAS ssNMR results alone cannot concretely determine the nature of the adsorbed water. However, variable temperature ^1H MAS ssNMR of 0.52 $H_2O/ZnPS_3$ (Figure A.10) reveals that the freezing point of the adsorbed water is depressed to about 205 K. Freezing point depression is consistent with confined molecular water and not "bulk"-like liquid water. [187, 188] Nonetheless, since H^+ species are present and obviously mobile, care must be taken to ensure that the enhanced conductivity is not solely due to H^+ conduction.

The ^{31}P MAS ssNMR spectra in Figure 4.5b reveals that the pristine $ZnPS_3$, 0.02 $H_2O/ZnPS_3$, and 0.09 $H_2O/ZnPS_3$ have a single resonance at 99 ppm that is assigned to the single Wyckoff site for P in $ZnPS_3$.[54] The spectrum of 0.52 $H_2O/ZnPS_3$ contains a second, minor resonance at 126 ppm ($\leq$ 5% of the total P environments), indicating the presence of an additional P environment. The 126 ppm resonance becomes the major feature in 2.38 $H_2O/ZnPS_3$. The 126 ppm resonance cannot be assigned to any likely decomposition products, e.g., ZnP_2, Zn_3P_2, $[PO_4]^{3-}$, or any species containing $[PS_4]^{3-}$ or other P–S polyanions. [67, 189–191] Since the 126 ppm resonance is eliminated by drying or evacuation in concert with the ^1H NMR signal and the emergent XRD reflections (Figure A.9c), it likely corresponds to the unidentified crystalline phase seen in XRD of x $\geq$ 0.52 materials.

To summarize the characterization data, water is adsorbed in $ZnPS_3$ after exposure to humid atmospheres. The amount of adsorbed water increases with the RH. The adsorbed water does not intercalate into the van der Waals gap, instead it is likely

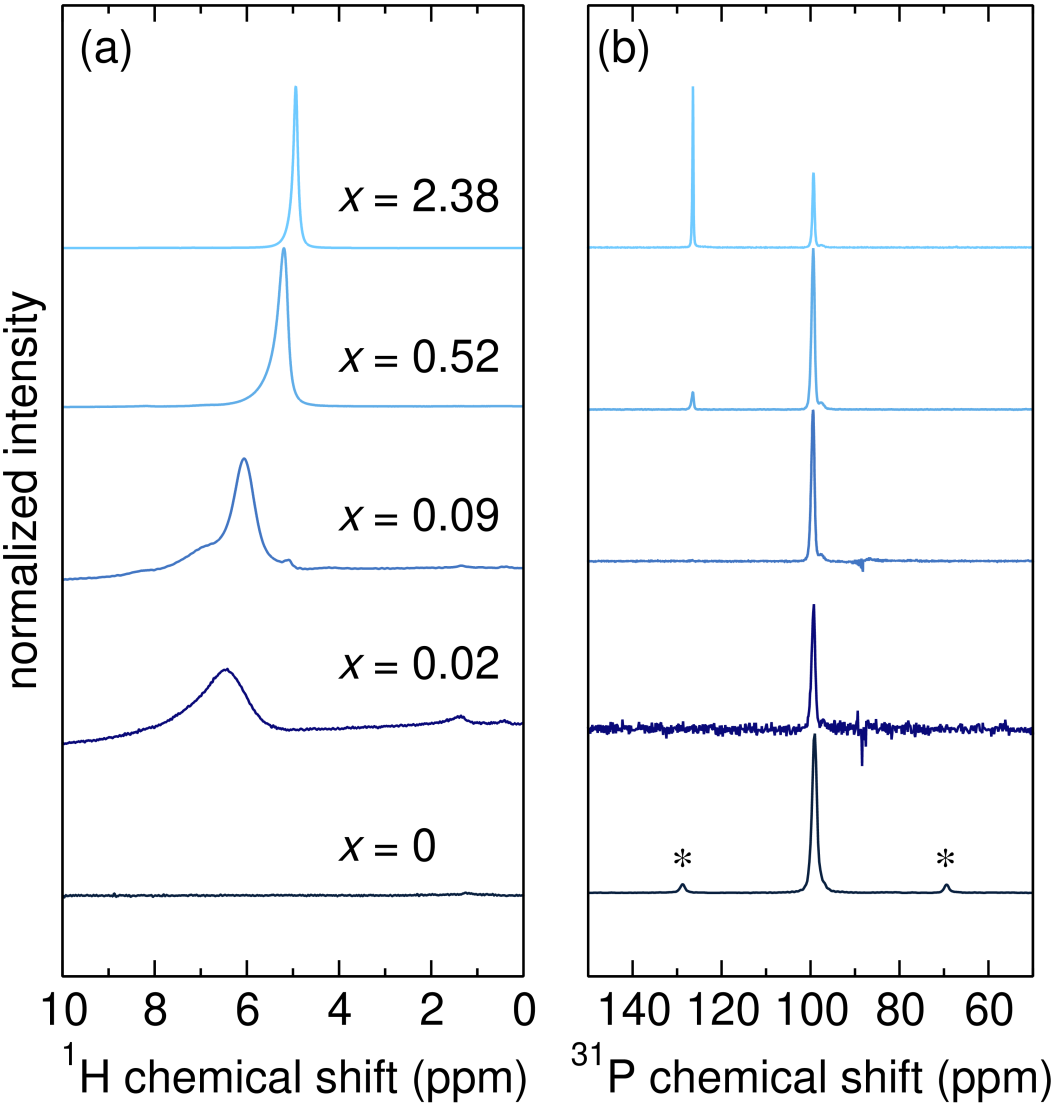

Figure 4.5: (a) ^{1}H NMR of x $H_2O/ZnPS_3$ illustrating that H^+ containing species are present in each water vapor exposed sample. A shoulder is present in water vapor exposed samples suggesting the presence of two H-containing species. The peak sharpens with more water incorporation, suggesting increased mobility of the H. (b) Normalized ^{31}P NMR of x $H_2O/ZnPS_3$ (* are spinning side bands) showing that after water adsorption the product is still $ZnPS_3$. At high water contents, an additional resonance is observed indicating a new P environment, which likely correlates to the new peaks in the XRD.

loosely bound to the surface of $ZnPS_3$ grains. Additionally, at high RH, excess adsorbed water results in the formation of an unidentified crystalline phase. Structural characterization confirms that $ZnPS_3$ is the majority phase present after exposure to 75% RH (0.52 $H_2O/ZnPS_3$) and is stable for at least one month. Therefore,

although the ionic conductivity of 2.38 $H_2O/ZnPS_3$ is higher than 0.52 $H_2O/ZnPS_3$, we focus on the 0.52 $H_2O/ZnPS_3$ material hereafter. The continuous introduction of a new unidentified phase with increased water adsorption increases cell-to-cell variability and raises concerns about whether the observed properties are inherent to water vapor exposed $ZnPS_3$ or the unidentified phase that appears at excess water adsorption. The unidentified phase will be the subject of a future study.

Experimental Evidence of Zn^{2+} Conduction

Since H^+ conducts more easily than multivalent ions in solid materials, H^+ conduction likely contributes to the enhanced ionic conductivity in water vapor exposed $ZnPS_3$. The question then becomes: Is Zn^{2+} conducting at all? However, decoupling the contributions of the two carriers is nontrivial. Several techniques used to decouple H^+ and Li^+ contributions are difficult to use with Zn^{2+}. ^{67}Zn MAS ssNMR, quasielastic neutron scattering, and muon spectroscopy require isotopic enrichment, dedicated facilities, and rigorous sample preparation for relevant multivalent systems.[158, 192] Instead, we focus on electrochemical methods to probe the identity of the charge carriers.

Blocking vs. Non-Blocking Electrode Comparison

The impedance response of 0.52 $H_2O/ZnPS_3$ with various blocking or non-blocking electrodes is compared to provide qualitative evidence that Zn^{2+} is a charge carrier in x $H_2O/ZnPS_3$. Au, Pt, Pd, and Ta are used as blocking electrodes for both H^+ and Zn^{2+}, PdH_x as a H^+ non-blocking electrode,[113, 193] and Zn metal as a Zn^{2+} non-blocking electrode. Attempts to utilize more reactive metals, like Mg, as a blocking electrode are convoluted by the reductive instability of $ZnPS_3$, resulting in non-linear responses at low frequencies (Figure A.12). Figure 4.6 shows the resulting Nyquist plots with the blocking and non-blocking electrodes. The Nyquist plots with blocking electrodes in a symmetric cell (e.g., Au|0.52 $H_2O/ZnPS_3$|Au) show a high frequency semicircle followed by a capacitive, "blocking" feature at low frequencies. As previously discussed, the high frequency semicircle is attributed to ionic conduction through the 0.52 $H_2O/ZnPS_3$ pellet, and the low-frequency feature is a result of mobile ion accumulation at the 0.52 $H_2O/ZnPS_3$–electrode interface. The bulk response observed at high frequency is comparable regardless of the electrodes. Symmetric cells using Zn metal or PdH_x electrodes show a second semi-circle at low frequencies. The low frequency semicircle is indicative of non-

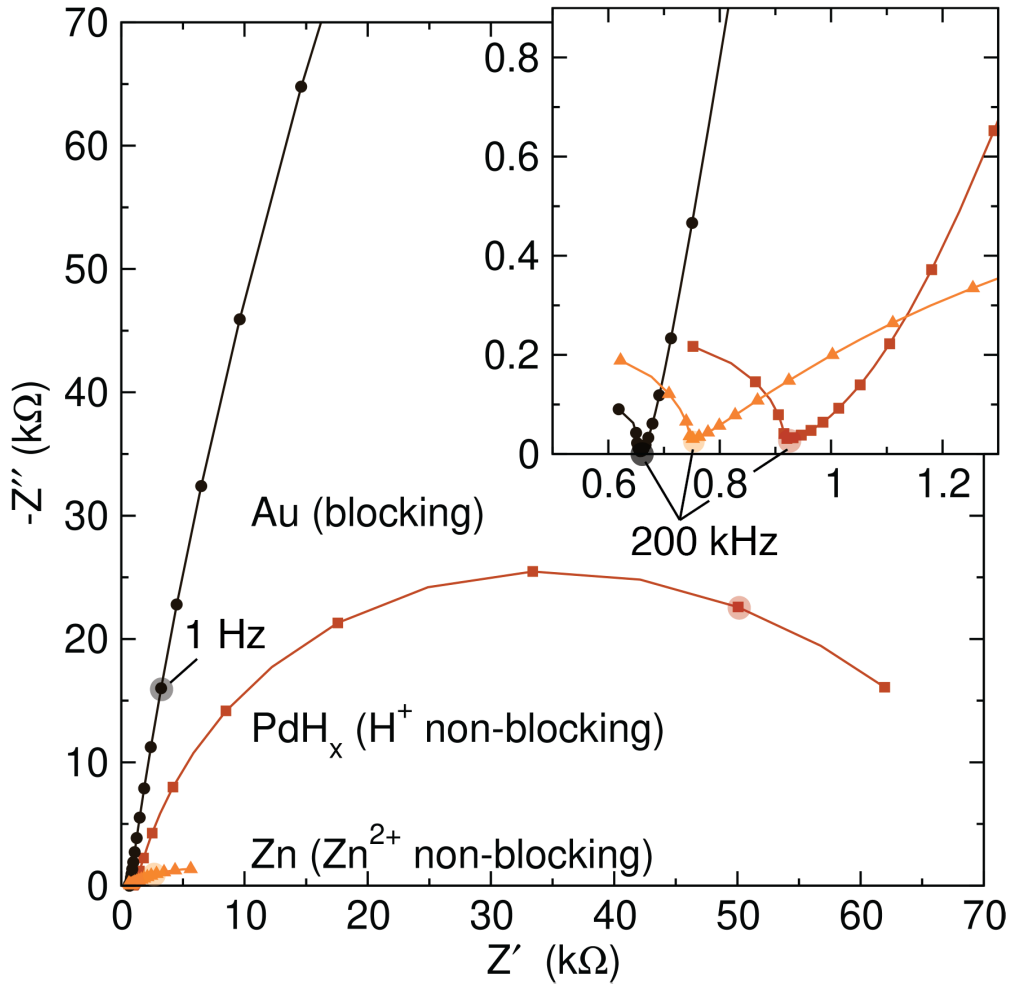

Figure 4.6: The Nyquist plots obtained from EIS of 0.52 $H_2O/ZnPS_3$ with symmetric cells of Au, PdH_x, or Zn electrodes (frequency range 3 MHz-100 mHz and voltage amplitude of 50 mV), to qualitatively identify charge carriers in 0.52 $H_2O/ZnPS_3$. Pd, Pt, and Ta behave identically to Au and thus are omitted from the figure for clarity. The highlighted points on the Nyquist plots show the response at 1 Hz. The inset shows that the bulk response observed at high frequency is comparable regardless of electrode. The highlighted points on the Nyquist plots in the inset show the response at 200 kHz.

blocking behavior, resulting from conduction across the 0.52 $H_2O/ZnPS_3$-electrode interface, indicating that both H^+ and Zn^{2+} are charge carriers in 0.52 $H_2O/ZnPS_3$.

DC Polarization and Transference Number Measurements

DC polarization is used to qualitatively illustrate the contribution of ionic charge carriers to the current response of 0.52 $H_2O/ZnPS_3$. Figure 4.7a shows the difference in current response when blocking electrodes (Au) are used as opposed to non-blocking Zn^{2+} electrodes (Zn). Upon polarization, a low steady-state current is observed with blocking electrodes ($\sim$ 5 nA). The steady-state current with blocking electrodes is an estimate of the electronic current. The electronic conductivity of 0.52 $H_2O/ZnPS_3$ is estimated to be approximately 10^{-5} mS cm^{-1}, five orders of magnitude lower than the ionic conductivity. With the Zn metal non-blocking electrodes, the steady-state current is several orders of magnitude greater than that with blocking electrodes due to the additional contribution from mobile ions, again suggesting that Zn^{2+} is indeed a mobile ion in 0.52 $H_2O/ZnPS_3$.

The DC polarization data can be used along with impedance data to estimate the relative contributions of H^+ and Zn^{2+} to the ionic conductivity. The relative contributions are quantified by the transference number, which can be estimated based on the Bruce-Vincent equation (Equation 4.1).[112] The Bruce-Vincent equation is often used to understand the relative contribution of cations vs. anions, but it has also been used to decouple two cationic charge carriers.[113]

$$T_{M^{x+}} = \frac{I_{ss}(\Delta V - I_o R_o)}{I_o(\Delta V - I_{ss} R_{ss})} \tag{4.1}$$

In the Bruce-Vincent equation (equation 4.1), $T_{M^{x+}}$ is the transference number of a species M^{x+}, ΔV is the applied potential, I_o is the initial current, I_{ss} is the steady-state current, R_o and R_{ss} are the interfacial ionic resistance before and after polarization, respectively. ΔV, I_o, and I_{ss} are obtained from DC polarization, whereas R_o and R_{ss} are obtained from EIS.[112] Specificity for species x is granted by the choice of electrode. Equation 4.1 strictly holds only under the following conditions: (1) the electrolytes should be ideal (i.e., ion-ion interactions can be ignored), (2) convection must not contribute to ion transport in the electrolyte, and (3) the applied potential must be small to avoid the establishment of large concentration gradients (the equation is not valid at applied potentials $\geq$ 30 mV).[112, 194] Neglecting to adhere to the constraints has led to a high variation in results for different studies of the same materials.[31, 195, 196] SSEs are particularly suited for investigation using the Bruce-Vincent method because there is an absence of both convection and complex speciation of the ionic charge carriers.[112, 194] Nonetheless, the presence

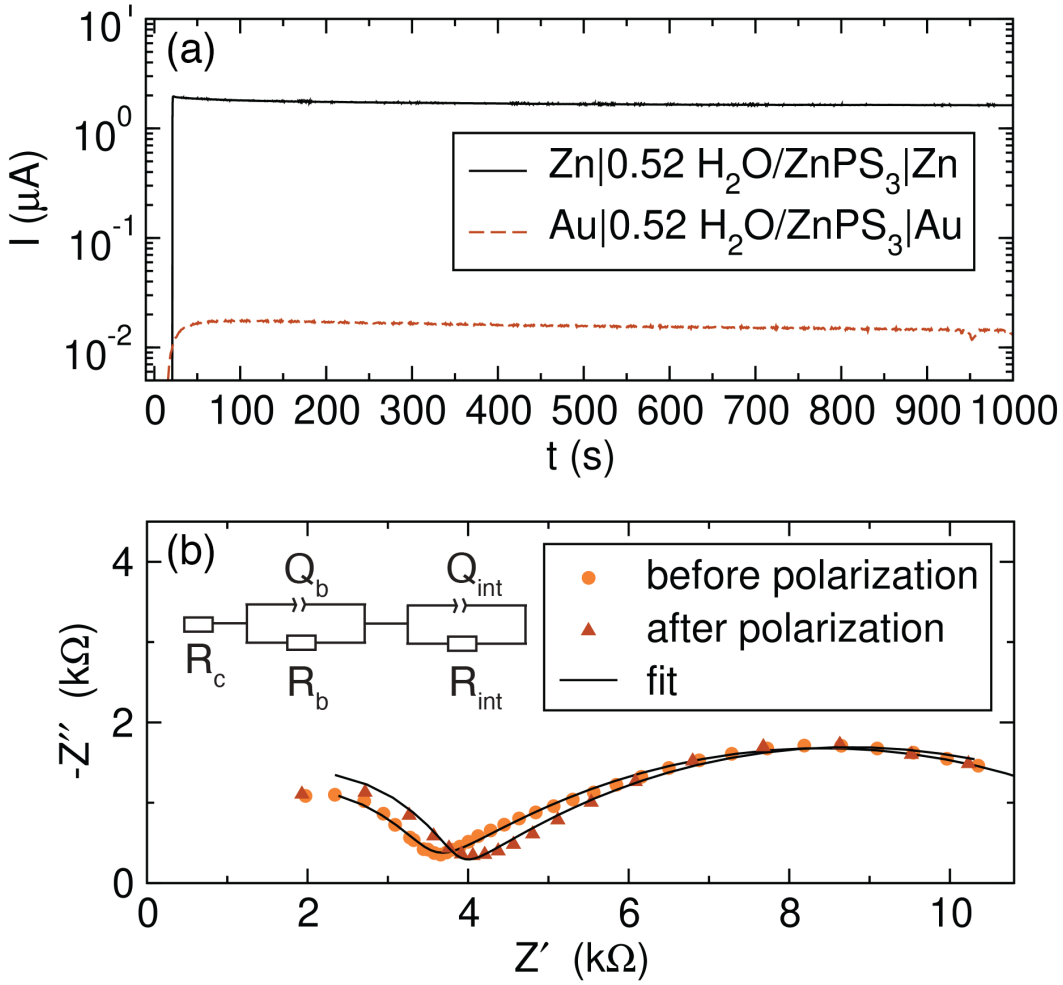

Figure 4.7: (a) Nyquist plots of a representative Zn|0.52 H_2O/$ZnPS_3$|Zn cell before and after 20 mV polarization to determine changes to the interfacial resistance. The spectra are fit with the equivalent circuit shown in the inset, where the Zn|$ZnPS_3$ interfacial resistance is taken as R_{int}. (b) Chronoamperometry of Zn|0.52 H_2O/$ZnPS_3$|Zn and Au|0.52 H_2O/$ZnPS_3$|Au cells to illustrate the different current responses to a 20 mV applied voltage with Zn^{2+} blocking vs. non-blocking electrodes.

of ion-ion interactions in the electrolyte, which are inevitable in most real systems, leads to an overestimation of the calculated transference number.[111] To determine the $T_{Zn^{2+}}$ in 0.52 H_2O/$ZnPS_3$ within the constraints of the Bruce-Vincent method, a polarization of 20 mV is applied. Figure 4.7b shows Nyquist plots of a representative Zn|0.52 H_2O/$ZnPS_3$|Zn cell before and after 20 mV polarization and the equivalent circuit used to fit the data. The $T_{Zn^{2+}}$ for 0.52 H_2O/$ZnPS_3$ is calculated to be 47 ±

4%, where the error represents cell-to-cell variation of three replicate cells. A $T_{Zn^{2+}}$ of 47% corresponds to a Zn^{2+} ionic conductivity of approximately 0.7 mS cm^{-1}.

Electrodeposition and stripping of Zn metal

Finally, we pursue the deposition and stripping of Zn metal using 0.52 $H_2O/ZnPS_3$ as an electrolyte as further evidence of Zn^{2+} conduction. Due to the low ionic conductivity of reported solid state multivalent ion conductors and challenges regarding optimization of the electrode-electrolyte interface, deposition of multivalent metals through SSEs is difficult and has not often been reported. To the best of our knowledge, the only reported deposition of multivalent metal through an inorganic SSE is of Mg metal with borohydride systems. For instance, using $Mg(BH_4)_2(en)$ as a SSE, Mg was deposited on Cu foil using a very low current density of approximately 3 nA cm^{-2} over 200 hours.[123] Another study reports using $Mg(BH_4)_2(NH_3BH_3)_2$ to deposit Mg on a Mo substrate at 30 °C.[49]

Cyclic voltammetry (CV) is used to probe the ability of 0.52 $H_2O/ZnPS_3$ to deposit and strip Zn on different metal substrates. Au and Pt are used as deposition substrates due to previous literature reports of Zn deposition on those substrates using ionic liquids.[197–201] Figure 4.8 shows the first cycle at 0.5 mV s^{-1} and 40 °C with Au or Pt working electrodes (WE). The first reduction event begins at 600 mV and 400 mV vs. Zn/Zn^{2+} with Pt and Au, respectively. During this first cathodic wave, H_2 is evolved as measured by gas chromatography (GC) and thus we assign the first reduction event to hydrogen evolution reaction (HER) ($2\,H^+ + 2\,e^- \longrightarrow H_{2(g)}$, E = 760 mV vs. Zn/Zn^{2+}). HER is known to have a lower overpotential on Pt than on Au,[202] which is consistent with our results. A second reduction event begins at -150 mV and -115 mV vs. Zn/Zn^{2+} on Pt and Au, respectively. SEM, EDS, and XPS of the metal substrate after extended galvanostatic deposition at similar potentials (*vide infra*) is used to assign the second region to Zn^{2+} reduction. H_2 generation during the Zn^{2+} redution is below the detection limit in GC. When the sweep is reversed, two oxidative peaks are seen when using a Au WE (255 mV and 440 mV) and one major peak is seen when using a Pt WE (275 mV). The two peaks with the Au WE can be attributed to stripping of Zn and Zn-Au alloys in accordance with previous literature reports.[197, 200] Zn-Pt alloys do not form as readily as do Zn-Au alloys,[199] and therefore only a single anodic peak corresponding to Zn stripping is observed. HER is irreversible as expected and does not have an accompanying oxidation peak. Subsequent cycles reveal a decrease in the current density which

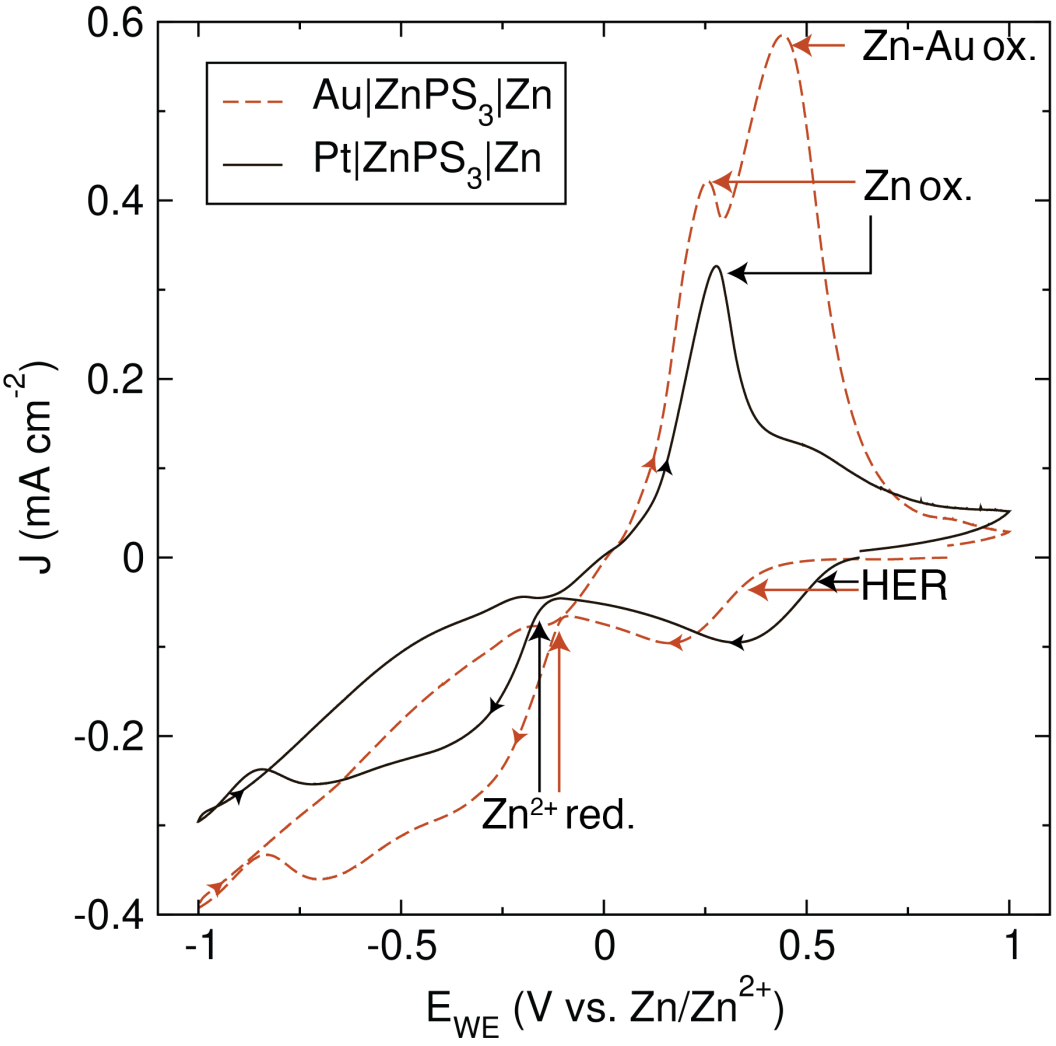

Figure 4.8: Cyclic voltammetry measured with the water vapor exposed $ZnPS_3$ as the electrolyte, Au or Pt working electrodes, and Zn counter electrodes at 0.5 mV s^{-1} and 40 °C. The arrows on the CVs indicate the direction of voltage sweep.

could be caused by degradation of the $ZnPS_3$-metal interface after each iteration of deposition and stripping or delamination due to evolved H_2 gas (Figure A.13).

Galvanostatic experiments are used to achieve sufficient Zn deposits for characterization. Figure 4.9a shows the potential transient during application of a -50 μA cm^{-2} current density at 40 °C with a Au WE. The potential transient contains two distinct regions that correlate to the cathodic processes observed in the CV. Again, we observe H_2 evolution by GC in the initial region from open circuit to approx. -100 mV vs. Zn/Zn^{2+} and thus the first region can be assigned to HER. Then, a nucleation dip is observed which is commonly observed for metal nucleation.[203]

The voltage then reaches a plateau that is stable for the duration of the electrolysis which is again consistent with metal deposition.

To determine if the plateau region is indeed due to Zn deposition, we perform SEM, EDS, and XPS characterization of the WE post electrolysis. First, the cell is disassembled and the electrolyte is exfoliated away with solvent, revealing the buried WE surface. Figure 4.9c shows an SEM image of the Au surface after a 2.05 C of charge is passed. The image shows nonuniform deposits 20 μm in diameter. Figure 4.9d shows the Zn metal counter electrode after a 2.05 C of charge is passed. The electrode shows clear signs of pitting which is commonly observed after metal stripping. Application of higher current densities (up to 100 μA cm^{-2}) results in greater overpotentials and smaller deposits (1 μm diameter) in agreement with classical nucleation and growth theory.[203]

The nature of the deposit is probed with spectroscopy. Figure 4.9b shows the Zn LMM Auger spectrum measured by XPS of the Au WE after deposition. The Auger spectrum is used as the primary analysis because the shift between chemical states of Zn is more significant than that in the Zn 2p spectrum (See Appendix A and Figure A.14). Zn metal is identified by the Zn^0 $L_3M_{45}M_{45}$ (^1G) at 991.7 eV and Zn^0 $L_3M_{45}M_{45}$ (^3F) at 995.2 eV (dashed lines). Zn^0 is present in the spectrum before sputtering, however, the spectrum is dominated by ZnO (988.1 eV) and $Zn(OH)_2$ (986.5 eV) which likely form on the surface of deposited Zn metal exfoliation of the electrolyte to prepare the sample for ex-situ characterization. The Zn^0 peaks increase in intensity after sputtering for 35 minutes and the oxide/hydroxide species decrease, showing that the surface film can be ablated to reveal the Zn metal below. Additional XPS data is available in the SI. EDS provides additional evidence of Zn deposition on Au and supports the presence of Zn-Au alloys (Figure A.17) . We also pursue deposition on a Pt substrate that does not alloy with Zn. The data can be found in Figure A.18.

The electrodeposition and stripping of Zn metal on Au and Pt cannot be achieved using pristine $ZnPS_3$, due to the prohibitively low conductivity. Therefore, the deposition and stripping results presented provide strong evidence that Zn^{2+} conductivity of $ZnPS_3$ is drastically enhanced after water adsorption.

Proposed Mechanism of Ionic Conduction in Water Vapor Exposed $ZnPS_3$

In pristine $ZnPS_3$, Zn^{2+} conduction is hypothesized to occur in the intralayer via a vacancy-mediated mechanism, which is explained in detail in our previous re-

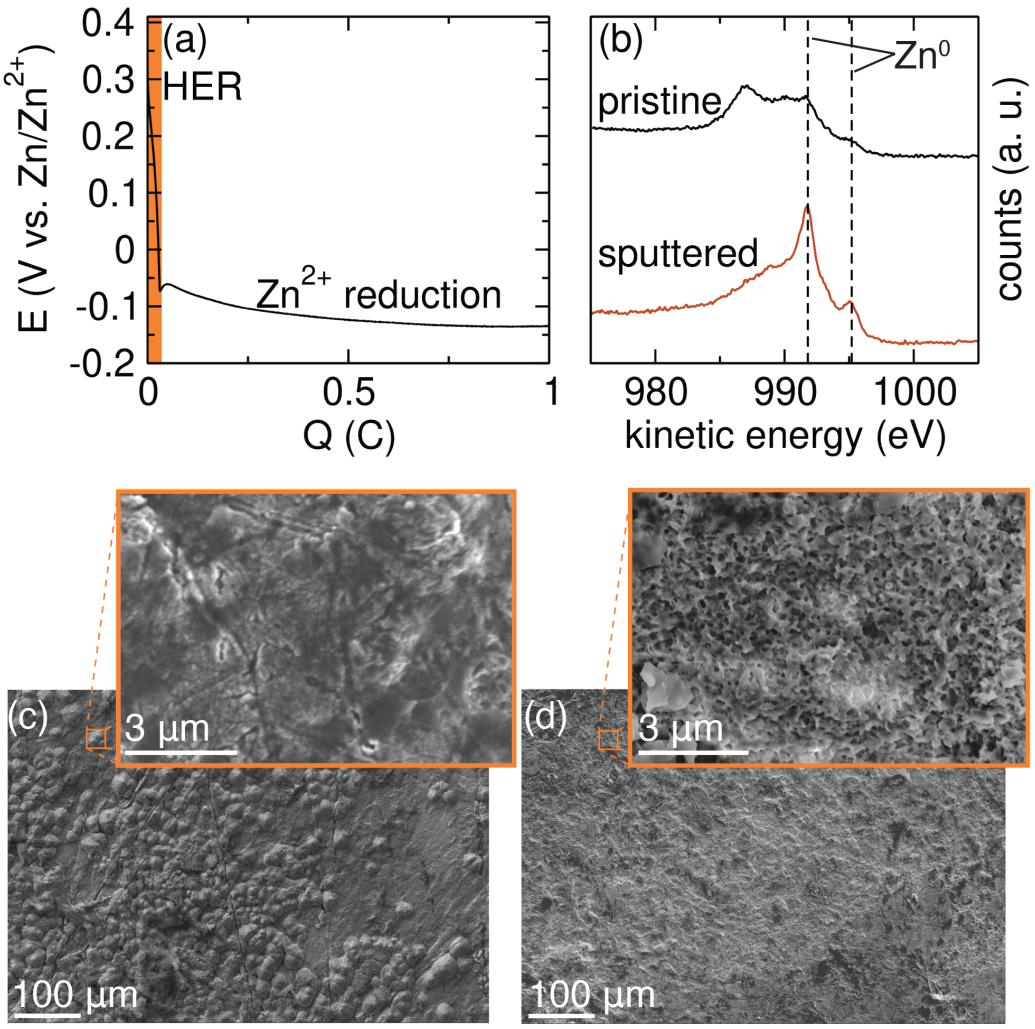

Figure 4.9: (a) The potential transient upon application of -50 μA cm^{-1} to 0.52 $H_2O/ZnPS_3$ sandwiched between a Au foil working electrode and Zn foil counter/reference electrode at 40 °C in a Swagelok cell under 3 kN of force. (b) Zn LMM Auger spectrum measured by XPS of the Au working electrode after deposition and exfoliation of the electrolyte. Zn^0 $L_3M_{45}M_{45}$ (^1G) at 991.7 eV and Zn^0 $L_3M_{45}M_{45}$ (^3F) 995.2 eV (shown as dashed lines) are used to identify Zn metal on the Au surface before and after sputtering. The intensity of Zn metal increases after sputtering as the surface films are removed. (c) SEM of the Au surface after deposition at two magnifications. (d) SEM of the Zn counter electrode surface at two magnifications showing pitting from uneven stripping of Zn.

port.[54] If Zn^{2+} conduction in 0.52 $H_2O/ZnPS_3$ was to occur through a similar mechanism, a substantial increase in vacancy concentration would be required to account for the drastic increase in conductivity. However, the structural characterization of 0.52 $H_2O/ZnPS_3$ does not indicate that significant additional vacancies

are formed. Therefore, Zn^{2+} conduction in x $H_2O/ZnPS_3$ likely occurs through a different mechanism than that in the pristine $ZnPS_3$.

Amorphization of SSEs often results in an increase in ionic conductivity.[204, 205] Excess water adsorption could result in the formation of amorphous domains within the material. However, NMR data shows that 0.52 $H_2O/ZnPS_3$ does not contain significant fractions of amorphous phases. Furthermore, amorphization of the anhydrous $ZnPS_3$ phase by ball milling does not result in significantly higher conductivity than pristine $ZnPS_3$ (Figure A.19). Thus, the high conductivity is not derived from amorphous domains within the bulk.

Since the superionic conductivity of 0.52 $H_2O/ZnPS_3$ is coupled to the presence of adsorbed water, the ionic conduction mechanism of 0.52 $H_2O/ZnPS_3$ may be more similar to that observed in solvent-adsorbed porous materials, like metal organic frameworks (MOFs) and covalent organic frameworks (COFs), as opposed to mechanisms that generally occur in dry inorganic solids. In almost all cases, ionic conduction in MOFs require "activation" by soaking the MOF in a liquid electrolyte containing the mobile ions of interest.[206] Ionically conductive MOFs exist somewhere between the extremes of liquid and solid electrolytes. The underlying mechanisms that enable ionic conduction in MOFs are still being investigated; however, generally M^{2+} ions are suggested to conduct via: (1) a hopping mechanism along a conduction pathway of anionic ligands,[207] or (2) within the pores.[208] Conduction in the pores must be mediated or enhanced by liquid or vapor solvent molecules.[209, 210] Moreover, a single-ion Zn^{2+} conducting COF was developed, in which Zn^{2+} from the COF conducts in liquid water within the pores.[114]. In many of these ion conductive frameworks, the total ionic conductivity is on the order of 10^{-4} S cm^{-1}, but the contribution of the multivalent ion to the total conductivity is not often reported in these complex systems.

Although $ZnPS_3$ is not a porous solid and has not been activated with a liquid electrolyte, the ionic conduction in water vapor exposed $ZnPS_3$ bears similarities to the solvent-mediated mechanism in MOFs. Since the water is present on the surface of grains or in the grain boundaries, and not in the van der Waals gap, we hypothesize that the superionic Zn^{2+} conduction in 0.52 $H_2O/ZnPS_3$ occurs via conduction of solvated Zn^{2+} ions in the grain boundaries or on grain surfaces. The question then is: What is the origin of the mobile Zn^{2+}? One possibility is that $ZnPS_3$ is dissolved into the adsorbed water at the surface, effectively creating a liquid electrolyte within the solid matrix. We investigate the stability of $ZnPS_3$ in water by immersing $ZnPS_3$

powder in excess water under a variety of conditions and then measuring ^{31}P NMR on the supernatant, for which the results can be found in Figure A.21. Dissolution of $ZnPS_3$ would lead to the presence of $[P_2S_6]^{4-}$ in the ^{31}P NMR spectra. Notably, in these control experiments the H_2O:$ZnPS_3$ ratio is 100 times greater than in 0.52 H_2O/$ZnPS_3$, and such a high ratio would in theory promote $ZnPS_3$ dissolution in the control. However, resonances that would correspond to dissolved $[P_2S_6]^{4-}$, around 100 ppm,[211] are absent from the ^{31}P NMR spectra after several days at RT, 40 °C, and even after sonication. Minor hydrolysis of $ZnPS_3$ does occur, as evidenced by the -0.05 and 2.6 ppm resonances that are likely due to formation of phosphates. After three days at 40 °C in excess water, the hydrolysis was limited to 3.7% of the $ZnPS_3$ present. Based on the NMR results, $ZnPS_3$ is largely insoluble in water under all conditions relevant to the present work, and therefore generation of Zn^{2+} and $[P_2S_6]^{4-}$ through dissolution cannot explain the observed behavior.

Another possibility to explain enhanced conductivity upon humidity exposure is that the inherent Zn^{2+} conductivity of $ZnPS_3$ allows Zn^{2+} to migrate out of the lattice onto the surface or into the grain boundary where it is then solvated. This is similar to the established "unusual cation-transfer intercalation process" observed in MPS_3 compounds, predominantly $CdPS_3$ and $MnPS_3$.[212] In aqueous solutions of ionic salts, $CdPS_3$ and $MnPS_3$ have been shown to intercalate guest cations into the interlayer spacing facilitated by the loss of water-solvated Cd^{2+} and Mn^{2+} from the lattice, in contrast to the electron-transfer process that governs intercalation in layered metal dichalcogenides.[164, 166, 213] The removal of Zn^{2+} from $ZnPS_3$ would result in a cation vacancy. The vacancy could be stabilized by incorporation of H^+, for instance. In $CdPS_3$, it is suggested that H^+ can occupy Cd^{2+} sites.[113] Importantly, such a mechanism would allow for Zn^{2+} to conduct in the absence of a counter-ion, yielding essentially a cation-only conductor. We picture the mechanism similar to the polymeric single-ion conductors in which the anion is covalently attached to a polymer backbone allowing for the the mobile cation (usually Li^+) to conduct.[214] Here, the anion is confined to the $ZnPS_3$ lattice as a cation vacancy and the Zn^{2+} is free to conduct solvated by water. In this mechanism, the solid state Zn^{2+} conductivity of $ZnPS_3$ is critical in enabling the superionic conductivity in the presence of adsorbed water. The proposed Zn^{2+} conduction mechanism is shown by the cartoon in Figure 4.10. ZnS is sometimes present as a minor impurity in $ZnPS_3$ batches (up to 5 wt%). We investigate the behavior of ZnS after exposure to water vapor as a control to rule out any contribution to the behavior observed with 0.52 H_2O/$ZnPS_3$, the details and results can be found in Figure A.22.

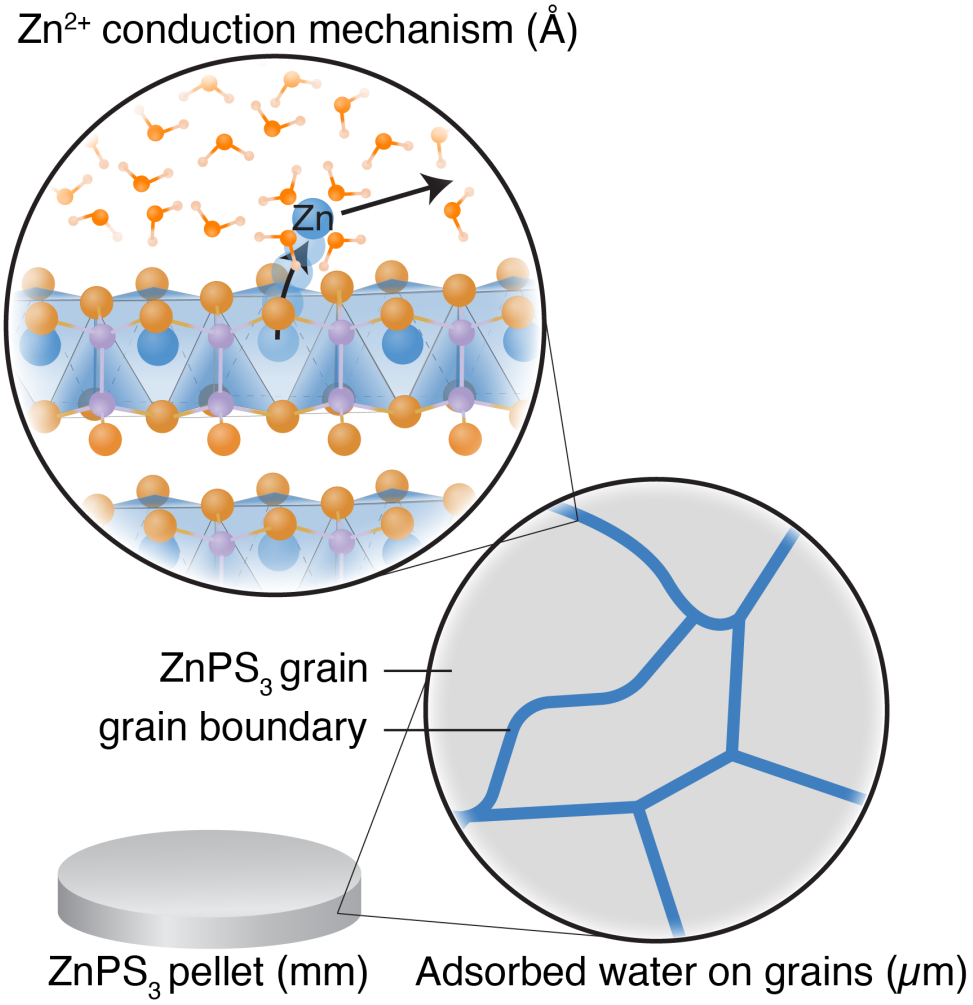

Figure 4.10: An illustration showing the water adsorption and Zn^{2+} conduction in 0.52 $H_2O/ZnPS_3$ at different length scales. The first zoom-in captures a micrometer scale, and highlights that water adsorbs onto the surface of $ZnPS_3$ grains and occupies the grain boundaries. The second zoom-in captures shows the proposed Zn^{2+} conduction mechanism. Zn^{2+} migrates out of the lattice where it is solvated by the adsorbed water and can conduct freely, while the $[P_2S_6]^{4-}$ is trapped in the lattice.

The accompanying H^+ conduction likely occurs through a Grotthuss mechanism, similar to the substituted $CdPS_3$-based membrane in which H^+ hop between hydrogen-bonded water molecules in the van der Waals gap.[113, 215] The Grotthuss mechanism is generally characterized by high conductivity and low E_a ($\leq$ 400 meV), and has been demonstrated to occur on the inter-granular surfaces of materials like hydrated SnO_2 and zirconium phosphates/phosphonates.[216–218]

4.4 Conclusions

Exposure of $ZnPS_3$ to humid environments results in adsorption of water onto the surface of the grains and within grain boundaries, as XRD shows no expansion of the $ZnPS_3$ layer spacing after significant water uptake. The water is weakly bound and is lost easily by evacuation in a glovebox antechamber or heating at temperatures ≥ 50 °C. Water incorporation does not significantly alter the structure or degrade the $ZnPS_3$ up to 0.52 $H_2O/ZnPS_3$. Despite minimal changes to the $ZnPS_3$ itself, 0.52 $H_2O/ZnPS_3$ exhibits superionic conduction. The ionic conductivity increases up to five orders of magnitude over anhydrous $ZnPS_3$ as a result of water adsorption. The dependence of ionic conductivity on adsorbed water also makes x $H_2O/ZnPS_3$ potentially useful as a humidity sensor. We show that Zn^{2+} and H^+ are mobile in 0.52 $H_2O/ZnPS_3$. The presence of H^+-containing species is confirmed by ^1H MAS ssNMR, and conduction of H^+ is confirmed by EIS with non-blocking PdH_x electrodes and electrochemical H_2 evolution via HER. Evidence of Zn^{2+} conduction is provided through EIS with non-blocking Zn electrodes, transference number measurements (~ 0.47), and the first demonstration of Zn deposition and stripping through a SSE onto various metal substrates. To the best of our knowledge, 0.52 $H_2O/ZnPS_3$ displays the highest Zn^{2+} conductivity in any solid-based system (σ = 1.44 mS cm^{-1} and $\sigma_{Zn^{2+}}$ = 0.67 mS cm^{-1}). We hypothesize that the Zn^{2+} conduction occurs via a water-mediated mechanism, in which solvated Zn^{2+} is mobile in the adsorbed water. Since $ZnPS_3$ is largely insoluble in water, it is unlikely that dissolution of $ZnPS_3$ results in the generation of mobile ions. Instead, we hypothesize that the mobility of Zn^{2+} in $ZnPS_3$ solid allows for the solvation of Zn^{2+} into the adsorbed water network, leaving the associated anion essentially confined to the $ZnPS_3$ lattice. This nuance potentially highlights the importance of the Zn^{2+} conduction in the pristine phase in enabling the superionic conductivity after water vapor exposure to result what we hypothesize is a cation-only conductor.

Interestingly, ionic conduction in 0.52 $H_2O/ZnPS_3$ bears more similarities to ionically conductive MOFs and COFs than to ionic conduction in other inorganic solids. However, 0.52 $H_2O/ZnPS_3$ does not require "activation" by soaking in a liquid electrolyte but rather acts as a reservoir of mobile Zn^{2+} in the presence of water vapor. The present work builds on numerous reports concerning water-assisted multivalent ionic conduction in intercalation cathodes, and opens a new avenue for the realization of superionic multivalent ion conductivity in electronically-insulating solid materials. We hesitate to denote this observed phenomenon as "solid state" ionic conduction due to the incorporation of water. However, the materials do not flow,

nor do they contain bulk liquid water. In fact, incorporation of some amount of solvent is likely necessary to wet interfaces in "solid state" batteries. Additionally, we demonstrate methods to qualitatively decouple Zn^{2+} and H^+ conduction in a water containing materials, and highlight the importance of doing so in water or air exposed systems, where H^+ could be responsible for the observed conductivity.

4.5 Experimental Section

Material Preparation

Synthesis

$ZnPS_3$ was prepared using traditional solid state methods from Zn metal powder (Alfa Aesar, 99.9%), P_2S_5 (Acros Organics, >98%), and elemental S (Acros Organics, >99.5%) in an Ar-filled glovebox without further purification. The Zn, P_2S_5, and S_8 were combined in a 2:1:1/8 molar ratio and ground thoroughly using a mortar and pestle. The reactants were then densified into pellets with an Arbor press and sealed in a vitreous silica ampoule under vacuum (<10 mtorr). The reaction vessel was placed in a box furnace, heated to 400 °C at a rate of 2 °C min^{-1}) (K min^{-1}) and allowed to react at 400 °C for 24 h. After the reaction was complete, the tube was allowed to cool to ambient temperature inside of the furnace. The resulting off-white powder was collected and handled in an Ar filled glovebox.

Pelletization

Between 40-60 mg of $ZnPS_3$ powder was pressed into a pellet in an Ar filled glovebox using a 12T max hydraulic press from Vivtek. The anhydrous powder was pressed using a 6 mm stainless steel die set at 2 tons for 5 minutes. The resulting pellets were between 0.5-1 mm thick. In some cases the pellets were sputtered with Au, Pt or Pd at 40 mA for 60 s on both flat surfaces using a Ted Pella 108 Auto Sputter Coater in an Ar filled glovebox.

Water Vapor Exposure of $ZnPS_3$

$ZnPS_3$ was exposed to different RH environments generated by saturated salt solutions in sealed chambers or ambient air to produce x $H_2O/ZnPS_3$. Atmospheres of 11%, 75%, and 96% RH were established using LiCl (Sigma-Aldrich, ≥99%), NaCl (Macron, ≥ 99%), and K_2SO_4 (Beantown Chemical, 99%), respectively. A hygrometer was placed in each of the chambers to ensure the desired RH value was achieved and maintained. $ZnPS_3$ pellets were exposed to each RH for two days to

ensure the adsorption of water into the pellet had reached equilibrium. The weight of the pellet did significantly change after 2 days when exposed to up to and including 75% RH. Similarly, "air-exposed pellets" were left on a bench top for 2 days, and a hygrometer was used to measure the ambient humidity during the duration of exposure.

Material Characterization

Powder X-ray Diffraction

XRD data were collected using a Rigaku SmartLab diffractometer (CuK_{α}). All patterns were collected using the Rigaku air-sensitive sample holder for consistency. The pristine sample was prepared in an Ar filled glovebox but the water vapor exposed samples were loaded into the sample holder in air. All patterns were collected from 5-60° 2θ as a step size of 0.03° and 5° per minute.

Raman Spectroscopy

Raman spectroscopy was measured using a Horiba Instruments XplorRA PLUS Raman Spectrometer equipped with 532 nm laser. The sample was mounted on a glass microscope slide. The signal was averaged over 200 acquisitions lasting 1 s each with a 50 μm slit and 500 μm hole. The laser power was kept between 1 and 10% to prevent local heating and sample degradation.

Thermogravimetric Analysis & Differential Scanning Calorimetry

TGA and DSC were conducted simultaneously on a Netzsch STA 499 F3 Jupiter (Netzsch Instrument North America LLC, Burlington, Massachusetts). A correction (blank) was run before the samples consisting of two empty alumina crucibles while flowing 25 mL/min of nitrogen to remove any contributions from the crucibles. Samples were removed from their humidity chambers in pellet form and crushed in an agate mortar and pestle into a powder. Approximately 12 mg of powder was weighed and placed in one of the alumina crucibles and heated to 250 °C at a rate of 5 °C min^{-1} (K min^{-1}). Mass loss was measured using the Netzsch Proteus Analysis Software.

Attenuated Total Reflection Fourier Transform Infrared Spectroscopy

ATR FTIR was measured using a Thermo Scientific Nicolet 6700 FTIR with a Diamond ATR Smart iTR accessory. Powders of the x $H_2O/ZnPS_3$ samples were placed

in direct contact with the ATR crystal on the sample stage. To load these samples, the powders had to be removed from the respective humidity environments and exposed to ambient humidity for a few minutes during preparation and measurement.

Scanning Electron Microscopy & Energy Dispersive X-ray Spectroscopy

After the deposition experiments were concluded, the Swagelok cells were disassembled and the electrodes and were submerged in octylamine (Aldrich, 99%) for exfoliation of $ZnPS_3$. The electrodes were retrieved, washed 3 times with acetone, and placed on carbon tape. SEM of Au working electrodes, Pt working electrodes, and Zn counter electrodes after extended polarization was performed using a ZEISS 1550VP field emission SEM with an acceleration voltage of 10 kV at 5kX, 10kX, and 30kX magnification. EDS data were collected using an Oxford X-MAX SSD system with an acceleration voltage of 10 kV or 20 kV.

Electrochemical Impedance Spectroscopy

EIS measurements were collected using a Bio-Logic VSP300 multichannel potentiostat with ultralow current probes. Symmetric cells were assembled with Au-sputtered, x $H_2O/ZnPS_3$ in 0.25 i.d. PTFE spring-loaded Swagelok cells. EIS was measured in a homemade Faraday cage immediately after assembly and at different temperatures, controlled by a convection oven. The cell temperature was allowed to equilibrate for 1 hour at each temperature. Cells that remain at $T \geq 50$ °C lose water over time, which results in a time dependent conductivity at elevated temperatures, see Figure A.2. Therefore,the temperature series are terminated at 50 °. The EIS spectra were collected using a sinusoidal voltage amplitude of 50 mV in a frequency range of 3 MHz to 100 mHz and averaged over 10 measurements. Three successive measurements were taken to ensure that the response was stable. The data were fit to an equivalent circuit using ZFit in the EC-Lab software.

DC Polarization & Transference Number Measurements

For DC polarization and transference number measurements the 0.52 $H_2O/ZnPS_3$ pellet was placed in a 0.25" i.d. PTFE Swagelok cell and sandwiched by relevant metal foils. Zn, Pt and Au foil were punched into 7/32" diameter circles, the Zn and Au foils were polished using 9, 3, and 1 μm diamond suspensions and then sonicated with acetone and IPA and dried under vacuum. The surface of the Pt foil was heated in a H_2 flame. A vice was used to apply a force of 3kN to ensure the

maintenance of sufficient contact between the metal foil and 0.52 $H_2O/ZnPS_3$. EIS was conducted with a 20 mV amplitude before and after DC polarization of 20 mV for 30 minutes.

Deposition of Zn with water vapor exposed $ZnPS_3$

The 0.52 $H_2O/ZnPS_3$ pellet was placed between the polished Zn metal and either Au or Pt in a 0.25" i.d. Swagelok cell in the vice as explained above. The pressurized cell was placed in an oven at 40 °C. The current was applied using a Bio-Logic VMP3 multichannel potentiostat. After deposition, the stack was removed from the Swagelok cell in air and the $ZnPS_3$ pellet was delaminated from the metal surface by exfoliation using n-octylamine overnight. The foil was then rinsed with acetone and dried in air before characterization.

Cyclic Voltametry

CVs were conducted using a Bio-logic VMP3 with in the same cell setup as the deposition experiments, with polished metal foil electrodes, 40 °C, and a vice to maintain cell pressure. The cells were swept from at 0.5 mV/s starting from OCV and sweeping to negative potentials.

X-ray Photoelectron spectroscopy

XPS data were collected using a Kratos AXIS Ultra spectrometer (Kratos Analytical, Manchester, UK) equipped with a monochromatic Al Kα_1 X-ray source (1486.7 eV). Data were collected at pressures of ~$5x10^{-8}$ Torr. The electron-collection lens aperture was set to sample a 700x300 μm spot, and the analyzer pass energy was 80 eV for survey spectra and 20 eV for high-resolution spectra. The element-specific scans were collected with a resolution of 0.1 eV, except for the Zn 2*p* scans, which were collected with a resolution of 0.2 eV. Ion gun etching of the surface was done using an Ar ion gun with a gun voltage of 3 kV and a spot size of 1 mm^2. The instrument energy scale and work function were calibrated using clean Au, Ag, and Cu standards. All spectra were recorded with an electron gun charge neutralizer to minimize charging effects and referenced to Au^0 $4f_{7/2}$ at 84 eV. The instrument was operated by Vision Manager software version 2.2.10 revision 5. The XPS data were analyzed using CasaXPS software (CASA Software Ltd).

Gas Chromatography

Ar was flowed through the 4-way Swagelok cell with the flow rate set as 1 sccm by an Alicat flow controller. The gasses that passed through the test cell were injected to GC/MS (Agilent 7820A Gas Chromatograph system/Agilent 5977E Mass Selective Detector) with Agilent Carboxen 1010 PLOT column and Ar as the carrier gas. H_2 was detected by a thermal conductivity detector (TCD) and quantified based on calibration curve collected from standard gas samples.

Solid State Magic Angle Spinning Nuclear Magnetic Resonance Spectroscopy

MAS ssNMR was performed using Bruker Avance 500 MHz spectrometer. All samples were packed in a 4 mm ZrO_2 HR-MAS rotor with 50 μl PTFE spacer (Cortecnet). 40 mg of powder was packed into the rotor. ^{1}H and ^{31}P MAS ssNMR spectra were recorded spinning at 8 kHz. For ^{31}P, a 4 μs to $\pi/2$ RF pulse was applied. The spectra were referenced to an external 85% H_3PO_4 standard at 0 ppm. For ^{1}H, a 4 μs to $\pi/2$ RF pulse was applied. The spectra were referenced to an external tetramethylsilane standard at 0 ppm.

Solution Nuclear Magnetic Resonance Spectroscopy

To probe $ZnPS_3$ dissolution in water, 500 μL of Milli-Q water was added to 20 mg of $ZnPS_3$ at room temperature, or 40 °C for up to 3 days, or sonicated at room temperature for 30 mins. After 6 hours, 1 day, 2 day, and 3 days, 100μL of the supernatant was collected and mixed with 1μL of trimethyl phosphate as internal standard. Appropriate amounts of D_2O was added to the NMR tube. ^{1}H-decoupled ^{31}P NMR spectra were collected on a Varian 400 MHz spectrometer, and was referenced to trimethyl phosphate at 3.8 ppm in D_2O.

Chapter 5

MODULAR MPS$_3$-BASED FRAMEWORKS FOR SUPERIONIC CONDUCTION OF MONOVALENT AND MULTIVALENT IONS

This chapter has been adapted from:

(1) **Iton, Zachery W. B.**; Irving-Singh, Z.; Hwang, S.-J.; Bhattacharya, A.; Das, T.; Shaker, S.; Clément, R. J.; Goddard III, W. A.; See, K. A. Modular MPS$_3$-Based Frameworks for Superionic Conduction of Monovalent and Multivalent Ions. *Manuscript submitted*.

5.1 Abstract

Next-generation batteries based on more sustainable working ions could offer improved performance, safety, and capacity over lithium-ion batteries, while also decreasing the cost. Development of next-generation battery technology using "beyond-Li" mobile ions is limited, in part, due to a lack of understanding of solid state conduction of these ions. Next-generation mobile ions tend to have relatively low mobility in solids due to: (1) larger ionic radii (Na^+, K^+, Ca^{2+}), which limit the accessible migration pathways, and/or (2) higher charge densities (Mg^{2+}, Zn^{2+}, Al^{3+}), which result in strong electrostatic interactions within the solid. Here, we introduce ligand-coordinated ions into MPS$_3$-based solid host crystals (M = Mn, Cd) to simultaneously increase the size of the bottlenecks within the migration pathway and screen the charge-dense ions. We employ X-ray diffraction, thermogravimetric analysis, inductively coupled plasma mass spectrometry, scanning electron microscopy, energy dispersive X-ray spectroscopy, solid state magic angle spinning nuclear magnetic resonance spectroscopy, pulsed field gradient nuclear magnetic resonance spectroscopy, density functional theory quantum mechanics, and electrochemical impedance spectroscopy to probe the ionic mobility, structural and chemical changes in the MPS$_3$ materials after ion exchange.

We show that the inclusion of coordinating ligands enables ambient temperature superionic conductivity of various next-generation mobile ions in an electronically-insulating MPS$_3$-based solid. These ion-intercalated MPS$_3$-based frameworks not only enable deeper understanding of ligand-coordination in solid state ionic conduction, but could potentially serve as a universal solid state electrolyte for various next-generation battery chemistries.

5.2 Introduction

The landscape of modern battery technology has been dominated by lithium-ion batteries (LIBs). However, material availability, scalability, cost, and escalating global energy demands,[6, 7, 160] motivate development of alternative battery chemistries. "Next-generation" mobile ions, such as Na^+, K^+, Mg^{2+}, Ca^{2+}, Zn^{2+}, and Al^{3+}, represent a promising frontier in battery technology due to their abundance and potential for high volumetric capacities.[158] However, one of the major challenges in developing battery technology based on next-generation mobile ions is the difficulty in achieving solid state conduction of those ions. Solid state conduction is crucial for ion transport in electrodes, interphases, and solid electrolytes. The larger size of ions like Na^+, K^+, Ca^{2+} restrict their movement through the typically rigid migration pathways available in solid materials. Additionally, the mobility of ions with higher charge densities, such as Mg^{2+}, Zn^{2+}, Al^{3+}, is impeded by the strong electrostatic interactions between these mobile ions and other ions within the solid. These challenges are outlined in detail in our recent perspective.[158] Difficulties with solid state ionic conduction are less pronounced in Li-based systems due to the relatively small size and low charge density of Li^+.

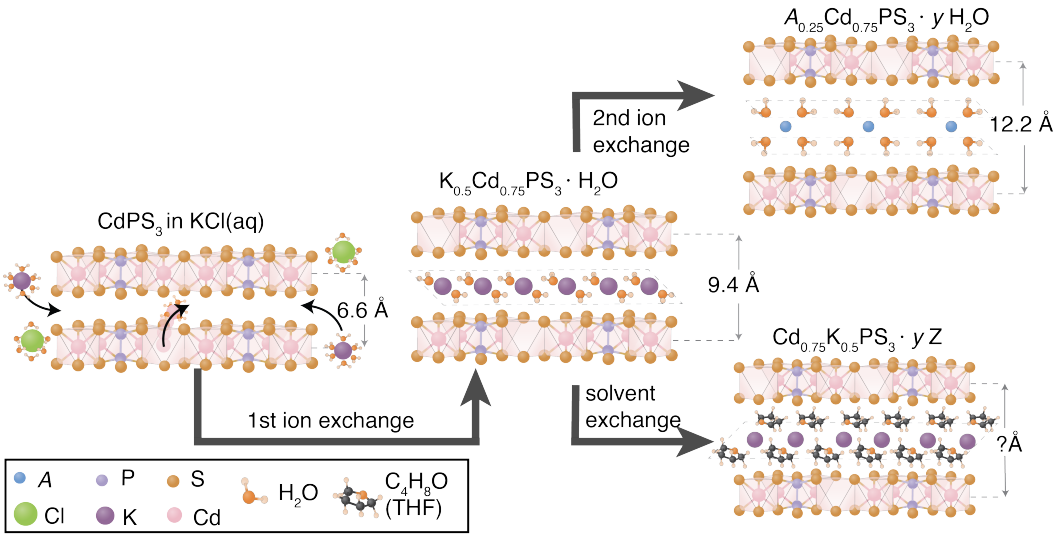

Figure 5.1: A schematic of the ion and ligand exchange used in the present study. In an aqueous KCl solution, $CdPS_3$ intercalates hydrated K^+ ions into the van der Waals gap and maintains charge neutrality by losing Cd^{2+} ions from the metal layer. After $K_{0.5}Cd_{0.75}PS_3$ is formed one can perform either: (1) a second ion exchange to introduce desired monovalent or multivalent mobile ions, or (2) a ligand exchange to replace H_2O in the system.

Solid state conduction of larger cations has typically been achieved in structures based on open frameworks with large migration bottlenecks, like Prussian blue analogues,[219–221] β-Alumina,[16, 32, 222, 223] or NASICON phases.[224–226] Whereas, solid state conduction of charge-dense ions has been mostly limited to electronically-conductive materials. In systems like Mo_6S_8, thiospinel Ti_2S_4, and $MgSc_2S_4$, the mobile electrons are hypothesized to facilitate ionic mobility by screening the charge-dense ions, decreasing the strength of electrostatic interactions within the solid.[45, 96, 101, 103, 227] For electronically-insulating materials, such as solid electrolytes or interphases, there is an absence of mobile electrons to screen the charge of the targeted ions. Only a handful of electronically-insulating inorganic solids have been shown to conduct charge-dense ions, such as Zn^{2+} in $ZnPS_3$,[54] or Mg^{2+} in borohydrides,[46, 48, 49, 51, 52, 123] but each have their own challenges associated with low room temperature conductivities (σ_{RT}) or high activation energy (E_a).

One path to enable the conduction of large or charge-dense cations in electronic insulators is to introduce ligands, like H_2O, that can coordinate to the targeted cations within the host crystal. Solid state mobility of ligand-coordinated ions was extensively studied in mica clays such as vermiculite and montmorillonite.[228–232]. However, in clays the σ is generally < 0.1 mS cm^{-1}. In battery systems, the addition of H_2O to increase multivalent ionic conduction has been primarily attempted for cathode materials, such as MnO_2 and V_2O_5 [105, 106, 161, 162]. Recently, this concept has been extended to electronically-insulating inorganic solids, like $Li_2Sn_2S_5$[110] and $ZnPS_3$[233], as well as various MOFs and COFs,[114, 208–210, 234] for solid state electrolyte applications.

Here, we leverage coordinated ligand molecules within solid frameworks based on MPS_3 materials (M = Mn, Cd) to achieve two primary goals: (1) increasing the size of the bottlenecks in migration pathways and (2) screening charge-dense ions to decrease electrostatic interactions within the lattice. By combining the advantages of large bottlenecks and charge screening we can devise a universal framework for ambient temperature superionic conduction of various ions within an inorganic, electronically-insulating solid.

$CdPS_3$ and $MnPS_3$ exhibit a peculiar mechanism for the intercalation of hydrated cations into the van der Waals gap.[164] Unlike the redox-based intercalation in common battery electrodes in which incorporation of a cation coincides with a Faradaic reduction of the host,[235] when cations are intercalated into MPS_3 mate-

rials, charge balance is maintained by M^{2+} loss in an ion exchange mechanism.[164, 212, 236] This mechanism is similar to that observed in clays.[228, 229, 237, 238] $CdPS_3$ and $MnPS_3$ form as monoclinic ($C2/m$) layered compounds with a slightly distorted hexagonal network of edge-sharing Cd^{2+} or Mn^{2+} octahedra. The Cd^{2+} or Mn^{2+} are coordinated by $[P_2S_6]^{4-}$ polyanions. The layers stack along the c-axis separated by a van der Waals gap of $\sim$ 3.5 Å.[239] The basal spacing ($d_{(001)}$) of $CdPS_3$ is slightly larger than that of $MnPS_3$ (6.55 vs. 6.49 Å) due to the larger size of Cd^{2+} over Mn^{2+} (0.95 vs. 0.83 Å).[240]

Here, we exploit the ability of $CdPS_3$ and $MnPS_3$ to host cations within the van der Waals gap to generate materials that contain various ions of interest through a sequential ion exchange strategy that is illustrated in Figure 5.1. First, a cation with a small hydrated radius (e.g. K^+) is intercalated into the van der Waals gap of an MPS_3 material.[212] Charge neutrality is maintained through the loss of the labile metal (Cd^{2+} or Mn^{2+}) from the metal layer (Equation 5.3), resulting in negatively charged sheets of MPS_3 sandwiching positively charged, hydrated ions. The hydrated K^+ ions can be further exchanged to introduce a larger hydrated cation (A), like Li^+ , Na^+ , Mg^{2+} , Ca^{2+}, Zn^{2+}, Al^{3+} (Equation 5.2). Direct insertion of large hydrated cations is kinetically limited, as such this sequential exchange method is preferred.

$$MPS_3 + KCl_{(aq)} \longrightarrow K_{2x}M_{1-x}PS_3 \cdot yH_2O + MCl_{2\,(aq)} \tag{5.1}$$

$$K_{2x}M_{1-x}PS_3 \cdot yH_2O + ACl_{n(aq)} \longrightarrow A_{2x/n}M_{1-x}PS_3 \cdot zH_2O + KCl_{(aq)} \tag{5.2}$$

Additionally, we demonstrate that the H_2O molecules can be exchanged for aprotic ligands, e.g. acetonitrile (MeCN), and tetrahydrofuran (THF). The ligand exchange serves several purposes: (1) to probe the effect of different ligand molecules on ionic mobilities, (2) to demonstrate that the mobile ions conduct in the absence of H^+, and (3) to broaden the applicability of these frameworks to H_2O-incompatible systems.

The ability of MPS_3 materials to intercalate a wide variety of guest ions and molecules has been useful for diverse applications. The areas of research span from non-linear optics[166, 168], photoluminescence[241], hosts for biomolecules

[242] or polymers,[243, 244] and superconducting magnets.[245] However, the ionic conductivity of these materials has been less rigorously explored. Some studies have investigated the mobility of hydrated Na^+, K^+, and Cs^+ in $CdPS_3$.[246–249] These studies concluded that Na^+ was slightly mobile (10^{-5} S cm^{-1}) but K^+ and Cs^+ were immobile. Another study investigated the conductivity of trivalent cations in MPS_3 in the dried state, finding no significant ionic conduction ($10^{-8} - 10^{-10}$ S cm^{-1}).[250] Notably, nanosheet-based membranes using $Cd_{0.85}PS_3Li_{0.15}H_{0.15}$ were found to have exceedingly high 2D H^+ conductivity (300 mS cm^{-1}at RT and 98 % relative humidity (RH)).[113]

Compound	x	y	H_2O/f.u.	H_2O/*A*	Nominal Formula
$K_xCd_yPS_3$	0.50 ± 0.02	0.79 ± 0.02	1.0 ± 0.1	2	$K_{0.5}Cd_{0.75}PS_3 \cdot H_2O$
$Li_xCd_yPS_3$	0.47 ± 0.01	0.85 ± 0.03	2.0 ± 0.7	4.4	$Li_{0.5}Cd_{0.75}PS_3 \cdot 2\ H_2O$
$Na_xCd_yPS_3$	0.51 ± 0.02	0.81 ± 0.02	2.0 ± 0.5	3.9	$Na_{0.5}Cd_{0.75}PS_3 \cdot 2\ H_2O$
$Mg_xCd_yPS_3$	0.24 ± 0.01	0.78 ± 0.05	1.9 ± 0.0	7.9	$Mg_{0.25}Cd_{0.75}PS_3 \cdot 1.9\ H_2O$
$Ca_xCd_yPS_3$	0.24 ± 0.02	0.81 ± 0.02	2.0 ± 0.5	8.3	$Ca_{0.25}Cd_{0.75}PS_3 \cdot 2\ H_2O$
$Zn_xCd_yPS_3$	0.41 ± 0.09	0.76 ± 0.24	0.25	0.63	$Zn_{0.4}Cd_{0.6}PS_3 \cdot 0.25\ H_2O$
$Al_xCd_yPS_3$	0.13 ± 0.01	0.81 ± 0.08	2.5 ± 0.6	14.5	$Al_{0.17}Cd_{0.75}PS_3 \cdot 2.3\ H_2O$
$K_xMn_yPS_3$	0.40 ± 0.05	0.80 ± 0.03	0.8 ± 0.2	2.1	$K_{0.4}Mn_{0.8}PS_3 \cdot 0.8\ H_2O$
$Li_xMn_yPS_3$	0.34 ± 0.03	0.84 ± 0.03	1.4 ± 0.2	4.0	$Li_{0.4}Mn_{0.8}PS_3 \cdot 1.4\ H_2O$
$Na_xMn_yPS_3$	0.59 ± 0.08	0.71 ± 0.04	1.7 ± 0.6	2.7	$Na_{0.6}Mn_{0.7}PS_3 \cdot 1.7\ H_2O$
$Mg_xMn_yPS_3$	0.19 ± 0.01	0.82 ± 0.01	1.8 ± 0.1	9.5	$Mg_{0.2}Mn_{0.8}PS_3 \cdot 1.8\ H_2O$
$Ca_xMn_yPS_3$	0.25 ± 0.02	0.76 ± 0.02	1.5 ± 0.1	6	$Ca_{0.25}Mn_{0.75}PS_3 \cdot 1.5\ H_2O$
$Zn_xMn_yPS_3$	0.46 ± 0.06	0.62 ± 0.06	1.6 ± 0.1	2.6	$Zn_{0.4}Mn_{0.6}PS_3 \cdot 1.6\ H_2O$
$Al_xMn_yPS_3$	0.12 ± 0.00	0.84 ± 0.01	2.4 ± 0.4	16	$Al_{0.13}Mn_{0.8}PS_3 \cdot 2.2\ H_2O$

Table 5.1: The stochiometry of each $A_{2x/n}M_yPS_3$ compound, x and y are measured by ICP-MS and normalized to P, which is assumed to be constant. The H_2O content of each compound, which is determined with a combination of TGA and measured mass pre- and post-drying using an analytical balance. The amount of H_2O per intercalated ion in each material, and the nominal formula of each compound based on the measured cation content.

Recently, Yu & Ren reported on $CdPS_3$-based nanosheet membranes with various intercalated cations.[251] The membranes boasted impressive 2D ionic conductivity but importantly, the conductivity was similar irrespective of the intercalated cation (170–330 mS cm^{-1} at RT and 98 % RH). In fact, the ion-intercalated membranes also displayed similar behavior in regards to layer expansion and activation energy. This is likely due to excess H_2O content within the restacked membranes which could lead to significant contribution from H^+ conduction through a Grotthus mechanism,[113, 215] or direct diffusion of solvated ions in a confined liquid electrolyte. Such a

mechanism is distinct to conduction of ligand-coordinated ions within a host crystal. The transition from ligand-coordinated solid state conduction to the conduction of solvated ions within a confined liquid in the solid framework at excess ligand/solvent concentrations has been noted in previous studies of hydrated $Li_2Sn_2S_5$, MOFs, and clays.[110, 252–254]

To minimize contributions from H^+ conduction and to reveal inherent structure-property relationships that can be drowned out in the presence of excess H_2O, here we investigate bulk, ion-intercalated $CdPS_3$ and $MnPS_3$ materials primarily at ambient RH (~ 40–55 %), and with coordinating ligands that range from H_2O to aprotic, neutral solvent molecules. This allows us to understand the nuanced differences between the effects of various frameworks, intercalated ions, and coordinating ligands on the ionics thereby deepening our understanding of ionic conduction in solids. Additionally, the 3D bulk conduction pathways in polycrystalline samples in this study are directly applicable to practical battery applications. We also introduce $MnPS_3$ as an environmental friendly alternative with comparable performance, and demonstrate non-aqueous analogues that would be more compatible with desirable electrode materials.

We employ several characterization techniques to study the structural and chemical changes after ion exchange, as well as the resulting ionic mobility. These techniques include: electrochemical impedance spectroscopy (EIS), X-ray diffraction (XRD), thermogravimetric analysis (TGA), inductively coupled plasma mass spectrometry (ICP-MS), scanning electron microscopy (SEM), energy dispersive X-ray spectroscopy (EDS), quantum mechanics simulations, solid state magic angle spinning nuclear magnetic resonance spectroscopy (MAS NMR), and pulsed field gradient nuclear magnetic resonance spectroscopy (PFG NMR). At ambient temperature and RH, all of the H_2O-coordinated interlayer cations, barring Al^{3+}-intercalated $MnPS_3$, exhibit "superionic", or practically useful, bulk conductivity (> 0.1 mS cm^{-1}) and relatively low E_a. Notably, in the polycrystalline samples studied here both σ_{RT} and E_a vary significantly depending on the identity of the intercalated cation. The ligand exchange to aprotic molecules generally results in decreased σ_{RT} and increased E_a, but achieving practically useful conductivity is still possible using ligands like MeCN.

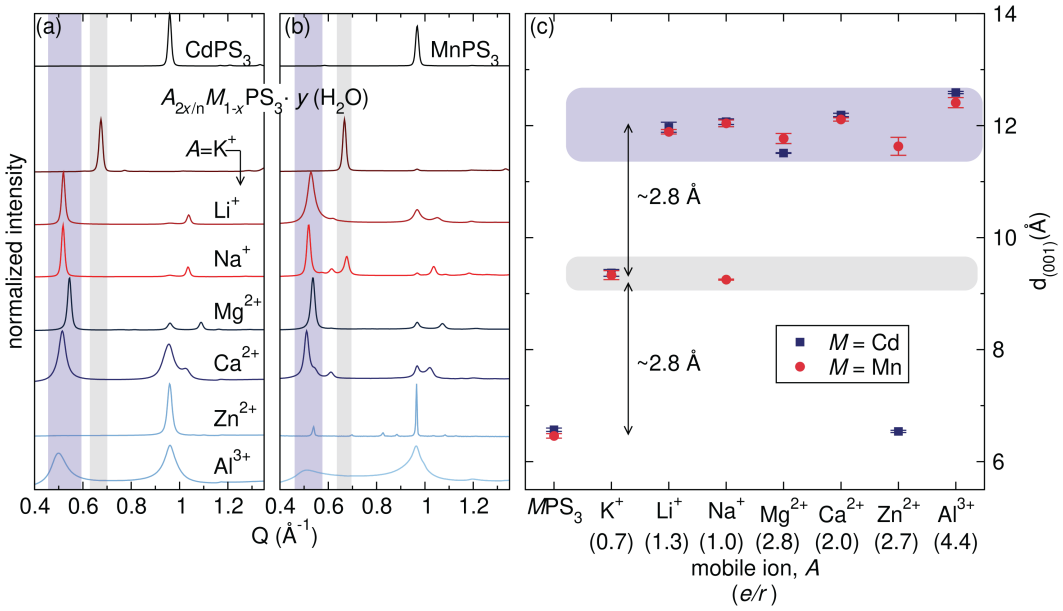

Figure 5.2: Characterization of the $A_{2x/n}M_{1-x}PS_3 \cdot y\ H_2O$ materials using powder XRD. XRD patterns of (a) $CdPS_3$-based and (b) $MnPS_3$-based compounds. (c) $d_{(001)}$ spacing of $A_{2x/n}M_{1-x}PS_3 \cdot y\ H_2O$. The error bars reflect the standard deviation of several XRD measurements, the differences are due to the range of ambient humidity ($\approx$ 40-55%). The gray regions highlight materials with a monolayer of H_2O and the purple regions highlight materials with a bilayer of H_2O. Note, the pattern of $Zn_{0.4}Mn_{0.6}PS_3 \cdot 1.6\ H_2O$ is collected using Cu K_α radiation because the sample inadvertently dehydrated during preparation for the synchrotron measurement.

5.3 Results and Discussion

5.4 Chemical and Structural Characterization After Ion Exchange

Elemental Analysis

$M PS_3$ materials can undergo ion exchange processes as outlined in Equations 5.3 and 5.2. The ion exchanges have been well characterized in previous reports.[166, 212] However, the amount of M that is replaced by A, described by 'x' in Equations 5.3 and 5.2, differs between various studies — ranging from $0.1 \leq x \leq 0.25$.[164, 166, 248, 251] Intuitively, x can be controlled by varying the MPS_3:$ACl_{n(aq)}$ ratio, as illustrated in Figure B.1. Here, we aimed for high A content ($x \simeq 0.25$ for $CdPS_3$-based samples and $\simeq 0.20$ for $MnPS_3$-based samples) to incorporate the largest number of charge carriers, which we hypothesize will lead to optimal conductivity. Table 5.1 shows the results of elemental analysis on the ion-intercalated MPS_3 compounds. The amount of A intercalated (x) and remaining M (y) are determined using ICP-MS and are normalized to the measured P content. The measured S content is inaccurate due to H_2S evolution during the sample digestion process, but it is also presumed to

stay constant. The standard deviations for the ICP-MS data are representative of a minimum of five different synthesis batches per material. Due to synthesis and measurement inaccuracies the precise stoichiometry of the $A_{2x/n}Cd_{1-x}PS_3$ compounds sometimes contains ≤10% excess Cd, however a comparison of "ideal" batches and those with excess Cd shows that there is no noticeable impact on the σ_{RT} and E_a (Figure B.2). The H_2O content is determined by a combination of TGA (Figure B.3) and changes in pellet masses pre- and post-drying, measured using an analytical balance. For the rest of this manuscript, the compounds are referred to by their nominal formula for simplicity. The differences in the degree of ion exchange that occurs, both for different ions within a given framework and between the frameworks ($CdPS_3$ vs. $MnPS_3$), is discussed in Supplementary Note 1.

Experimental Structural Investigation

The changes to the crystal structure of the MPS_3 materials after ion exchange is investigated using XRD. Figure 5.2a and b show the low Q regions of representative XRD patterns of ion-exchanged $CdPS_3$-based and $MnPS_3$-based compounds, respectively, to highlight the layer spacing. Full XRD patterns are shown in Figure B.4. After ion exchange, all of the materials are vacuum filtered until dry and then equilibrated at ambient RH before XRD is taken. Previous work has confirmed that the structure within the metal layers is maintained upon ion exchange.[166, 246, 255]. Raman spectra are measured for the $CdPS_3$-based compounds to confirm that the polyanion remains intact and its environment in the metal layer is largely unchanged (Figure B.5).

Figure 5.2c shows the extracted $d_{(001)}$ values for all compounds. Error bars are shown to reflect the deviation associated with fluctuating RH at the time of replicate measurements. The original (001) reflection of the pristine MPS_3 phase occurs at Q = 0.95 and 0.97 for M = Cd and Mn, respectively. The expanded (001) reflection of the ion-exchanged materials appears between Q = 0.49 and 0.67 Å and the subsequent (002) reflections can be seen around Q ≃ 1.05 Å. Layer expansion suggests incorporation of the ions into the van der Waals gap and SEM confirms that the layered platelet morphology of the particles is maintained. EDS confirms that the intercalated ions are homogeneously dispersed within the particles (Figure B.6).

It is clear from Figure 5.2c that the $d_{(001)}$ spacing after ion exchange can be grouped into two main categories. The layer spacing of the hydrated structures increases by

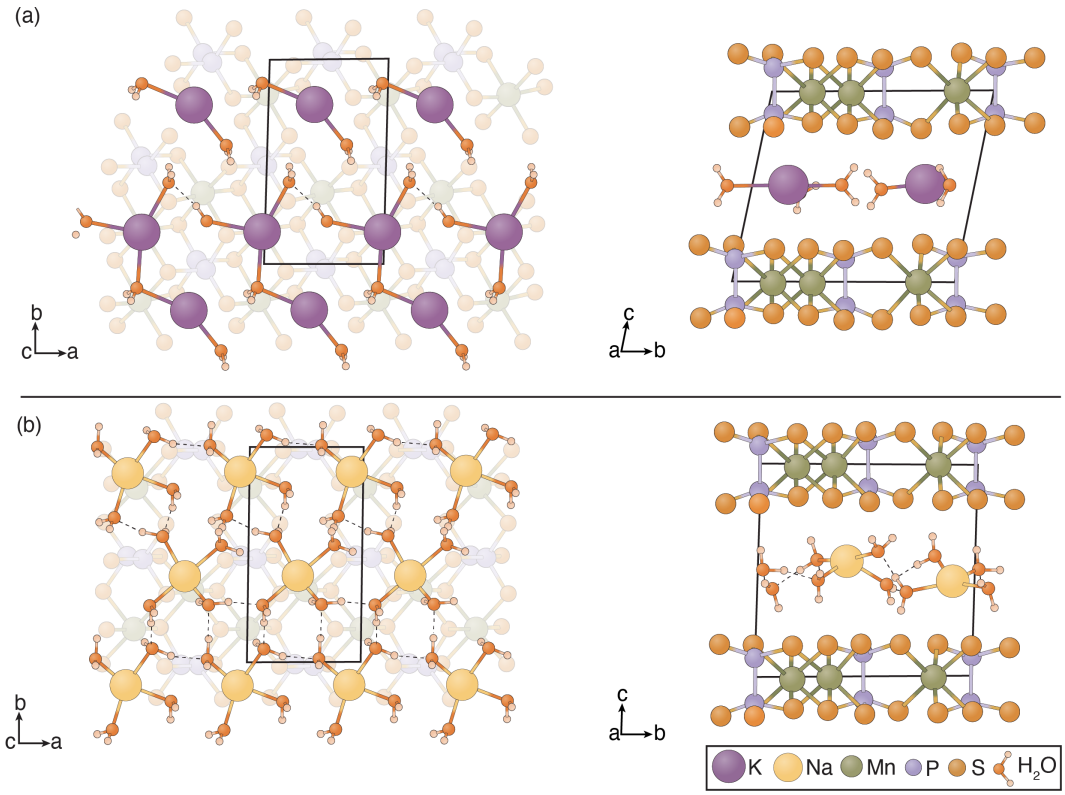

Figure 5.3: Computationally relaxed structures of (a) $K_{0.5}Mn_{0.75}PS_3 \cdot H_2O$ and (b) $Na_{0.5}Mn_{0.75}PS_3 \cdot 2\ H_2O$. The left images show the view down the *c* axis after removing the metal layer above the hydrated interlayer cations, the metal layer below is made partially transparent for clarity. The right images show the view down the *a* axis. Hydrogen bonds between H_2O molecules are shown as dotted black lines. The H_2O molecules are inaccurately depicted as being smaller than the interlayer cation for clarity.

either ~ 2.8 Å or ~ 5.6 Å. These expansions correspond to the van der Waals radius of one or two H_2O molecules, respectively. Therefore, the layer spacing increase is likely due to the formation of either a monolayer or bilayer of H_2O around the intercalated cations in the van der Waals gap, rather than following the expected hydrated cation radii of the inserted ions. The formation of hydrated MPS_3 materials containing mono or bilayer H_2O has been noted in previous works on monovalent cation intercalated MPS_3 materials.[166, 212, 248] However, to the best of our knowledge, the hydrated structure of MPS_3 phases containing other ions has not been explored.

The occurrence of mono or bilayer H_2O structures with the other ions is similar to the results in clays, transition metal dichalcogenides (MS_2), or MXenes, which also

exhibit hydrated structures containing mono or bilayer H_2O with a wide range of interlayer cations.[229, 253, 256–259]

Whittingham, in addition to Lerf and Schöllhorn, independently investigated the hydration of interlayer ions in MS_2 compounds, (M = Ti, Nb, Ta).[257, 258] These studies showed that the resulting structure of the hydrated compounds is governed by the cation-ligand interaction. Specifically, the ability of the cation-ligand interaction to offset the loss in electrostatic lattice energy incurred by separating the cations from the anionic sulfide layers. Lerf and Schöllhorn found that this behavior can be described empirically by the charge/radius ratio (e/r) of the interlayer cations, which is correlated with the hydration energy. These rules translated well to other layered hydrated structures, like MXenes[259]. Cations for which $e/r < 1$ (large and low charge, e.g., K^+) can only stabilize a monolayer of H_2O, whereas if $e/r > 1$ (small and high charge, e.g. Li^+ and multivalents) then a bilayer of H_2O can be stabilized. In Figure 5.2c, we show the e/r value for each mobile ion and confirm the relationship between e/r and the layer spacing in the ion-intercalated MPS_3 materials. The e/r of Na^+ is $\simeq 1$, suggesting that it can stabilize either a monolayer or bilayer of H_2O. Indeed, isolated forms of monolayer or bilayer H_2O, or even a mixture of both, can be achieved when $A = Na^+$ depending on the RH (Figure B.7). Furthermore, the TGA and derivative thermogravimetry (DTG) results (Figure B.3) show that $Na_{0.5}Cd_{0.75}PS_3 \cdot 2\ H_2O$ is the only $CdPS_3$-based compound with two distinct H_2O loss events, corresponding to the transition between the stable monolayer and bilayer H_2O structures. The H_2O content of materials containing multivalents, e.g. $Ca_{0.25}Mn_{0.75}PS_3$, changes as the RH is varied but a phase transition to a structure with monolayer H_2O is not observed for multivalent intercalated compounds at any RH due to the higher hydration energies of the multivalent ions. The solvation shells of multivalent ions are likely incomplete at low RH, but the overall bilayer structure is maintained (Figure B.8). This also agrees with the findings of Lerf and Schöllhorn for MS_2 compounds.[257] Notably, in contrast to the structure observed by Yu *et al.* in $CdPS_3$-based membranes,[251] bulk $K_{0.5}Cd_{0.75}PS_3$ could not be forced into a bilayer H_2O structure even at 96 % RH (Figure B.9), perhaps due to the more rigid constraints of the polycrystalline powders.

Structural Effects Associated with the Mobile Ion

Next, we consider the structural effects associated with (1) the identity of the mobile ion and (2) the $CdPS_3$ vs. the $MnPS_3$ host structure. First, we consider the structure of a given MPS_3 framework with different ions. As outlined above, of the ions selected for this study only K^+ stabilizes a hydrated structure with a monolayer of H_2O, while the other ions stabilize a bilayer at ambient RH in both MPS_3-based frameworks. Although two main categories of layer spacings exist as the mobile ion is changed, there is a measurable deviation of the layer spacing within the bilayer regime depending on the intercalated cation. We plot the charge density of the mobile ion for structures that reside in the bilayer regime vs. the $d_{(001)}$ layer spacing (shown in Figure B.10) and find that the layer spacing is inversely related to the charge density of the intercalated ions. More charge-dense ions, such as Mg^{2+}, interact more strongly with the H_2O ligands, creating shorter bonds and therefore, a smaller total diameter of the hydrated cation complex. Al^{3+} is an outlier in this trend likely because the very high charge density of the cation attracts more H_2O which expands the layer. In fact, the Al-containing material contains more mol equivalents of H_2O (~16:1 H_2O:Al) then can be accommodated in a first shell coordination environment. However, the H_2O does not behave as "free" water as evidenced by ^{1}H NMR (*vide infra*).

Ion exchange with Zn^{2+} in both structures behaves differently compared to most of the other ions. In both host materials, reflections associated with the pristine MPS_3 phase dominate the diffraction patterns, though a small peak associated with an expanded lattice is observed for the $MnPS_3$ framework. We note that Zn is indeed incorporated into the materials (see Table 5.1). For the $CdPS_3$-based material, we interpret these data to mean that most of the Zn^{2+} prefers to occupy the vacancies in the metal layer, which would suggest that the material does not contain substantial ligand-coordinated Zn^{2+}. Indeed, the $Zn_{0.4}Cd_{0.6}PS_3$ material does not contain a significant amount of H_2O (Table 5.1). The $Zn_{0.6}Mn_{0.4}PS_3$, which shows a small expanded reflection, does contain some water due to the small ligand-coordinated Zn^{2+} content. Zn^{2+} is thermodynamically stable in the metal layer as evidenced by the $ZnPS_3$, which is a stable endmember that is isostructural to $CdPS_3$ and $MnPS_3$.[260]

The Difference in Structural Changes Between Frameworks

Next, we discuss trends between $CdPS_3$ and $MnPS_3$ frameworks. A comparison of the two frameworks reveals that generally the $CdPS_3$-based compounds have a larger $d_{(001)}$ than the $MnPS_3$-based compounds, which is consistent with the pristine materials (Figure 5.2c). However, $Mg_{0.2}Mn_{0.8}PS_3 \cdot 1.8\ H_2O$ has a larger basal spacing than $Mg_{0.25}Cd_{0.75}PS_3 \cdot 1.9\ H_2O$. At this time, we do not know why this is. $Na_{0.6}Mn_{0.7}PS_3 \cdot 1.6\ H_2O$ forms a two phase mixture of mono and bilayer H_2O at ambient RH while only the bilayer is formed with the $CdPS_3$ host at ambient RH. Even though the Mn analogue has more intercalated Na^+, it absorbs less H_2O at a given RH. This is likely because the smaller lattice of $MnPS_3$ demands a larger energy cost for expansion, therefore a higher driving force for H_2O absorption (i.e. higher RH) is required to stabilize the bilayer structure.

Density Functional Theory (DFT) Simulations

The stable monolayer hydrated structure of $K_{0.5}Mn_{0.75}PS_3 \cdot H_2O$ and bilayer hydrated structure of $Na_{0.5}Mn_{0.75}PS_3 \cdot 2\ H_2O$ are investigated using DFT simulations to gain further insight into the organization of H_2O molecules and interlayer cations. Such information is difficult to obtain experimentally due to the lack of long range order of the interlayer cations and ligated H_2O – no superstructure peaks are observed in the diffraction. Figure 5.3a shows the relaxed structure of $K_{0.5}Mn_{0.75}PS_3 \cdot H_2O$ and 5.3b shows the relaxed structure of $Na_{0.5}Mn_{0.75}PS_3 \cdot 2\ H_2O$. The interlayer cation and H_2O organization is highlighted viewed down the *c* axis and down the *a* axis. In $K_{0.5}Mn_{0.75}PS_3 \cdot H_2O$, some of the H_2O is bridging between two K^+ ions, while the others are more isolated to one K^+ ion. The isolated H_2O ligands are hydrogen bonded to neighbors and located approximately within the same *ab* plane, supporting the experimentally measured $d_{(001)}$ spacing that suggests roughly a monolayer of H_2O. Many other configurations of $K_{0.5}Mn_{0.75}PS_3 \cdot H_2O$ are similarly stable and are shown and discussed in Figure B.11. The variety of possible structures explains the lack of K ordering in the experimental data with multiple possible configurations likely coexisting at room temperature.

On the other hand, the structure of $Na_{0.5}Mn_{0.75}PS_3 \cdot 2\ H_2O$ contains no bridging H_2O ligands. The H_2O coordinates to Na^+ and participates in hydrogen bonding with nearby H_2O ligands. The higher density of H_2O molecules in $Na_{0.5}Mn_{0.75}PS_3 \cdot 2\ H_2O$ forces the H_2O to distort in the *c* direction and results in roughly a bilayer structure in the *ab* plane, again supporting the experimentally observed $d_{(001)}$ spacing

that suggests bilayer H_2O in the interlayer when two H_2O per formula unit are introduced. The $d_{(001)}$ spacing of the monolayer and bilayer relaxed structures are 8.9 Å and 10.3 Å respectively, which are smaller than the XRD measured values of 9.3 Å and 12.0 Å for $K_{0.5}Mn_{0.75}PS_3 \cdot H_2O$ and $Na_{0.5}Mn_{0.75}PS_3 \cdot 2\ H_2O$, respectively, likely due to thermal expansion at room temperature compared to the calculated structure at 0 K.

5.5 Electrochemical Characterization of the Ionic Mobility

The elemental and structural analysis provides evidence that the intercalated ions are introduced into MPS_3 frameworks and occupy the interlayer space. These results are consistent with previous work on alkali metal ion-intercalated MPS_3 materials,[164, 166, 212, 246] and show that the concept is extendable to many other ions. Due to the increased bottleneck size in the migration pathway, as well as the screened Coulombic interactions between the interlayer cation and anion framework, we hypothesize that the intercalated ions should exhibit enhanced mobility.

To probe the ionics of the materials, the ionic conductivity and activation energy of all compounds is measured using EIS on cold-pressed pellets with a 6 mm diameter. The pellets are assembled in PTFE Swagelok cells with symmetric ion-blocking electrodes. For each material, EIS is measured at a range of temperatures from room temperature (RT) to 70 ° C. Representative Nyquist plots for all compounds are shown in Figure B.13 and B.14, and an example of a fit using an equivalent circuit model for a sample where the high frequency semicircle can be resolved is shown in Figure B.15. The E_a is determined using the well-established Arrhenius-type relationship that governs the thermally activated ionic conduction process.[70, 158] Figure B.16 and B.17 show average Arrhenius-type plots of $\ln(\sigma T)$ vs. T^{-1} for all studied ion-exchanged compounds. The σ_{RT} values and E_a for all studied compounds are plotted in Figure 5.4a and b, respectively. Figure 5.4a and b show the mean and standard deviations obtained from at least three replicate cells, each from a different synthesis batch, and these values are also listed in Table S1. In general, all of the compounds containing solvated ions in the interlayer show high total ionic conductivities at RT, and by 70 ° C all exhibit practically useful conductivities > 0.1 mS cm^{-1}.

Detailed analysis of the dataset enabled by this modular framework facilitates the development structure-property relationships for ligand-coordinated ion conduction in rigid solids.

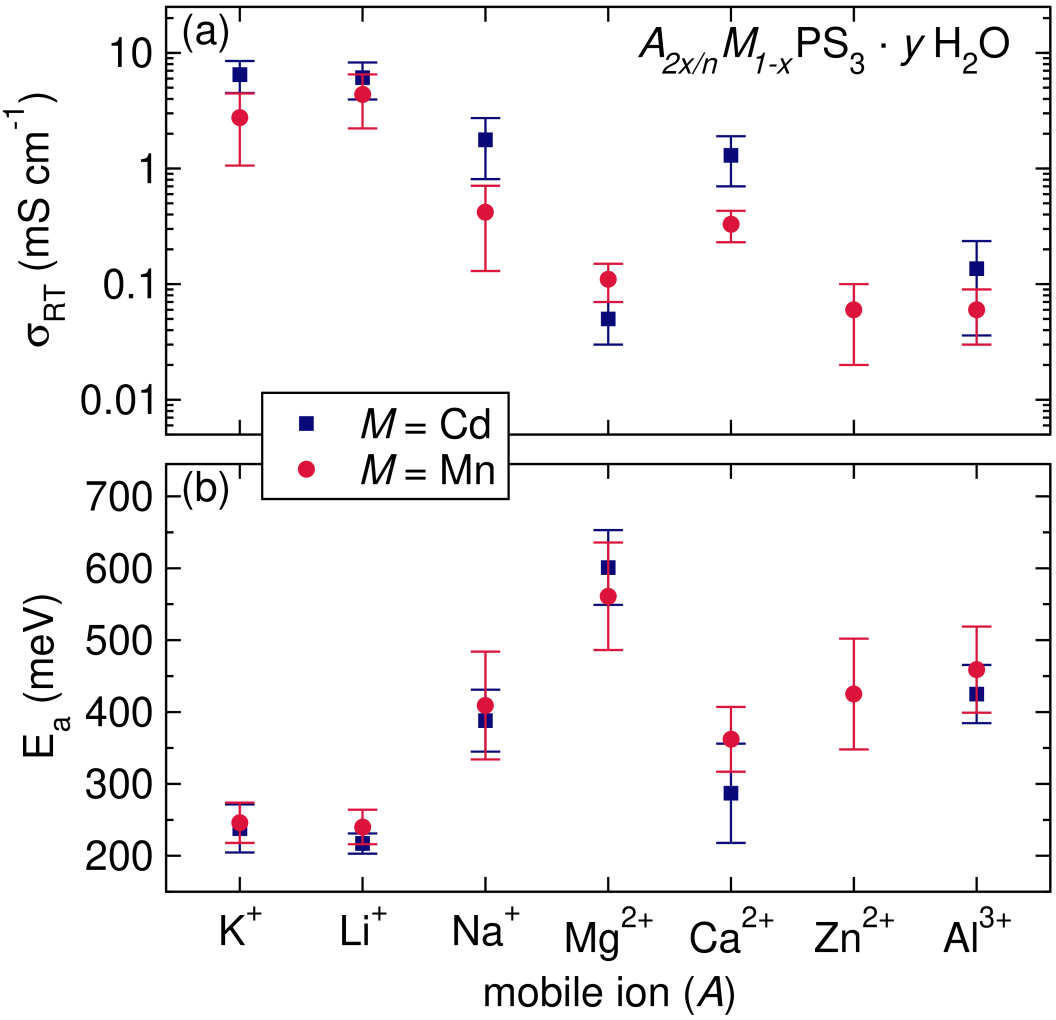

Figure 5.4: (a) The room temperature ionic conductivity (σ_{RT}) and (b) activation energy (E_a) of all ion-intercalated materials at ambient RH. $Zn_{0.4}Cd_{0.6}PS_3 \cdot 0.25\ H_2O$ is not shown here because the σ_{RT} is too low (10^{-9} S cm^{-1}).

The Mobility of Various Ions in a Given Framework

The differences in performance between various ions in a given framework elucidates the effect of charge density and bottleneck size on mobility. It is evident that the ions with higher charge density generally exhibit a lower σ_{RT} and a higher E_a. Thus, the charge density of the mobile ion is a strong factor in determining its mobility, suggesting that the coordinating H_2O is not completely screening the charge. In an aqueous solution, ions with greater charge density attract more H_2O molecules to screen the charge. However, within a rigid solid framework, there is a limit to the number of H_2O molecules that can surround the ion due to spatial constraints. For example, $Mg_{0.25}Cd_{0.75}PS_3 \cdot 1.9\ H_2O$ and $Ca_{0.25}Cd_{0.75}PS_3 \cdot 2\ H_2O$ both contain

bilayer H_2O and both have ~ 8 H_2O per cation. If the mobile ions migrate with the bound H_2O via a "vehicular mechanism" (discussed in detail later), the mobile complex to be considered is the $A^{n+} \cdot y\ H_2O$ species. In this case, assuming each H_2O molecule provides the same degree of charge screening, the mobile complex $Mg^{2+} \cdot 8\ H_2O$ is more charge-dense than the $Ca^{2+} \cdot 8\ H_2O$ complex. Alternatively, if the mobile ions conduct via a hopping mechanism between H_2O molecules the charge density differences between the cations must still be considered.

Furthermore, the charge density of the intercalated ion will affect the size of the hydrated complex and therefore also change the interlayer spacing. The migration bottleneck in these materials is essentially the interlayer spacing, which is directly related to the change in $d_{(001)}$. Mg^{2+}– OH_2 bonds are stronger than the Ca^{2+}– OH_2 bonds, as indicated by the higher peak mass loss temperature observed in TGA and DTG analyses (Figure B.3). The stronger bond in the $Mg^{2+} \cdot 8\ H_2O$ complex pulls the H_2O molecules closer to the cation, leading to less layer expansion and thus a more narrow bottleneck in $Mg_{0.25}Cd_{0.75}PS_3 \cdot 1.9\ H_2O$ compared to $Ca_{0.25}Cd_{0.75}PS_3 \cdot 2\ H_2O$. Again Al^{3+} is the outlier to this trend due to the excess water absorption, as discussed previously.

The combination of the higher charge density of the mobile complex and a narrower bottleneck explains the lower mobility of the charge-dense ions. These trends hold when comparing Na^+ and K^+ in the monolayer structures as well (Figure B.18).

The Ionic Mobility Differences Between Frameworks

In most cases, the performance of a given ion between frameworks is similar (K^+, Li^+, Mg^{2+}, and Al^{3+}). In these cases, slight differences in performance between the two frameworks can be understood in the context of bottleneck size. The $MnPS_3$-based Zn-intercalated compound exhibits significantly better performance than the $CdPS_3$ analogue, while the $MnPS_3$-based compounds for Na^+ and Ca^{2+} ions both perform notably worse than the $CdPS_3$ analogue. Exploring these pronounced differences between frameworks allows us to highlight the impact of ligand-coordinated interlayer ions, the hydration state, and the charge screening by coordinated ligands.

The Effect of Diffusion Bottleneck Size. In the cases where the frameworks have similar performance for a given ion, K^+, Li^+, Na^+, Mg^{2+}, and Al^{3+}, the subtle differences can be explained by considering the bottleneck size. In the framework with the wider bottleneck, the σ_{RT} is slightly higher and E_a is slightly lower. As discussed previously, typically the $CdPS_3$-based framework has the larger bottleneck

and thus we observe that most ion-exchanged $CdPS_3$ phases have higher σ_{RT} and lower E_a than the $MnPS_3$ analogues. The exception is again the Mg^{2+} intercalated compounds, which show the opposite trend in $d_{(001)}$ spacing. This is reflected in the higher σ_{RT} and lower E_a for the $MnPS_3$ host compared to $CdPS_3$. The observed trend in performance highlights the impact of bottleneck size on ion mobility, with larger bottlenecks facilitating improved ion transport.

The Effect of Ligand-Coordinated Interlayer Ions. The σ_{RT} of $Zn_{0.4}Cd_{0.6}PS_3$ is on the order of 10^{-9} S cm^{-1} (not shown in Figure 5.4), which is four orders of magnitude lower than that of $Zn_{0.6}Mn_{0.4}PS_3$. The superior performance of $Zn_{0.6}Mn_{0.4}PS_3$ is due to the presence of some hydrated Zn^{2+} ions in the van der Waals gap, whereas in $Zn_{0.4}Cd_{0.6}PS_3$ the Zn^{2+} ions are immobilized in the metal-layer lattice sites. This illustrates that the solvated interlayer cations are crucial to achieve high ionic conductivity.

The Effect of Hydration State. The disparity in Na^+ performance can be explained by the fact that $Na_{0.6}Mn_{0.7}PS_3 \cdot 1.6\ H_2O$ is a two phase mixture of the monolayer and bilayer hydrated structures. The monolayer structure will have a much lower Na^+ mobility than the bilayer structure due to the decreased bottleneck size and less effective charge screening (this is discussed in detail in the SI). The performance of $Na_{0.6}Mn_{0.7}PS_3 \cdot 1.6\ H_2O$ reflects the combined properties of both hydration states. By equilibrating the material at 75 % RH, the bilayer structure ($Na_{0.6}Mn_{0.7}PS_3 \cdot 2\ H_2O$) can be isolated. $Na_{0.6}Mn_{0.7}PS_3 \cdot 2\ H_2O$ exhibits a conductivity more similar to that of $Na_{0.5}Cd_{0.75}PS_3 \cdot 2\ H_2O$ as expected (Figure B.18).

The Effect of Charge Screening with Ligand Molecules. Similarly to the Na-containing frameworks, $Ca_{0.25}Mn_{0.75}PS_3 \cdot 1.5\ H_2O$ absorbs less H_2O than $Ca_{0.25}Cd_{0.75}PS_3 \cdot 2\ H_2O$ at ambient RH. However, despite the lower H_2O content, the layer spacing associated with the bilayer phase is maintained and does not collapse to the monolayer structure. Instead, we assume the solvation shells around the Ca^{2+} ions in the $MnPS_3$ host are incomplete relative to the $CdPS_3$ host at ambient RH. The maintenance of a bilayer H_2O structure despite H_2O loss allows us to isolate the effect of charge screening from the impact of bottleneck size. Clearly, the difference in H_2O content and solvation significantly impacts the ionic conduction, as evidenced by the 25% higher E_a in $Ca_{0.25}Mn_{0.75}PS_3 \cdot 1.5\ H_2O$ (362 meV) compared to $Ca_{0.25}Cd_{0.75}PS_3 \cdot 2\ H_2O$ (287 meV). Notably, the $Ca_{0.25}Mn_{0.75}PS_3 \cdot 1.5\ H_2O$ also contains 25% less water compared to $Ca_{0.25}Cd_{0.75}PS_3 \cdot 2\ H_2O$. Therefore, the E_a increase and corresponding σ_{RT} decrease in the Mn-based framework is attributed

to the less effective screening of Ca^{2+} in $Ca_{0.25}Mn_{0.75}PS_3 \cdot 1.5\ H_2O$ due to the lower H_2O per cation. This highlights the crucial role of charge screening in facilitating high ionic mobility in MPS_3 frameworks.

5.6 Identification of the Mobile Ion

Though we can draw several structure-property relationships using the range of materials discussed above while assuming the charge carriers are primarily the hydrated cations, the use of H_2O as the coordinating ligand introduces the possibility of H^+ conduction. It has long been debated whether the ionic conductivity of ion-intercalated hydrated clays is a result of primarily H^+ conduction or migration of the intercalated ions.[229–231, 254] Therefore, care must be taken to identify the majority charge carrier in $A_{2x/n}M_{1-x}PS_3 \cdot y\ H_2O$ materials.

Mobile H^+ in $A_{2x/n}M_{1-x}PS_3 \cdot y\ H_2O$ could potentially arise through either surface acidity,[261] or hydrolysis of H_2O bound to intercalated cations that act as Lewis bases.[230, 231]. Since S-based materials tend to adsorb less surface H_2O than O-based materials, due to weaker hydrogen bonds between H_2O and S, surface acidity likely plays a less significant role in MPS_3-based frameworks than in clays. To estimate the contribution of H^+ from surface acidity to the total conductivity, we investigate the ionic conductivity of pure MPS_3 phases under ambient relative humidity (the EIS results are shown in Figure B.19). The σ_{RT} of $MnPS_3$ and $CdPS_3$ are 3×10^{-9} and 4×10^{-10} S cm^{-1}, respectively, which is four or five orders of magnitude lower than that of the worst performing $A_{2x/n}M_{1-x}PS_3 \cdot y\ H_2O$ compounds. Therefore, the observed ionic conductivity in $A_{2x/n}M_{1-x}PS_3 \cdot y\ H_2O$ materials is likely either due to mobile H^+ from the acidity of the ion-solvating H_2O or due to the conduction of the interlayer cations themselves.

Several characteristics of $A_{2x/n}M_{1-x}PS_3 \cdot y\ H_2O$ suggest that the intercalated cations are the majority charge carriers. The fact that the ions are able to be inserted and removed by ion exchange in an aqueous solution indicates their inherent mobility within the structure. Additionally, the absence of superstructure peaks at low Q regions of the XRD patterns suggests that the intercalated ions are not ordered and thus points to the ions' high mobility.[258] Furthermore, the strong correlation between the E_a and σ_{RT} with the identity of the intercalated ion underscores the importance of these ions on charge transport. The E_a for H^+ conduction through a Grotthuss type mechanism, where H^+ are being exchanged by neighboring H_2O molecules, is typically < 400 meV.[113, 215] The variation in E_a measured in the

materials reported here is between 216 and 622 meV, which is more consistent with the conduction of mobile complexes of different charge densities, as discussed above. The observed trends in σ_{RT} also do not align with H^+ being the majority charge carrier. The H^+ concentration would depend on the acidity of the absorbed H_2O, which is influenced by the charge density of the intercalated cation. Therefore, the trend in pK_a of the hydrated cations can be used to predict the trend in H^+ concentration in $A_{2x/n}M_{1-x}PS_3 \cdot y\ H_2O$. In general, the more charge-dense the cation, the more acidic the bound H_2O will be due to A–O bond strength. The pK_a trend of the intercalated ions is overlaid onto the σ_{RT} data in Figure B.20. The $A_{2x/n}M_{1-x}PS_3 \cdot y\,H_2O$ compounds with more acidic interlayer ions (e.g., Mg^{2+}, Zn^{2+}, Al^{3+}) should have the highest H^+ concentration but show the lowest measured ionic conductivities. Thus the observed electrochemical performance is not adequately explained by assuming H^+ is the majority charge carrier.

Ionic Mobility Characterization with MAS NMR

We employ MAS NMR to directly probe the ionic mobility in $A_{2x/n}Cd_{1-x}PS_3 \cdot y\,H_2O$. Performing MAS NMR measurements on $MnPS_3$-based compounds is challenging due to the presence of paramagnetic Mn^{2+}, however, we anticipate that the results of the $CdPS_3$-based compounds can be extended to the $MnPS_3$-based analogues.

Figure 5.5a shows ^1H MAS NMR spectra of all $A_{2x/n}Cd_{1-x}PS_3 \cdot y\ H_2O$ materials to explore the dynamics of H_2O or H^+. The chemical shifts of the central band are provided next to the corresponding spectra, and are listed in Table S2 along with the FWHM of the spectra.

For the $A_{2x/n}Cd_{1-x}PS_3 \cdot y\ H_2O$ compounds, the ^1H NMR spectra all contain a single resonance appearing within a very narrow range of resonant frequencies, indicating a single ^1H environment or that all ^1H environments are exchanging faster than the NMR timescale in each compound. The observed chemical shifts are within the range expected for H in H_2O molecules (around 5 ppm),[181–183, 262] but are noticeably shifted and broader than the signal of "bulk" free H_2O, which is characterized by a sharp peak at $\sim$ 4.75 ppm.[130, 263] The ^1H chemical shift values trend with the charge density of the intercalated cation. Cations with higher charge density experience stronger interactions with the O in H_2O and are thus stronger bases, resulting in more deshielded hydrogen nuclei. Even though $Al_{0.17}Cd_{0.75}PS_3 \cdot 2.3\ H_2O$ has more H_2O than can fit directly around each Al^{3+} ion in the bilayer structure, the NMR spectrum suggests that this excess water is not free.

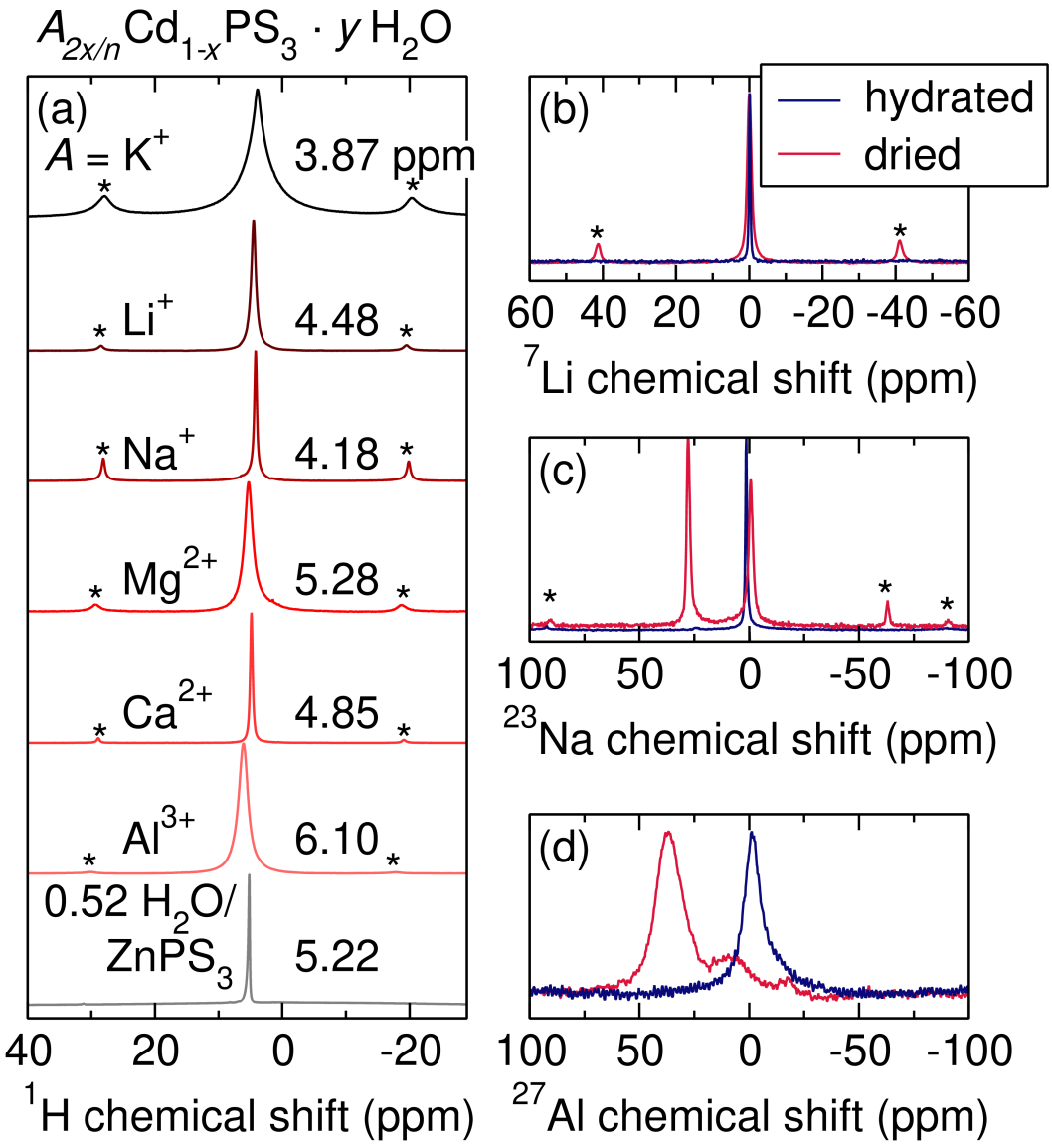

Figure 5.5: MAS NMR study of $A_{2x/n}Cd_{1-x}PS_3 \cdot y\ H_2O$ materials. (a) ^{1}H MAS NMR spectra of $A_{2x/n}Cd_{1-x}PS_3 \cdot y\ H_2O$ compounds and 0.52 $H_2O/ZnPS_3$ for comparison. (b) ^{7}Li spectra of $Li_{0.5}Cd_{0.75}PS_3 \cdot 2\ H_2O$, (c) ^{23}Na spectra of $Na_{0.5}Cd_{0.75}PS_3 \cdot 2\ H_2O$, and (d) ^{27}Al MAS NMR spectra of $Al_{0.17}Cd_{0.75}PS_3 \cdot 2.3\ H_2O$. The metal MAS NMR spectra are collected on the materials at ambient RH (hydrated), and after drying under vacuum at 200 ° C for ≈ 10 hours (dried). * marks the spinning sidebands.

There is potentially a second "shell" of H_2O around the Al^{3+} ions in the interlayer. Exchange of the H_2O in the first and second shell could result in averaging of the H environments into the broad signal that we observe in Figure 5.5a. In general, these

results indicate that the H_2O molecules in $A_{2x/n}Cd_{1-x}PS_3 \cdot y\ H_2O$ are bound to the intercalated cations, in agreement with the TGA results.

Additionally, narrow line widths are typically indicative of high H^+ mobility in inorganic solid materials that contain H_2O;[183, 233, 262, 264] however, all $A_{2x/n}Cd_{1-x}PS_3 \cdot y\ H_2O$ materials exhibit relatively broad line widths. A relevant material to compare the line widths to is H_2O-exposed $ZnPS_3$, which is denoted as 0.52 $H_2O/ZnPS_3$ in Figure 5.5a. When $ZnPS_3$ is exposed to humid air, the H_2O adsorbs at the grain boundaries resulting in solvation of Zn^{2+} into confined water environments yielding mobile Zn^{2+}, however, the H^+ are also mobile and account for roughly 50% of the charge carriers.[233] Notably, the line widths measured for the $A_{2x/n}Cd_{1-x}PS_3 \cdot y\ H_2O$ materials are much broader suggesting less mobile H^+. Additionally, the appearance of spinning sidebands in the ^1H NMR spectra of $A_{2x/n}Cd_{1-x}PS_3 \cdot y\ H_2O$ materials further underlines that the H^+/H_2O molecules are bound to the cations and exhibit limited mobility.

We can additionally evaluate the mobility of the intercalated cations for NMR-active nuclei. Figure 5.5b, c, and d show ^7Li, ^{23}Na, and ^{27}Al MAS NMR spectra, respectively, in both hydrated and dehydrated states in order to probe the mobility of the intercalated cations with and without H_2O ligands. The comparison between the hydrated and dehydrated materials can be found in the next subsection. The ^7Li and ^{23}Na MAS NMR spectra of the respective hydrated ion-intercalated $CdPS_3$ samples both show narrow line widths and an absence of spinning sidebands, suggesting that the cations are sufficiently mobile to average out anisotropic interactions. The chemical shifts for Li and Na are 0.1 ppm and 1.34 ppm, respectively, which are consistent with previous reports of interlayer ions in bilayer H_2O-containing hydrated structures of $Li_2Sn_2S_5$ and Na-containing mica clays.[110, 265, 266] The ^{23}Na spectrum of the hydrated phase is consistent with previous ^{23}Na MAS NMR studies on $Na_{0.50}Cd_{0.75}PS_3 \cdot 2\ H_2O$,[246, 248] which postulated that the Na^+ ions likely conduct with the bound H_2O molecules in the interlayer.

In the case of $Al_{0.17}Cd_{0.75}PS_3 \cdot 2.3\ H_2O$, the ^{27}Al MAS NMR spectrum contains a single resonance at -1.5 ppm which is consistent with Al^{3+} that is octahedrally coordinated by H_2O (~0 ppm).[267, 268] The broader line width is consistent with the lower mobility of Al^{3+} but could also be related to quadrupolar effects due to the potential asymmetry of the coordination environment in the interlayer.

The observed correlation between electrochemical properties and the intercalated ions strongly suggests that the ionic mobility observed in all of these compounds is

predominantly due to the intercalated ions. Furthermore, this claim is supported by the lack of evidence for rapid H^+ exchange, along with the clear indications of metal ion mobility from our NMR studies of the selected ions (^{7}Li, ^{23}Na, and ^{27}Al). Note, conducting metal cation NMR analyses on the K^+, Mg^{2+}, Ca^{2+} and Zn^{2+} materials is prohibitively challenging due to the low natural abundance of their NMR-active isotopes and quadrupolar effects.

Mechanistic Investigation of Ionic Conduction with PFG NMR

To determine if the ionic conduction mechanism is associated with a hopping vs. vehicular mechanism, we use ^{7}Li and ^{1}H PFG NMR to directly measure the diffusivity and E_a of Li and H in $Li_{0.5}Cd_{0.75}PS_3 \cdot 2\ H_2O$. The normalized echo signal attenuation data obtained by PFG NMR are best fit to a biexponential for both ^{7}Li and ^{1}H (Figure B.21). The Tanner-Stejskal equation[269, 270] used to analyze the results assumes an isotropic diffusion process, which is justified here given the polycrystalline nature and morphology of the particles, and presumable lack of preferred orientation of individual crystallites. Hence, we rule out the possibility of having two different diffusing species/pathways in the *ab* plane, or different in-plane diffusivity (in the *ab* plane) compared to the out-of-plane diffusivity (*c* direction), and instead suggest that the presence of two ^{1}H/^{7}Li diffusing components results from nuclei primarily diffusing within a grain, or at or across a grain boundary during the measurement. A two component model also best captured the behavior observed in a PFG NMR study of hydrated $Li_2Sn_2S_5$ by Joos *et al.*[110] In that study, the authors suggested it was likely due to in-plane vs. out-of-plane diffusion in hydrated $Li_2Sn_2S_5$, but also did not rule out grain boundary contributions.

Figure 5.6 shows Arrehnius-type plots of ln(D) vs. 1000/T for both the Li- and H-containing species, where D is the diffusivity of the diffusing components. The room temperature diffusivities of the Li components are 1.62×10^{-10} and 3.09×10^{-11} $m^2\ s^{-1}$, which is associated with 57% and 43% of the Li species measured, respectively. The diffusivities of the H species are 1.13×10^{-12} and 1.55×10^{-14} $m^2\ s^{-1}$, which is associated with 18% and 82% of the H species, respectively. The second, low diffusivity component is not shown in Figure 5.6b. Since the Li diffusivity is a few orders of magnitude higher than that of H, we can deduce that Li are the majority charge carriers and that the Li^+ conduct through a hopping mechanism between H_2O molecules, instead of a vehicular mechanism in which Li^+ conducts with its solvation shell. Interestingly, this mechanism is in

contrast to that suggested in case of hydrated $Li_2Sn_2S_5$ in which the Li and H diffusivities were comparable leading to the conclusion of a vehicular ionic conduction mechanism.[110]

The E_a can be obtained from the Arrehnius-type plots in Figure 5.6. The PFG NMR determined E_a for Li diffusion are 180 and 150 meV for component one and two, respectively. These E_a values are consistent to that measured by EIS (217 ± 14 meV). The E_a measured for the H-containing component is even lower than the Li components at 120 meV, though we note this value is more of an estimate due to the low measured diffusivity. Though the E_a for the H-containing component is low, the much lower diffusivity suggests that the majority charge carrier measured with EIS is Li.

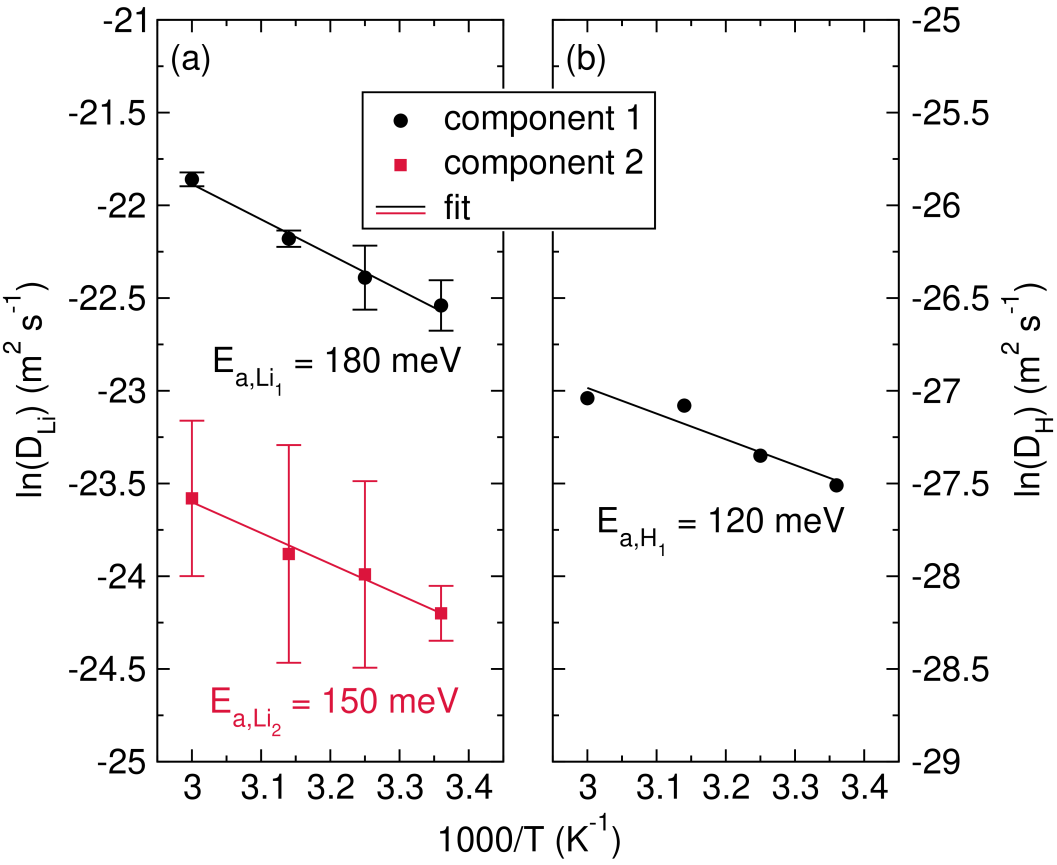

Figure 5.6: Arrhenius-type relationships of the diffusivity (D) measured with (a) ^{7}Li and (b) ^{1}H PFG NMR. The second component of associated with the H-containing species is not shown due to the low diffusivity.

Structural and Electrochemical Characterization of Dried $A_{2x/n}Cd_{1-x}PS_3$

Although the primary charge carriers are likely the intercalated ions rather than mobile H^+, the H_2O ligands play a critical role in enabling the high conductivity. We use MAS NMR and XRD to investigate the local and long-range structural changes that occur after drying in a vacuum oven at T $\geq$ 100 ° C for at least 10 hours, and EIS to probe the electrochemical performance.

The XRD patterns of $A_{2x/n}Cd_{1-x}PS_3$ pre- and post-drying are shown in Figure B.22. Lattice contraction is observed after drying all samples. For the majority of the dry samples, the basal spacing resembles that of the pristine $CdPS_3$ phase. Only dried $K_{0.5}Cd_{0.75}PS_3$ and $Na_{0.5}Cd_{0.75}PS_3$ materials display a larger basal spacing than the pristine $CdPS_3$ material.

The removal of the majority of water in the dried $A_{2x/n}Cd_{1-x}PS_3 \cdot y\,H_2O$ compounds is confirmed by the significant reduction of the ^1H signal (an example is shown in Figure B.23).

Without H_2O, the intercalated cations are destabilized within the van der Waals gap, causing them to occupy the vacant *M* sites. This has been shown previously for Li^+-intercalated $MnPS_3$,[166] as well as A^{3+}-ion intercalated $CdPS_3$.[271] For monovalent ions, there are twice as many intercalated ions as there are vacancies in the metal layer, therefore at least half of the ions may remain trapped in the van der Waals gap. In the case of K-intercalated MPS_3, the K^+ is too large to occupy the vacant sites in the metal layer, and therefore all of the K^+ likely remains in the van der Waals gap. This is evidenced by the lack of a reflection resembling the pristine material lattice spacing in dried $K_{0.5}Cd_{0.75}PS_3$, and is supported by DFT structural calculations discussed in the Supporting Information. In the case of dried $Na_{0.5}Cd_{0.75}PS_3$, the XRD pattern shows a reflection corresponding to the spacing of pristine $CdPS_3$ in addition to a reflection indicating a slightly expanded lattice. The ^{23}Na MAS NMR of dried $Na_{0.5}Cd_{0.75}PS_3$, shown in Figure 5.5c, contains two distinctive resonances which could be assigned to even distributions of Na in two different chemical environments. The ^{23}Na spectrum of dried $Na_{0.5}Cd_{0.75}PS_3$ strongly resembles the ^{23}Na spectrum of $Na_4P_2S_6$.[272] The -0.7 ppm resonance likely corresponds to the interlayer Na^+ and the 27.7 ppm resonance is attributed to the Na^+ that occupies the metal layer. These values are slightly different than $Na_4P_2S_6$ (5.6 ppm and 18.2 ppm respectively) due to the structural and chemical changes imparted by the Cd ions in $Na_{0.5}Cd_{0.75}PS_3$.

Although 0.25 equivalents of Li^+ likely remains in the van der Waals gap in dried $Li_{0.5}Cd_{0.75}PS_3$,[166] layer expansion is not observed because Li is small enough to occupy the interlayer without expanding the $d_{(001)}$ spacing, as is the case in $Li_4P_2S_6$. However, typically ^{7}Li MAS NMR does not permit differentiation between the different chemical environments. [273–275]

For multivalent ion intercalated samples, no layer expansion is observed in the dried materials because the number of intercalated ions is less than or equal to the number of vacancies, so all of the ions occupy the metal layer. As evidenced in Figure 5.5d, after drying, the ^{27}Al resonance shifts to 36 ppm, which is more reminiscent of Al octahedrally coordinated by S.[268]

The dried multivalent-intercalated compounds do not exhibit any meaningful ionic conductivity ($< 10^{-9}$ S cm^{-1}), however the remnant interlayer monovalent ions in the dried monovalent-intercalated compounds enable the study of metal cation mobility in MPS_3 frameworks in the absence of solvating ligands. Notably, the ^{7}Li and ^{23}Na MAS NMR spectra show broadening of the signals and emergence of spinning sidebands after drying, indicating reduced mobility.

Figure 5.7a shows the basal spacing of $A_{2x/n}Cd_{1-x}PS_3$ (A = Li, Na, K) pre- and post-drying. In contrast to the hydrated phases, where the basal spacing is determined firstly by the amount of H_2O absorbed and secondly by the charge density of the ion and by extension the size of the hydrated complex, the $d_{(001)}$ spacing of the dried phases trends with the intercalated ionic radius. In the absence of the bottleneck expansion and charge screening, the σ_{RT} drops by up to six orders of magnitude, and the E_a increases up to three-fold. In this case, the trend in electrochemical behavior is in line with what is expected of traditional solid state electrolytes. $Li_{0.5}Cd_{0.75}PS_3$ exhibits the highest conductivity, due to the inherent mobility of the small, low charge density Li^+ cation.

5.7 Ligand Exchange of $A_{2x/n}M_{1-x}PS_3 \cdot y\ H_2O$

The absorbed H_2O ligands are vital for enabling high ionic mobility. However, in many battery systems, H_2O can cause undesired side reactions that impair performance. To extend the applicability of these materials to non-aqueous systems, the H_2O can be replaced with more stable organic molecules. Further, the ligand exchange helps to elucidate the effect of the ligands on ionic conduction, specifically by comparing the impact of opening the diffusion bottleneck and the degree of charge screening. As a proof of concept we exchange H_2O ligands for other solvent

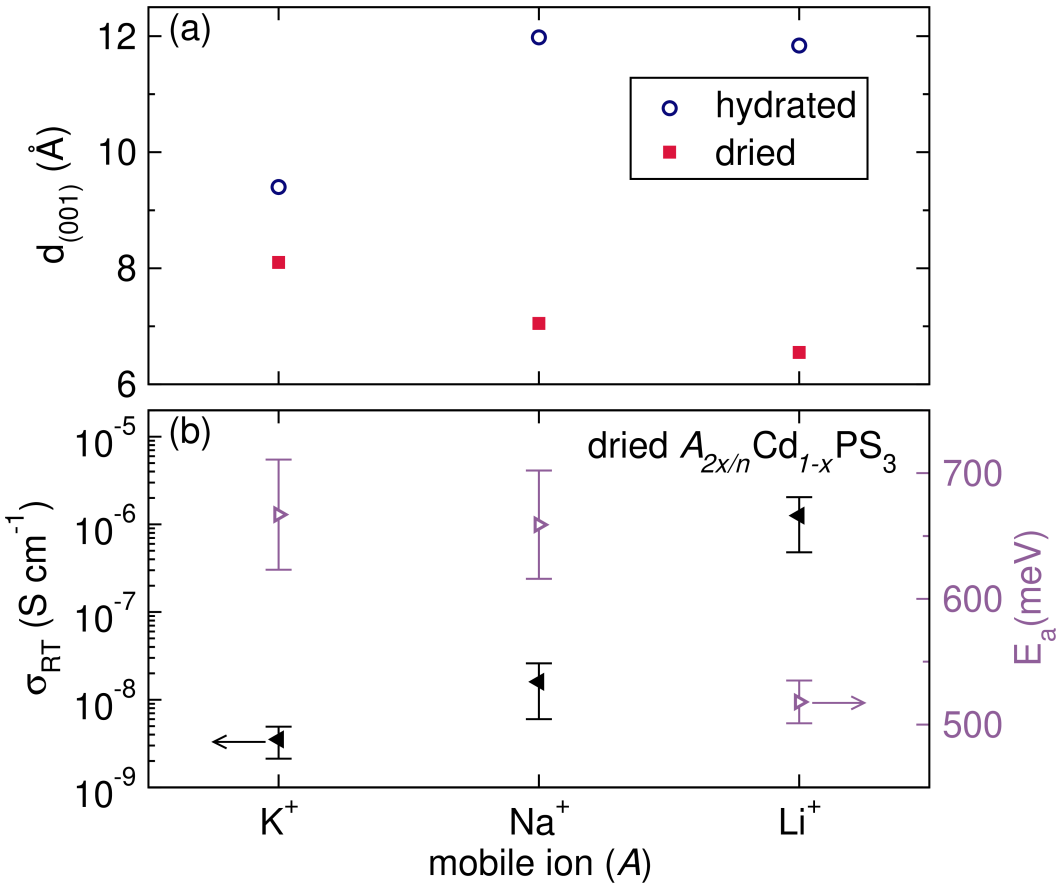

Figure 5.7: (a) The $d_{(001)}$ spacing of monovalent-ion intercalated $CdPS_3$ in the hydrated and dried state, and (b) σ_{RT} and E_a of dried monovalent ion-intercalated $CdPS_3$.

molecules that are frequently used in next-generation battery liquid electrolytes: MeCN and THF. These molecules cover a range of dielectric constants, as shown in Figure 5.8a, allowing us to further probe the effect of charge screening.

The solvent exchange is done by first exposing $K_{0.5}Cd_{0.75}PS_3$ to vacuum to at least partially dry the material followed by stirring the $K_{0.5}Cd_{0.75}PS_3$ in dried solvent in a glovebox for 1 h. To confirm that the organic solvent is incorporated, Raman is measured on the resulting materials. In all cases, the Raman modes associated with the new ligand are observed (Figure B.24). To further confirm ligand exchange, we analyze the basal spacing after the exchange which is shown in Figure 5.8b (XRD patterns available in Figure B.25). The basal spacing increases in the order of H_2O < MeCN < THF, correlating with the size of the ligand molecules. The increase in basal spacing with THF (4.5 Å) approximately matches the radius of a flat THF molecule (4.2 Å).[276] Figure 5.8c and d show the σ_{RT} and E_a, respectively, of

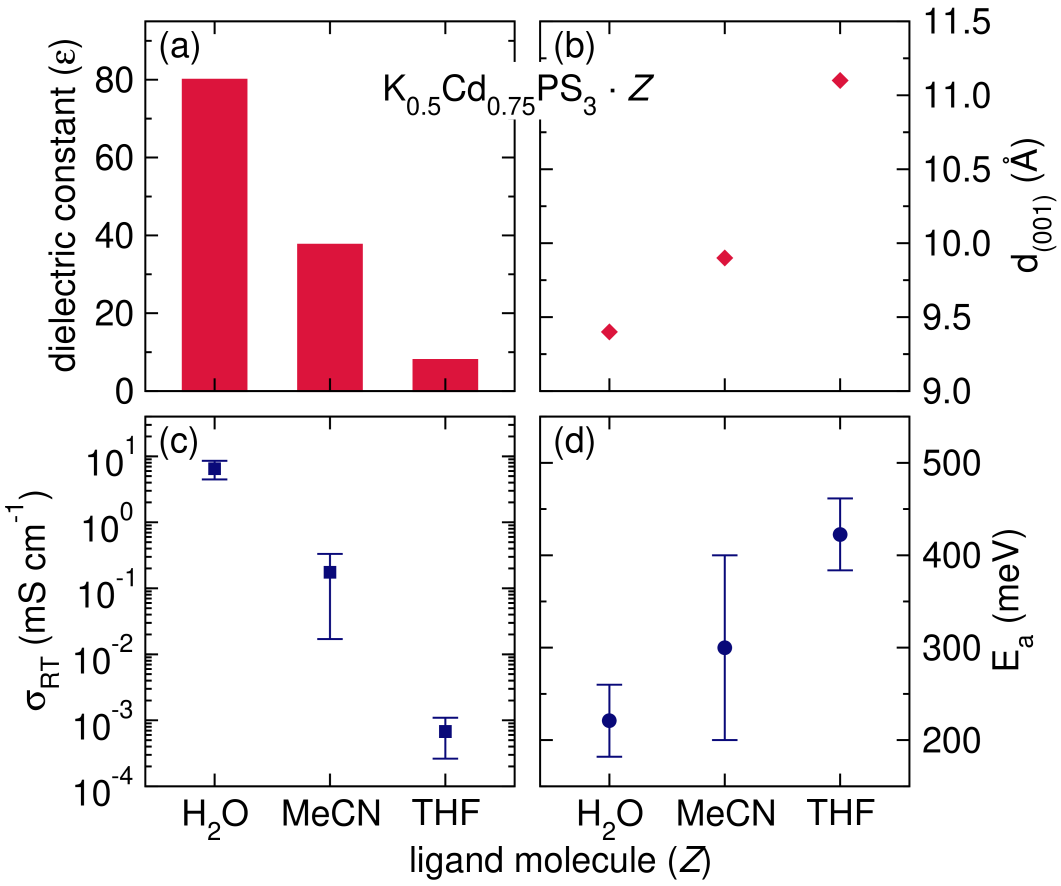

Figure 5.8: (a) A bar chart showing the reported dielectric constants of H_2O, MeCN, and THF, and comparisons of (b) $d_{(001)}$, (c) σ_{RT}, and (d) E_a of $K_{0.5}Cd_{0.75}PS_3 \cdot Z$ (Z = H_2O, MeCN, or THF).

$K_{0.5}Cd_{0.75}PS_3 \cdot Z$ (Z = H_2O, MeCN, THF). Replacing H_2O with MeCN or THF decreases the σ_{RT} by one or three orders of magnitude and increases the E_a by ~ 70 meV or 200 meV, respectively. Given that the framework and mobile ion remain constant, the variation in mobility is attributed to the interplay between an increase in bottleneck size and decrease in the extent of charge screening. Despite THF creating the largest diffusion bottleneck as evidenced by the basal spacing, the THF-containing compounds show low σ_{RT} and high E_a due to either ineffective charge screening by THF or a bottleneck that is effectively too large. However, the conductivity with absorbed THF is still two orders of magnitude higher than dried $K_{0.5}Cd_{0.75}PS_3$. Although MeCN absorption results in a smaller bottleneck than THF, its superiority in terms of screening the mobile ion charge leads to a significantly higher σ_{RT} and lower E_a. The variation in dielectric constant of the selected ligands (53 % decrease for MeCN, 90 % decrease for THF) is larger than

the resulting variation in bottleneck size (5 % increase for MeCN, 18 % increase for THF). Therefore, the variation in screening ability plays the dominant role in governing the mobility. Consequently, $K_{0.5}Cd_{0.75}PS_3 \cdot$ MeCN exhibits a high ionic conductivity of 0.18 mS cm^{-1} in the absence of H_2O, enabling potential application in non-aqueous systems. In addition, achieving high ionic conductivity with an aprotic ligand provides further evidence that the majority charge carriers are the interlayer cations and not H^+. Future work will explore the integration of aprotic solvents with high dielectric constants into MPS_3 frameworks with various next-generation mobile ions.

5.8 Ionic Conduction in $A_{2x/n}M_{1-x}PS_3$ Compared to Previous Reports

Now that we have discussed in-depth the structure-property relationships associated with ionic conduction in the $A_{2x/n}M_{1-x}PS_3$ materials, we will next discuss our work in the context of similar studies.

In the late 90s, Jeevanandam *et al.* measured ionic conductivity using admittance measurements of $K_{0.5}Cd_{0.75}PS_3 \cdot H_2O$ and $Na_{0.5}Cd_{0.75}PS_3 \cdot 2\ H_2O$.[246, 247] The studies concluded that Na^+ is mobile while K^+ is not. However, the EIS analysis presented here conclusively shows very high ionic conductivity for K^+ in $K_{0.5}Cd_{0.75}PS_3 \cdot H_2O$ (Nyquist plots can be seen in Figure B.13). Additionally, we find that the σ_{RT} of $Na_{0.5}Cd_{0.75}PS_3 \cdot 2\ H_2O$ is two orders of magnitude higher than in their previous reports. These discrepancies may arise from sample preparation or EIS measurement errors, but it is difficult to pinpoint the exact cause using the experimental conditions that were reported.

The recent study by Yu and Ren, in which exceedingly high 2D ionic conductivity was observed in $CdPS_3$-based membranes, provides an opportunity to compare solvent-assisted ionic conductivity to confined liquid electrolytes. In the study by Yu and Ren, there is no discussion of the quantity of H_2O present in each membrane. However, since the basal spacing, σ_{RT}, and E_a are largely uncorrelated to the identity of the intercalated ion, reminiscent of a confined liquid electrolyte we speculate that the membranes likely contain excess amounts of H_2O. In the case of ligand-assisted ionic conduction in bulk $A_{2x/n}M_{1-x}PS_3$ materials, although the intercalated ions are screened they still interact with the framework, explaining the strong dependence of the electrochemical performance on intercalated ion identity. A comparison of the results of their 2D σ_{RT} and E_a with the finding of this study is shown in Figure B.26. The measured conductivity of $CdPS_3$-based membranes is between

two and four orders of magnitude higher than the bulk polycrystalline $A_{2x/n}M_{1-x}PS_3$ samples reported here. This is logical because the inherent conduction pathways in this structure are 2D, bulk 3D conduction is achieved in polycrystalline pellets through a series of 2D conduction processes within randomly oriented particles. However, particularly for energy storage applications considering general materials processing and cell assembly steps, the bulk 3D measurement is more representative of materials performance. Furthermore, operating within the ligand-assisted regime combines the benefits of high ionic mobility with the advantages of using a solid state electrolyte. Additionally, there is limited free H_2O in the material, which minimizes H_2O-related undesired side reactions, and limits the impact of H^+ conduction. However, in the confined liquid electrolyte regime the materials may become softer and sticky due to excess H_2O,[110] and the free H_2O can lead to undesired reactivity and increased H^+ conduction in battery systems.

5.9 Conclusions

The introduction of ligand molecules into solids can drastically increase the ionic mobility of both larger cations (Na^+, K^+, Ca^{2+}) and charge-dense cations (Mg^{2+}, Zn^{2+}, Al^{3+}) by expanding the diffusion bottlenecks and screening charge-dense mobile ions. In MPS_3-based materials (M = Mn, Cd), ion-intercalated compounds of the form $A_{2x/n}M_{1-x}PS_3 \cdot y\ H_2O$ can be obtained containing hydrated interlayer A cations. These intercalated structures contain either a monolayer H_2O, K^+ and Na^+ (at low RH); or bilayer H_2O: Li^+, Na^+, Mg^{2+}, Zn^{2+}, Ca^{2+}, and Al^{3+}, depending on the hydration energy of the intercalated cation. All $A_{2x/n}M_{1-x}PS_3 \cdot y\ H_2O$ materials show exceptionally high bulk conductivity (generally > 0.1 mS cm^{-1}) at RT and ambient RH. Therefore, leveraging ligand-assisted ionic conduction in solid state electrolytes is a promising avenue to achieving high ionic mobility of next-generation mobile ions, which has historically been very challenging. [110, 206, 209, 210, 277] Furthermore, $A_{2x/n}M_{1-x}PS_3 \cdot y\ H_2O$ materials exhibit bulk ionic conductivities that are among the highest reported values of any electronically-insulating inorganic solid for all of the mobile ions studied. Notably, these compounds exhibit higher conductivities than other reported solids containing solvated ions (e.g. clays and MOFs), due in part to the more polarizable S-based anion framework in MPS_3-based materials. Employing ligand-assisted ionic conduction seems to be more effective for achieving exceedingly high conductivity for less charge-dense ions, like Li^+, Na^+, K^+, and Ca^{2+}, but still provides suitable results for charge-dense ions.

This work highlights the impact of expanding the diffusion bottleneck, by showing that with identical ions and ligands the framework with the larger bottleneck has a higher σ_{RT} and lower E_a. Furthermore, the impact of charge screening is illustrated by the systematic increase in E_a and decrease in σ_{RT} for similar structures when some of the solvating H_2O ligands are removed.

Since the introduction of H_2O introduces the possibility of H^+ conduction, we provide strong evidence that the intercalated cations are the majority carriers. The observed electrochemical behavior is much more adequately explained by mobile intercalated ions than mobile H^+. Additionally, MAS NMR demonstrates absence of H^+ exchange and high mobility of Li^+ and Na^+. PFG NMR demonstrates that in the case of $Li_{0.5}Cd_{0.75}PS_3 \cdot 2\ H_2O$ the Li diffusivity is two to four orders of magnitude higher than that of H. This result further suggests that the intercalated cation is the majority charge carrier and that the conduction occurs through a hopping mechanism, where the cations are moving between H_2O molecules, instead of a vehicular mechanism.

Although H^+ are likely not the mobile ions, the drastically inferior performance of the dried phases emphasizes that H_2O ligands are crucial for the high mobility of the intercalated ions. Finally, exchanging H_2O for aprotic ligands like MeCN and THF in $K_{0.5}Cd_{0.75}PS_3 \cdot H_2O$ provides further evidence that H^+ is not the majority carrier. The ionic mobility of the intercalated cations with these ligands depends on the interplay between bottleneck expansion and the effective charge screening. Specifically, $K_{0.5}Cd_{0.75}PS_3 \cdot MeCN$ exhibits a high ionic conductivity demonstrating the potential application of $A_{2x/n}M_{1-x}PS_3$ to non-aqueous systems.

$A_{2x/n}M_{1-x}PS_3$ materials represent a modular system in which we can change the mobile ion, the framework (M = Cd for slightly higher performance vs. Mn for environmental friendliness), or the ligand molecules to tailor the performance for specific applications. Fundamentally, this modular framework allows us to develop structure property relationships to better understand solid state ionic conduction of next-generation mobile ions, particularly ligand-assisted ionic conduction. Additionally, the high performance of $A_{2x/n}M_{1-x}PS_3$ materials suggests that these, or similar compounds, could be used as a "universal" solid electrolyte for a variety of battery chemistries with different mobile ions.

5.10 Experimental Section

Material Preparation

Synthesis

The MPS$_3$ (M = Mn, Cd) materials were prepared using traditional solid state methods from Mn (Alfa Aesar, 99.3%) or Cd (Thermo Scientific, 99.99%) metal powder, respectively, elemental S (Acros Organics, >99.5%), and 10% excess P_2S_5 (Acros Organics, >98%) in an Ar-filled glovebox without further purification.

The M, P_2S_5, and S_8 were combined in a 2:1.1:1/8 molar ratio and ground thoroughly using a mortar and pestle. The reactants were then pressed into pellets with an Arbor press and sealed in a vitreous silica ampule under vacuum (<10 mtorr). The reaction vessel was placed in a box furnace, heated to 650 °C at a rate of 1 °C min^{-1}) (K min^{-1}) and allowed to react at 650 °C for 24 h. After the reaction was complete, the tube was allowed to cool to ambient temperature inside of the furnace. The resulting green ($MnPS_3$) or off-white ($CdPS_3$) powder was collected and handled in an Ar filled glovebox.

Ion-Exchange Reaction

The ion-exchange reactions were conducted by stirring powder MPS$_3$ samples in aqueous solution of the appropriate metal chloride. A typical K-exchange reaction involved stirring 400 mg of $MnPS_3$ or 500 mg of $CdPS_3$ in 10 ml of a 3 M or 2 M solution, respectively, of aqueous KCl at room temperature for three hours. For $CdPS_3$, 0.1 M EDTA, in a 1 M K_2CO_3/$KHCO_3$ buffer solution, is added as a complexing agent. After the reaction was complete, the mixture was filtered using a fritted glass vacuum filter, washed three times with water and once with ethanol and allowed to dry for at least 30 minutes. The second ion exchanges were conducted on the material obtained from the first exchange. In this case, 100-150 mg of K-exchanged MPS$_3$ was added to 10 ml of 1 M solutions of the relevant metal chloride, no complexing agents were added. The drying and washing procedures were the same as the first exchange. The Li-exchanged samples were allowed to dry overnight. After the ion exchanges were complete the samples were stored in vials at ambient conditions. A hygrometer was used to measure the ambient RH, if there was a period in which the humidity was < 40%, the materials were stored in a humidity chamber maintained at 53% RH using super saturated solutions of magnesium nitrate.

Ligand-Exchange Reaction

The ligand exchange was carried out in a dry N_2-filled glove box. Samples of $K_{0.5}Cd_{0.75}PS_3 \cdot H_2O$ were partially dried through three 10-minute vacuum-backfill cycles in the glovebox antechamber. MeCN (99.9%,Fisher Scientific) and THF (99.9%, Fischer Scientific) were dried on a solvent purification system (Pure Process Technology) and transferred into the glovebox, without exposure to air, and stored over 3 Å molecular sieves. Before use, the measured a water content of both solvents was less than 20 ppm via KF titration. In the glovebox, $K_{0.5}Cd_{0.75}PS_3$ was added to 5 mL of the solvent in a scintillation vial and mixed on a magnetic stir plate for one hour. The mixture was vacuum filtered over a fritted glass filter for a couple seconds until the material visibly changed from it's dark gray "wet" state to the drier light gray state. Quickly, the material was scraped off the filter and put into Swagelok cells for impedance characterization or an empty scintillation vial for absorbed solvent characterization.

Absorbed solvent was characterized by mass loss measurements. An initial mass was obtained from the sample immediately following removal from the filter. This sample was then allowed to passively lose solvent to the dry atmosphere.

Dried Sample

To prepare dried ion-exchanged materials for structural and electrochemical characterization, the powders were transferred into a Ar-filled glovebox and placed in a vacuum oven at 120 ° C for 10 hours.

Pelletization

Between 15-30 mg of powder was pressed into a pellet in ambient atmosphere using a 12 ton hydraulic press from Carver (unit 3912). The powder was pressed using a 6 mm stainless steel die set at 2 tons for 5 minutes. The resulting pellets were between 0.2-0.6 mm thick. In most cases the pellets were sputtered with Au at 40 mA for 60 s on both flat surfaces using a Ted Pella 108 Auto Sputter Coater in an Ar filled glovebox. Then removed from the glovebox and allowed to re-equilibrate at ambient RH for at least 2 days.

Material Characterization

Powder X-ray Diffraction

High-resolution synchrotron powder x-ray diffraction patterns were collected on samples sealed in 1.0 mm (o.d) glass capillaries (to prevent changes in RH). The samples were measured on beamline 28-ID-1 (λ = 0.1665 Å) at the National Synchrotron Light Source II at Brookhaven National Laboratory.

Additional XRD data were collected using a Rigaku SmartLab diffractometer (CuK_{α}). The hydrated samples were placed on a glass slide sample holder at ambient RH, while the dried samples were prepared in a glovebox and measured in a Rigaku air free sample holder. All patterns were collected from 5-60° 2θ as a step size of 0.03 ° and 5 ° per minute.

Raman Spectroscopy

Raman spectroscopy was measured using a Horiba Instruments XplorRA PLUS Raman Spectrometer equipped with 532 nm laser. The sample was mounted on a glass microscope slide. The signal was averaged over 200 acquisitions lasting 1 s each with a 50 μm slit and 500 μm hole. The laser power used was either 1 or 10% to prevent local heating and sample degradation.

Thermogravimetric Analysis

TGA was performed using a TA Instruments TGA 550. Powder samples (5-30 mg) were loaded into a tared high-temperature pan composed of an Inconel coated bail wire and platinum pan as a flat, evenly distributed layer and heated under a nitrogen flow (25 mL/min) at 5 ° C/min from room temperature (19-25 ° C) to 200 ° C, at which it was held constant for 1 min. The instrument was calibrated using a nickel Curie temperature standard as per the manufacturer's directions.

Inductively Coupled Plasma Mass Spectrometry

ICP-MS was performed on Agilent 8800. About 2 mg of each synthesized batch of material was digested in 2 ml of 70% nitic acid at 80 ° C for 4 hours. After the initial digestion, the solutions were diluted twice in 5% nitric acid to reach x2500 dilution. Five different concentrations of standard solutions were made from stock solutions of Cd, Mn, P, S, Li, Na, Mg, Ca, Zn, and Al to generate a calibration curve.

Scanning Electron Microscopy & Energy Dispersive X-ray Spectroscopy

SEM was performed on select materials using a ZEISS 1550VP field emission SEM with an acceleration voltage of 10 kV at 5kX, 10kX, and 30kX magnification. Before SEM was performed the materials were sputtered with Pt for 5 s at 40 mA to avoid charging during the measurement. EDS data were collected using an Oxford X-MAX SSD system with an acceleration voltage of 10 kV or 20 kV.

Electrochemical Impedance Spectroscopy

EIS measurements were collected using a Bio-Logic VSP300 multichannel potentiostat with ultralow current probes. Typically, symmetric cells were assembled with Au-sputtered, in 0.25 i.d. PTFE spring-loaded Swagelok cells. EIS was measured at different temperatures, controlled by a convection oven. The cell temperature was allowed to equilibrate for 30 minutes at each temperature. The temperature series were terminated at 70 ° C. The EIS spectra were collected using a sinusoidal voltage amplitude of 50 mV in a frequency range of 3 MHz to 1 Hz and averaged over 10 measurements. At least three successive measurements were taken to ensure that the response was stable. Equivalent results were obtained without pelletization, by making a pellet *in situ* in the PTFE Swagelok cell by applying at least 3 kN of force with a vice. In this case, either polished Au foil or the stainless steel plungers were used as electrodes. This method was primarily utilized for the Al-exchanged samples, which took a long time to re-equilibrate after pelletization, it was also used for replicates of other samples to ensure consistency. Since for the vast majority of samples the high frequency semi circle in the Nyquist plot could not be resolved even at RT, the x intercept of the Nyquist plot is taken as a "worst case" approximation for the total impedance for all samples, which we conservatively approximate as the electrolyte impedance. For the few samples where a high frequency semicircle could be resolved, the data were fit to an equivalent circuit using ZFit in the EC-Lab software, e.g., Figure B.15, to ensure that the capacitance of this feature corresponded with that expected for bulk ionic conductivity in solids.

Solid State Magic Angle Spinning Nuclear Magnetic Resonance Spectroscopy

Multinuclear MAS NMR experiments were performed using a Bruker Avance I-500 MHz spectrometer and using a Bruker 4mm MAS NMR probe. A powder sample was packed into a zirconia (ZrO_2) rotor at the ambient condition, and spun at 10 kHz. ^{1}H NMR (500.2 MHz) spectra were acquired after 4 μs-90 degree pulse.

NMR signal of metal ions (quadrupole nuclei) were recorded after applying short tip angle rf pulses (1/12π for I=3/2 nuclei (^{7}Li and ^{23}Na) or 1/18π pulse for ^{27}Al) and strong ^{1}H decoupling pulse. Chemical shifts were externally calibrated to TMS for ^{1}H, 1 M aqueous solution of LiCl, NaCl, and Al(NO_3) for ^{7}Li, ^{23}Na, and ^{27}Al nuclei, respectively. For NMR measurements after dehydration, a 4 mm rotor containing packed powder sample was inserted into a 80 mm long-5 mm glass NMR tube, and the glass NMR tube was attached to a 1/4"-Cajon-VCR-T fitting and the side arm was connected to a vacuum manifold for high temperature evacuation overnight. In this special setup, a glass rod with sealing kel-F rotor cap at the end was attached at the top of the 1/4"-Cajon-VCR-T. The rod was able to slide down, closing the 4 mm rotor with a tightly fit o-ring. The rotor underwent heating in an 10 mm-cylinder furnace with evacuation. The setup was filled with Ar gas before sealing, resulting in complete avoidance of exposure to air for the dried powder sample.

Pulsed Field Gradient Nuclear Magnetic Resonance Spectroscopy

$Li_{0.5}Cd_{0.5}PS_3 \cdot 2\ H_2O$ sample was packed and sealed inside a 4 mm ZrO_2 rotor, which was itself placed in an airtight 5 mm NMR tube. ^{1}H and ^{7}Li PFG-NMR measurements were conducted on a 7.05 T (^{1}H, 300 MHz) Bruker Avance III super wide-bore NMR spectrometer equipped with a Diff50 probe under static condition. Diffusion measurements were performed from low (25 °C) to high temperature (60 °C) after a 30 minute equilibration period at each temperature, and the temperature was regulated by a heater and using N_2 gas flowing at a rate of 800 L/h. The sample temperature was calibrated using dry ethylene glycol solution. Self-diffusion coefficients were measured using a stimulated echo pulse sequence[269] with variable magnetic field gradient pulses. Self-diffusion coefficients, D_i, of all the nuclei were determined by fitting the integrated signal intensity, I_i, as a function of the variable gradient strength , g, using the Stejskal-Tanner equation.[270, 278]

$$I = I_0 \exp\left(-D_i\,(\gamma\delta g)^2\left(\Delta - \frac{\delta}{3}\right)\right) = I_0 \exp\left(-D_i B\right) \qquad \text{where } B = (\gamma\delta g)^2\left(\Delta - \frac{\delta}{3}\right) \tag{5.3}$$

I_0 is the initial signal intensity, δ is the gradient duration, and Δ is the diffusion time. The δ, Δ, and g values were selected to ensure sufficient decay window. The NMR data were processed with TOPSPIN 4.3.0 and fitted using Origin software.

Theoretical Methods

Structure Relaxations

We used density functional theory implemented in the Vienna Ab Initio Simulation Package (VASP 6.4.2)[279–281] along with Projector Augmented Wave (PAW)[282, 283] pseudopotentials to determine the lowest energy configurations of dehydrated and hydrated $K_{0.5}Mn_{0.75}PS_3$ and $Na_{0.5}Mn_{0.75}PS_3$. The stoichiometries were rounded to the stated values for computational simplicity. PAW potentials were used with valence configurations of $3s^2 3p^6 4s^1$ for K, $2s^2 2p^4$ for O, $3s^2 3p^3$ for P, $3s^2 3p^4$ for S, $4s^1 3d^6$ for Mn and $1s^1$ for H to describe the valence electrons. Our calculations employed the Perdew-Burke-Ernzerhof (PBE)[284] Generalized Gradient Approximation (GGA) and included vdW corrected DFT-D3 (Becke-Johnson)[285, 286] along with empirical dispersion corrections. To ensure accuracy, we included all plane waves of energy up to 650 eV and set electronic minimization energy criteria to 10^{-6} eV. Ionic relaxation was stopped when the norms of all Hellmann-Feynman forces were less than 10^{-2}/Å, and we utilized a 4x2x4 Γ-centered k-mesh for Brillouin zone integration within the unit cells so that a k-spacing of less than 0.2 $Å^{-1}$ was sufficient for the required accuracy for electronic energy minimization.

The structures in Figure 5.3 were obtained through a heating and cooling approach using Ab initio Molecular Dynamics (AIMD) and the Nosé and Hoover NVT ensemble in VASP 6.4.2.[287–290] The structures were brought from 20K to 300K, held at 300K then cooled back to 20K and were relaxed with DFT minimization from there. Initial estimate structures were optimized with the parameters described above. All AIMD simulations were run with 1 fs time steps, a fixed cell shape and volume, and the same parameters above except as noted. The heating and cooling were both performed over 2 ps with a 1x1x1 Γ-centered k-mesh. Between these steps the simulation was held at 300 K over 5 ps with a 2x1x2 Γ-centered k-mesh.

Chapter 6

CONCLUSION

6.1 Summary and Conclusion

This thesis has investigated the structure-property relationships that are hypothesized to effect solid state conduction of next-generation mobile ions in inorganic materials. Chapter 2 lays the foundation by discussing the fundamentals of solid state ionic conductivity, the measurement techniques involved, and the unique challenges associated with multivalent ions.

Throughout the rest of this work, the combination of materials based on polarizable anion frameworks, such as sulfides, and the introduction of ligand molecules to screen the charge-dense ions is shown to result in superionic conduction due to a significant decrease in strong electrostatic interactions within the material. Chapter 3 details the achievement of superionic conductivity in hydrated $ZnPS_3$. Exposure of $ZnPS_3$ to humid environments results in adsorption of water onto the surface of the grains and within grain boundaries and subsequently an increase int he ionic conductivity of up to five orders of magnitude over anhydrous $ZnPS_3$. Through a combination of electrochemical techniques we show that both Zn^{2+} and H^+ are mobile in 0.52 $H_2O/ZnPS_3$. Additionally, this study is the first demonstration of Zn deposition and stripping through a SSE onto various metal substrates and to the best of our knowledge, 0.52 $H_2O/ZnPS_3$ displays the highest Zn^{2+} conductivity in any solid-based system (σ = 1.44 mS cm^{-1} and $\sigma_{Zn^{2+}}$ = 0.67 mS cm^{-1}). We hypothesize that the Zn^{2+} conduction occurs via a water-mediated mechanism, in which solvated Zn^{2+} is mobile in the adsorbed water. Furthermore, we demonstrate methods to qualitatively decouple Zn^{2+} and H^+ conduction in a water containing materials, and highlight the importance of doing so in water or air exposed systems, where H^+ could be responsible for the observed conductivity.

Chapter 4 seeks to expand this concept to achieve superionic conductivity of other next-generation mobile ions in electronically-insulating inorganic solids. Here, we turn to different MPS_3-based materials (M = Mn, Cd), which are known to form ion-intercalation compounds of the form $A_{2x/n}M_{1-x}PS_3 \cdot y\ H_2O$, where hydrated A^{n+} cations occupy the van der Waals gap. The presence of ligand molecules drastically increases the ionic mobility of both larger cations (Na^+, K^+, Ca^{2+}) and

charge-dense cations (Mg^{2+}, Zn^{2+}, Al^{3+}) by simultaneously expanding the diffusion bottlenecks and screening charge-dense mobile ions. The ion-intercalated MPS$_3$ materials not only exhibit the highest reported bulk conductivity for several ions but also provide a robust model for studying and optimizing ligand-assisted ionic conduction. Specifically, we show how the bottleneck size, cation charge density, and degree of charge screening affects the ionic conductivity. We provide strong evidence that the interlayer cations, not H^+, are the majority carriers and that the conduction occurs through a hopping mechanism, where the cations are moving between H_2O molecules, instead of a vehicular mechanism.

Finally, replacing H_2O with aprotic ligands like MeCN and THF in $K_{0.5}Cd_{0.75}PS_3$ enables the investigation of the interplay between bottleneck expansion and the effective charge screening on the resulting mobility of a given ion and opens up further applications in various industrial and technological contexts.

$A_{2x/n}M_{1-x}PS_3$ materials represent a modular system in which we can change the mobile ion, the framework (M = Cd for slightly higher performance vs. Mn for environmental friendliness), or the ligand molecules to tailor the performance for specific applications. The high performance of $A_{2x/n}M_{1-x}PS_3$ materials suggests that these, or similar compounds, could be used as a "universal" solid electrolyte for a variety of battery chemistries with different mobile ions.

This thesis not only elucidates critical structure-property relationships and mechanisms underlying ligand-assisted ionic conduction in new solid electrolyte systems but also identifies a high performance, modular system that may be useful in a variety of battery chemistries with different mobile ions or other applications such as ion exchange membranes or humidity sensors.

6.2 Outlook on Ligand-Assisted Ionic Conduction and MPS$_3$ Materials

Leveraging ligand-assisted ionic conduction in solid state electrolytes is a promising avenue to achieving high ionic mobility of next-generation mobile ions, which has historically been very challenging. [110, 206, 209, 210, 277] Utilizing materials with ligand-assisted ionic conduction combines the benefits of high ionic mobility with those of using a solid state electrolytes. Notably, this approach minimizes issues like increased H^+ conduction, undesired reactivity, and electrode dissolution, commonly experienced when using some aqueous/liquid electrolytes due to excess solvent.[110]

Since the introduction of H_2O introduces the possibility of H^+ conduction care must be taken to determine the identity of the mobile ion in hydrated systems. The methods used in Chapter 3 to decouple Zn^{2+} and H^+ conduction may not be transferable to all multivalent systems. For instance, non-blocking electrode tests with strongly reducing metals, such as Mg and Ca, can be convoluted by interfacial instability of the material of interest. Additionally, significant interfacial and cell optimization is required to achieve either metal deposition or ion intercalation into cathodes. Therefore, the development of universally applicable, straightforward techniques to accurately measure and distinguish between ionic contributions in such systems remains crucial. This advancement will ensure that improvements in multivalent ion conduction are not erroneously attributed to proton conduction.

Notably, water-assisted ion conduction can be most readily employed in Zn-based systems, as other metal anodes will spontaneously reduce water molecules in a hydrated SSE. Although, if charge screening via ligand molecules proves to be the most successful avenue to achieving next-generation ionic conduction in solids, protective membranes could be developed to protect the metal anodes from the ligand molecules.[105]

In ion-exchanged MPS$_3$ phases, the presence of interlayer cations facilitates the introduction of aprotic ligands, this is difficult to achieve in materials like $ZnPS_3$, where only surface adsorption occurs. Here we showed that ligands with high dielectric constants resulted in greater ionic conductivity due to better charge screening. Therefore, molecules with large dielectric constants, such as formamide, should be investigated and may provide even higher conductivities than hydrated samples. Future work will also focus extensively on ligand exchange in multivalent ion containing MPS$_3$, addressing a significant gap in the availability of reliable non-aqueous multivalent ion electrolytes. Notably, even without water the stability of these materials will likely be limited by the reduction potential of the $[P_2S_6]^{4-}$ polyanion. Nonetheless, if successful these materials will be a very valuable addition to the field as they may enable the reliable testing of novel electrode materials for multivalent ions.

6.3 Outlook on Conduction of Next-Generation Mobile Ions in Solids

The landscape of solid-state ionics, particularly for next-generation mobile ions, is marked by unique challenges that demand novel solutions. While the field related to Li systems is well-established,[77] offering robust design rules for identifying

promising materials, the extension of these principles to ambient temperature multivalent ion systems has yet to be truly validated. Previous studies suggested some design rules for multivalent ionics, the most promising of which involved the utilization of more polarizable anion sublattices. Building upon that, this thesis describes several examples of introduction of ligand molecules resulting in superionic conductivity MPS$_3$-based compounds. However, conclusive experimental evidence that multivalent ions can display high conductivity in solids at RT without some form of charge screening remains elusive. To achieve this, future research should include the thorough investigation of additional materials with open structures — including skeleton structures,[224] high temperature polymorphs — these are generally higher volume phases, and materials with the potential for structural flexibility, such as amorphous phases or materials with flexible polyanions. Such materials will facilitate larger bottlenecks and reduce the strong electrostatic interactions plaguing multivalent ions. In addition, leveraging complex migration mechanisms, like concerted migration or the paddlewheel effect, may be helpful to achieve high multivalent ion diffusion in solids, especially electronically insulating solids. Although metastable phases may not be ideal for practical application due to inherent instability, they may be promising in the pursuit of deeper understanding. Notably, some metastable Li^+ ion conducting phases that could not be synthesized through traditional solid state methods were synthesized using mechanochemical methods.[149] Metastable phases are also more likely to have ions in less favorable coordination environments, which can provide more experimental evidence to confirm or rule out the lattice site coordination environment hypothesis.

Moreover, many of the characterization techniques that are commonly utilized to evaluate diffusivity and probe mechanisms in monovalent conductors are not easily applied to multivalent ion systems. Therefore, the development of new techniques tailored towards multivalent ion systems that can be used to corroborate EIS results will be a critical development in the field, as computational studies alone are not sufficient to concretely corroborate EIS results.

The importance of computational studies to identify materials that are likely to possess low activation energies and thus have the potential for high ionic conductivity near RT should not be underestimated, although they were not applied here. There are $\sim$ 30,000 reported Mg, Ca, Zn containing compounds in the ICSD. In lieu of concretely established design principles motivated by experimentally verified structure-property relationships, computational results provide a logical way to filter

promising compounds. However, it should be noted that experimental corroboration of several materials a low NEB-derived E_a has not been achieved,[69, 291, 292] highlighting that other factors, such as sufficient carrier concentration, or optimization of the precursor (σ_0) are likely to be key to observing high RT conductivity. Additionally, future computational investigations should consider the MN energy of the compound to ensure that a low E_a is ideal.

Ultimately, it will likely require creative combination of many of the proposed design rules in a single material to realize high next-generation ion conduction without charge screening. At this point any material, especially an electronic insulator, that concretely exhibits multivalent ion conduction, in particular, is of fundamental interest, and structure-property relationships for that material family should be elucidated. Even materials with low conductivity will be important steps on the journey to the development of superionic conductors for next-generation ions.

Appendix A

SUPPORTING INFORMATION FOR CHAPTER IV: WATER VAPOR INDUCED SUPERIONIC CONDUCTIVITY IN $ZNPS_3$

A.1 Supplementary Notes

Optimization of Conditions for Zn Deposition

Achieving deposition of Zn using 0.52 $H_2O/ZnPS_3$ as an electrolyte in both CV and galvanostatic experiments was significantly challenging. Simultaneous optimization of stack pressure, temperature, and the magnitude of applied current was necessary. Attempts in which the stack pressure was not sufficient to maintain intimate contact between the pellet and metal foils, e.g., using a spring-loaded Swagelok instead of a vice, led to instant polarization due to large potential drops across the 0.52 $H_2O/ZnPS_3$ | electrode interfaces. Optimizing the temperature required balancing the benefit of faster kinetics at elevated temperature with detrimental effects of water loss from the sample. Since significant water loss occurred at T $\geq$ 50 °C, the deposition experiments were conducted at 40 °C. Achieving deposition at lower temperature (for instance room temperature) or with current densities $\geq$ 100 μA cm^{-2} was possible, but was accompanied by significantly higher overpotentials, up to $\sim$ 3 V. At such high overpotentials decomposition of $ZnPS_3$ could not be entirely ruled out. Even after optimization of the experimental conditions, there was still some batch-to-batch variation between experiments. Different batches of $ZnPS_3$, amongst which the only obvious difference is the amount of ZnS impurity (max. 5wt%), display varying durations of sustained Zn^{2+} reduction (from several hours to several days before polarization) despite showing similar ionic conductivities. Involvement of the ZnS in the high ionic conductivity or Zn deposition after hydration was ruled out by control experiments, the results of which are shown and discussed in Figure A.22. The origin of this variation is potentially due to interfacial degradation or inconsistencies. Samples with more adsorbed water tend to less reliably sustain extended periods of Zn^{2+} reduction, possibly due to sufficient degradation of the surface from extensive HER.

XPS of Zn Deposits on Au Substrate

The Zn 2*p* binding energies exhibit minimal shifts on the order of 0.2 eV from Zn metal to ZnO, which makes it not suitable for identification of the Zn oxidation state

on the deposit[293]. In contrast, Zn *LMM* Auger kinetic energies shift by *approx.* 3 eV from Zn metal to ZnO[293, 294], which make it a much more useful region to look at. However, when the Zn metal substrate is in contact with a conductive substrate, an electron gun charge neutralizer can be used to differentially charge the insulating oxide layer to shift it more negative of the metal in the Zn 2*p* XPS spectrum[295]. As seen in Figure A.14, with the charge neutralizer on, two distinct peaks are observed. While the peak at a higher binding energy (1021.6 eV) can be assigned to Zn metal[293], the peak at a lower binding energy (1019 eV) is lower than any reported binding energies for a Zn species. However, when the neutralizer is turned off, the peak at 1021.6 eV does not shift, while the peak at 1019 eV shifts positively to 1023.1 eV, which is more positive than ZnO or $Zn(OH)_2$. This suggests that with the neutralizer on, the electron guns charge the insulating surface oxide species negatively, shifting it to unphysically small binding energies. Without the neutralizer on, the x-ray beam charges the insulating layer positively, resulting in a positive shift in binding energy. The conducting Zn metal does not experience any charging, and therefore its binding energy does not shift with or without the neutralizer.

The Zn *LMM* Auger spectrum is shown in Figure A.15. As is the case in the Zn 2*p* XPS spectrum, the two Auger peaks assigned to Zn^0, at 991.7 and 995.2 eV[294] do not shift regardless of charge neutralization. However, upon turning off the electron gun charge neutralizer, a broad peak appears at *approx.* 987 eV, which is around the region where ZnO and $Zn(OH)_2$ are observed[293]. When the charge neutralizer is active, the insulating oxide species charges to a higher kinetic energy and disappearing into the shoulder of the larger Zn^0 peak, but when the charge neutralizer is turned off, the oxide charges positively, thus shifting to a lower kinetic energy. This result is in agreement with the interpretation of the Zn 2*p* XPS spectra.

The XPS survey spectra of the Zn-deposited electrodes are shown in Figure A.16. The expected peaks for Zn, Au, C, and O are all present. Trace amounts of P and S are attributed to remnant $ZnPS_3$ on the substrate.

A.2 Supplementary Figures

As with the Au electrode, two plateaus are observed due to first HER then Zn^{2+} reduction. HER is observed at lower overpotentials because Pt is a better electrocatalyst than Au for HER. The SEM/EDS analysis shows flat deposits on the Pt electrode composed mostly Zn and some O, but P and S are notably absent. The

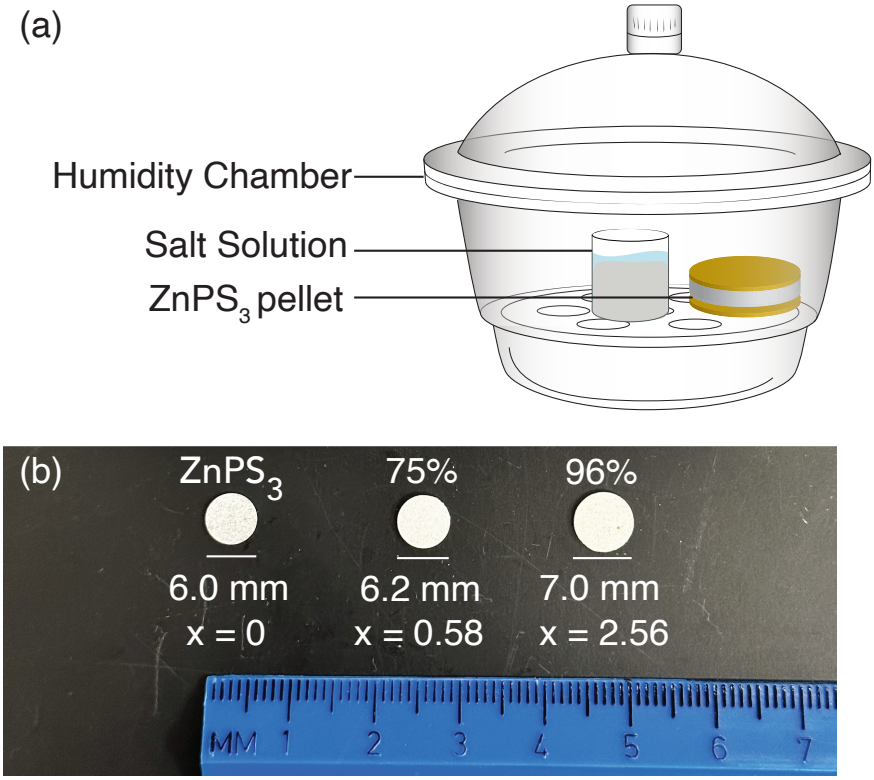

Figure A.1: (a)Illustration of experimental setup used to hydrate $ZnPS_3$ pellets with water vapor. (b) Expansion of the diameter of $ZnPS_3$ pellets after exposure to different RH environments.

absence of Pt from the deposited region supports that Zn-Pt alloys are not formed, in congruence with CV results.

Between 0 and 5 wt% of ZnS is present as an impurity phase in some batches of $ZnPS_3$. The batches with higher % of impurities adsorbed less water and display slightly lower conductivity after hydration. As a control, we investigated the conductivity and ability of commercial ZnS (Alpha Aesar, 99.99%) to plate and strip Zn under similar conditions as $ZnPS_3$ from the present study. A pellet of ZnS was prepared by pressing 40 mg of ZnS in an Ar filled glovebox at 2 tons for 5 minutes and then sputtering on both sides. The pellet was then exposed to 75% RH for 2 days in an equivalent manner used to form 0.52 $H_2O/ZnPS_3$. After this equilibration period, the measured weight gain indicated that the pellet had adsorbed 0.11 equiva-

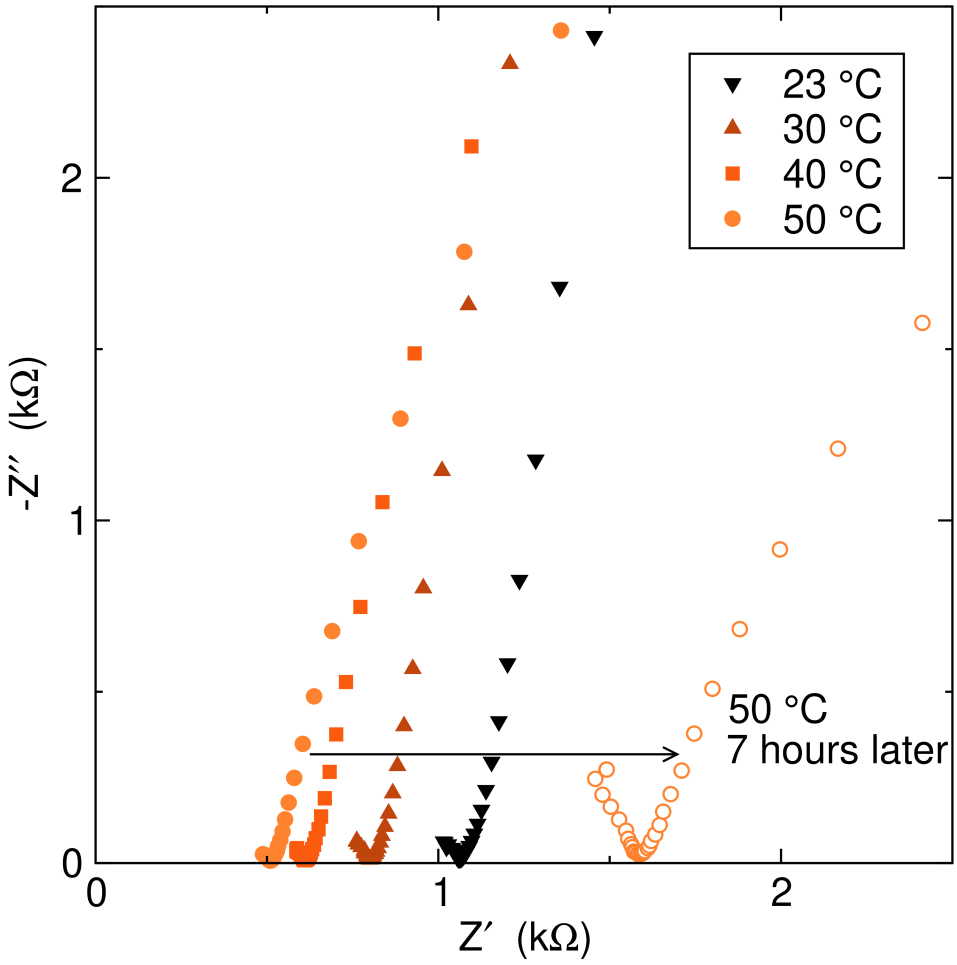

Figure A.2: Nyquist plot of a temperature series of a Au | 0.52 $H_2O/ZnPS_3$ | Au cell from RT to 50 °C showing the increase in impedance at 50 °C due to water loss. The impedance increase is accelerated at higher temperatures so all of the EIS temperature series were terminated at 50 °C).

lents of H_2O per mole of ZnS - suggesting that ZnS does not adsorb water as readily as $ZnPS_3$. The conductivity of 0.11 H_2O/ZnS is found to be 1.1×10^{-7} S cm^{-1}, which is about 2.5 orders of magnitude lower than the conductivity of $ZnPS_3$ with a similar ratio of adsorbed water (0.09 $H_2O/ZnPS_3$), and 4 orders of magnitude lower than $ZnPS_3$ prepared under similar conditions (0.52 $H_2O/ZnPS_3$). CV studies of Au | 0.11 H_2O/ZnS | Zn were used to probe Zn deposition and stripping and showed no Faradaic current, ruling out any contribution from ZnS impurities in the Zn deposition and stripping observed with 0.52 $H_2O/ZnPS_3$.

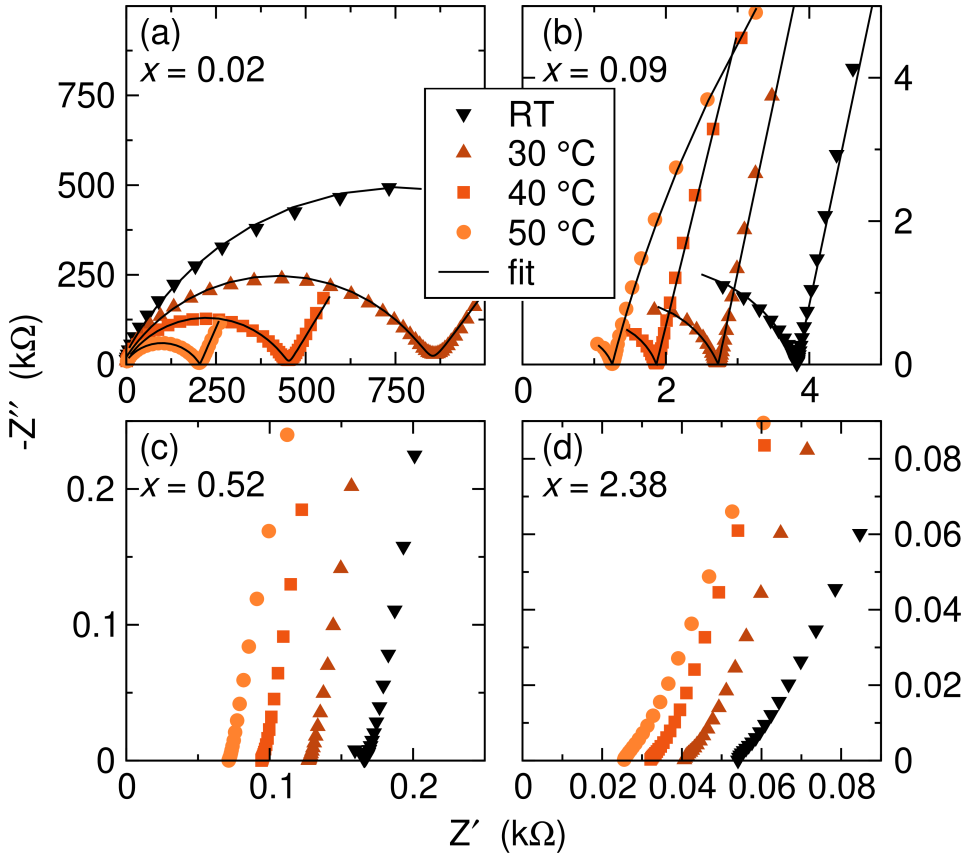

Figure A.3: Representative Nyquist plots for different levels of $ZnPS_3$ hydration in symmetric cells with sputtered Au electrodes. (a) $x = 0.02$, (b) $x = 0.09$ (c) $x = 0.52$ (d) $x = 2.38$.

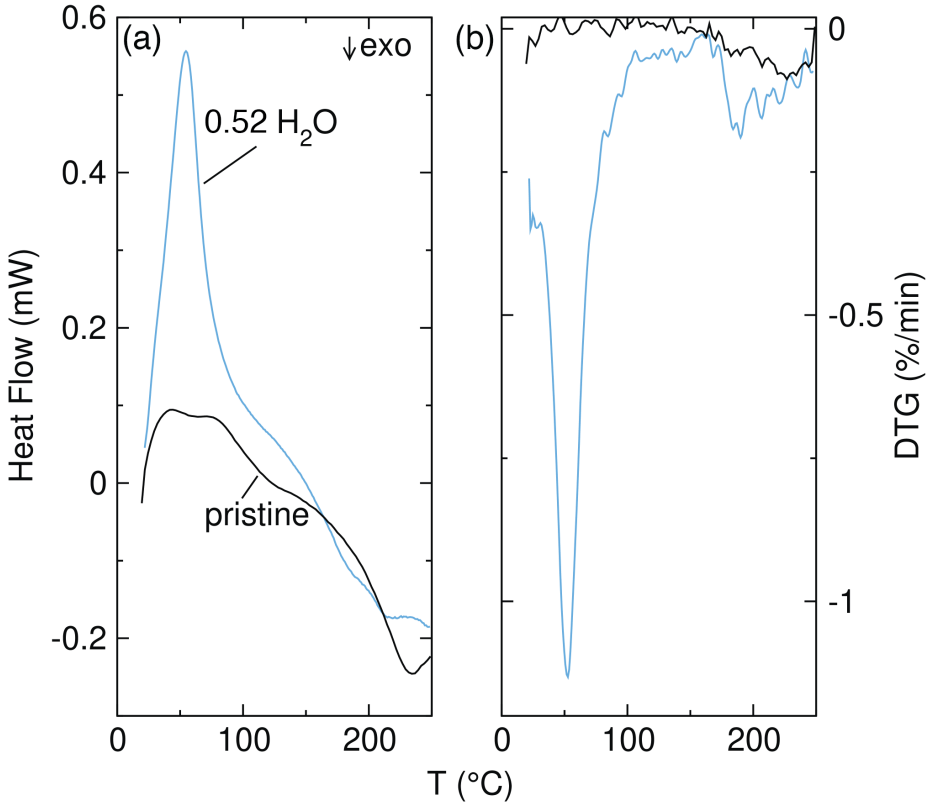

Figure A.4: (a) Differential scanning calorimetry of $x = 0$ and 0.52, showing a single peak in the hydrated sample at low temperature. This suggests that all of the adsorbed water has a similar, low binding energy, pointing towards weakly bound surface water and not strongly bound crystalline water. (b) Derivative thermogravimetry showing a single weight loss event below 100 °C. At T ≥ 150 °C an exothermal weight loss event is observed in both the $x = 0$ and 0.52 that could be related to sulfur loss or elevated temperature hydrolysis.

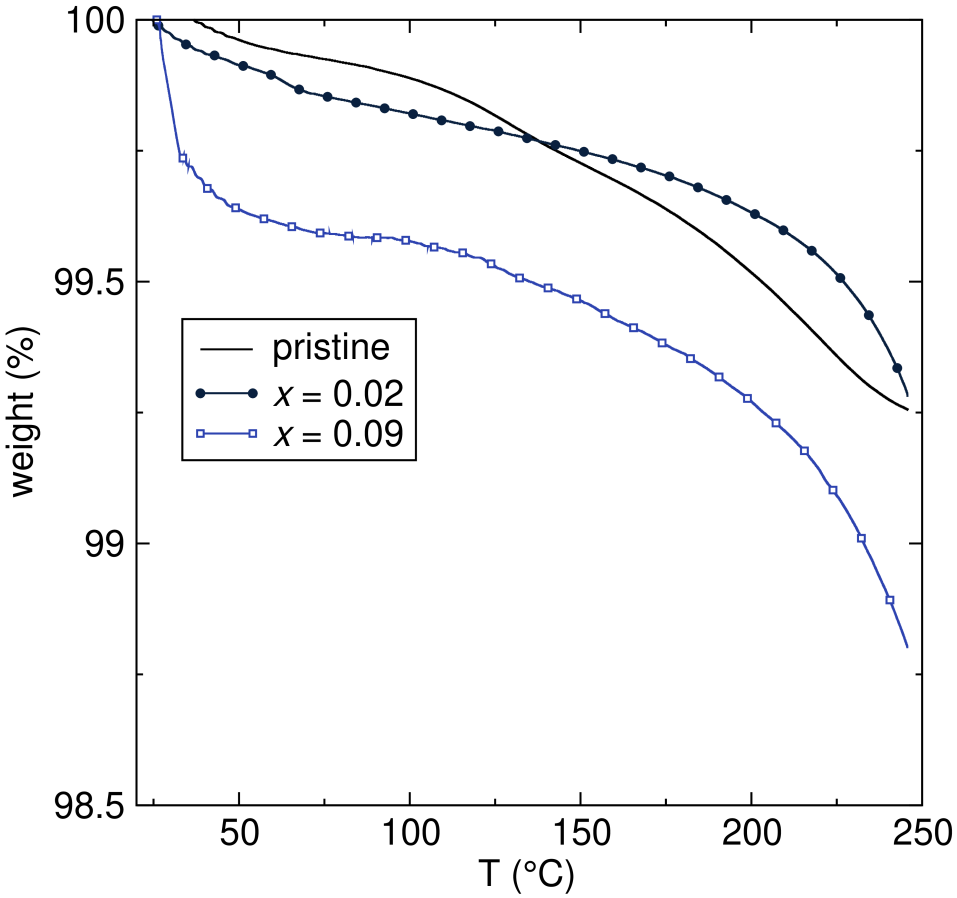

Figure A.5: Magnified TGA to provide a clear view of pristine, $x = 0.02$ and 0.14. The pristine material shows similar total mass loss to the $x = 0.02$ (11% RH) sample due to the fact that the sample is exposed to air ($\sim$ 50% RH) for about an hour in preparation for and during the measurement. Water adsorption in the 0.02 material was corroborated by measurements of mass gain using a bench top balance, in which case the time spent outside of the equilibration environment is limited to a few seconds (Table S1).

RH (%)	H_2O from TGA (mol/f.u.)	H_2O from balance ((mol/f.u.)
0	0.02	0
11	0.02 ± 0.01	0.02 ± 0.02
45-55	0.09 ± 0.04	0.06 ± 0.01
75	0.52 ± 0.25	0.71 ± 0.17
96	2.38 ± 0.21	3.99 ± 0.10

Table A.1: H_2O content measured by TGA and a bench top balance after exposure to various RH environments. Both methods have experimental limitations, but the trend of higher humidity exposure resulting in more adsorbed water holds in both cases. The TGA values were used to represent the water content in the manuscript. However, the water content of the high humidity materials is likely underestimated due to water loss during TGA preparation in air, which is a lower humidity environment (50%)

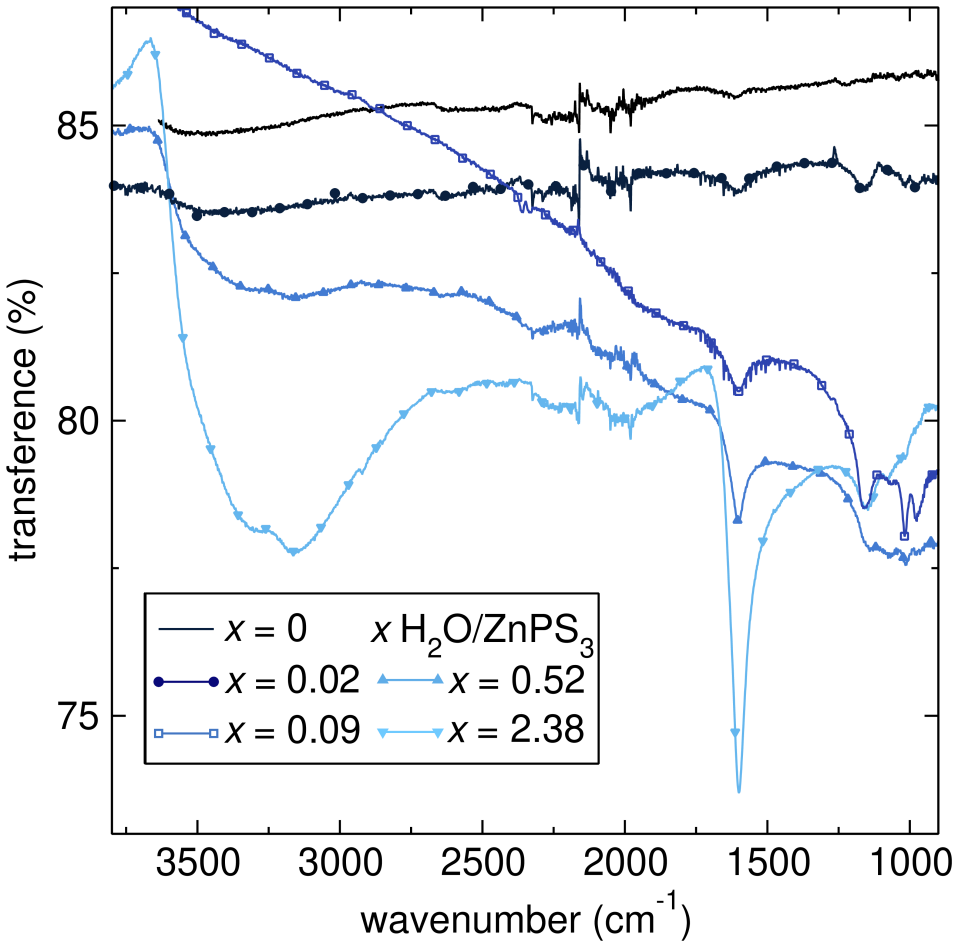

Figure A.6: Magnified FTIR spectra to show the 1600 cm^{-1} O-H bending mode in 0.02 $H_2O/ZnPS_3$. A lower intensity feature is present at 1600 cm^{-1} in the pristine material due to air exposure during the measurement.

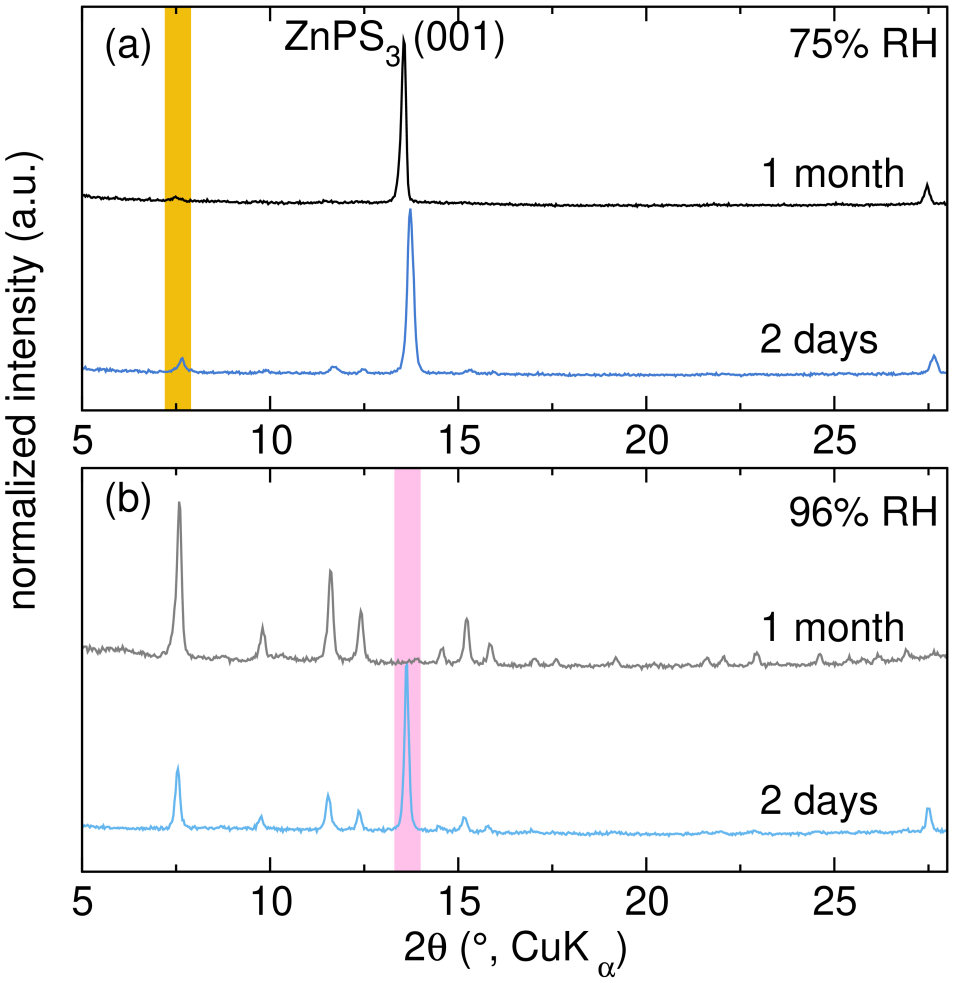

Figure A.7: XRD patterns of $ZnPS_3$ that remained in a (a) 75 % RH and (b) 96 % RH environment for 2 days (the standard equilibration time used in the present study) vs. after 1 month. In (a) the orange highlighted region shows that the strongest reflection of the emergent phase has not increased in intensity over 1 month, suggesting that the hydration at 75 % RH is self limiting and does not result in complete transformation of $ZnPS_3$ into another phase. In (b) the pink highlighted region surrounds the (001) reflection of $ZnPS_3$. After extended time in high humidity environments, the crystal structure of $ZnPS_3$ has been completely replaced by the novel hydrated crystalline phase.

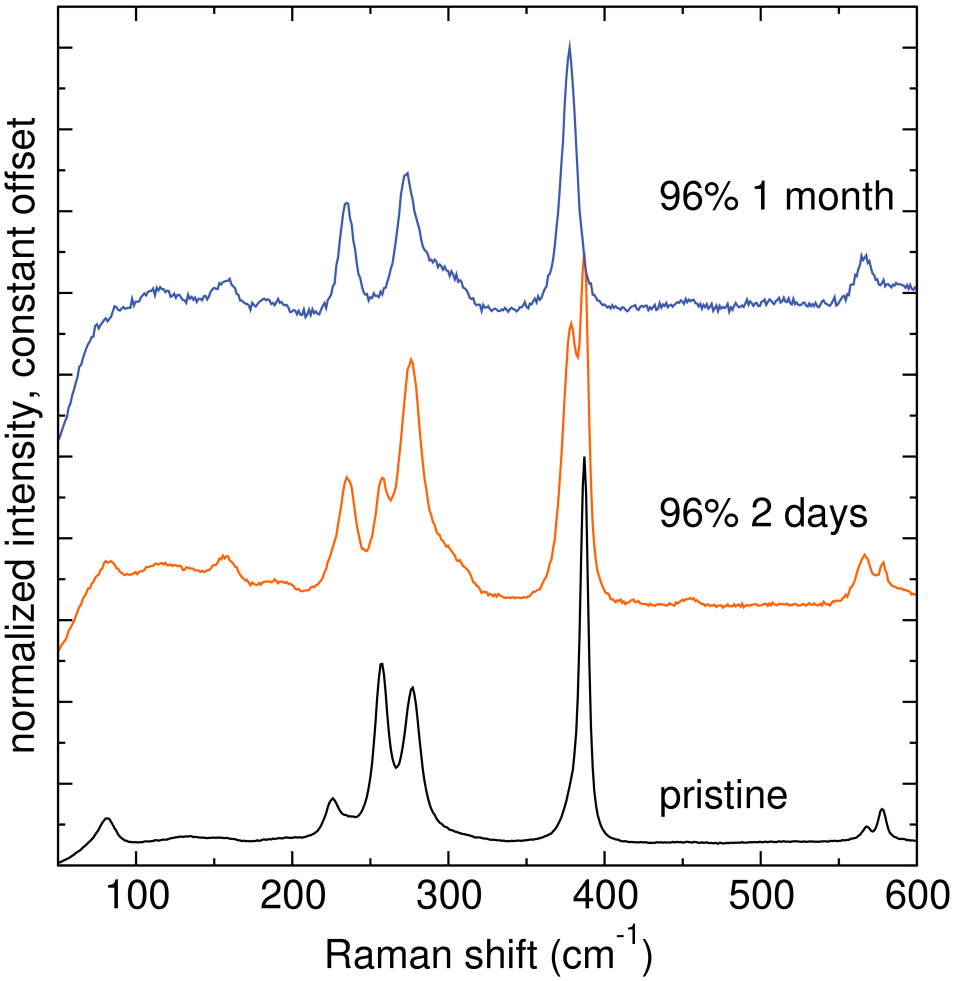

Figure A.8: Raman spectra of pristine $ZnPS_3$, 2.38 $H_2O/ZnPS_3$ (96 % for 2 days) and after complete transformation to the new hydrated crystalline phase (96 % for 1 month). The Raman spectra of 2.38 $H_2O/ZnPS_3$ contains a combination of modes of $ZnPS_3$ and those related to the hydrated crystalline phase. The Raman spectrum of spots of the 2.38 $H_2O/ZnPS_3$ sample are identical to pristine $ZnPS_3$ corresponding to areas of unconverted material.

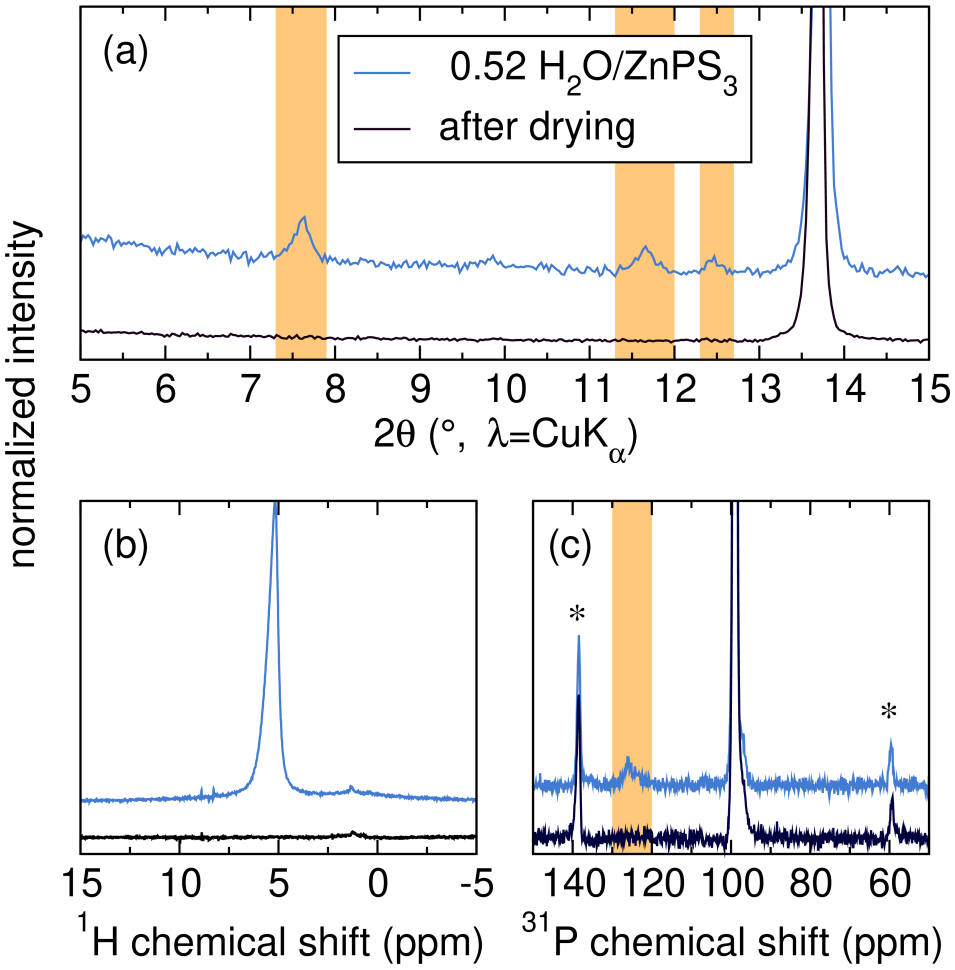

Figure A.9: (a) XRD (b) ^{1}H ssNMR and (c) ^{31}P ssNMR of 0.52 $H_2O/ZnPS_3$ before and after drying at 100 °C overnight. Equivalent results are achieved after evacuation of 0.52 $H_2O/ZnPS_3$ in a glovebox antechamber for 30 minutes.

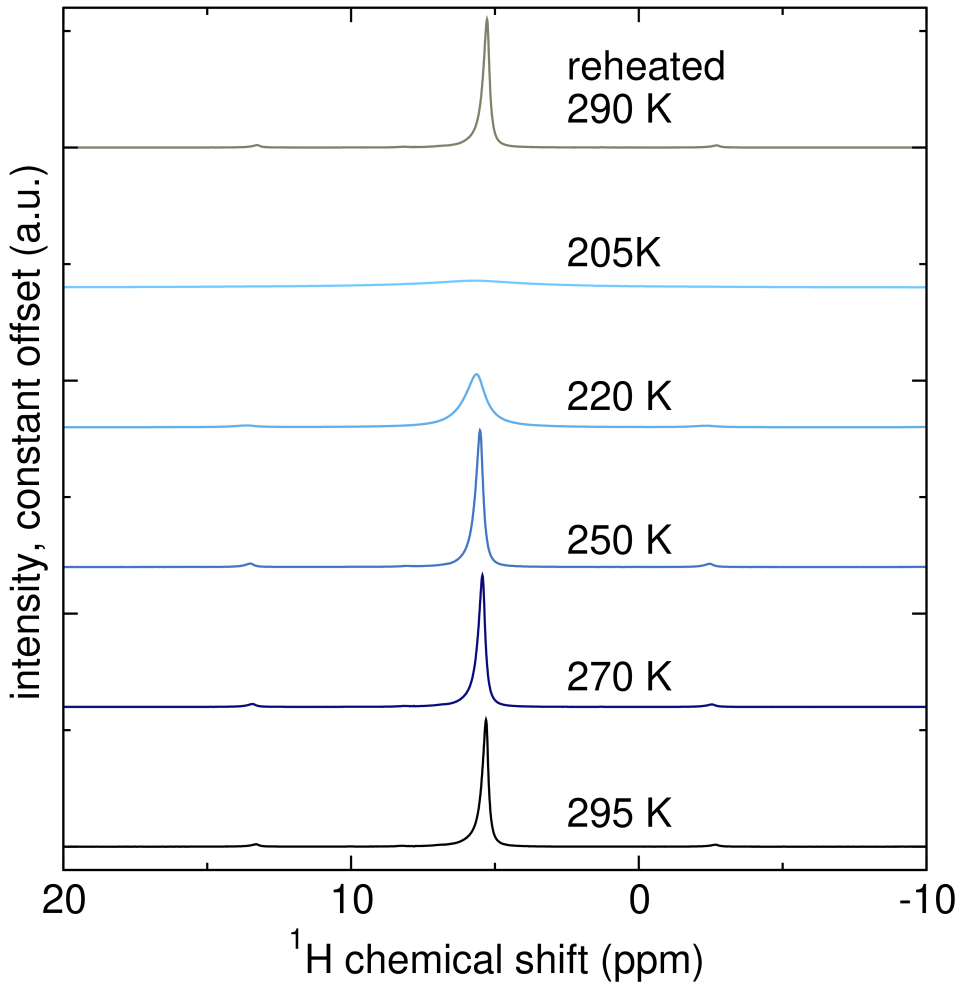

Figure A.10: Variable temperature ^{1}H NMR of 0.52 $H_2O/ZnPS_3$ at 295 K initially, then cooled through 270, 250, 220 and 205 K, and finally after reheating to 290 K. The resonance broadens with temperature reduction, begins to decrease in intensity at 220 K and completely freezes out at 205 K. This is significantly lower than the freezing point of bulk liquid water and suggests that the adsorbed water in 0.52 $H_2O/ZnPS_3$ is confined water.

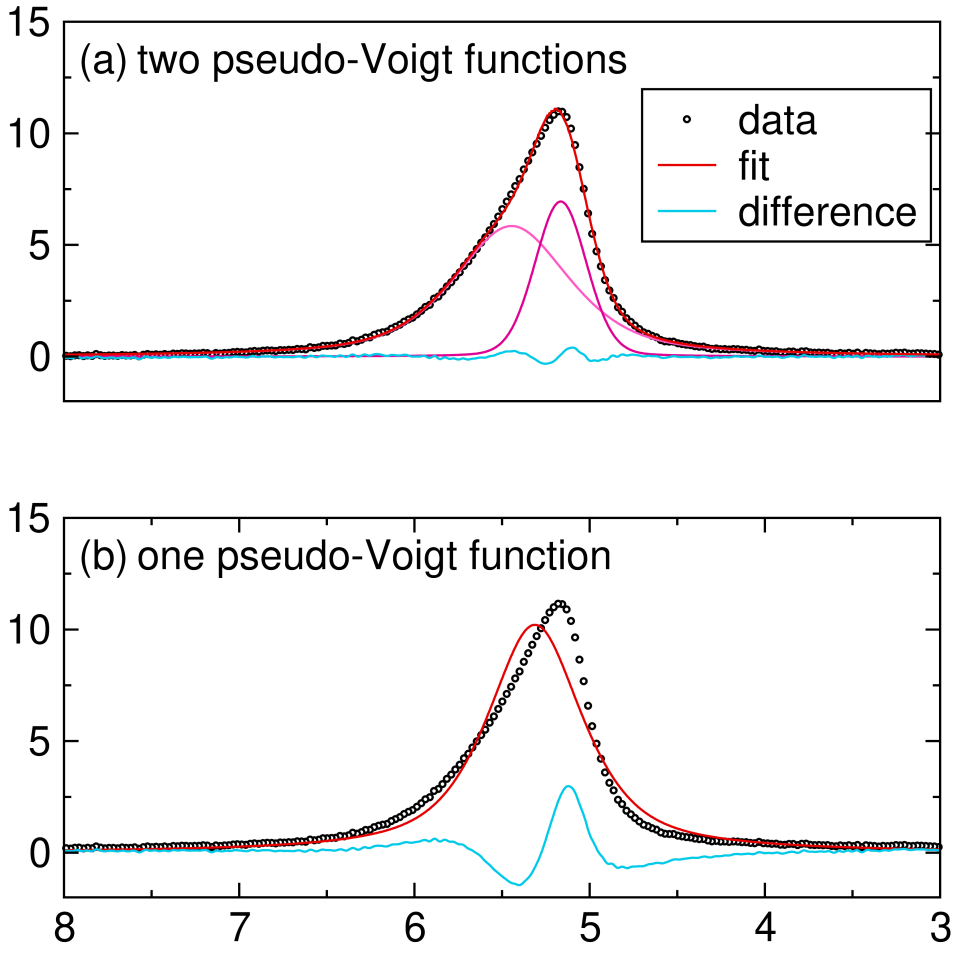

Figure A.11: (a) The ^{1}H ssNMR spectrum of 0.52 $H_2O/ZnPS_3$ is fit with two psuedo-Voigt functions. The broad shoulder at 5.5 ppm has a T_1 of 43.4 ms and the sharper peak at 5.1 has a T_1 of 89.6 ms. The sharper peak is closer to the expected value of free water ~4.8 ppm. This resonance could be due to H in the adsorbed water in the system, whereas the broader shoulder that is down-field could be due to H in water that is solvating Zn^{2+}. (b) Showing the poor fit of the ^{1}H ssNMR spectrum of 0.52 $H_2O/ZnPS_3$ when using one psuedo-Voigt function.

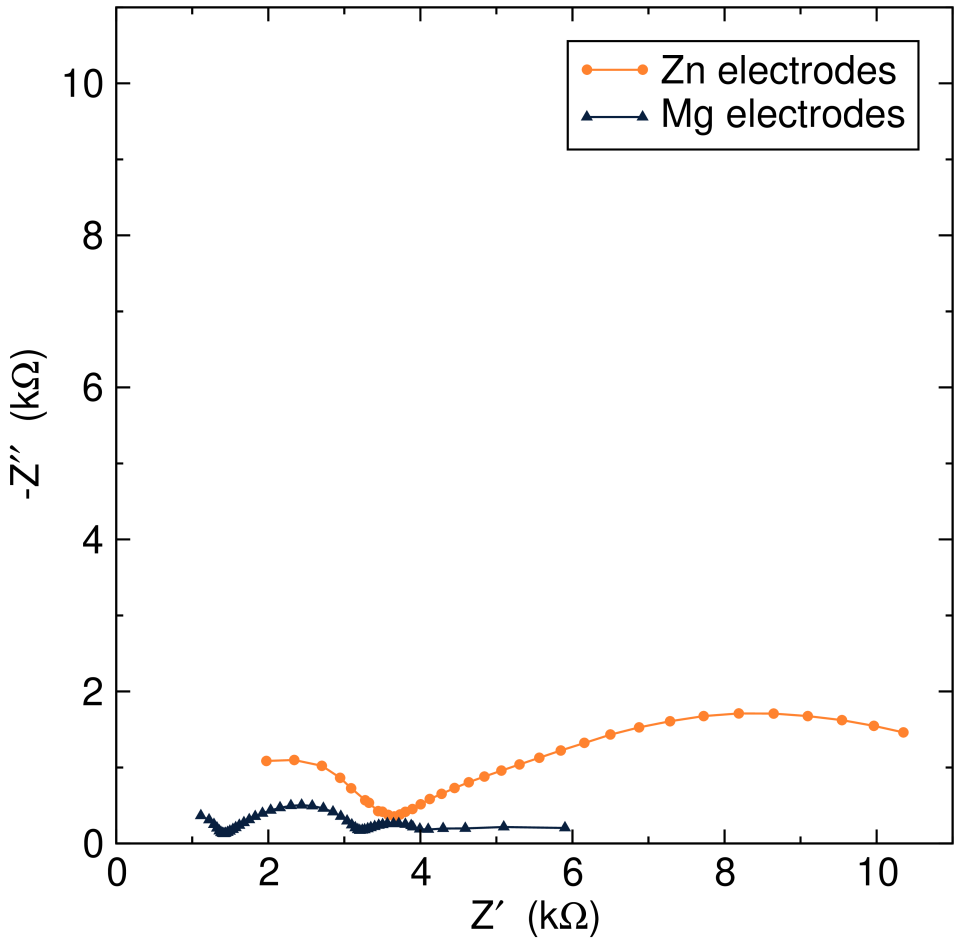

Figure A.12: EIS of 0.52 $H_2O/ZnPS_3$ in a symmetric cell with Zn electrodes or Mg electrodes. With Zn electrodes, a second semicircular feature is observed at low frequency, which is attributed to conduction of Zn^{2+} through the 0.52 $H_2O/ZnPS_3$ | Zn interface. With Mg electrodes, the low frequency behavior is not a semicircular feature but is constantly increasing with time which is likely the result of interfacial reactivity.

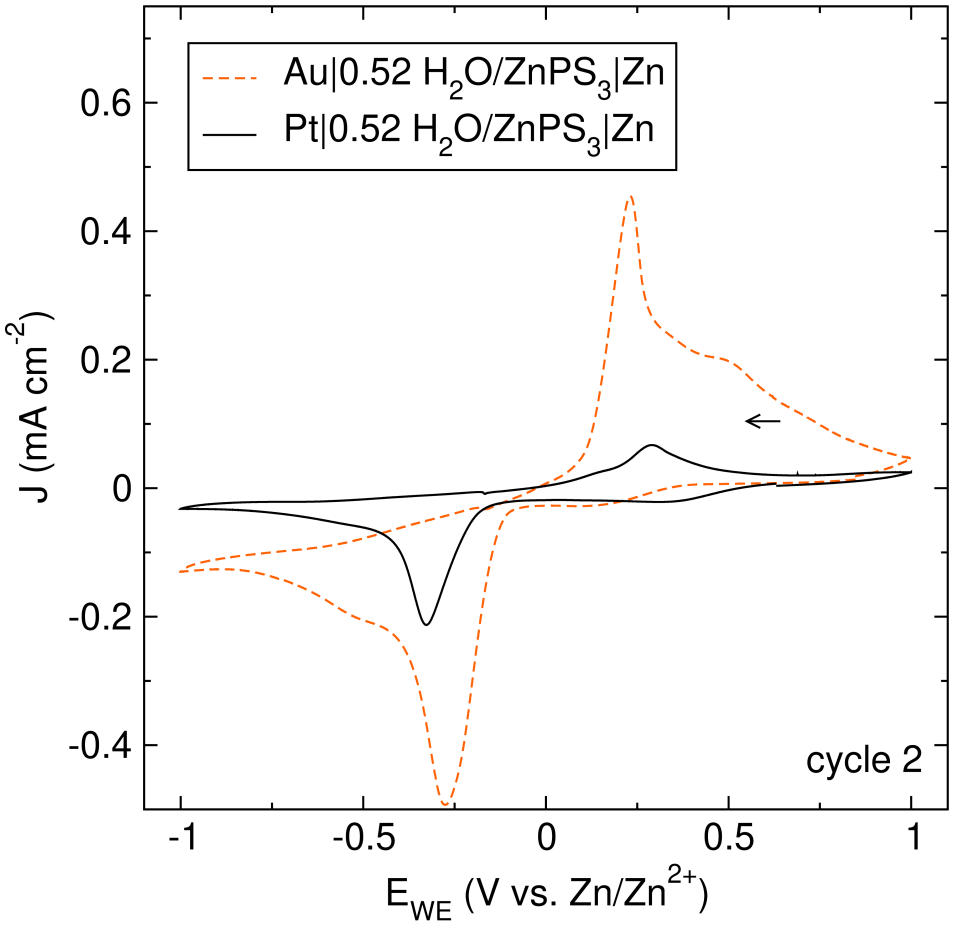

Figure A.13: Cycle two of the CVs showed in Figure 8, showing a decrease in J, potentially due to degradation of the interfaces during plating and stripping.

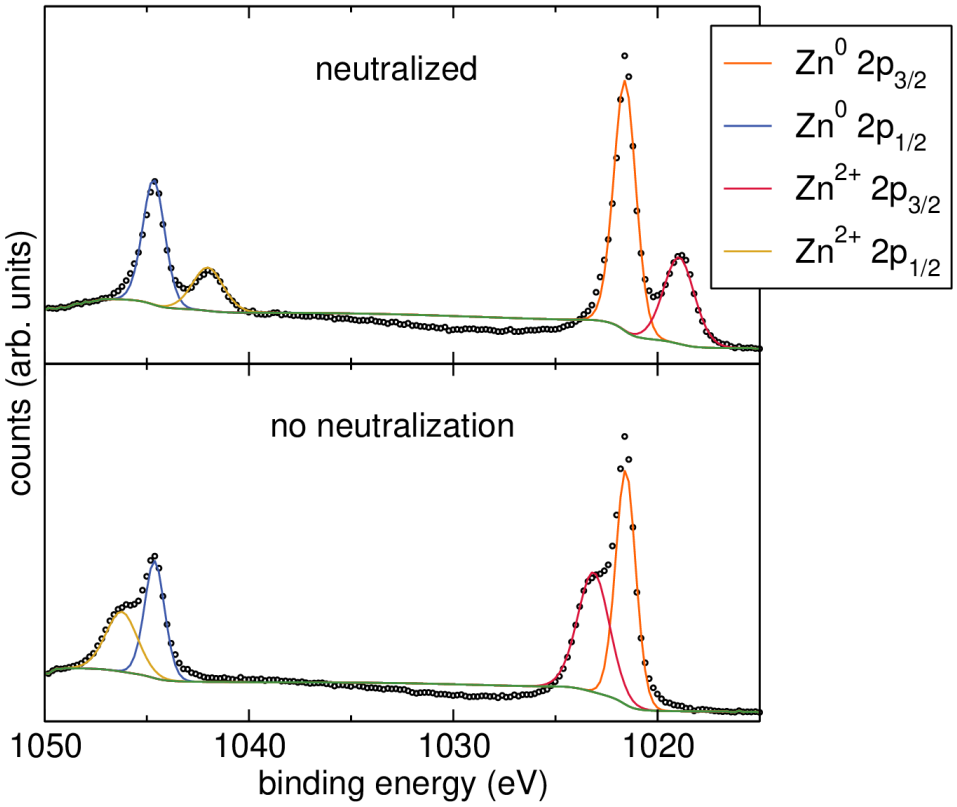

Figure A.14: XPS spectra of the Zn 2*p* region of the Zn-deposited Au electrodes. Top: with the charge neutralizer on to compensate for positive surface charging. Bottom: with the charge neutralizer off. In the neutralized sample, the insulating Zn^{2+} species is overneutralized, thereby shifting to a more negative binding energy. With no neutralization, the Zn^{2+} species shifts to a positive binding energy due to positive charging.

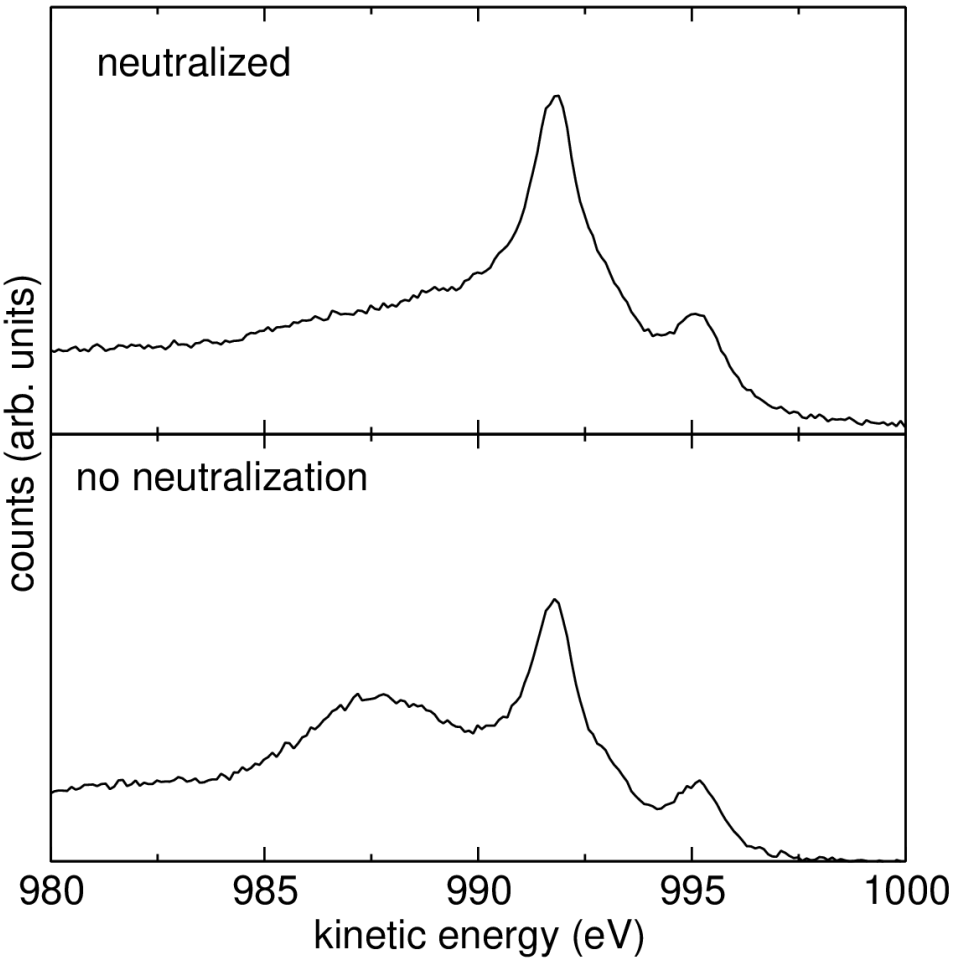

Figure A.15: XPS spectra of the Zn *LMM* Auger region of the Zn-deposited Au electrodes. Top: with the charge neutralizer on. Bottom: with the charge neutralizer off. In the neutralized sample, the insulating Zn^{2+} species is overneutralized, thereby shifting to a more positive kinetic energy, disappearing into the shoulder of the large Zn^0 Auger peak. With no neutralization, the Zn^{2+} species shifts to a more negative kinetic energy due to positive charging.

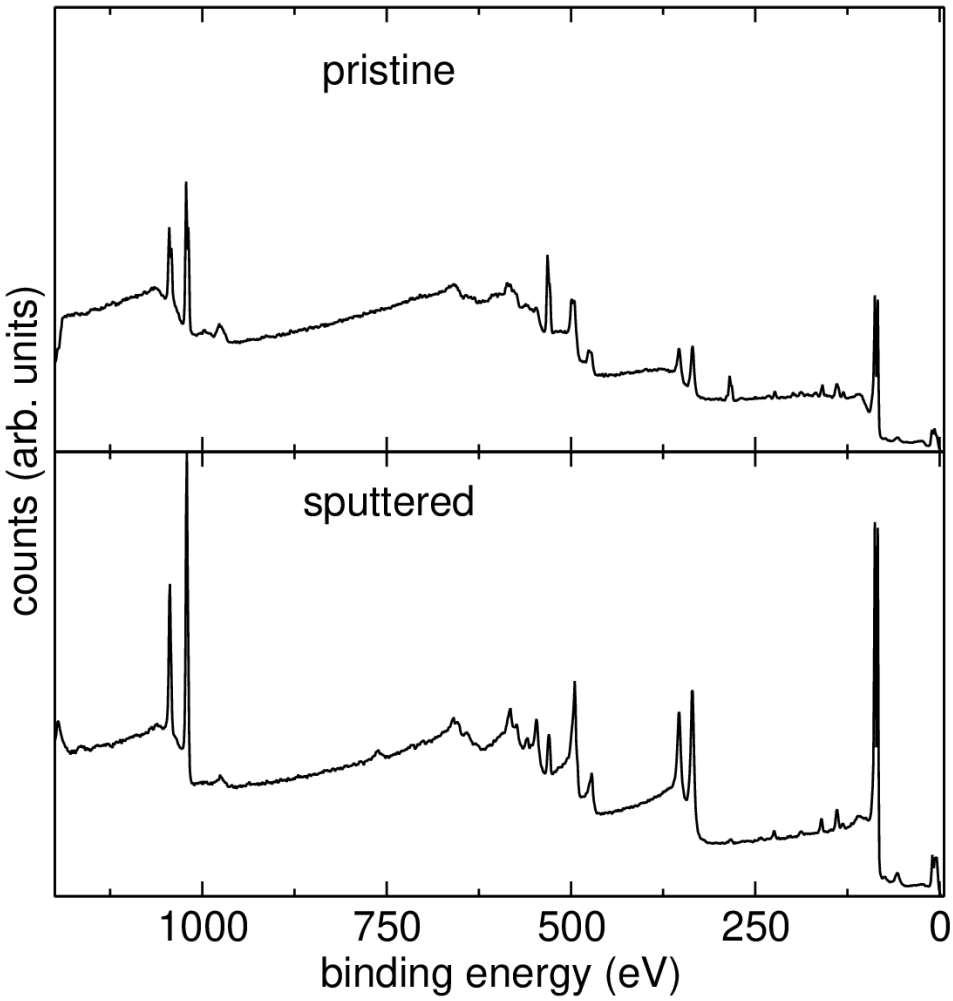

Figure A.16: XPS survey spectra of the Zn-deposited Au electrodes. Top: pristine electrode as-prepared. Bottom: sputtered with an Ar ion gun for 35 minutes.

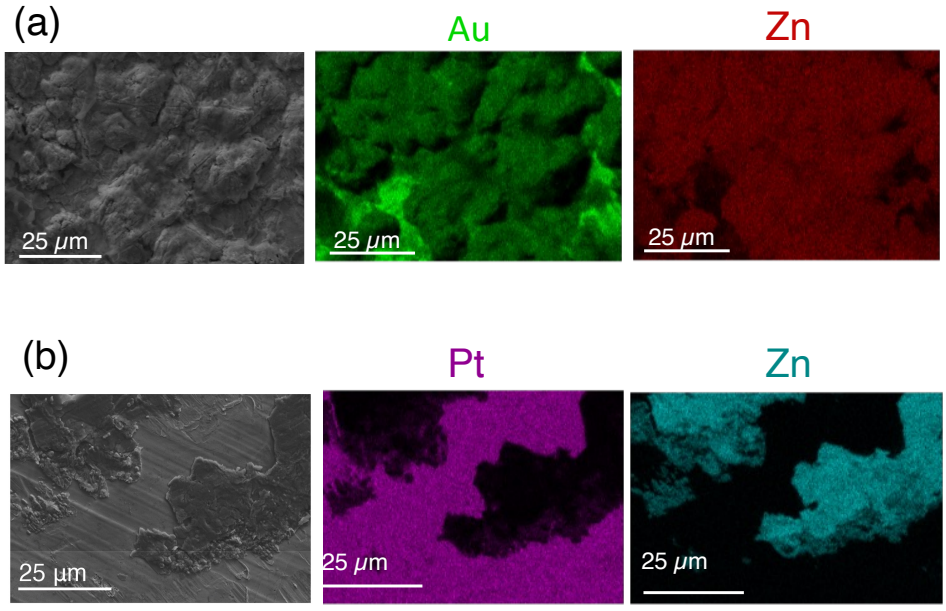

Figure A.17: SEM and EDS with 0.52 $H_2O/ZnPS_3$ on (a) Au and (b) Pt substrates, showing possible Au-Zn alloys after deposition on Au foil as the deposits contain Au by EDS. However, the deposits on Pt only contain Zn (and not Pt) by EDS, in agreement with the CV results.

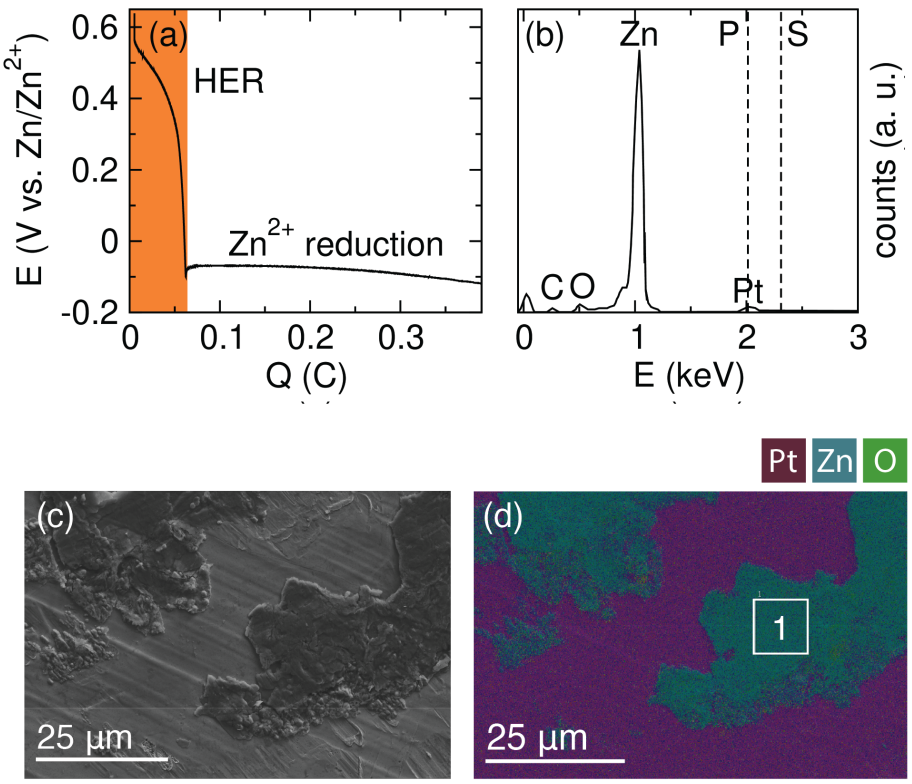

Figure A.18: The potential transient upon application of -10 μA cm^{-1} to 0.52 $H_2O/ZnPS_3$ sandwiched between a Pt foil working electrode and Zn foil counter/reference electrode at 40 °C in a Swagelok cell under 3 kN of force. (b) EDS spectrum of the area enclosed by the white box showing that the deposits primarily contain Zn and do not contain any P or S (expected P and S energies shown with dotted lines). (c) SEM of the Pt surface after deposition. (d) EDS map of the Pt surface after deposition, showing that the deposits contain only Zn and O.

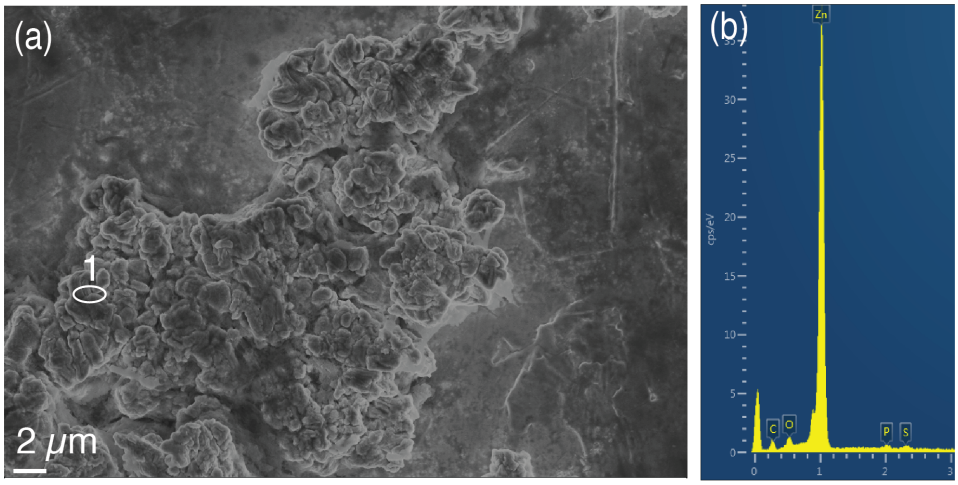

Figure A.19: (a) Higher magnification SEM image of Zn deposits on Pt electrode and (b) EDS of region 1 showing Zn is present with trace amounts of P and S.

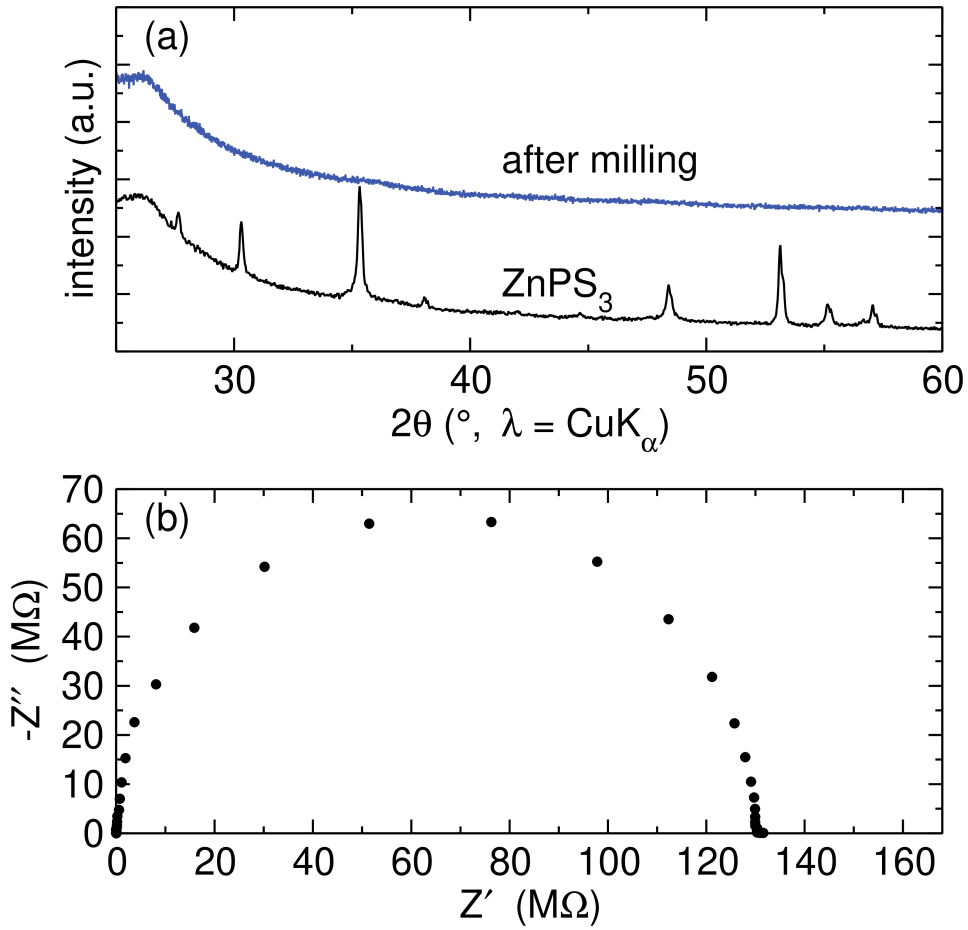

Figure A.20: (a) XRD pattern of $ZnPS_3$ powder before and after ball milling 500 mg of powder in 50 ml ZnO_2 milling jars with 15 g of balls (1:30 powder:ball ratio - 6.1 g of 5 mm balls and 8.8 g of 3 mm balls) at (1) 380 rpm for 16 hrs and then (2) 580 rpm for 12 h in a MSE PRO Bench Top Mini High Energy Vertical Planetary Ball Mill. The XRD was collected by placing powder on a glass slide under kapton tape to prevent air exposure. Due to the background of the Kapton, the diffraction patterns are viewed above 25 ° 2θ (b) Nyquist plot of anhydrous, amorphous $ZnPS_3$ at room temperature.

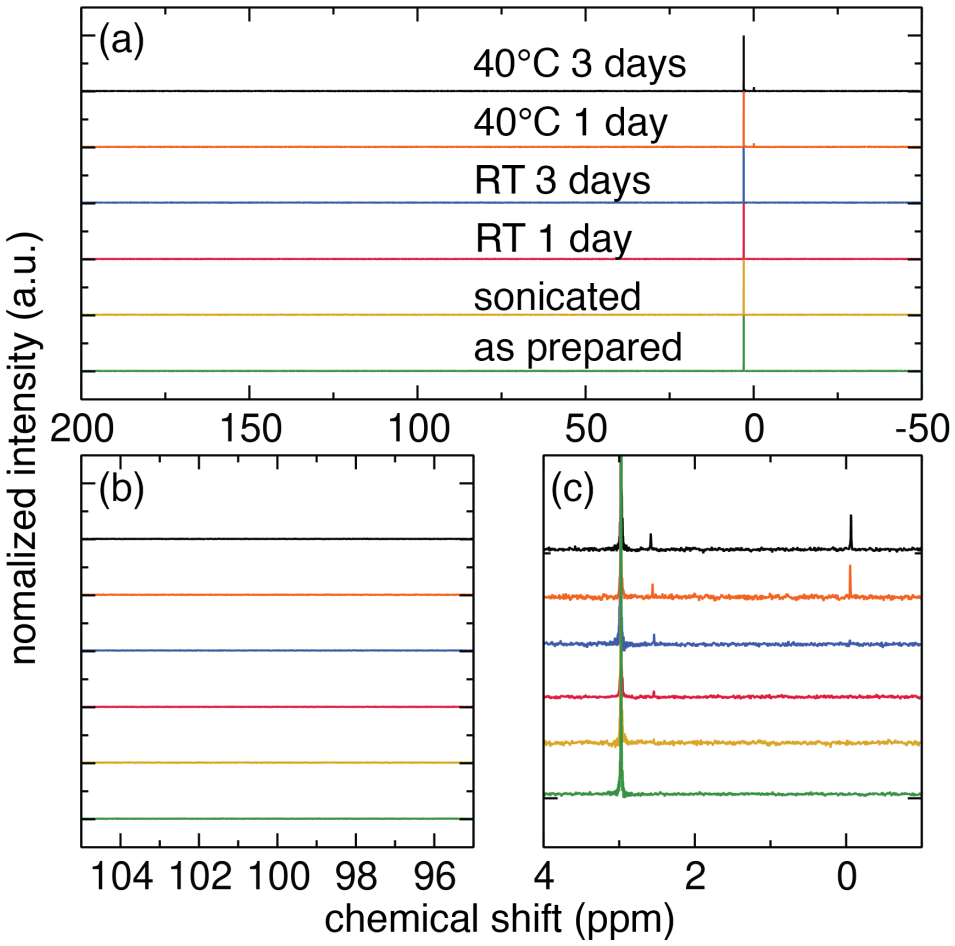

Figure A.21: ^{31}P solution NMR to probe the dissolution of $ZnPS_3$ in water under different conditions. (a) Full spectral window, (b) the region of interest for $[P_2S_6]^{4-}$ resonance, and (c) -1 to 4 ppm showing resonances that appear at -0.05 and 2.6 ppm likely due to the formation of phosphates. The resonance at 3 ppm is due to the trimethyl phosphate internal reference. Note that in these experiments, the H_2O:$ZnPS_3$ ratio is 100x greater than in 0.52 H_2O/$ZnPS_3$.

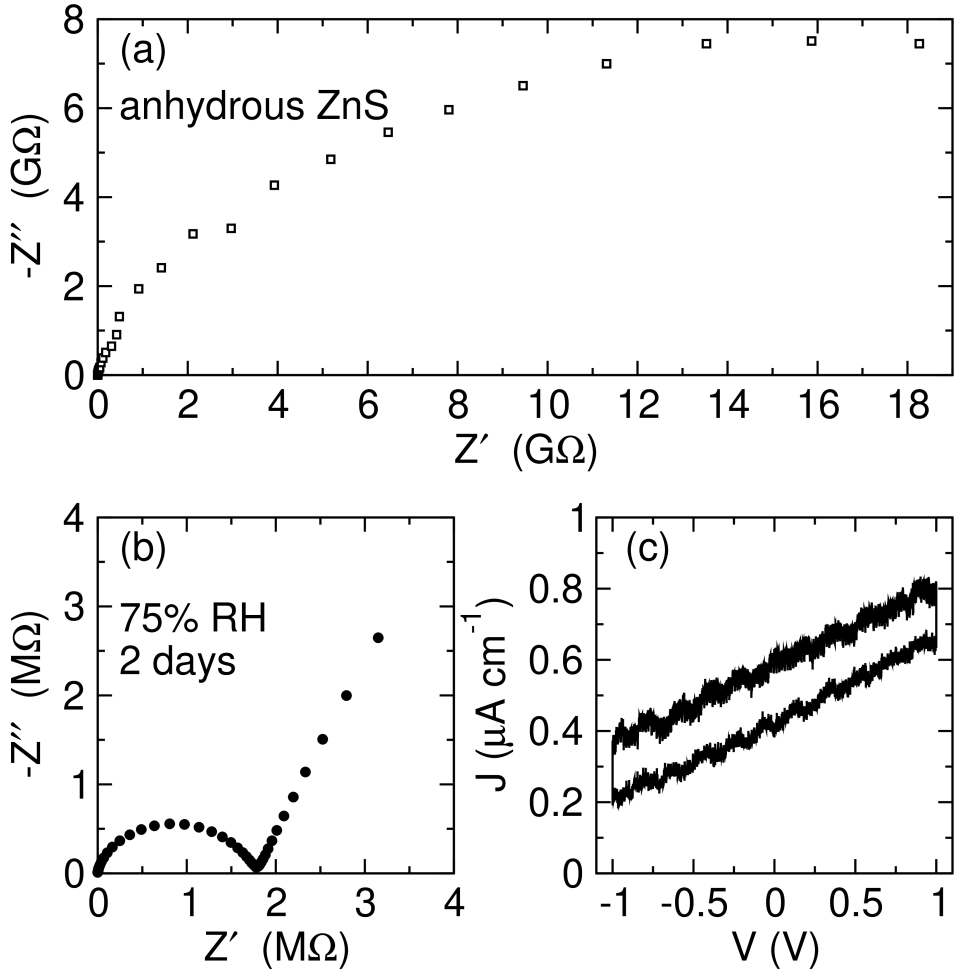

Figure A.22: (a) Nyquist plot of anhydrous ZnS (Alpha Aesar, 99.99% without further purification) EIS was conducted from 3 MHz-100 mHz at room temperature. (b) Nyquist plot of the same pellet after 2 day in 75% RH chamber (0.11 H_2O/ZnS), showing an increased conductivity after hydration. (c) CV of Au | 0.11 H_2O/ZnS | Zn under the same conditions as $ZnPS_3$ described in the manuscript.

Appendix B

SUPPORTING INFORMATION FOR CHAPTER V: MODULAR *M*PS_3-BASED FRAMEWORKS FOR SUPERIONIC CONDUCTION OF BOTH MONOVALENT AND MULTIVALENT IONS.

B.1 Supplementary Notes

Ion Exchange Reaction in *M*PS_3 Phases

The ion exchange reaction occurs in a less controlled manner with $MnPS_3$ than $CdPS_3$. With $CdPS_3$, a chelating agent — such as ethylenediaminetetraacetic acid (EDTA) — must be added to the ion exchange reaction in order for Cd^{2+} to leave the $CdPS_3$ lattice. Whereas, with $MnPS_3$ the more labile Mn^{2+} readily leaves $MnPS_3$ in the aqueous solution without EDTA. As a result, the final Mn content of the exchanged materials differs depending on the intercalated ion. For example, during the second ion exchange to insert Na^+ or Ca^{2+}, in addition to replacing the K^+ from the first exchange, some additional Mn^{2+} from the metal layer is replaced. However, for the second exchanges with $CdPS_3$ no EDTA is added, so no additional Cd^{2+} is expected to be leached from the compound.

Furthermore, the pristine $MnPS_3$ does not completely react in the conditions used in this study (small amounts are still present in the XRD, Figure B.1). Attempts to use higher molarity KCl solutions or to add EDTA to facilitate full transformation to $K_{0.5}Mn_{0.75}PS_3$ often led to exfoliation or degradation of the material due to loss of excess Mn.$K_{0.5}Mn_{0.75}PS_3$ could be obtained through a second successive K^+ exchange, but we found that it did not significantly affect the electrochemical properties, therefore for simplicity the study was carried out using the product of the single K^+ exchange, $K_{0.4}Mn_{0.80}PS_3$.

B.2 Supplementary Figures

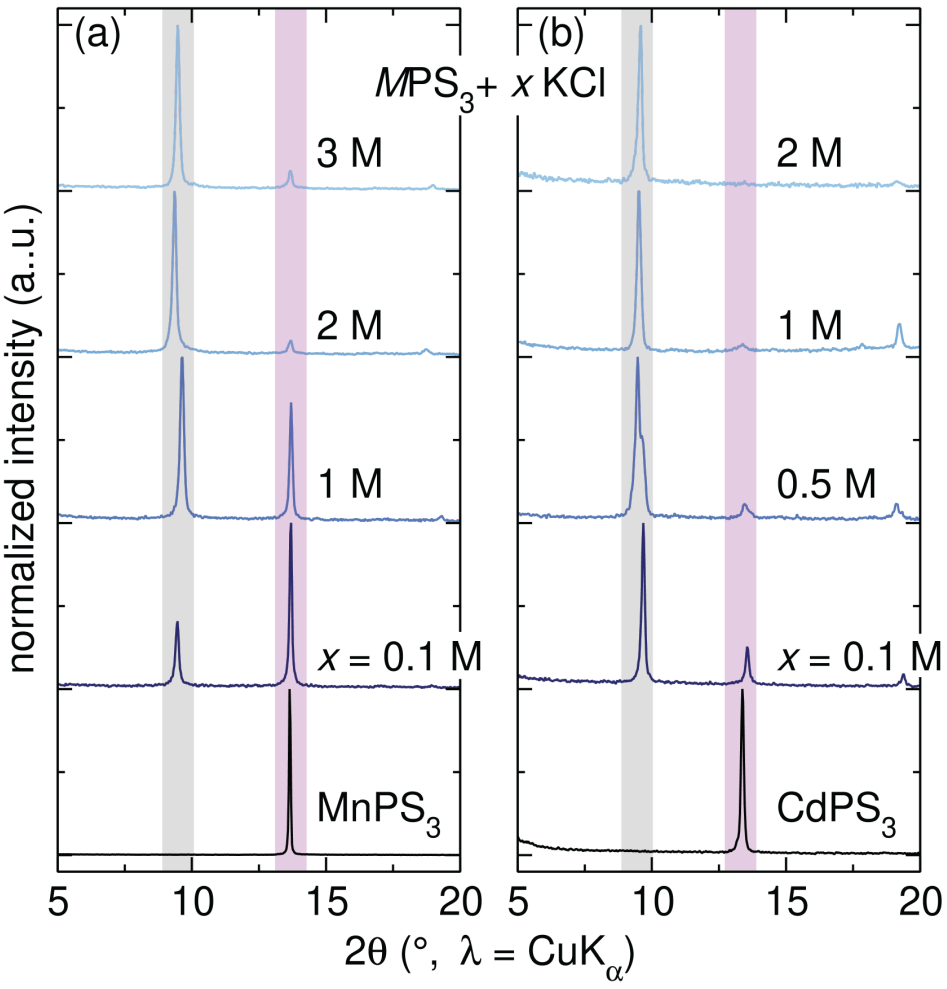

Figure B.1: XRD patterns of K^+ ion exchange reactions with (a) $MnPS_3$ and (b) $CdPS_3$ using different concentrations of $KCl_{(aq)}$ solutions. For $MnPS_3$, XRD reflections pertaining to the pristine material were still present after a reaction with 3 M KCl. Therefore, under these reaction conditions a two phase mixture of $MnPS_3$ and $K_{.50}Mn_{.75}PS_3$ is formed, which corresponds to an overall stoichiometry of $K_{.40}Mn_{.8}PS_3$. The pristine $CdPS_3$ phase is no longer present after reaction in 2 M KCl with EDTA and the buffer solution.

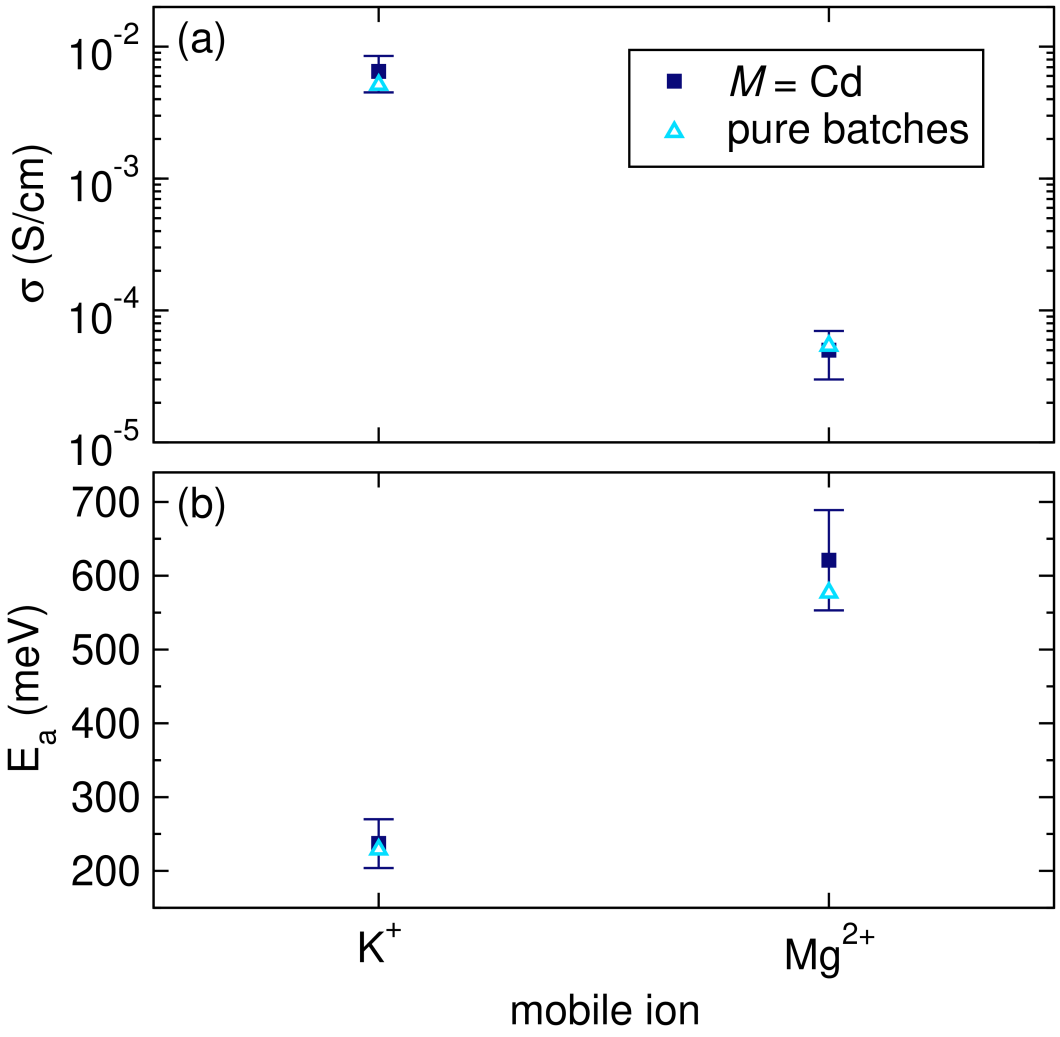

Figure B.2: A comparison of (a) σ_{RT} and (b) E_a of pure batches (by elemental analysis) with the average values of select $CdPS_3$-based ion exchange materials. The electrochemical performance of the pure batches is within error of the overall average, suggesting that the presence of a small amount of impurities in some batches doesn't affect the electrochemical performance.

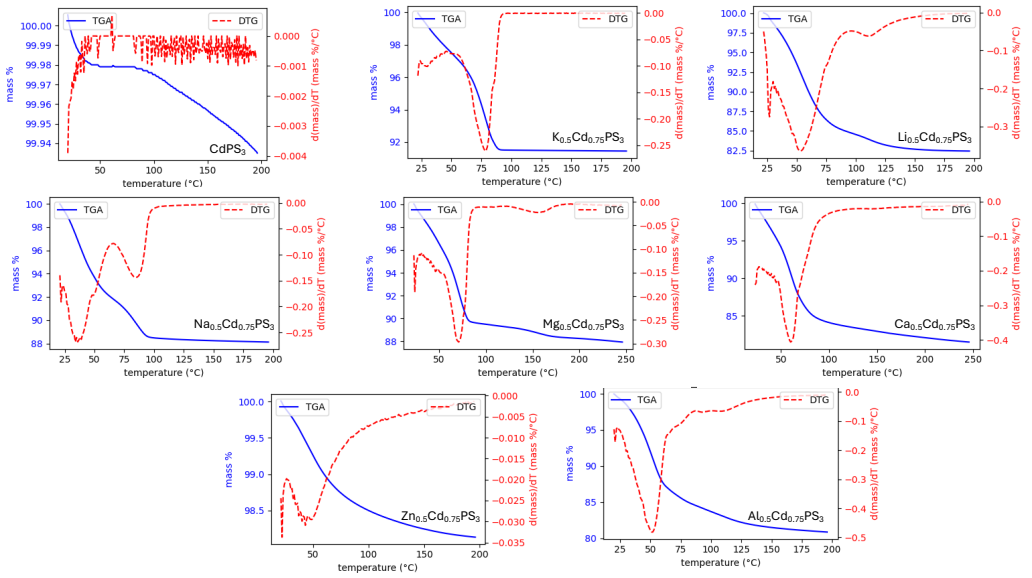

Figure B.3: TGA and DTG analysis of pristine $CdPS_3$ and all $CdPS_3$-based ion exchanged compounds. All compounds were equilibrated at 53% RH before TGA was measured. The initial mass loss event shown in the DTG plot is due to loss of surface adsorbed water, but is insignificant in comparison to the total mass loss.

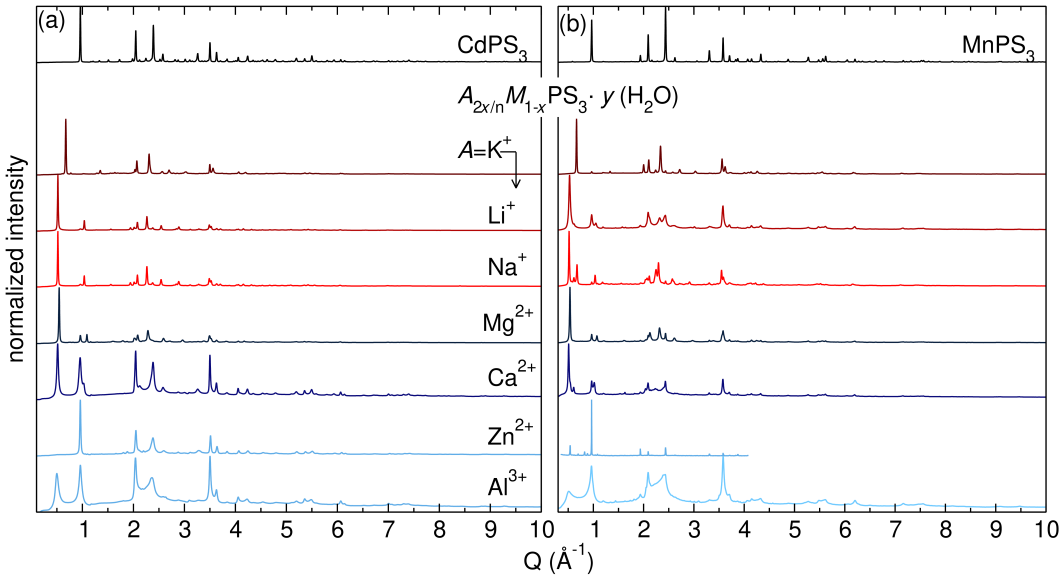

Figure B.4: XRD patterns of ion exchange reactions with (a) $CdPS3_3$ and (b) $MnPS3_3$. Note, the pattern of $Zn_{0.4}Mn_{0.6}PS_3 \cdot 1.6\ H_2O$ is collected using Cu K_α radiation because the sample inadvertently dehydrated during preparation for the synchrotron measurement. The other pattens were collected using synchrotron radiation.

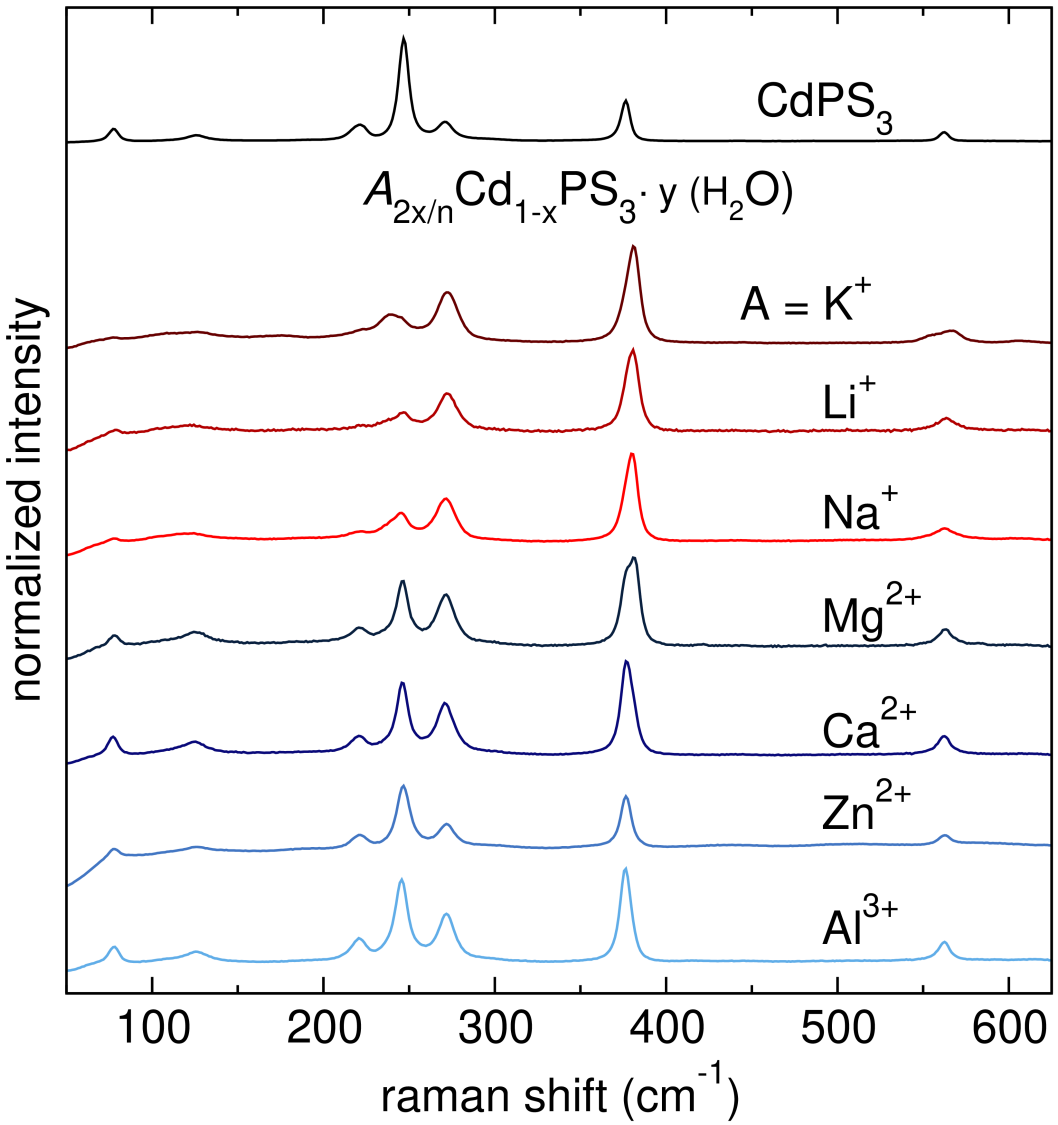

Figure B.5: Raman spectra of $CdPS_3$ and all ion-exchanged compounds, the modes around 222, 248, 271, 377 and 565 cm^{-1} are related to the $[P_2S_6]^{4-}$ polyanion bending, stretching, and wobbling. These modes are all present after ion exchange, confirming that the $[P_2S_6]^{4-}$ polyanion remains in tact after ion exchange, suggesting that the intralayer environments are similar before and after ion exchange. The intensity of these modes changes after exchange, as previously noted for monovalent-ion intercalated $CdPS_3$ by Barj *et al.*[255]

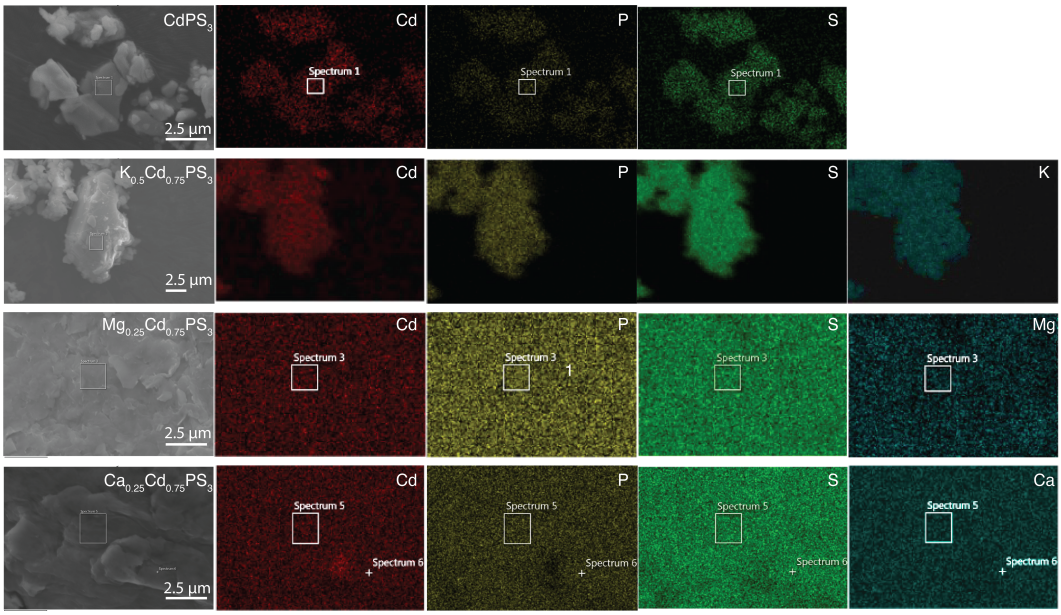

Figure B.6: SEM and EDS of pristine $CdPS_3$ and select ion-exchanged compounds to show that the intercalated ions are homogeneously dispersed within the material after ion exchange. After the 2nd exchange, Mg and Ca shown here, the particle size is significantly bigger than the pristine and K-exchanged compounds.

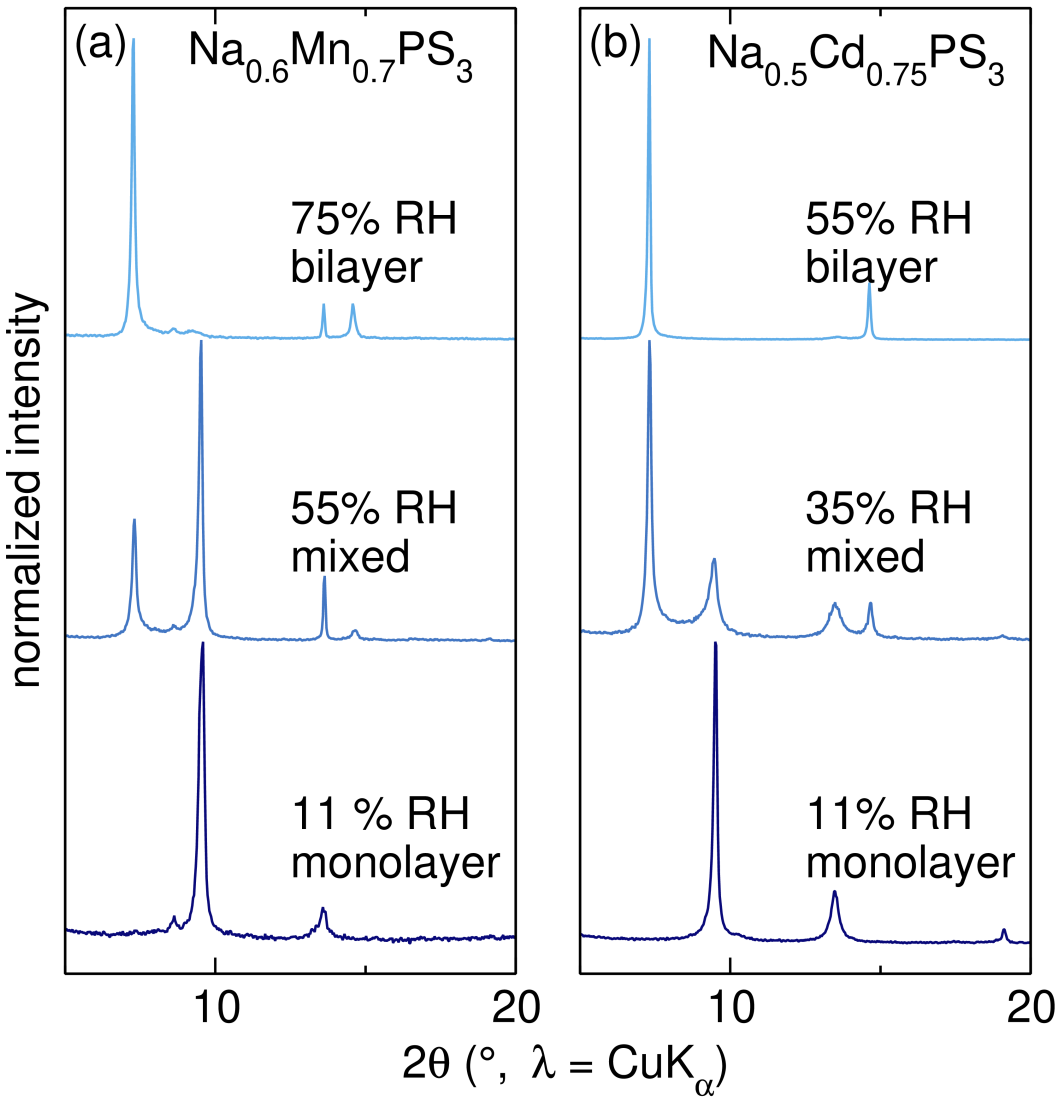

Figure B.7: XRD patterns of (a) $Na_{0.6}Mn_{0.7}PS_3$ and (b) $Na_{0.5}Cd_{0.75}PS_3$ in different RH environments to show that the monolayer, bilayer, or a mixture of both hydrated phases can be obtained depending on the RH.

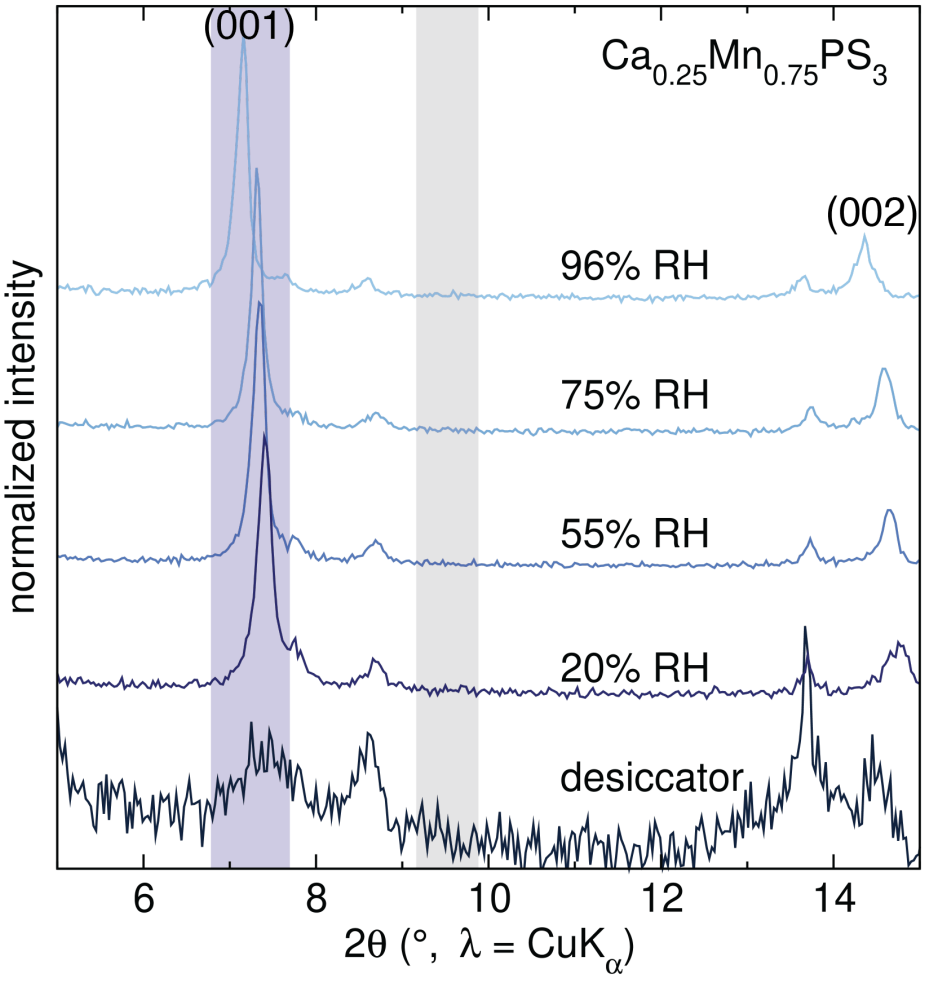

Figure B.8: XRD patterns of $Ca_{0.25}Mn_{0.75}PS_3$ in different RH environments to show that instead of forming the monolayer H_2O structure (which would appear around 9.5 ° 2θ, in the gray region) the bilayer structure is maintained at all RH. However, the water content changes depending on the RH, which likely corresponds to incomplete solvent shells around the Ca^{2+} ions, and is reflected by small changes in the position of the reflection.

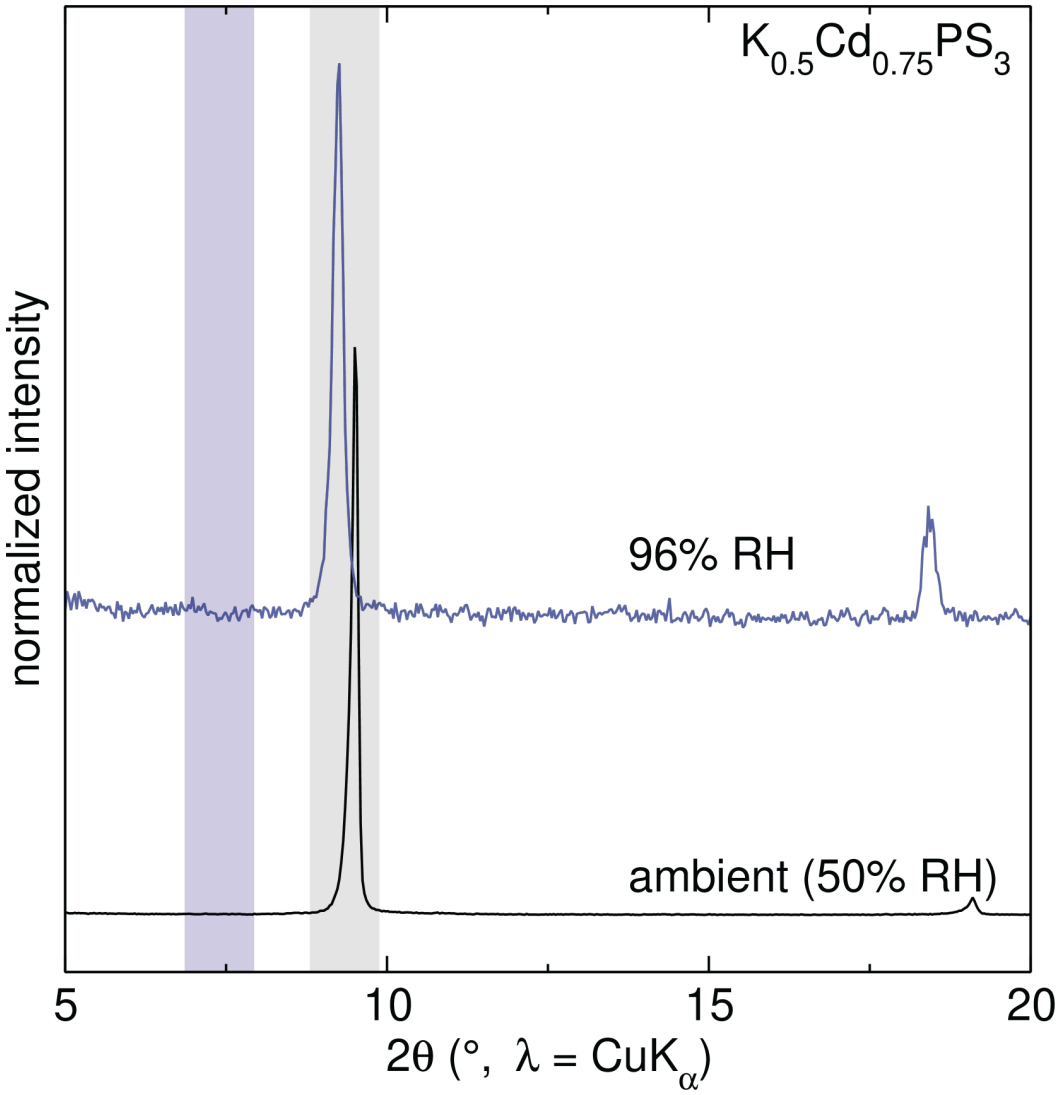

Figure B.9: XRD patterns of $K_{0.5}Cd_{0.75}PS_3$ at ambient and high RH (96%), illustrating that $K_{0.5}Cd_{0.75}PS_3$ maintains the monolayer H_2O structure instead of forming a bilayer H_2O structure (which would appear around 7.5 ° 2θ, in the purple region) even at high RH.

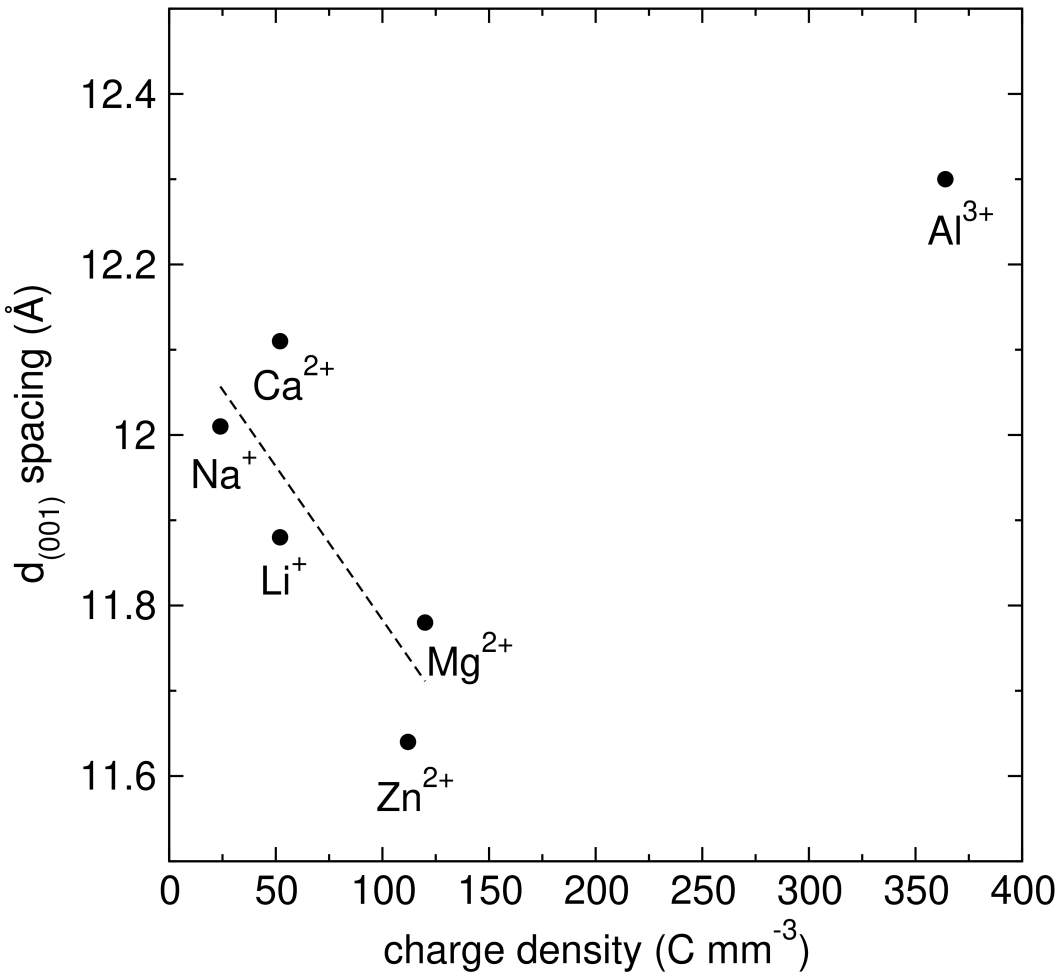

Figure B.10: The $d_{(001)}$ spacing of $MnPS_3$-based ion exchanged materials that form hydrated bilayer H_2O structures vs. the charge density of the intercalated ion. The higher the charge density of the intercalated ion, the stronger the interactions with the bound water and thus the smaller the $d_{(001)}$ spacing. Al^{3+} is an outlier to this trend due to the excess water present in the material which expands the interlayer spacing.

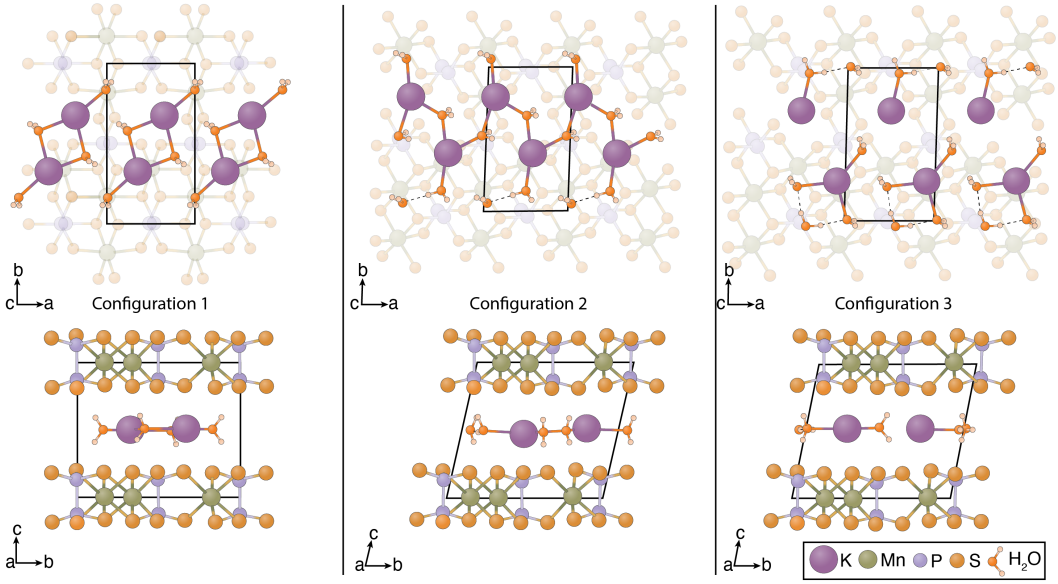

Figure B.11: The three most stable configurations of $K_{0.5}Mn_{0.75}PS_3 \cdot H_2O$. These structures are only relaxed with DFT and are not subjected to the heating and cooling approach using AIMD. The top images show the view down the *c* axis after removing the metal layer above the hydrated K^+, the metal layer below is made partially transparent for clarity. The bottom images show the view down the *a* axis. Hydrogen bonds between H_2O molecules are shown as dotted black lines. The H_2O molecules are inaccurately depicted as being smaller than the K atoms for clarity. Configuration 1 is made up of $K_2(H_2O)_4$ dimers with bridging H_2O, configuration 2 consists of a network of sheets of K with bridging H_2O, the sheets are connected by hydrogen bonds between H_2O molecules, and configuration 3 is mostly made up of isolated, hydrated K^+ with an absence of bridging H_2O. These configurations are separated in energy by < 1 meV, therefore it is likely the a combination of these configurations is present at RT. The presence of a combination of these configurations is supported by the fact that neither superstructure peaks nor those associated with ordered, hydrated K in the interlayer are present in the XRD patterns.

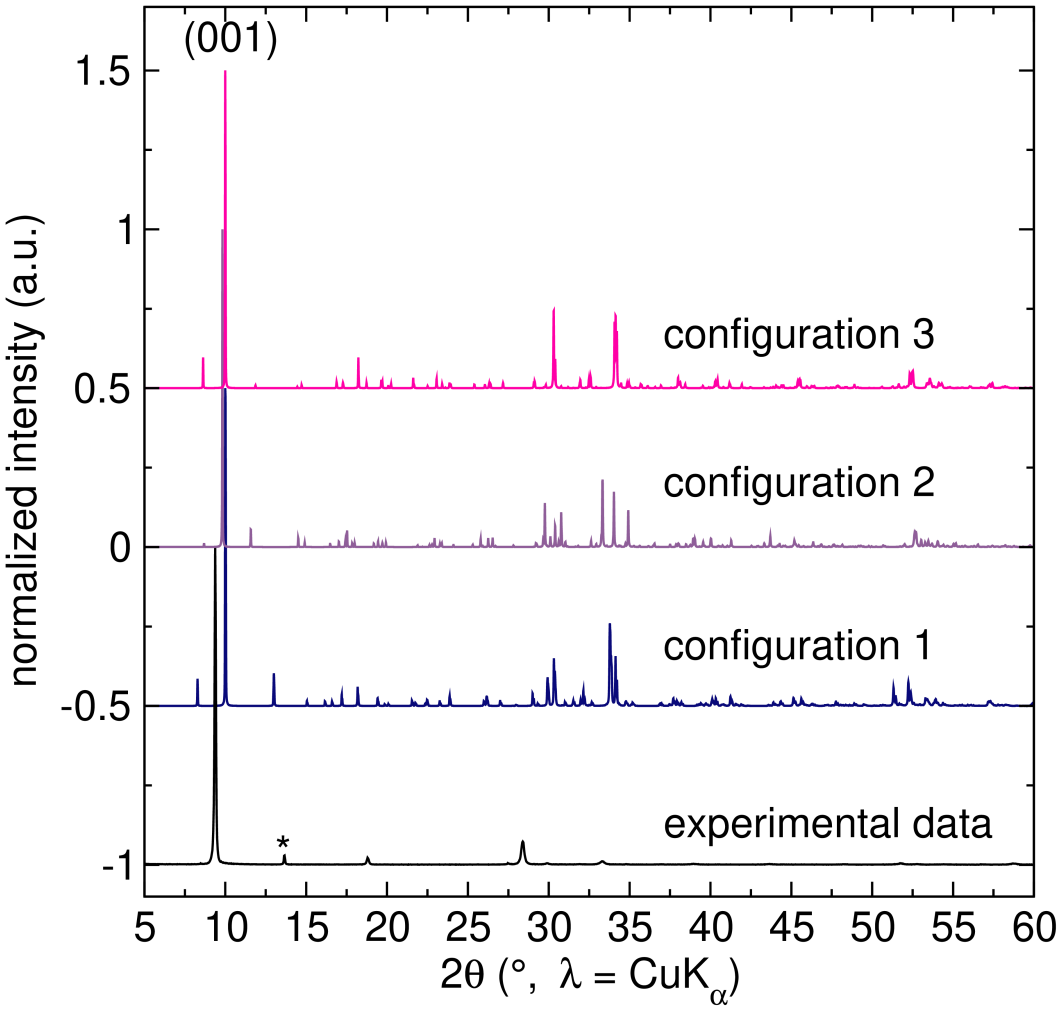

Figure B.12: The experimental XRD pattern of $K_{0.4}Mn_{0.8}PS_3$ at ambient RH compared to the computed pattens of the stable relaxed structures (configuration 1, 2, and 3). The reflection marked with "*" is the remaining pristine $MnPS_3$. Several reflections associated with ordered interlayer hydrated K are present in the relaxed structures, but are absent in the experimental data —- suggesting that the interlayer K is disordered.

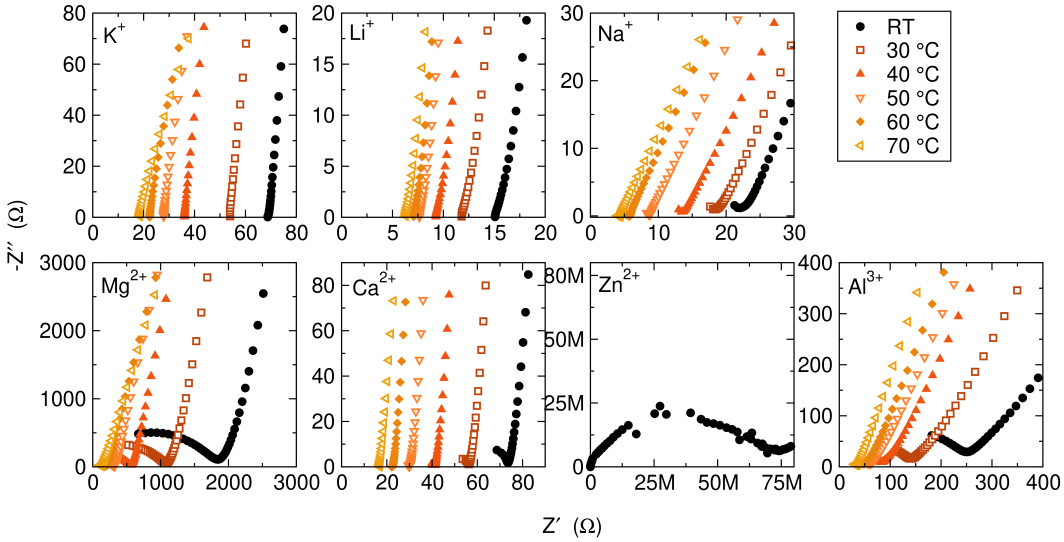

Figure B.13: Representative Nyquist plots of all $CdPS_3$-based ion exchanged compounds, equilibrated at ambient humidity (40-55%). The measurements were taken at RT and then from 30 to 70 ° C. A temperature series was not attempted for the Zn intercalated compound because of the very high impedance and noisy data.

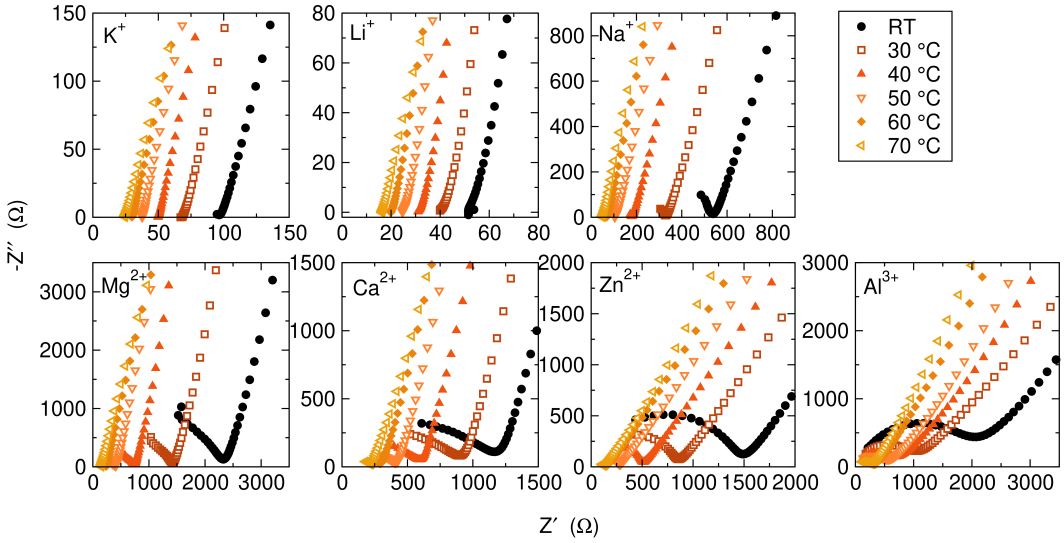

Figure B.14: Representative Nyquist plots of all $MnPS_3$-based ion exchanged compounds, equilibrated at ambient humidity (40-55%). The measurements were taken at RT and then from 30 to 70 ° C.

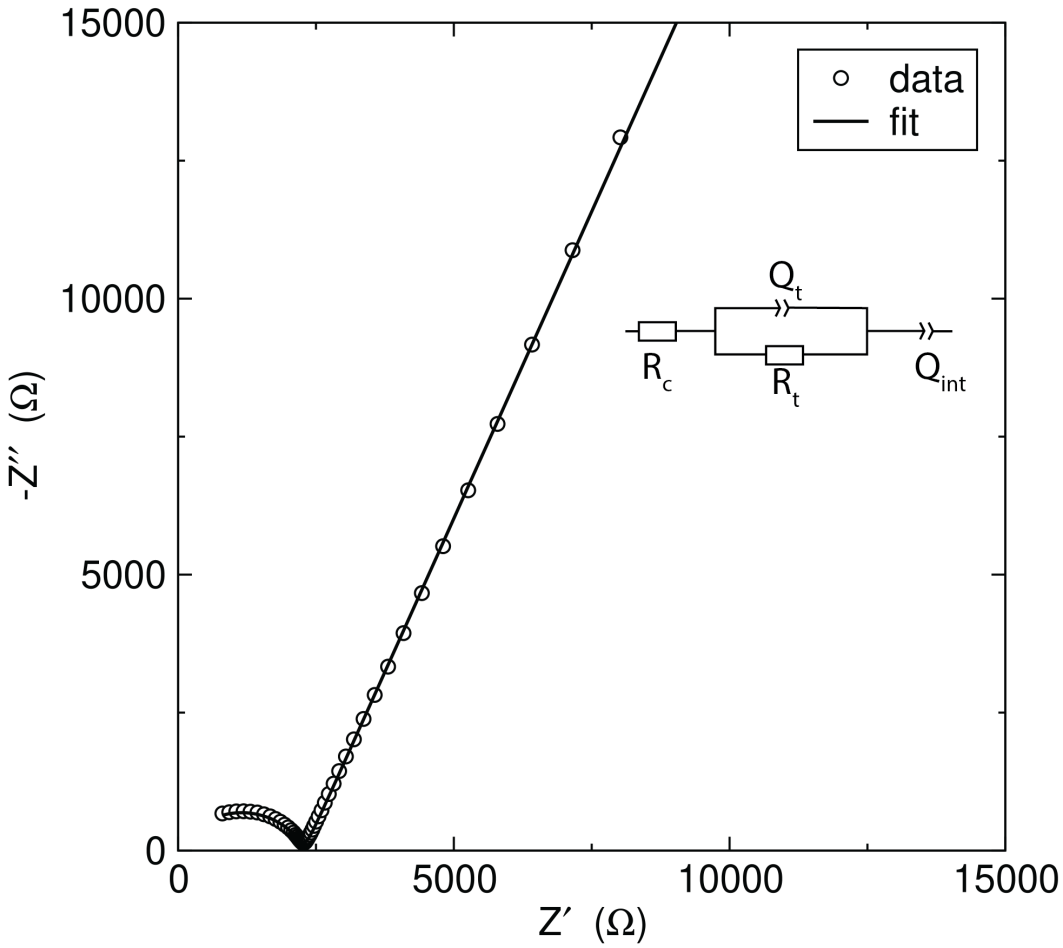

Figure B.15: Representative fit of Nyquist plots of $MnPS_3$-based Mg exchanged compound at 30 ° C. This is an example of a situation where the high frequency feature of the Nyquist plot is resolved. It is fit with an equivalent circuit consisting of a resistor (R_c) in series with a RQ circuit (resistor, R_t, in parallel with a constant phase element, Q_t) in series with an additional Q_{int}. This model is comprised of a resistor (R_c) in series with a RQ circuit (a resistor, R_t, in parallel with a constant phase element, Q_t) followed in series with a second constant phase element, Q_{int}. Here, R_c represents the circuit resistance and is typically near zero, R_t and Q_t are measures of the total electrolyte resistance and capacitance, while Q_{int} represents the capacitive charge buildup at the interface of the solid electrolyte and the ion-blocking electrode. The capacitance values of the high frequency feature (10^{-10}–10^{-9} F) are in line with those expected for solid state ionic conduction.[49, 54, 81, 233] Therefore, the high frequency feature is attributed to total ionic conduction through the pellet — a combination of bulk and grain boundary contributions.

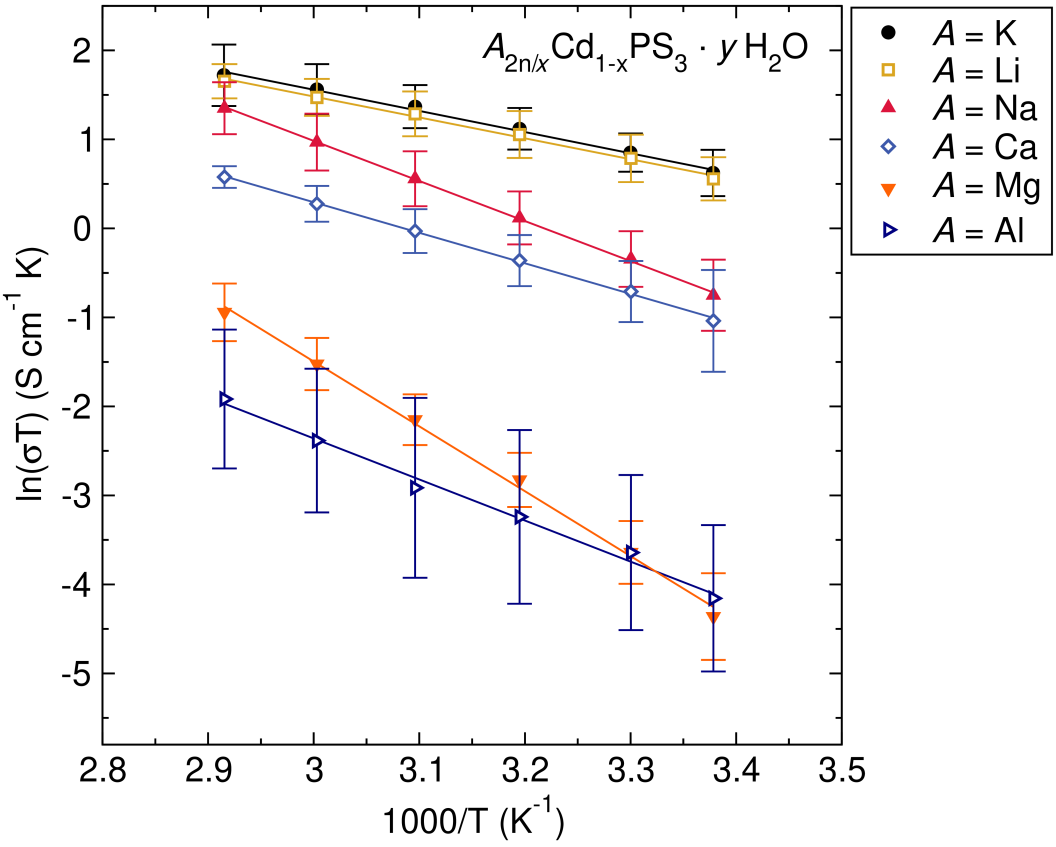

Figure B.16: Arrhenius-type plots of $CdPS_3$-based ion intercalated materials at ambient RH. The plotted points are the mean of at least three replicate cells, and the error bars represent the associated standard deviations.

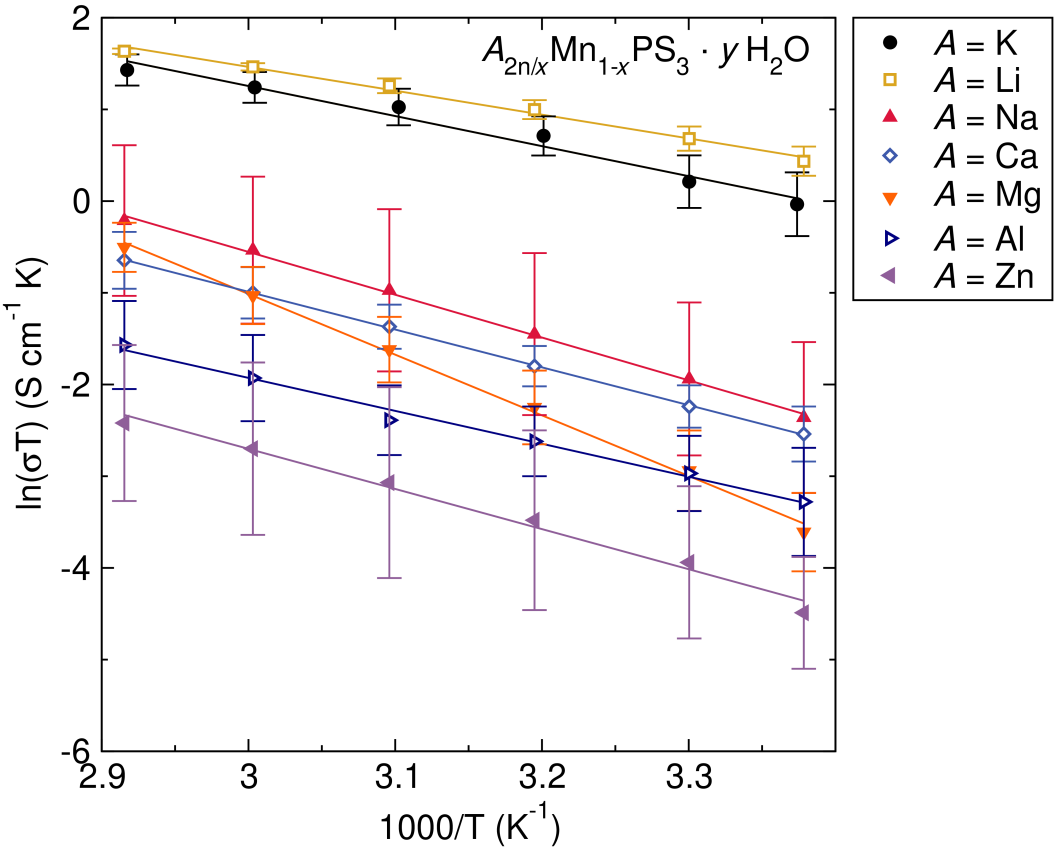

Figure B.17: Arrhenius-type plots of $MnPS_3$-based ion intercalated materials at ambient RH. The plotted points are the mean of at least three replicate cells, and the error bars represent the associated standard deviations.

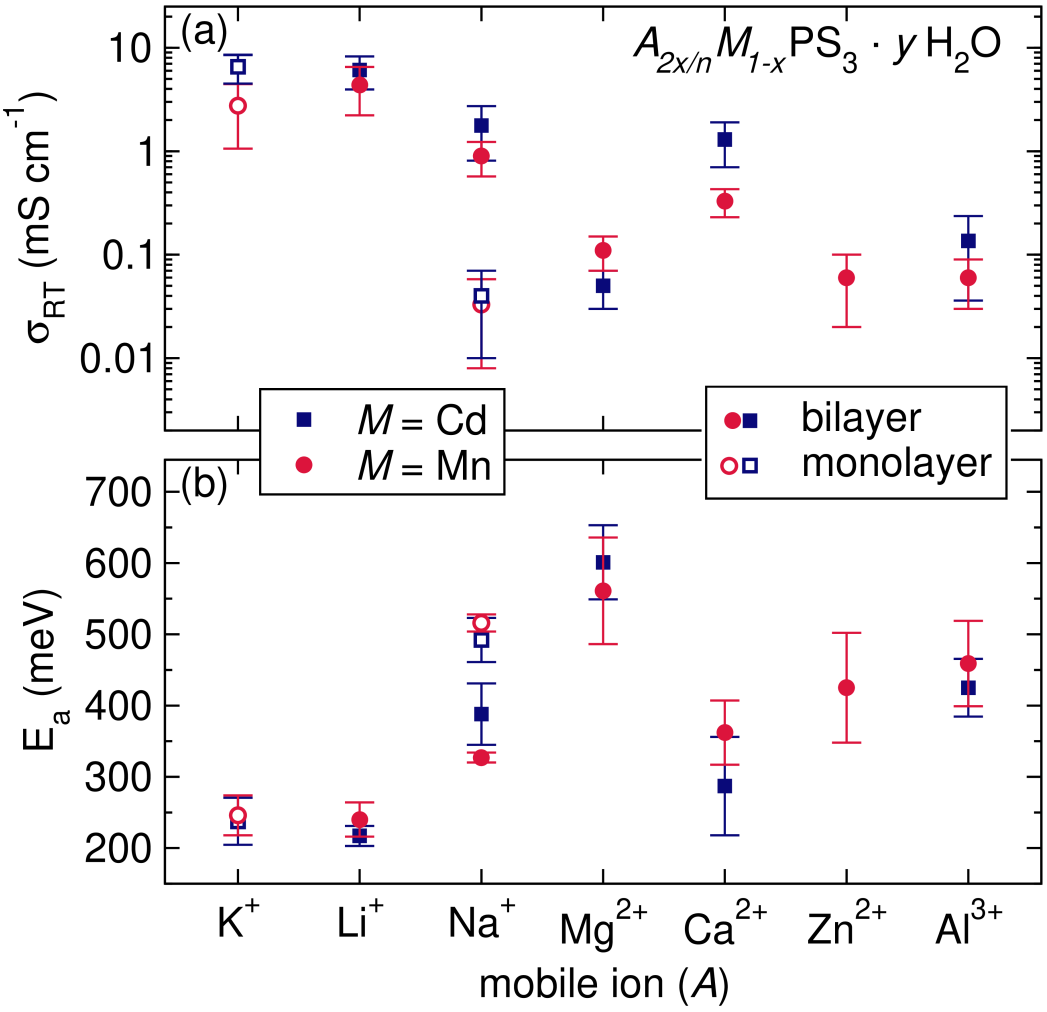

Figure B.18: (a) The σ_{RT} and (b) E_a of the ion-intercalated MPS$_3$ materials. The electrochemical behaviors of the isolated monolayer and bilayer Na-intercalated materials are shown here, in comparison to the other materials at ambient RH. The bilayer and monolayer MnPS$_3$-based Na intercalated compounds were isolated by equilibration at 75% and 11% RH, respectively. The monolayer CdPS$_3$-based Na intercalated compound was obtained via equilibration at 11% RH. Here, it is evident that the bilayer MnPS$_3$-based Na compound behavior is more in line with that of the bilayer CdPS$_3$-based Na compound at ambient RH. Additionally, the monolayer compounds follow the same trend as the bilayer compounds, where the more charge dense Na^+ perform worse than the less charge dense K^+ in the intercalated compounds.

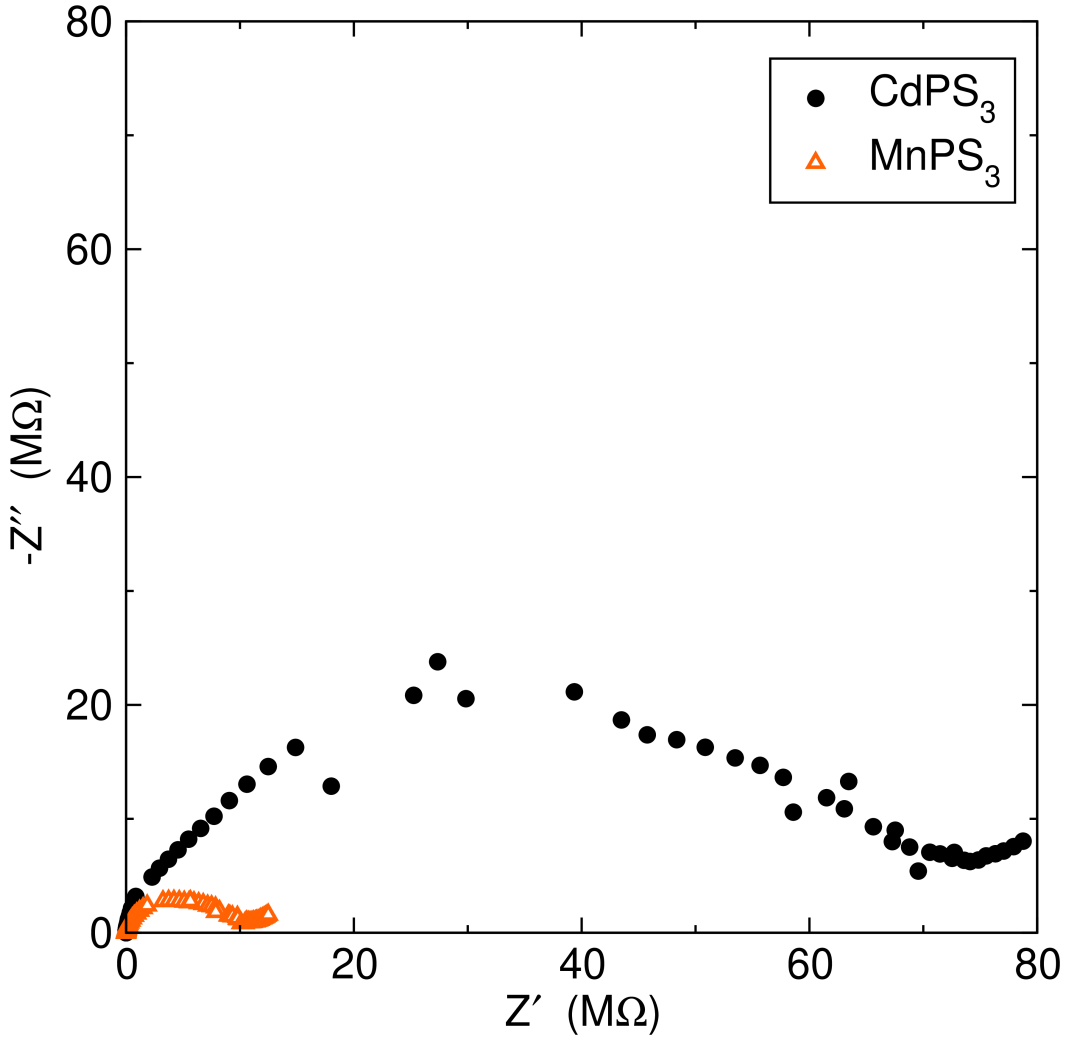

Figure B.19: Nyquist plots of pristine MPS_3 materials at room temperature after equilibration at ambient RH for several days. These materials were measured as a *in situ* pellet in PTFE Swagelok cells with stainless steel plungers as the electrodes to avoid water loss via evacuation.

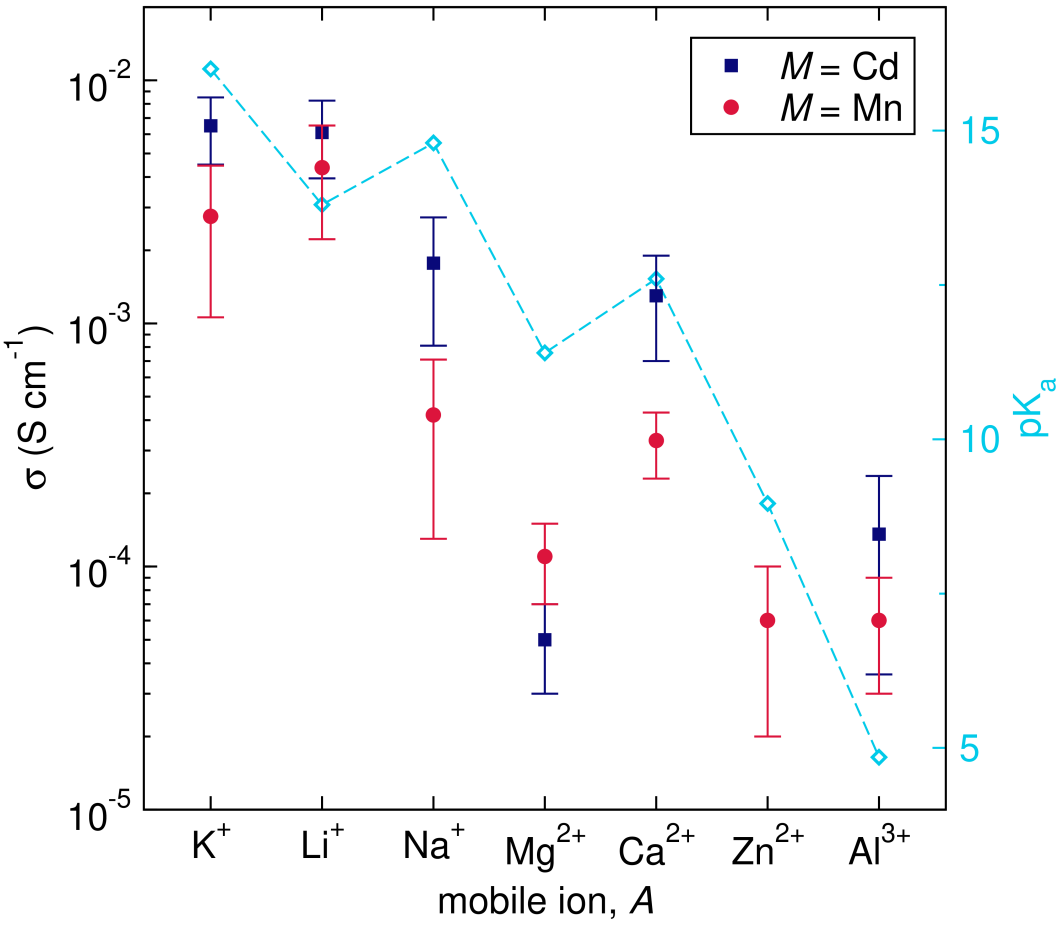

Figure B.20: The σ_{RT} of the ion-intercalated MPS$_3$ compounds at ambient RH overlaid with the pK$_a$ of the intercalated ions based on their behavior in aqueous solutions. The ions with the lower pK$_a$ (the more charge dense ions) would have more H$^+$ from hydrolysis of the coordinated water.

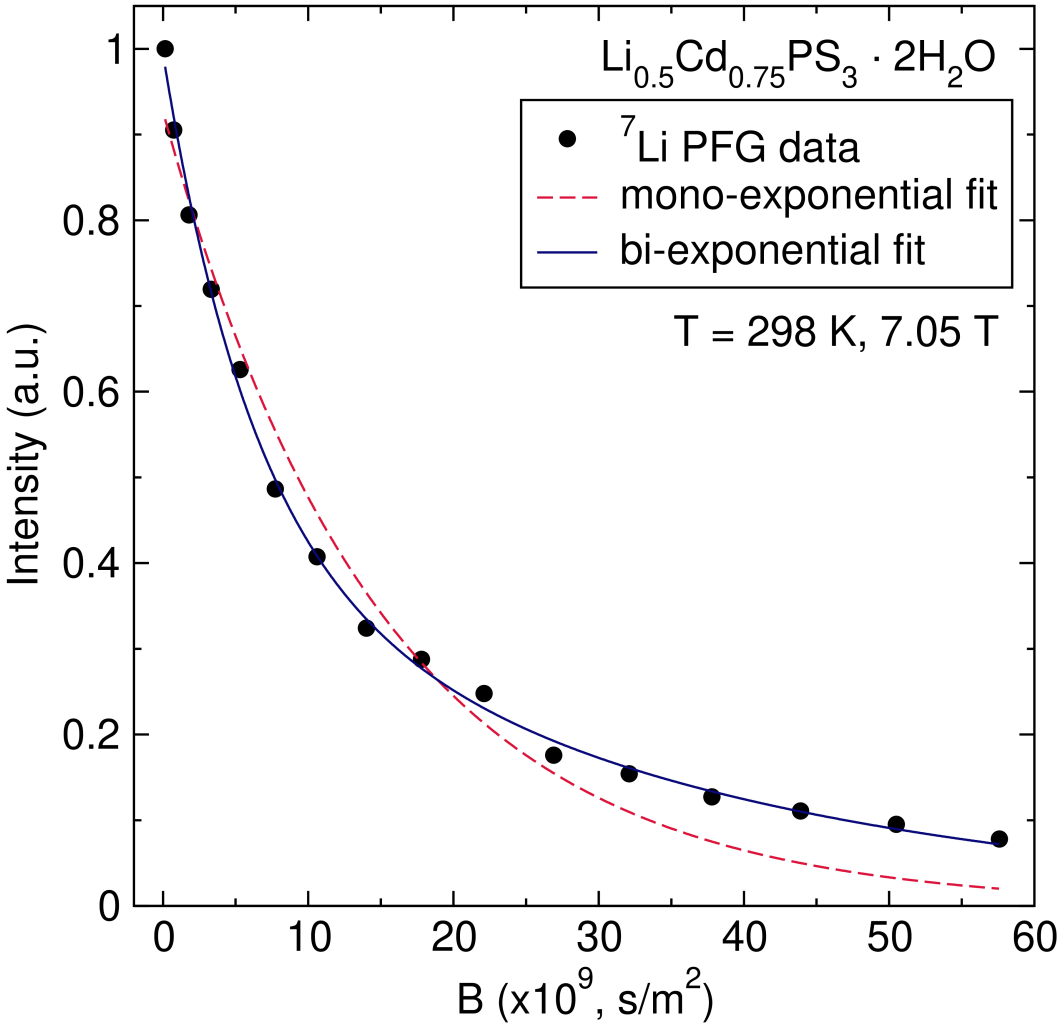

Figure B.21: ^{7}Li PFG NMR data at room temperature which is better fit by a bi-exponential than a mono-exponential function. This is representative of ^{7}Li PFG NMR and ^{1}H PFG NMR at all temperatures measure (up to 60 °C).

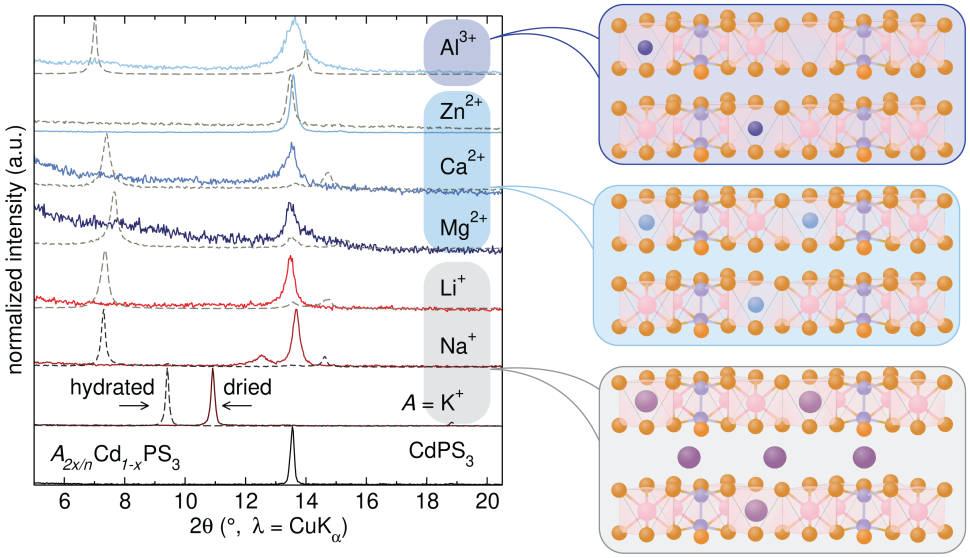

Figure B.22: XRD patterns of hydrated and dried $CdPS_3$ ion-exchanged compounds. Illustrations of the dried structures containing monovalent, divalent, or trivalent ions are shown.

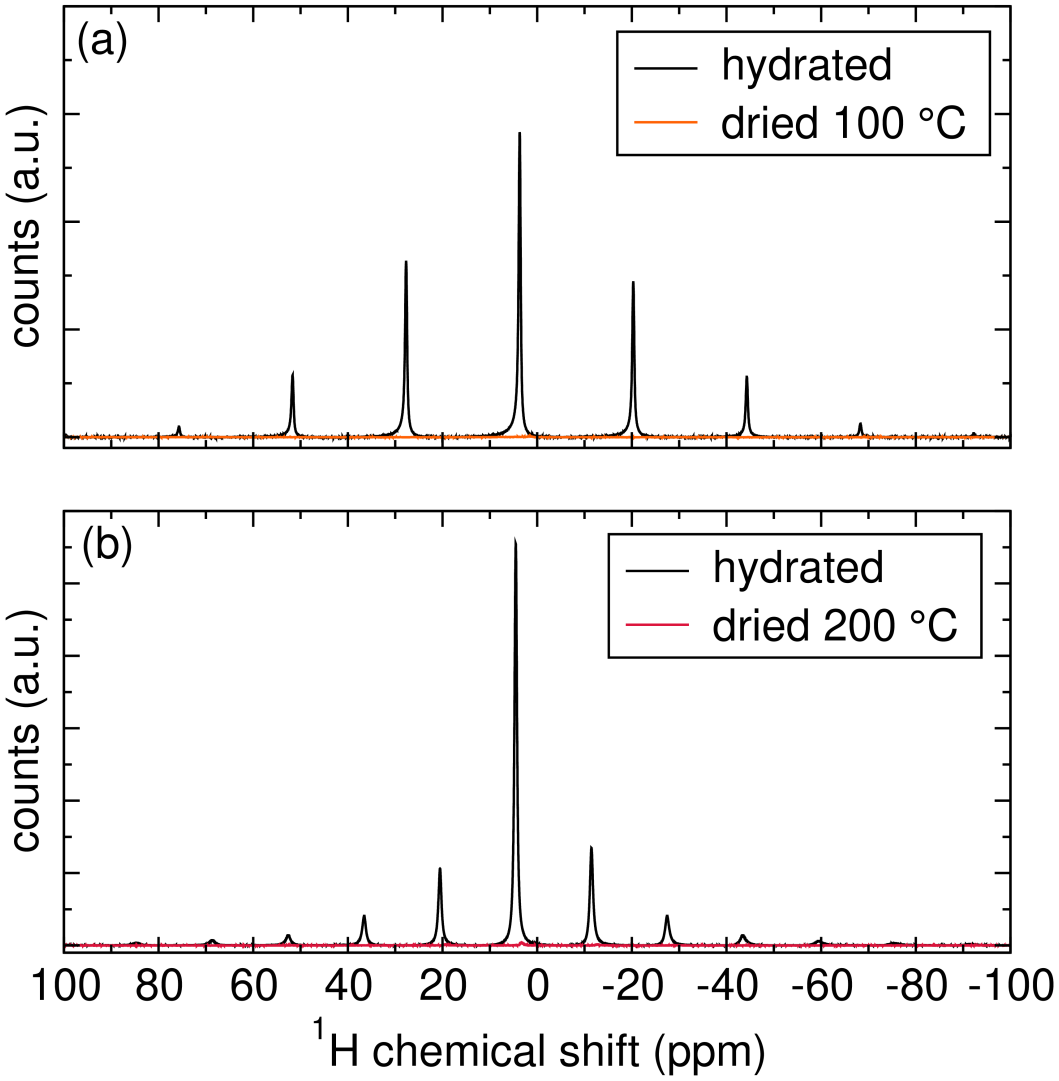

Figure B.23: Examples of ^{1}H MAS NMR before and after the different drying conditions used in this study. (a) $K_{0.5}Cd_{0.75}PS_3$ at ambient RH and dried at 100 ° C and (b) $Li_{0.5}Cd_{0.75}PS_3$ at ambient RH and dried at 200 ° C, < 1% of the H signal remains after drying.

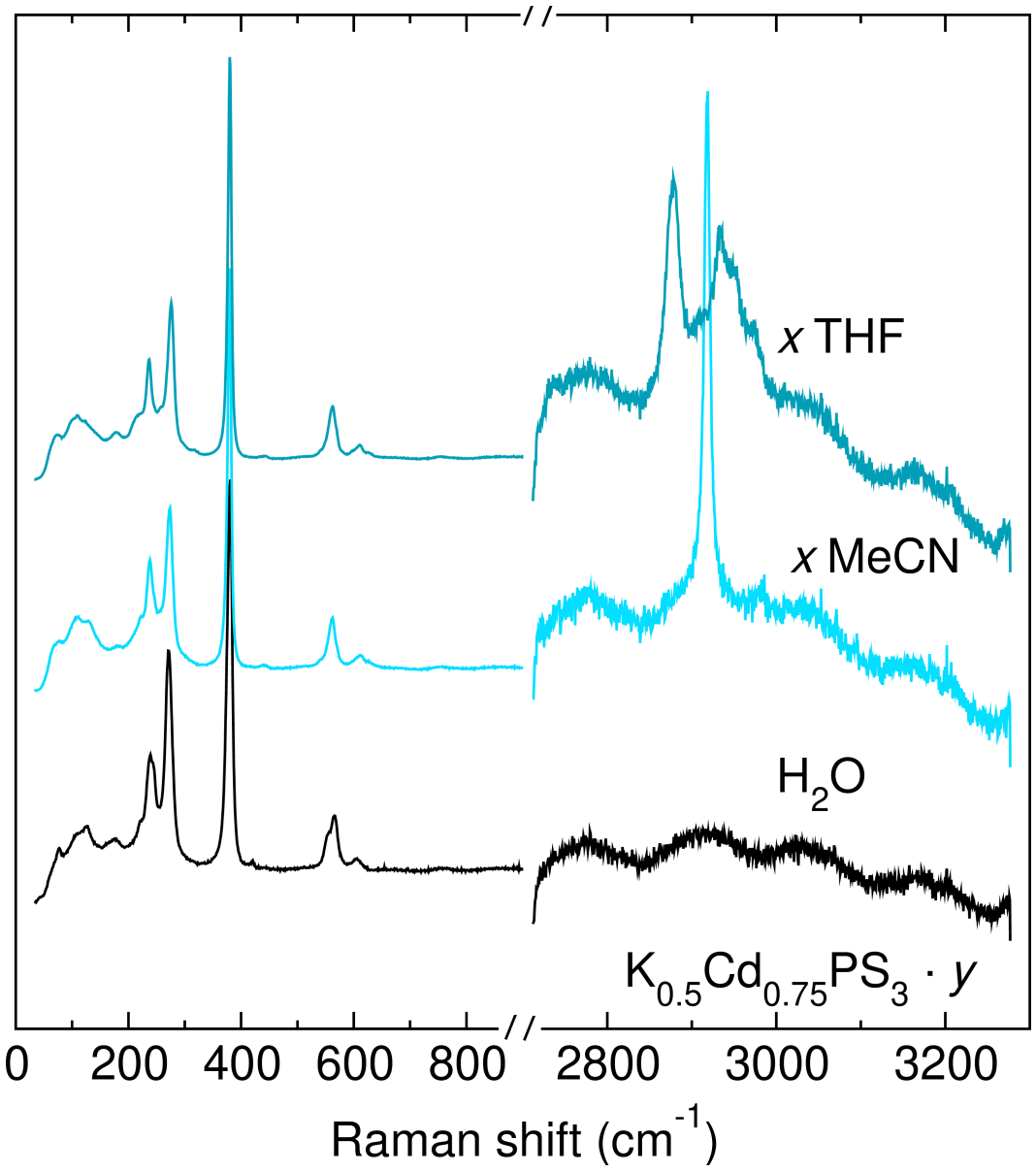

Figure B.24: Raman spectra of hydrated and ligand-exchanged $K_{0.5}Cd_{0.75}PS_3$ from 50-850 and 2700-3300 wavenumbers. The low Raman shift region suggests that no obvious changes to the local structure occurs in the metal layer after ligand exchange – the modes associated with the P_2S_6 polyanions are maintained. The high frequency region shows that the characteristic modes of the MeCN and THF ligands are present after ligand exchange.

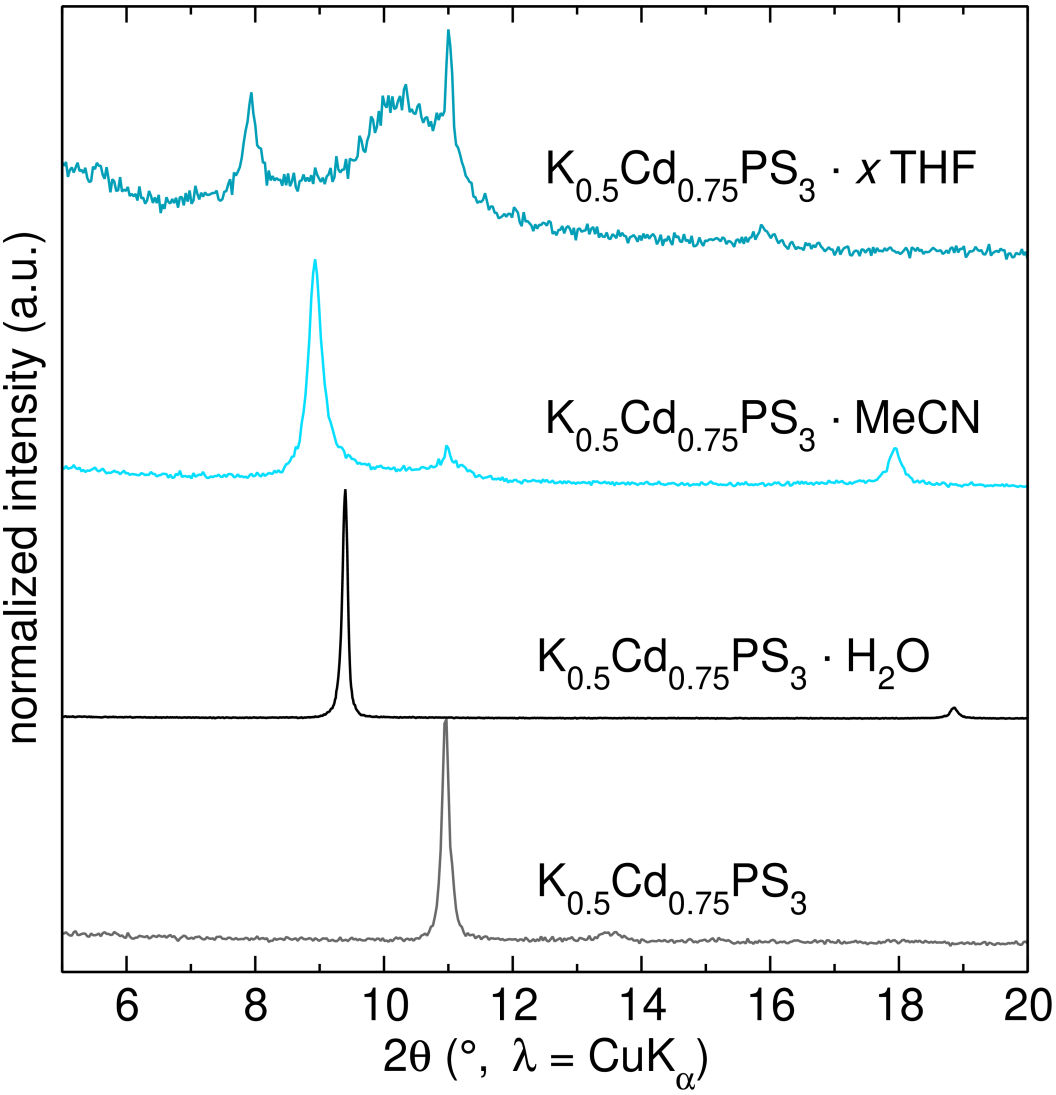

Figure B.25: XRD patterns of $K_{0.5}Cd_{0.75}PS_3$ in the dried and hydrated state and after ligand exchange with MeCN and THF. The reflection corresponding the hydrated phase is absent after the ligand exchange, but the reflection corresponding to the dried material is present because the exchanged ligands are very volatile and some of the absorbed THF or MeCN ligands was lost during the preparation of the samples.

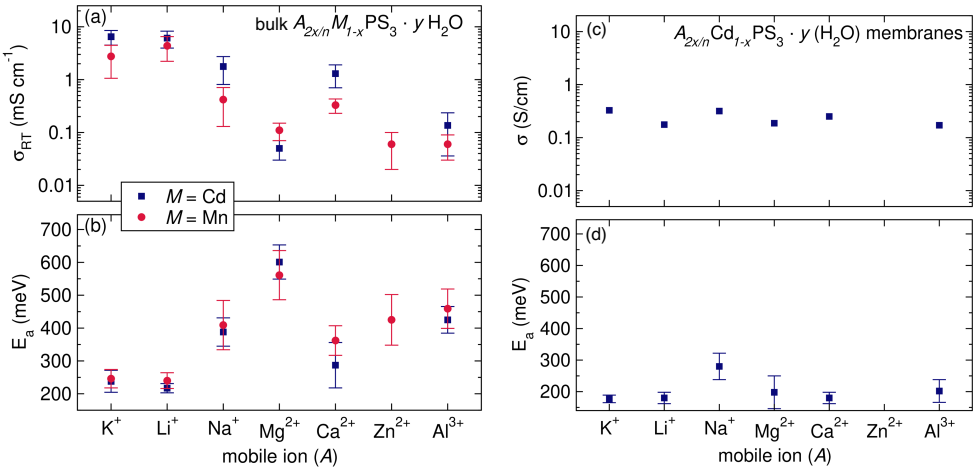

Figure B.26: A comparison of (a) the ionic σ_{RT} and (b) E_a of the ligand-assisted ionic conduction in bulk, polycrystalline MPS$_3$ materials investigated in this study (left) with that of the recently published CdPS$_3$-based membranes by Yu and Ren (right), which likely represents ionic conduction in a confined liquid electrolyte. Here, the data from their study is plotted on a comparable scale to that of this study. The electrochemical performance of the bulk, polycrystalline materials at ambient RH has a much stronger dependence on the identity of the intercalated ion than that of the membranes at high RH.

Material	σ_{RT} **(mS cm^{-1})**	$\sigma_{70^\circ C}$ **(mS cm^{-1})**	$\mathbf{E}_a$ **(meV)**
Hydrated samples			
$K_{0.5}Cd_{0.75}PS_3 \cdot H_2O$	6.5 ± 2.0	19.6 ± 8.3	238 ± 34
$Li_{0.5}Cd_{0.75}PS_3 \cdot 2\ H_2O$	6.1 ± 2.2	15.5 ± 4.1	217 ± 14
$Na_{0.5}Cd_{0.75}PS_3 \cdot 2\ H_2O$	1.8 ± 1.0	11.8 ± 4.2	388 ± 43
$Na_{0.5}Cd_{0.75}PS_3 \cdot H_2O$	0.04 ± 0.03	0.59 ± 0.08	492 ± 31
$Mg_{0.25}Cd_{0.75}PS_3 \cdot 2\ H_2O$	0.05 ± 0.02	1.19 ± 0.39	621 ± 68
$Ca_{0.25}Cd_{0.75}PS_3 \cdot 2\ H_2O$	1.3 ± 0.6	5.5 ± 2.2	287 ± 69
$Al_{0.167}Cd_{0.75}PS_3 \cdot 2.3\ H_2O$	0.16 ± 0.15	0.88 ± 0.73	425 ± 41
$K_{0.4}Mn_{0.8}PS_3 \cdot 0.8\ H_2O$	2.8 ± 1.7	12.8 ± 3.6	246 ± 28
$Li_{0.4}Mn_{0.8}PS_3 \cdot 1.4\ H_2O$	4.4 ± 2.2	15.0 ± 3.6	241 ± 24
$Na_{0.6}Mn_{0.7}PS_3 \cdot 1.7\ H_2O$	0.4 ± 0.3	3.1 ± 2.0	409 ± 76
$Na_{0.6}Mn_{0.7}PS_3 \cdot H_2O$	0.03 ± 0.025	0.56 ± 0.24	517 ± 12
$Mg_{0.2}Mn_{0.8}PS_3 \cdot 1.8\ H_2O$	0.10 ± 0.05	1.8 ± 0.6	551 ± 69
$Ca_{0.25}Mn_{0.75}PS_3 \cdot 1.5\ H_2O$	0.29 ± 0.11	1.8 ± 0.5	362 ± 45
$Zn_{0.4}Mn_{0.6}PS_3 \cdot 1.6\ H_2O$	0.04 ± 0.02	0.026 ± 0.013	423 ± 28
$Al_{0.13}Mn_{0.8}PS_3 \cdot 2.2\ H_2O$	0.06 ± 0.03	0.23 ± 0.25	460 ± 61
Dried samples			
$Li_{0.5}Cd_{0.75}PS_3$	$(1.3 \pm 0.8) \times 10^{-3}$	$(1.0 \pm 1.1) \times 10^{-2}$	519 ± 17
$Na_{0.5}Cd_{0.75}PS_3$	$(1.6 \pm 1.5) \times 10^{-5}$	$(6.8 \pm 9.4) \times 10^{-4}$	659 ± 53
$K_{0.5}Cd_{0.75}PS_3$	$(3.5 \pm 1.4) \times 10^{-6}$	$(9.1 \pm 3.8) \times 10^{-5}$	667 ± 44
Ligand Exchange			
$K_{0.5}Cd_{0.75}PS_3 \cdot MeCN$	0.18 ± 0.16	0.51 ± 0.47	281 ± 104
$K_{0.5}Cd_{0.75}PS_3 \cdot THF$	$(6.8 \pm 4.2) \times 10^{-4}$	$(3.4 \pm 3.0) \times 10^{-3}$	423 ± 39

Table B.1: The mean and standard deviation of conductivity at RT and 70 ° C, and activation energy of the ion-intercalated MPS$_3$ materials in this study.

mobile ion, A	chemical shift (ppm)	FWHM (Hz)	sample conditions
^{1}H NMR			
K	3.87	1807	hydrated
Li	4.48	487	hydrated
Na	4.18	257	hydrated
Mg	5.28	513	hydrated
Ca	4.85	197	hydrated
Al	6.1	960	hydrated
^{7}Li NMR			
Li	-0.08	68	hydrated
Li	0.18	122	dried
^{23}Na NMR			
Na	1.35	108	hydrated
Na	-0.7	285	dried, peak 1 (50%)
Na	27.7	233	dried, peak 2 (50%)
^{27}Al NMR			
Al	-1.47	1252	hydrated
Al	36	1525	dried

Table B.2: ^{1}H, ^{7}Li, ^{23}Na, and ^{27}Al MAS NMR data for various mobile ions in $CdPS_3$-based intercalation compounds under different conditions.

BIBLIOGRAPHY

(1) Masson-Delmotte, V. et al. Global Warming of 1.5 °C: IPCC Special Report on Impacts of Global Warming of 1.5 °C Above Pre-Industrial Levels in Context of Strengthening Response to Climate Change, Sustainable Development, and Efforts to Eradicate Poverty. *Cambridge University Press* **2022**.

(2) Barbir, F.; Veziroğlu, T.; Plass, H. Environmental Damage Due to Fossil Fuels Use. *International Journal of Hydrogen Energy* **1990**, *15*, 739–749.

(3) Dincer, I. Renewable Energy and Sustainable Development: A Crucial Review. *Renewable and Sustainable Energy Reviews* **2000**, *4*, 157–175.

(4) Kalair, A.; Abas, N.; Saleem, M. S.; Kalair, A. R.; Khan, N. Role of Energy Storage Systems in Energy Transition from Fossil Fuels to Renewables. *Energy Storage* **2021**, *3*, e135.

(5) Choi, D.; Shamim, N.; Crawford, A.; Huang, Q.; Vartanian, C. K.; Viswanathan, V. V.; Paiss, M. D.; Alam, M. J. E.; Reed, D. M.; Sprenkle, V. L. Li-Ion Battery Technology for Grid Application. *Journal of Power Sources* **2021**, *511*, 230419.

(6) Olivetti, E. A.; Ceder, G.; Gaustad, G. G.; Fu, X. Lithium-Ion Battery Supply Chain Considerations: Analysis of Potential Bottlenecks in Critical Metals. *Joule* **2017**, *1*, 229–243.

(7) Sun, X.; Hao, H.; Hartmann, P.; Liu, Z.; Zhao, F. Supply Risks of Lithium-Ion Battery Materials: An Entire Supply Chain Estimation. *Materials Today Energy* **2019**, *14*, 100347.

(8) Ziegler, M. S.; Mueller, Joshua M.; Pereira, G. D.; Song, J.; Ferrara, M.; Yet-Ming, C.; Trancik, J. E. Storage Requirements and Costs of Shaping Renewable Energy Toward Grid Decarbonization. *Joule* **2019**, *3*, 2134–2153.

(9) Faraday, M. XX. Experimental Researches in Electricity.— Fourth Series. *Philosophical Transactions of the Royal Society of London* **1833**, *123*, 507–522.

(10) Faraday, M. VII. Experimental Researches in Electricity. —Twelfth Series. *Philosophical Transactions of the Royal Society of London* **1838**, *128*, 83–123.

(11) Whittingham, M. S. Solid-State Ionics: The Key to the Discovery and Domination of Lithium Batteries: Some Learnings from β-Alumina and Titanium Disulfide. *MRS Bulletin* **2021**, *46*, 168–173.

(12) Wien 1864-1928., W. (; Fajans, K.; Ebert, L.; Tubandt, C., *Handbuch der experimentalphysik*; Akademische Verlagsgesellschaft: Leipzig, 1932.

(13) Tubandt, C.; Lorenz, E. Molekularzustand Und Elektrisches Leitvermögen Kristallisierter Salze. *Zeitschrift für Physikalische Chemie* **1914**, *87U*, 513–542.

(14) Takahashi, T. Solid Silver Ion Conductors. *Journal of Applied Electrochemistry* **1973**, *3*, 79–90.

(15) Owens, B. B.; Argue, G. R. High Conductivity Solid Electrolyte System Rbl-AgI. *J. Electrochem. Soc.* **1970**, *117*, 898.

(16) Yung-Fang Yu Yao; Kummer, J. Ion Exchange Properties of and Rates of Ionic Diffusion in Beta-Alumina. *Journal of Inorganic and Nuclear Chemistry* **1967**, *29*, 2453–2475.

(17) Kato, Y.; Hori, S.; Saito, T.; Suzuki, K.; Hirayama, M.; Mitsui, A.; Yonemura, M.; Iba, H.; Kanno, R. High-Power All-Solid-State Batteries Using Sulfide Superionic Conductors. *Nat Energy* **2016**, *1*, 16030.

(18) Kato, Y.; Shiotani, S.; Morita, K.; Suzuki, K.; Hirayama, M.; Kanno, R. All-Solid-State Batteries with Thick Electrode Configurations. *J. Phys. Chem. Lett.* **2018**, *9*, 607–613.

(19) Hu, Y.-S. Batteries: Getting Solid. *Nat Energy* **2016**, *1*, 16042.

(20) Jung, K.-N.; Shin, H.-S.; Park, M.-S.; Lee, J.-W. Solid-State Lithium Batteries: Bipolar Design, Fabrication, and Electrochemistry. *ChemElectroChem* **2019**, *6*, 3842–3859.

(21) Manthiram, A.; Yu, X.; Wang, S. Lithium Battery Chemistries Enabled by Solid-State Electrolytes. *Nat Rev Mater* **2017**, *2*, 16103.

(22) Bachman, J. C.; Muy, S.; Grimaud, A.; Chang, H.-H.; Pour, N.; Lux, S. F.; Paschos, O.; Maglia, F.; Lupart, S.; Lamp, P.; Giordano, L.; Shao-Horn, Y. Inorganic Solid-State Electrolytes for Lithium Batteries: Mechanisms and Properties Governing Ion Conduction. *Chem. Rev.* **2016**, *116*, 140–162.

(23) Ohno, S.; Banik, A.; Dewald, G. F.; Kraft, M. A.; Krauskopf, T.; Minafra, N.; Till, P.; Weiss, M.; Zeier, W. G. Materials Design of Ionic Conductors for Solid State Batteries. *Prog. Energy* **2020**, *2*, 022001.

(24) Li, Z.; Liu, P.; Zhu, K.; Zhang, Z.; Si, Y.; Wang, Y.; Jiao, L. Solid-State Electrolytes for Sodium Metal Batteries. *Energy Fuels* **2021**, *35*, 9063–9079.

(25) Canepa, P.; Sai Gautam, G.; Hannah, D. C.; Malik, R.; Liu, M.; Gallagher, K. G.; Persson, K. A.; Ceder, G. Odyssey of Multivalent Cathode Materials: Open Questions and Future Challenges. *Chem. Rev.* **2017**, *117*, 4287–4341.

(26) Johnson, I. D.; Ingram, B. J.; Cabana, J. The Quest for Functional Oxide Cathodes for Magnesium Batteries: A Critical Perspective. *ACS Energy Lett.* **2021**, *6*, 1892–1900.

(27) Jaschin, P. W.; Gao, Y.; Li, Y.; Bo, S.-H. A Materials Perspective on Magnesium-Ion-Based Solid-State Electrolytes. *J. Mater. Chem. A* **2020**, *8*, 2875–2897.

(28) Rong, Z.; Malik, R.; Canepa, P.; Sai Gautam, G.; Liu, M.; Jain, A.; Persson, K.; Ceder, G. Materials Design Rules for Multivalent Ion Mobility in Intercalation Structures. *Chem. Mater.* **2015**, *27*, 6016–6021.

(29) Nestler, T.; Meutzner, F.; Kabanov, A. A.; Zschornak, M.; Leisegang, T.; Meyer, D. C. Combined Theoretical Approach for Identifying Battery Materials: Al^{3+} Mobility in Oxides. *Chem. Mater.* **2019**, *31*, 737–747.

(30) Aubrey, M. L.; Ameloot, R.; Wiers, B. M.; Long, J. R. Metal–Organic Frameworks as Solid Magnesium Electrolytes. *Energy Environ. Sci.* **2014**, *7*, 667.

(31) Schauser, N. S.; Seshadri, R.; Segalman, R. A. Multivalent Ion Conduction in Solid Polymer Systems. *Mol. Syst. Des. Eng.* **2019**, *4*, 263–279.

(32) Farrington, G. Divalent Beta″-Aluminas: High Conductivity Solid Electrolytes for Divalent Cations. *Solid State Ionics* **1982**, *7*, 267–281.

(33) Semkow, K. W.; Sammells, A. F. Ionic and Electronic Conductivity Measurements on Polycrystalline Calcium Conducting β''-Alumina. *J. Electrochem. Soc.* **1988**, *135*, 244–247.

(34) Nomura, K.; Ikeda, S.; Ito, K.; Einaga, H. Framework Structure, Phase Transition, and Transport Properties in $M^{II} Zr_4 (PO_4)_6$ Compounds (M^{II} = Mg, Ca, Sr, Ba, Mn, Co, Ni, Zn, Cd, and Pb). *BCSJ* **1992**, *65*, 3221–3227.

(35) Nomura, K.; Ikeda, S.; Ito, K.; Einaga, H. Framework Structure, Phase Transition, and Transport Properties in $M^{II} Zr_4 (PO_4)_6$ Compounds (M^{II} = Mg, Ca, Sr, Ba, Mn, Co, Ni, Zn, Cd, and Pb). *BCSJ* **1992**, *65*, 3221–3227.

(36) Guin, M.; Tietz, F. Survey of the Transport Properties of Sodium Superionic Conductor Materials for Use in Sodium Batteries. *Journal of Power Sources* **2015**, *273*, 1056–1064.

(37) Ikeda, S.; Takahashi, M.; Ishikawa, J.; Ito, K. Solid Electrolytes with Multivalent Cation Conduction. 1. Conducting Species in MgZrPO4 System. *Solid State Ionics* **1987**, *23*, 125–129.

(38) Ikeda, S. Solid Electrolytes with Multivalent Cation Conduction (2) Zinc Ion Conduction in Zn$z.Sbnd;Zr$z.Sbnd;PO4 System. *Solid State Ionics* **1990**, *40–41*, 79–82.

(39) Tamura, S.; Yamane, M.; Hoshino, Y.; Imanaka, N. Highly Conducting Divalent Mg2+ Cation Solid Electrolytes with Well-Ordered Three-Dimensional Network Structure. *Journal of Solid State Chemistry* **2016**, *235*, 7–11.

(40) Imanaka, N. Divalent Magnesium Ionic Conduction in the Magnesium Phosphate Based Composites. *Electrochem. Solid-State Lett.* **1999**, *3*, 327.

(41) Imanaka, N.; Okazaki, Y.; Adachi, G. Divalent Magnesium Ionic Conduction in Mg1-2x(Zr1-x Nbx)4P6O24 (x = 0-0.4) Solid Solutions. **2000**, 4.

(42) Nomura, K.; Ikeda, S.; Ito, K.; Einaga, H. Substitution Effect of Framework Constituents on Electrical Property of Solid Electrolytes with Beta -$Fe_2(SO_4)_3$-Type Structure, $M_{1+x}Zr_2P_{3-x}Si_xO_{12}$ (M = Li, 1/2Mg, and 1/2Zn). *Chem. Lett.* **1992**, *21*, 1897–1900.

(43) Ishihara, T.; Matsuda, H.; Takita, Y. Doped LaGaO3 Perovskite Type Oxide as a New Oxide Ionic Conductor. *J. Am. Chem. Soc.* **1994**, *116*, 3801–3803.

(44) FENG, M.; GOODENOUGH, J. B. A Superior Oxide-Ion Electrolyte. *Eur. j. solid state inorg. chem* **1994**, *31*, 663–672.

(45) Canepa, P.; Bo, S.-H.; Sai Gautam, G.; Key, B.; Richards, W. D.; Shi, T.; Tian, Y.; Wang, Y.; Li, J.; Ceder, G. High Magnesium Mobility in Ternary Spinel Chalcogenides. *Nat Commun* **2017**, *8*, 1759.

(46) Higashi, S.; Miwa, K.; Aoki, M.; Takechi, K. A Novel Inorganic Solid State Ion Conductor for Rechargeable Mg Batteries. *Chem. Commun.* **2014**, *50*, 1320–1322.

(47) Le Ruyet, R.; Berthelot, R.; Salager, E.; Florian, P.; Fleutot, B.; Janot, R. Investigation of $Mg(BH_4)(NH_2)$-Based Composite Materials with Enhanced Mg^{2+} Ionic Conductivity. *J. Phys. Chem. C* **2019**, *123*, 10756–10763.

(48) Le Ruyet, R.; Fleutot, B.; Berthelot, R.; Benabed, Y.; Hautier, G.; Filinchuk, Y.; Janot, R. $Mg_3(BH_4)_4(NH_2)_2$ as Inorganic Solid Electrolyte with High Mg^{2+} Ionic Conductivity. *ACS Appl. Energy Mater.* **2020**, *3*, 6093–6097.

(49) Kisu, K.; Kim, S.; Inukai, M.; Oguchi, H.; Takagi, S.; Orimo, S.-i. Magnesium Borohydride Ammonia Borane as a Magnesium Ionic Conductor. *ACS Appl. Energy Mater.* **2020**, *3*, 3174–3179.

(50) Burankova, T.; Roedern, E.; Maniadaki, A. E.; Hagemann, H.; Rentsch, D.; Łodziana, Z.; Battaglia, C.; Remhof, A.; Embs, J. P. Dynamics of the Coordination Complexes in a Solid-State Mg Electrolyte. *J. Phys. Chem. Lett.* **2018**, *9*, 6450–6455.

(51) Yan, Y.; Dononelli, W.; Jørgensen, M.; Grinderslev, J. B.; Lee, Y.-S.; Cho, Y. W.; Černý, R.; Hammer, B.; Jensen, T. R. The Mechanism of Mg^{2+} Conduction in Ammine Magnesium Borohydride Promoted by a Neutral Molecule. *Phys. Chem. Chem. Phys.* **2020**, *22*, 9204–9209.

(52) Yan, Y.; Grinderslev, J. B.; Jørgensen, M.; Skov, L. N.; Skibsted, J.; Jensen, T. R. Ammine Magnesium Borohydride Nanocomposites for All-Solid-State Magnesium Batteries. *ACS Appl. Energy Mater.* **2020**, *3*, 9264–9270.

(53) Tomita, Y.; Saito, R.; Morishita, M.; Yamane, Y.; Kohno, Y. Synthesis, Crystal Structure and Ionic Conductivity of MgAl2X8 (X = Cl, Br). *Solid State Ionics* **2021**, *361*, 115566.

(54) Martinolich, A. J.; Lee, C.-W.; Lu, I.-T.; Bevilacqua, S. C.; Preefer, M. B.; Bernardi, M.; Schleife, A.; See, K. A. Solid-State Divalent Ion Conduction in $ZnPS_3$. *Chem. Mater.* **2019**, *31*, 3652–3661.

(55) Murch, G. The Haven Ratio in Fast Ionic Conductors. *Solid State Ionics* **1982**, *7*, 177–198.

(56) Gao, Y.; Nolan, A. M.; Du, P.; Wu, Y.; Yang, C.; Chen, Q.; Mo, Y.; Bo, S.-H. Classical and Emerging Characterization Techniques for Investigation of Ion Transport Mechanisms in Crystalline Fast Ionic Conductors. *Chem. Rev.* **2020**, *120*, 5954–6008.

(57) Adeli, P.; Bazak, J. D.; Park, K. H.; Kochetkov, I.; Huq, A.; Goward, G. R.; Nazar, L. F. Superionic Argyrodites by Halide Substitution. *Angew. Chem. Int. Ed.* **2019**, 20.

(58) Balluffi, R. W.; Allen, S. M.; Carter, W. C.; Kemper, R. A., *Kinetics of Materials*; J. Wiley & Sons: Hoboken, N.J, 2005.

(59) Murch, G. E. The Nernst-Einstein Equation in High-Defect-Content Solids. *Philosophical Magazine A* **1982**, *45*, 685–692.

(60) Murch, G. E. In *Phase Transformations in Materials*, Kostorz, G., Ed.; Wiley-VCH Verlag GmbH & Co. KGaA: Weinheim, FRG, 2005, pp 171–238.

(61) Friauf, R. J. Diffusion of Silver in Silver Bromide and Evidence for Interstitialcy Migration. *Phys. Rev.* **1957**, *105*, 843–848.

(62) Imre, Á. W.; Staesche, H.; Voss, S.; Ingram, M. D.; Funke, K.; Mehrer, H. Pressure-Dependent Diffusion Coefficients and Haven Ratios in Cation-Conducting Glasses. *J. Phys. Chem. B* **2007**, *111*, 5301–5307.

(63) Sai Gautam, G.; Canepa, P.; Urban, A.; Bo, S.-H.; Ceder, G. Influence of Inversion on Mg Mobility and Electrochemistry in Spinels. *Chem. Mater.* **2017**, *29*, 7918–7930.

(64) Krauskopf, T.; Muy, S.; Culver, S. P.; Ohno, S.; Delaire, O.; Shao-Horn, Y.; Zeier, W. G. Comparing the Descriptors for Investigating the Influence of Lattice Dynamics on Ionic Transport Using the Superionic Conductor $Na_3PS_{4-x}Se_x$. *J. Am. Chem. Soc.* **2018**, *140*, 14464–14473.

(65) Culver, S. P.; Koerver, R.; Krauskopf, T.; Zeier, W. G. Designing Ionic Conductors: The Interplay between Structural Phenomena and Interfaces in Thiophosphate-Based Solid-State Batteries. *Chem. Mater.* **2018**, *30*, 4179–4192.

(66) Boyce, J.; Huberman, B. Superionic Conductors: Transitions, Structures, Dynamics. *Physics Reports* **1979**, *51*, 189–265.

(67) Dietrich, C.; Sadowski, M.; Sicolo, S.; Weber, D. A.; Sedlmaier, S. J.; Weldert, K. S.; Indris, S.; Albe, K.; Janek, J.; Zeier, W. G. Local Structural Investigations, Defect Formation, and Ionic Conductivity of the Lithium Ionic Conductor $Li_4P_2S_6$. *Chem. Mater.* **2016**, *28*, 8764–8773.

(68) Muy, S.; Bachman, J. C.; Chang, H.-H.; Giordano, L.; Maglia, F.; Lupart, S.; Lamp, P.; Zeier, W. G.; Shao-Horn, Y. Lithium Conductivity and Meyer-Neldel Rule in Li_3PO_4–Li_3VO_4–Li_4GeO_4 Lithium Superionic Conductors. *Chem. Mater.* **2018**, *30*, 5573–5582.

(69) Kim, K.; Siegel, D. J. Multivalent Ion Transport in Anti-Perovskite Solid Electrolytes. *Chem. Mater.* **2021**, *33*, 2187–2197.

(70) Famprikis, T.; Canepa, P.; Dawson, J. A.; Islam, M. S.; Masquelier, C. Fundamentals of Inorganic Solid-State Electrolytes for Batteries. *Nat. Mater.* **2019**, *18*, 1278–1291.

(71) Almond, D.; West, A. Entropy Effects in Ionic Conductivity. *Solid State Ionics* **1986**, *18–19*, 1105–1109.

(72) Meyer, W.; Neldel, H. Relation between the Energy Constant and the Quantity Constant in the Conductivity–Temperature Formula of Oxide Semiconductors. *Z. tech. Phys* **1937**, *18*, 588–593.

(73) Yelon, A.; Movaghar, B.; Branz, H. M. Origin and Consequences of the Compensation (Meyer-Neldel) Law. *Phys. Rev. B* **1992**, *46*, 12244–12250.

(74) Kraft, M. A.; Culver, S. P.; Calderon, M.; Böcher, F.; Krauskopf, T.; Senyshyn, A.; Dietrich, C.; Zevalkink, A.; Janek, J.; Zeier, W. G. Influence of Lattice Polarizability on the Ionic Conductivity in the Lithium Superionic Argyrodites Li_6PS_5X (X = Cl, Br, I). *J. Am. Chem. Soc.* **2017**, *139*, 10909–10918.

(75) Krauskopf, T.; Pompe, C.; Kraft, M. A.; Zeier, W. G. Influence of Lattice Dynamics on Na^+ Transport in the Solid Electrolyte $Na_3PS_{4-x}Se_x$. *Chem. Mater.* **2017**, *29*, 8859–8869.

(76) Gao, Y.; Li, N.; Wu, Y.; Yang, W.; Bo, S.-H. Rethinking the Design of Ionic Conductors Using Meyer–Neldel–Conductivity Plot. *Adv. Energy Mater.* **2021**, *11*, 2100325.

(77) He, X.; Zhu, Y.; Mo, Y. Origin of Fast Ion Diffusion in Super-Ionic Conductors. *Nat Commun* **2017**, *8*, 15893.

(78) Smith, J. G.; Siegel, D. J. Low-Temperature Paddlewheel Effect in Glassy Solid Electrolytes. *Nat Commun* **2020**, *11*, 1483.

(79) Lechner, R. Quasielastic Neutron Scattering and Super-Protonic Conductors. *Solid State Ionics* **1993**, *61*, 3–11.

(80) Karlsson, M.; Matic, A.; Engberg, D.; Björketun, M. E.; Koza, M. M.; Ahmed, I.; Wahnström, G.; Börjesson, L.; Eriksson, S.-G. Quasielastic Neutron Scattering of Hydrated BaZr0.90A0.10O2.95 (A=Y and Sc). *Solid State Ionics* **2009**, *180*, 22–28.

(81) Irvine, J. T. S.; Sinclair, D. C.; West, A. R. Electroceramics: Characterization by Impedance Spectroscopy. *Adv. Mater.* **1990**, *2*, 132–138.

(82) Hui, J.; Gossage, Z. T.; Sarbapalli, D.; Hernández-Burgos, K.; Rodríguez-López, J. Advanced Electrochemical Analysis for Energy Storage Interfaces. *Anal. Chem.* **2019**, *91*, 60–83.

(83) Levi, M. D.; Aurbach, D. In *Characterization of Materials*, Kaufmann, E. N., Ed.; John Wiley & Sons, Inc.: Hoboken, NJ, USA, 2012, com125.

(84) McClelland, I.; Johnston, B.; Baker, P. J.; Amores, M.; Cussen, E. J.; Corr, S. A. Muon Spectroscopy for Investigating Diffusion in Energy Storage Materials. *Annu. Rev. Mater. Res.* **2020**, *50*, 371–393.

(85) Ohno, S. et al. How Certain Are the Reported Ionic Conductivities of Thiophosphate-Based Solid Electrolytes? An Interlaboratory Study. *ACS Energy Lett.* **2020**, *5*, 910–915.

(86) Kraft, M. A.; Ohno, S.; Zinkevich, T.; Koerver, R.; Culver, S. P.; Fuchs, T.; Senyshyn, A.; Indris, S.; Morgan, B. J.; Zeier, W. G. Inducing High Ionic Conductivity in the Lithium Superionic Argyrodites $Li_{6+x}P_{1-x}Ge_xS_5I$ for All-Solid-State Batteries. *J. Am. Chem. Soc.* **2018**, *140*, 16330–16339.

(87) Schlem, R.; Muy, S.; Prinz, N.; Banik, A.; Shao-Horn, Y.; Zobel, M.; Zeier, W. G. Mechanochemical Synthesis: A Tool to Tune Cation Site Disorder and Ionic Transport Properties of Li_3MCl_6 (M = Y, Er) Superionic Conductors. *Adv. Energy Mater.* **2020**, *10*, 1903719.

(88) Krasnikova, I. V.; Pogosova, M. A.; Sanin, A. O.; Stevenson, K. J. Toward Standardization of Electrochemical Impedance Spectroscopy Studies of Li-Ion Conductive Ceramics. *Chem. Mater.* **2020**, *32*, 2232–2241.

(89) Wang, L.-P.; Zhao-Karger, Z.; Klein, F.; Chable, J.; Braun, T.; Schür, A. R.; Wang, C.-R.; Guo, Y.-G.; Fichtner, M. MgSc2Se4 —A Magnesium Solid Ionic Conductor for All-Solid-State Mg Batteries? *ChemSusChem* **2019**, *12*, 2286–2293.

(90) Sears, V. F. Neutron Scattering Lengths and Cross Sections. *null* **1992**, *3*, 26–37.

(91) Deiss, E. Spurious Chemical Diffusion Coefficients of Li+ in Electrode Materials Evaluated with GITT. *Electrochimica Acta* **2005**, *50*, 2927–2932.

(92) Horner, J. S.; Whang, G.; Ashby, D. S.; Kolesnichenko, I. V.; Lambert, T. N.; Dunn, B. S.; Talin, A. A.; Roberts, S. A. Electrochemical Modeling of GITT Measurements for Improved Solid-State Diffusion Coefficient Evaluation. *ACS Appl. Energy Mater.* **2021**, acsaem.1c02218.

(93) Nickol, A.; Schied, T.; Heubner, C.; Schneider, M.; Michaelis, A.; Bobeth, M.; Cuniberti, G. GITT Analysis of Lithium Insertion Cathodes for Determining the Lithium Diffusion Coefficient at Low Temperature: Challenges and Pitfalls. *J. Electrochem. Soc.* **2020**, *167*, 090546.

(94) Kolli, S. K.; Van der Ven, A. Elucidating the Factors That Cause Cation Diffusion Shutdown in Spinel-Based Electrodes. *Chem. Mater.* **2021**, *33*, 6421–6432.

(95) Park, M. J.; Yaghoobnejad Asl, H.; Manthiram, A. Multivalent-Ion versus Proton Insertion into Battery Electrodes. *ACS Energy Lett.* **2020**, *5*, 2367–2375.

(96) Aurbach, D.; Lu, Z.; Schechter, A.; Gofer, Y.; Gizbar, H.; Turgeman, R.; Cohen, Y.; Moshkovich, M.; Levi, E. Prototype Systems for Rechargeable Magnesium Batteries. *Nature* **2000**, *407*, 724–727.

(97) Levi, E.; Levi, M. D.; Chasid, O.; Aurbach, D. A Review on the Problems of the Solid State Ions Diffusion in Cathodes for Rechargeable Mg Batteries. *J Electroceram* **2009**, *22*, 13–19.

(98) Thöle, F.; Wan, L. F.; Prendergast, D. Re-Examining the Chevrel Phase Mo $_6$ S $_8$ Cathode for Mg Intercalation from an Electronic Structure Perspective. *Phys. Chem. Chem. Phys.* **2015**, *17*, 22548–22551.

(99) Wan, L. F.; Wright, J.; Perdue, B. R.; Fister, T. T.; Kim, S.; Apblett, C. A.; Prendergast, D. Revealing Electronic Structure Changes in Chevrel Phase Cathodes upon Mg Insertion Using X-ray Absorption Spectroscopy. *Phys. Chem. Chem. Phys.* **2016**, *18*, 17326–17329.

(100) Yu, P.; Long, X.; Zhang, N.; Feng, X.; Fu, J.; Zheng, S.; Ren, G.; Liu, Z.; Wang, C.; Liu, X. Charge Distribution on S and Intercluster Bond Evolution in Mo $_6$ S $_8$ during the Electrochemical Insertion of Small Cations Studied by X-ray Absorption Spectroscopy. *J. Phys. Chem. Lett.* **2019**, *10*, 1159–1166.

(101) Sun, X.; Bonnick, P.; Duffort, V.; Liu, M.; Rong, Z.; Persson, K. A.; Ceder, G.; Nazar, L. F. A High Capacity Thiospinel Cathode for Mg Batteries. *Energy Environ. Sci.* **2016**, *9*, 2273–2277.

(102) Bonnick, P.; Blanc, L.; Vajargah, S. H.; Lee, C.-W.; Sun, X.; Balasubramanian, M.; Nazar, L. F. Insights into Mg^{2+} Intercalation in a Zero-Strain Material: Thiospinel $Mg_xZr_2S_4$. *Chem. Mater.* **2018**, 11.

(103) Sun, X.; Bonnick, P.; Nazar, L. F. Layered TiS_2 Positive Electrode for Mg Batteries. *ACS Energy Lett.* **2016**, *1*, 297–301.

(104) Emly, A.; Van der Ven, A. Mg Intercalation in Layered and Spinel Host Crystal Structures for Mg Batteries. *Inorg. Chem.* **2015**, *54*, 4394–4402.

(105) Nam, K. W. et al. The High Performance of Crystal Water Containing Manganese Birnessite Cathodes for Magnesium Batteries. *Nano Lett.* **2015**, *15*, 4071–4079.

(106) Song, J.; Noked, M.; Gillette, E.; Duay, J.; Rubloff, G.; Lee, S. B. Activation of a MnO_2 Cathode by Water-Stimulated Mg^{2+} Insertion for a Magnesium Ion Battery. *Phys. Chem. Chem. Phys.* **2015**, *17*, 5256–5264.

(107) Hyoung, J.; Heo, J. W.; Hong, S.-T. Investigation of Electrochemical Calcium-Ion Energy Storage Mechanism in Potassium Birnessite. *Journal of Power Sources* **2018**, *390*, 127–133.

(108) Lim, S.-C.; Lee, J.; Kwak, H. H.; Heo, J. W.; Chae, M. S.; Ahn, D.; Jang, Y. H.; Lee, H.; Hong, S.-T. Unraveling the Magnesium-Ion Intercalation Mechanism in Vanadium Pentoxide in a Wet Organic Electrolyte by Structural Determination. *Inorg. Chem.* **2017**, *56*, 7668–7678.

(109) Sa, N.; Wang, H.; Proffit, D. L.; Lipson, A. L.; Key, B.; Liu, M.; Feng, Z.; Fister, T. T.; Ren, Y.; Sun, C.-J.; Vaughey, J. T.; Fenter, P. A.; Persson, K. A.; Burrell, A. K. Is Alpha-V_2O_5 a Cathode Material for Mg Insertion Batteries? *Journal of Power Sources* **2016**, *323*, 44–50.

(110) Joos, M.; Schneider, C.; Münchinger, A.; Moudrakovski, I.; Usiskin, R.; Maier, J.; Lotsch, B. V. Impact of Hydration on Ion Transport in $Li_2Sn_2S_5{\cdot}xH_2O$. *J. Mater. Chem. A* **2021**, *9*, 16532–16544.

(111) Bruce, P. G.; Hardgrave, M. T.; Vincent, C. A. The Determination of Transference Numbers in Solid Polymer Electrolytes Using the Hittorf Method. *Solid State Ionics* **1992**, *53–56*, 1087–1094.

(112) Bruce, P. G.; Vincent, C. A. Steady State Current Flow in Solid Binary Electrolyte Cells. *Journal of Electroanalytical Chemistry and Interfacial Electrochemistry* **1987**, *225*, 1–17.

(113) Qian, X.; Chen, L.; Yin, L.; Liu, Z.; Pei, S.; Li, F.; Hou, G.; Chen, S.; Song, L.; Thebo, K. H.; Cheng, H.-M.; Ren, W. $CdPS_3$ Nanosheets-Based Membrane with High Proton Conductivity Enabled by Cd Vacancies. *Science* **2020**, *370*, 596–600.

(114) Park, S.; Kristanto, I.; Jung, G. Y.; Ahn, D. B.; Jeong, K.; Kwak, S. K.; Lee, S.-Y. A Single-Ion Conducting Covalent Organic Framework for Aqueous Rechargeable Zn-ion Batteries. *Chem. Sci.* **2020**, *11*, 11692–11698.

(115) Malik, R.; Burch, D.; Bazant, M.; Ceder, G. Particle Size Dependence of the Ionic Diffusivity. *Nano Lett.* **2010**, *10*, 4123–4127.

(116) Jaiswal, N.; Tanwar, K.; Suman, R.; Kumar, D.; Upadhyay, S.; Parkash, O. A Brief Review on Ceria Based Solid Electrolytes for Solid Oxide Fuel Cells. *Journal of Alloys and Compounds* **2019**, *781*, 984–1005.

(117) Omote, A.; Yotsuhashi, S.; Zenitani, Y.; Yamada, Y. High Ion Conductivity in MgHf(WO4)3 Solids with Ordered Structure: 1-D Alignments of Mg2+ and Hf4+ Ions. *Journal of the American Ceramic Society* **2011**, *94*, ed. by Edwards, D., 2285–2288.

(118) Yang, S.; Li, D.; Zhang, T.; Tao, Z.; Chen, J. First-Principles Study of Zigzag MoS $_2$ Nanoribbon As a Promising Cathode Material for Rechargeable Mg Batteries. *J. Phys. Chem. C* **2012**, *116*, 1307–1312.

(119) Liang, Y.; Yoo, H. D.; Li, Y.; Shuai, J.; Calderon, H. A.; Robles Hernandez, F. C.; Grabow, L. C.; Yao, Y. Interlayer-Expanded Molybdenum Disulfide Nanocomposites for Electrochemical Magnesium Storage. *Nano Lett.* **2015**, *15*, 2194–2202.

(120) Yin, L.; Kwon, B. J.; Choi, Y.; Bartel, C. J.; Yang, M.; Liao, C.; Key, B.; Ceder, G.; Lapidus, S. H. Operando X-ray Diffraction Studies of the Mg-Ion Migration Mechanisms in Spinel Cathodes for Rechargeable Mg-Ion Batteries. *J. Am. Chem. Soc.* **2021**, *143*, 10649–10658.

(121) Bonnick, P.; Sun, X.; Lau, K.-C.; Liao, C.; Nazar, L. F. Monovalent versus Divalent Cation Diffusion in Thiospinel Ti_2 S_4. *J. Phys. Chem. Lett.* **2017**, *8*, 2253–2257.

(122) Van der Ven, A.; Bhattacharya, J.; Belak, A. A. Understanding Li Diffusion in Li-Intercalation Compounds. *Acc. Chem. Res.* **2013**, *46*, 1216–1225.

(123) Roedern, E.; Kühnel, R.-S.; Remhof, A.; Battaglia, C. Magnesium Ethylenediamine Borohydride as Solid-State Electrolyte for Magnesium Batteries. *Sci Rep* **2017**, *7*, 46189.

(124) Muy, S.; Schlem, R.; Shao-Horn, Y.; Zeier, W. G. Phonon–Ion Interactions: Designing Ion Mobility Based on Lattice Dynamics. *Adv. Energy Mater.* **2021**, *11*, 2002787.

(125) Yoo, H. D. et al. Intercalation of Magnesium into a Layered Vanadium Oxide with High Capacity. *ACS Energy Lett.* **2019**, *4*, 1528–1534.

(126) Johnson, I. D.; Nolis, G.; McColl, K.; Wu, Y. A.; Thornton, D.; Hu, L.; Yoo, H. D.; Freeland, J. W.; Corà, F.; Cockcroft, J. K.; Parkin, I. P.; Klie, R. F.; Cabana, J.; Darr, J. A. Probing Mg Intercalation in the Tetragonal Tungsten Bronze Framework V $_4$ Nb $_{18}$ O $_{55}$. *Inorg. Chem.* **2020**, *59*, 9783–9797.

(127) Johnson, I. D.; Nolis, G.; Yin, L.; Yoo, H. D.; Parajuli, P.; Mukherjee, A.; Andrews, J. L.; Lopez, M.; Klie, R. F.; Banerjee, S.; Ingram, B. J.; Lapidus, S.; Cabana, J.; Darr, J. A. Enhanced Charge Storage of Nanometric ζ-V $_2$ O $_5$ in Mg Electrolytes. *Nanoscale* **2020**, *12*, 22150–22160.

(128) Verrelli, R.; Black, A.; Pattanathummasid, C.; Tchitchekova, D.; Ponrouch, A.; Oró-Solé, J.; Frontera, C.; Bardé, F.; Rozier, P.; Palacín, M. On the Strange Case of Divalent Ions Intercalation in V2O5. *Journal of Power Sources* **2018**, *407*, 162–172.

(129) Bayliss, R. D.; Key, B.; Sai Gautam, G.; Canepa, P.; Kwon, B. J.; Lapidus, S. H.; Dogan, F.; Adil, A. A.; Lipton, A. S.; Baker, P. J.; Ceder, G.; Vaughey, J. T.; Cabana, J. Probing Mg Migration in Spinel Oxides. *Chem. Mater.* **2020**, *32*, 663–670.

(130) Kwon, B. J. et al. High Voltage Mg-Ion Battery Cathode via a Solid Solution Cr–Mn Spinel Oxide. *Chem. Mater.* **2020**, *32*, 6577–6587.

(131) Lancry, E.; Levi, E.; Gofer, Y.; Levi, M.; Salitra, G.; Aurbach, D. Leaching Chemistry and the Performance of the Mo_6S_8 Cathodes in Rechargeable Mg Batteries. *Chem. Mater.* **2004**, *16*, 2832–2838.

(132) Levi, M.; Lancri, E.; Levi, E.; Gizbar, H.; Gofer, Y.; Aurbach, D. The Effect of the Anionic Framework of MoX Chevrel Phase (X=S, Se) on the Thermodynamics and the Kinetics of the Electrochemical Insertion of Mg Ions. *Solid State Ionics* **2005**, *176*, 1695–1699.

(133) Brown, I. D. What Factors Determine Cation Coordination Numbers? *Acta Crystallogr B Struct Sci* **1988**, *44*, 545–553.

(134) Wang, Y.; Richards, W. D.; Ong, S. P.; Miara, L. J.; Kim, J. C.; Mo, Y.; Ceder, G. Design Principles for Solid-State Lithium Superionic Conductors. *Nature Mater* **2015**, *14*, 1026–1031.

(135) Orikasa, Y.; Kisu, K.; Iwama, E.; Naoi, W.; Yamaguchi, Y.; Yamaguchi, Y.; Okita, N.; Ohara, K.; Munesada, T.; Hattori, M.; Yamamoto, K.; Rozier, P.; Simon, P.; Naoi, K. Noncrystalline Nanocomposites as a Remedy for the Low Diffusivity of Multivalent Ions in Battery Cathodes. *Chem. Mater.* **2020**, *32*, 1011–1021.

(136) Yamanaka, T.; Hayashi, A.; Yamauchi, A.; Tatsumisago, M. Preparation of Magnesium Ion Conducting MgS–P2S5–MgI2 Glasses by a Mechanochemical Technique. *Solid State Ionics* **2014**, *262*, 601–603.

(137) Levi, M.; Lancry, E.; Gizbar, H.; Gofer, Y.; Levi, E.; Aurbach, D. Phase Transitions and Diffusion Kinetics during Mg2+- and Li+-Ion Insertions into the Mo6S8 Chevrel Phase Compound Studied by PITT. *Electrochimica Acta* **2004**, *49*, 3201–3209.

(138) Ling, C.; Suto, K. Thermodynamic Origin of Irreversible Magnesium Trapping in Chevrel Phase Mo_6S_8 : Importance of Magnesium and Vacancy Ordering. *Chem. Mater.* **2017**, *29*, 3731–3739.

(139) Levi, E.; Lancry, E.; Mitelman, A.; Aurbach, D.; Isnard, O.; Djurado, D. Phase Diagram of Mg Insertion into Chevrel Phases, $Mg_xMo_6T_8$ (T = S, Se). 2. The Crystal Structure of Triclinic $MgMo_6Se_8$. *Chem. Mater.* **2006**, *18*, 3705–3714.

(140) Levi, E.; Lancry, E.; Mitelman, A.; Aurbach, D.; Ceder, G.; Morgan, D.; Isnard, O. Phase Diagram of Mg Insertion into Chevrel Phases, $Mg_xMo_6T_8$ (T = S, Se). 1. Crystal Structure of the Sulfides. *Chem. Mater.* **2006**, *18*, 5492–5503.

(141) Aurbach, D.; Suresh, G. S.; Levi, E.; Mitelman, A.; Mizrahi, O.; Chusid, O.; Brunelli, M. Progress in Rechargeable Magnesium Battery Technology. *Adv. Mater.* **2007**, *19*, 4260–4267.

(142) Levi, E.; Mitelman, A.; Aurbach, D.; Brunelli, M. Structural Mechanism of the Phase Transitions in the Mg-Cu-Mo $_6$ S $_8$ System Probed by Ex Situ Synchrotron X-ray Diffraction. *Chem. Mater.* **2007**, *19*, 5131–5142.

(143) Kilner, J. A. Fast Oxygen Transport in Acceptor Doped Oxides. *Solid State Ionics* **2000**, 11.

(144) Skinner, S. J.; Kilner, J. A. Oxygen Ion Conductors. *Materials Today* **2003**, *6*, 30–37.

(145) Chen, H.; Wong, L. L.; Adams, S. *SoftBV* – a Software Tool for Screening the Materials Genome of Inorganic Fast Ion Conductors. *Acta Crystallogr B Struct Sci Cryst Eng Mater* **2019**, *75*, 18–33.

(146) Adams, S. Modelling Ion Conduction Pathways by Bond Valence Pseudopotential Maps. *Solid State Ionics* **2000**, *136–137*, 1351–1361.

(147) Nishitani, Y.; Adams, S.; Ichikawa, K.; Tsujita, T. Evaluation of Magnesium Ion Migration in Inorganic Oxides by the Bond Valence Site Energy Method. *Solid State Ionics* **2018**, *315*, 111–115.

(148) Bubenzer, A.; Grieshaber, E. The Crystal Structure of the Cubic Cadmium Phosphorus Sulphide Iodide Cd13P4S2212. 5.

(149) Strauss, F.; Zinkevich, T.; Indris, S.; Brezesinski, T. Li $_7$ GeS $_5$ Br—An Argyrodite Li-Ion Conductor Prepared by Mechanochemical Synthesis. *Inorg. Chem.* **2020**, *59*, 12954–12959.

(150) Michelet, A.; Flahaut, ¸ Sur Les Composes Du Type La6MnSi2S14. *CR Seances Acad. Sci., Ser. C* **1969**, *269*, 1203–1205.

(151) Kabanov, A. A.; Morkhova, Y. A.; Osipov, V. T.; Rothenberger, M.; Leisegang, T.; Blatov, V. A. A Novel Class of Multivalent Ionic Conductors with the La_3CuSiS_7 Structure Type: Results of Stepwise ICSD Screening. *Phys. Chem. Chem. Phys.* **2024**, *26*, 2622–2628.

(152) Ding, J.; Sun, S.; Yan, W.; Bao, J.; Gao, C. Photocatalytic H2 Evolution on a Novel CaIn2S4 Photocatalyst under Visible Light Irradiation. *International Journal of Hydrogen Energy* **2013**, *38*, 13153–13158.

(153) Xiao, Y.; Jun, K.; Wang, Y.; Miara, L. J.; Tu, Q.; Ceder, G. Lithium Oxide Superionic Conductors Inspired by Garnet and NASICON Structures. *Adv. Energy Mater.* **2021**, *11*, 2101437.

(154) Chang, C.-M.; Lee, Y. I.; Hong, S.-H.; Park, H.-M. Spark Plasma Sintering of LiTi2(PO4)3-Based Solid Electrolytes. *J American Ceramic Society* **2005**, *88*, 1803–1807.

(155) Anuar, N.; Adnan, S.; Mohamed, N. Characterization of Mg0.5Zr2(PO4)3 for Potential Use as Electrolyte in Solid State Magnesium Batteries. *Ceramics International* **2014**, *40*, 13719–13727.

(156) Hayashi, A.; Hama, S.; Morimoto, H.; Tatsumisago, M.; Minami, T. Preparation of Li2S-P2S5 Amorphous Solid Electrolytes by Mechanical Milling. *Journal of the American Ceramic Society* **2004**, *84*, 477–79.

(157) Hargis, C. W.; Moon, J.; Lothenbach, B.; Winnefeld, F.; Wenk, H.-R.; Monteiro, P. J. M. Calcium Sulfoaluminate Sodalite ($Ca_4Al_6O_{12}SO_4$) Crystal Structure Evaluation and Bulk Modulus Determination. *J. Am. Ceram. Soc.* **2014**, *97*, ed. by Biernacki, J., 892–898.

(158) Iton, Z. W. B.; See, K. A. Multivalent Ion Conduction in Inorganic Solids. *Chem. Mater.* **2022**, *34*, 881–898.

(159) Muldoon, J.; Bucur, C. B.; Gregory, T. Quest for Nonaqueous Multivalent Secondary Batteries: Magnesium and Beyond. *Chem. Rev.* **2014**, *114*, 11683–11720.

(160) Grey, C. P.; Tarascon, J. M. Sustainability and in Situ Monitoring in Battery Development. *Nature Mater* **2017**, *16*, 45–56.

(161) Novák, P.; Desilvestro, J. Electrochemical Insertion of Magnesium in Metal Oxides and Sulfides from Aprotic Electrolytes. *J. Electrochem. Soc.* **1993**, *140*, 140–144.

(162) Kundu, D.; Adams, B. D.; Duffort, V.; Vajargah, S. H.; Nazar, L. F. A High-Capacity and Long-Life Aqueous Rechargeable Zinc Battery Using a Metal Oxide Intercalation Cathode. *Nat Energy* **2016**, *1*, 16119.

(163) Sun, X.; Duffort, V.; Mehdi, B. L.; Browning, N. D.; Nazar, L. F. Investigation of the Mechanism of Mg Insertion in Birnessite in Nonaqueous and Aqueous Rechargeable Mg-Ion Batteries. *Chem. Mater.* **2016**, *28*, 534–542.

(164) Clement, R. A Novel Route to Intercalation into Layered $MnPS_3$. *J. Chem. Soc., Chem. Commun.* **1980**, 647.

(165) Ichimura, K.; Sano, M. Electrical Conductivity of Layered Transition-Metal Phosphorus Trisulfide Crystals. *Synthetic Metals* **1991**, *45*, 203–211.

(166) Lagadic, I.; Lacroix, P. G.; Clément, R. Layered MPS_3 (M = Mn, Cd) Thin Films as Host Matrixes for Nonlinear Optical Material Processing. *Chem. Mater.* **1997**, *9*, 2004–2012.

(167) Foot, P. J. S.; Nevett, B. A. Properties of $NiPS_3$ and $ZnPS_3$ Prepared at Ambient Temperature. *J. Chem. Soc., Chem. Commun.* **1987**, 380.

(168) Coradin, T.; Clément, R.; Lacroix, P. G.; Nakatani, K. From Intercalation to Aggregation: Nonlinear Optical Properties of Stilbazolium Chromophores-MPS_3 Layered Hybrid Materials. *Chem. Mater.* **1996**, *8*, 2153–2158.

(169) Tang, B.; Shan, L.; Liang, S.; Zhou, J. Issues and Opportunities Facing Aqueous Zinc-Ion Batteries. *Energy Environ. Sci.* **2019**, *12*, 3288–3304.

(170) Fang, G.; Zhou, J.; Pan, A.; Liang, S. Recent Advances in Aqueous Zinc-Ion Batteries. *ACS Energy Lett.* **2018**, *3*, 2480–2501.

(171) Shin, J.; Lee, J.; Park, Y.; Choi, J. W. Aqueous Zinc Ion Batteries: Focus on Zinc Metal Anodes. *Chem. Sci.* **2020**, *11*, 2028–2044.

(172) Han, C.; Li, W.; Liu, H. K.; Dou, S.; Wang, J. Principals and Strategies for Constructing a Highly Reversible Zinc Metal Anode in Aqueous Batteries. *Nano Energy* **2020**, *74*, 104880.

(173) Wang, F.; Borodin, O.; Gao, T.; Fan, X.; Sun, W.; Han, F.; Faraone, A.; Dura, J. A.; Xu, K.; Wang, C. Highly Reversible Zinc Metal Anode for Aqueous Batteries. *Nature Mater* **2018**, *17*, 543–549.

(174) Blanc, L. E.; Kundu, D.; Nazar, L. F. Scientific Challenges for the Implementation of Zn-Ion Batteries. *Joule* **2020**, *4*, 771–799.

(175) Wan, F.; Zhou, X.; Lu, Y.; Niu, Z.; Chen, J. Energy Storage Chemistry in Aqueous Zinc Metal Batteries. *ACS Energy Lett.* **2020**, *5*, 3569–3590.

(176) Lopez, M.; Yoo, H. D.; Hu, L.; Andrews, J. L.; Banerjee, S.; Cabana, J. Does Water Enhance Mg Intercalation in Oxides? The Case of a Tunnel Framework. *ACS Energy Lett.* **2020**, *5*, 3357–3361.

(177) Rezania, B.; Severin, N.; Talyzin, A. V.; Rabe, J. P. Hydration of Bilayered Graphene Oxide. *Nano Lett.* **2014**, *14*, 3993–3998.

(178) Manríquez, V.; Barahona, P.; Ruiz, D.; Avila, R. Intercalation of Polyethylene Oxide PEO in Layered MPS_3 (M=Ni, Fe) Materials. *Materials Research Bulletin* **2005**, *40*, 475–483.

(179) Mathey, Y.; Clement, R.; Sourisseau, C.; Lucazeau, G. Vibrational Study of Layered MPX_3 Compounds and of Some Intercalates with Co(η^5-$C_5H_5)^{2+}$ or Cr(η^6-$C_6H_6)^{2+}$. *Inorg. Chem.* **1980**, *19*, 2773–2779.

(180) Sourisseau, C.; Forgerit, J.; Mathey, Y. Vibrational Study of Layered $ZnPS_3$ Compounds Intercalated with [Co(η^5-$C_5H_5)^{2+}$] and [Cr(η^6-$C_6H_6)^{2+}$] Cations. *Journal of Physics and Chemistry of Solids* **1983**, *44*, 119–124.

(181) Hatz, A.-K.; Moudrakovski, I.; Bette, S.; Terban, M. W.; Etter, M.; Joos, M.; Vargas-Barbosa, N. M.; Dinnebier, R. E.; Lotsch, B. V. Fast Water-Assisted Lithium Ion Conduction in Restacked Lithium Tin Sulfide Nanosheets. *Chem. Mater.* **2021**, *33*, 7337–7349.

(182) Ye, G.; Janzen, N.; Goward, G. R. Solid-State NMR Study of Two Classic Proton Conducting Polymers: Nafion and Sulfonated Poly(Ether Ether Ketone)s. *Macromolecules* **2006**, *39*, 3283–3290.

(183) Ratcliffe, C.; Ripmeester, J.; Tse, J. NMR Chemical Shifts of Dilute ^{1}H in Inorganic Solids. *Chemical Physics Letters* **1985**, *120*, 427–432.

(184) Ladizhansky, V.; Hodes, G.; Vega, S. Solid State NMR Study of Water Binding on the Surface of CdS Nanoparticles. *J. Phys. Chem. B* **2000**, *104*, 1939–1943.

(185) Kweon, J. J.; Fu, R.; Steven, E.; Lee, C. E.; Dalal, N. S. High Field MAS NMR and Conductivity Study of the Superionic Conductor LiH_2PO_4 : Critical Role of Physisorbed Water in Its Protonic Conductivity. *J. Phys. Chem. C* **2014**, *118*, 13387–13393.

(186) Gill, L.; Beste, A.; Chen, B.; Li, M.; Mann, A. K. P.; Overbury, S. H.; Hagaman, E. W. Fast MAS ^{1}H NMR Study of Water Adsorption and Dissociation on the (100) Surface of Ceria Nanocubes: A Fully Hydroxylated, Hydrophobic Ceria Surface. *J. Phys. Chem. C* **2017**, *121*, 7450–7465.

(187) Hansen, E. W.; Stöcker, M.; Schmidt, R. Low-Temperature Phase Transition of Water Confined in Mesopores Probed by NMR. Influence on Pore Size Distribution. *J. Phys. Chem.* **1996**, *100*, 2195–2200.

(188) Hansen, E. W.; Schmidt, R.; Stöcker, M. Pore Structure Characterization of Porous Silica by ^{1}H NMR Using Water, Benzene, and Cyclohexane as Probe Molecules. *J. Phys. Chem.* **1996**, *100*, 11396–11401.

(189) Adolphi, N. L.; Stoddard, R.; Goel, S. C.; Buhro, W. E.; Gibbons, P. C.; Conradi, M. S. The ^{31}P NMR Spectra of Cd_3P_2 and Zn_3P_2. *Journal of Physics and Chemistry of Solids* **1992**, *53*, 1275–1278.

(190) Eckert, H.; Liang, C. S.; Stucky, G. D. Phosphorus-31 Magic Angle Spinning NMR of Crystalline Phosphorus Sulfides: Correlation of Phosphorus-31 Chemical Shielding Tensors with Local Environments. *J. Phys. Chem.* **1989**, *93*, 452–457.

(191) Lock, H.; Xiong, J.; Wen, Y.-C.; Parkinson, B. A.; Maciel, G. E. Solid-State ^{29}Si, ^{113}Cd, ^{119}Sn, and ^{31}P NMR Studies of II-IV-P_2 Semiconductors. *Solid State Nuclear Magnetic Resonance* **2001**, *20*, 118–129.

(192) Gao, Y.; Mishra, T. P.; Bo, S.-H.; Gautam, G. S.; Canepa, P. Design and Characterization of Host Frameworks for Facile Magnesium Transport. *Annu. Rev. Mater. Res.* **2022**, *52*, 129–158.

(193) Hu, S.; Lozada-Hidalgo, M.; Wang, F. C.; Mishchenko, A.; Schedin, F.; Nair, R. R.; Hill, E. W.; Boukhvalov, D. W.; Katsnelson, M. I.; Dryfe, R. A. W.; Grigorieva, I. V.; Wu, H. A.; Geim, A. K. Proton Transport through One-Atom-Thick Crystals. *Nature* **2014**, *516*, 227–230.

(194) Xu, K. Navigating the Minefield of Battery Literature. *Commun Mater* **2022**, *3*, 31.

(195) Ma, Y.; Doyle, M.; Fuller, T. F.; Doeff, M. M.; De Jonghe, L. C.; Newman, J. The Measurement of a Complete Set of Transport Properties for a Concentrated Solid Polymer Electrolyte Solution. *J. Electrochem. Soc.* **1995**, *142*, 1859–1868.

(196) Doyle, M.; Newman, J. Analysis of Transference Number Measurements Based on the Potentiostatic Polarization of Solid Polymer Electrolytes. *J. Electrochem. Soc.* **1995**, *142*, 3465–3468.

(197) Borissov, D.; Pareek, A.; Renner, F. U.; Rohwerder, M. Electrodeposition of Zn and Au–Zn Alloys at Low Temperature in an Ionic Liquid. *Phys. Chem. Chem. Phys.* **2010**, *12*, 2059.

(198) Liu, Z.; Zein El Abedin, S.; Endres, F. Electrodeposition and Stripping of Zinc from an Ionic Liquid Polymer Gel Electrolyte for Rechargeable Zinc-Based Batteries. *J Solid State Electrochem* **2014**, *18*, 2683–2691.

(199) Huang, J.-F.; Sun, I.-W. Electrodeposition of PtZn in a Lewis Acidic $ZnCl_2$–1-Ethyl-3-Methylimidazolium Chloride Ionic Liquid. *Electrochimica Acta* **2004**, *49*, 3251–3258.

(200) Huang, J.-F.; Sun, I.-W. Fabrication and Surface Functionalization of Nanoporous Gold by Electrochemical Alloying/Dealloying of Au-Zn in an Ionic Liquid, and the Self-Assembly of L-Cysteine Monolayers. *Adv. Funct. Mater.* **2005**, *15*, 989–994.

(201) Liu, Z.; Abedin, S. Z. E.; Endres, F. Electrodeposition of Zinc Films from Ionic Liquids and Ionic Liquid/Water Mixtures. *Electrochimica Acta* **2013**, *89*, 635–643.

(202) Uosaki, K.; Elumalai, G.; Dinh, H. C.; Lyalin, A.; Taketsugu, T.; Noguchi, H. Highly Efficient Electrochemical Hydrogen Evolution Reaction at Insulating Boron Nitride Nanosheet on Inert Gold Substrate. *Sci Rep* **2016**, *6*, 32217.

(203) Pei, A.; Zheng, G.; Shi, F.; Li, Y.; Cui, Y. Nanoscale Nucleation and Growth of Electrodeposited Lithium Metal. *Nano Lett.* **2017**, *17*, 1132–1139.

(204) Qiao, A.; Tao, H.; Yue, Y. Enhancing Ionic Conductivity in Ag_3PS_4 via Mechanical Amorphization. *Journal of Non-Crystalline Solids* **2019**, *521*, 119476.

(205) Laskowski, F. A. L.; McHaffie, D. B.; See, K. A. Identification of Potential Solid-State Li-ion Conductors with Semi-Supervised Learning. *Energy Environ. Sci.* **2023**, *16*, 1264–1276.

(206) Kharod, R. A.; Andrews, J. L.; Dincă, M. Teaching Metal-Organic Frameworks to Conduct: Ion and Electron Transport in Metal-Organic Frameworks. *Annu. Rev. Mater. Res.* **2022**, *52*, 103–128.

(207) Duan, X.; Ouyang, Y.; Zeng, Q.; Ma, S.; Kong, Z.; Chen, A.; He, Z.; Yang, T.; Zhang, Q. Two Carboxyl-Decorated Anionic Metal–Organic Frameworks as Solid-State Electrolytes Exhibiting High Li^+ and Zn^{2+} Conductivity. *Inorg. Chem.* **2021**, *60*, 11032–11037.

(208) Miner, E. M.; Park, S. S.; Dincă, M. High Li^+ and Mg^{2+} Conductivity in a Cu-Azolate Metal–Organic Framework. *J. Am. Chem. Soc.* **2019**, *141*, 4422–4427.

(209) Yoshida, Y.; Yamada, T.; Jing, Y.; Toyao, T.; Shimizu, K.-i.; Sadakiyo, M. Super Mg^{2+} Conductivity around 10^{-3} Scm^{-1} Observed in a Porous Metal–Organic Framework. *J. Am. Chem. Soc.* **2022**, *144*, 8669–8675.

(210) Yoshida, Y.; Kato, K.; Sadakiyo, M. Vapor-Induced Superionic Conduction of Magnesium Ions in a Metal–Organic Framework. *J. Phys. Chem. C* **2021**, *125*, 21124–21130.

(211) Prouzet, E.; Fukatani, M.; Barj, M.; Janvier, P. Oxygen Substitution of the Hexathiodiphosphate(IV) Ion in Aqueous Solution. *J. Chem. Soc., Dalton Trans.* **1999**, 635–638.

(212) Clement, R.; Garnier, O.; Jegoudez, J. Coordination Chemistry of the Lamellar MPS_3 Materials: Metal-Ligand Cleavage as the Source of an Unusual "Cation-Transfer" Intercalation Process. *Inorg. Chem.* **1986**, *25*, 1404–1409.

(213) Ichimura, K.; Miyazaki, T.; Matsuzaki, S.; Sano, M. Electrical Conductivities and Electronic States of Metal Phosphorus Trisulfides M_xPS_3 and Their Intercalation Compounds. *MSF* **1992**, *91–93*, 505–510.

(214) Zhu, J.; Zhang, Z.; Zhao, S.; Westover, A. S.; Belharouak, I.; Cao, P.-F. Single-Ion Conducting Polymer Electrolytes for Solid-State Lithium–Metal Batteries: Design, Performance, and Challenges. *Adv. Energy Mater.* **2021**, *11*, 2003836.

(215) Agmon, N. The Grotthuss Mechanism. *Chemical Physics Letters* **1995**, *244*, 456–462.

(216) Casciola, M. From Layered Zirconium Phosphates and Phosphonates to Nanofillers for Ionomeric Membranes. *Solid State Ionics* **2019**, *336*, 1–10.

(217) Yaroslavtsev, A. B. Proton Conductivity of Inorganic Hydrates. *Russ. Chem. Rev.* **1994**, *63*, 429–435.

(218) Casciola, M.; Bianchi, D. Frequency Response of Polycrystalline Samples of α−$Zr(HPO_4)_2{\cdot}H_2O$ at Different Relative Humidities. *Solid State Ionics* **1985**, *17*, 287–293.

(219) Lundgren, C. A.; Murray, R. W. Observations on the Composition of Prussian Blue Films and Their Electrochemistry. *Inorg. Chem.* **1988**, *27*, 933–939.

(220) Itaya, K.; Uchida, I.; Neff, V. D. Electrochemistry of Polynuclear Transition Metal Cyanides: Prussian Blue and Its Analogues. *Acc. Chem. Res.* **1986**, *19*, 162–168.

(221) Lee, H.-W.; Wang, R. Y.; Pasta, M.; Woo Lee, S.; Liu, N.; Cui, Y. Manganese Hexacyanomanganate Open Framework as a High-Capacity Positive Electrode Material for Sodium-Ion Batteries. *Nat Commun* **2014**, *5*, 5280.

(222) Kummer, J. Beta-Alumina Electrolytes. *Progress in Solid State Chemistry* **1972**, *7*, 141–175.

(223) Whittingham, M. S.; Huggins, R. A. Measurement of Sodium Ion Transport in Beta Alumina Using Reversible Solid Electrodes. *The Journal of Chemical Physics* **1971**, *54*, 414–416.

(224) Goodenough, J.; Hong, H.-P.; Kafalas, J. Fast Na^+-Ion Transport in Skeleton Structures. *Materials Research Bulletin* **1976**, *11*, 203–220.

(225) Pal, S. K.; Saha, R.; Kumar, G. V.; Omar, S. Designing High Ionic Conducting NASICON-type $Na_3Zr_2Si_2PO_{12}$ Solid-Electrolytes for Na-Ion Batteries. *J. Phys. Chem. C* **2020**, *124*, 9161–9169.

(226) Guin, M.; Tietz, F.; Guillon, O. New Promising NASICON Material as Solid Electrolyte for Sodium-Ion Batteries: Correlation between Composition, Crystal Structure and Ionic Conductivity of $Na_{3+x}Sc_2Si_xP_{3-x}O_{12}$. *Solid State Ionics* **2016**, *293*, 18–26.

(227) Glaser, C.; Wei, Z.; Indris, S.; Klement, P.; Chatterjee, S.; Ehrenberg, H.; Zhao-Karger, Z.; Rohnke, M.; Janek, J. To Be or Not to Be – Is $MgSc_2Se_4$ a Mg-Ion Solid Electrolyte? *Advanced Energy Materials* **2023**, 2301980.

(228) Whittingham, S. Transport Properties of the Mineral Vermiculite. *Solid State Ionics* **1989**, *32–33*, 344–349.

(229) Whittingham, M. Sodium Ion Conduction in Single Crystal Vermiculite. *Solid State Ionics* **1987**, *25*, 295–300.

(230) Maraqah, H.; Li, J.; Whittingham, M. S. Ion Transport in Single Crystals of the Clay-Like Aluminosilicate, Vermiculite. *MRS Proc.* **1990**, *210*, 351.

(231) Slade, R. Conduction and Diffusion in Exchanged Montmorillonite Clays. *Solid State Ionics* **1987**, *24*, 289–295.

(232) Ruiz-Hitzky, E.; Casal, B. Crown Ether Intercalations with Phyllosilicates. *Nature* **1978**, *276*, 596–597.

(233) Iton, Z. W. B.; Lee, B. C.; Jiang, A. Y.; Kim, S. S.; Brady, M. J.; Shaker, S.; See, K. A. Water Vapor Induced Superionic Conductivity in $ZnPS_3$. *J. Am. Chem. Soc.* **2023**, *145*, 13312–13325.

(234) Iliescu, A.; Andrews, J. L.; Oppenheim, J. J.; Dincă, M. A Solid Zn-Ion Conductor from an All-Zinc Metal–Organic Framework Replete with Mobile Zn2+ Cations. *J. Am. Chem. Soc.* **2023**.

(235) Whittingham, M. S. The Role of Ternary Phases in Cathode Reactions. *J. Electrochem. Soc.* **1976**, *123*, 315–320.

(236) Clément, R.; Lagadic, I.; Léaustic, A.; Audière, J. P.; Lomas, L. In *Chemical Physics of Intercalation II*, Bernier, P., Fischer, J. E., Roth, S., Solin, S. A., Eds.; Springer US: Boston, MA, 1993; Vol. 305, pp 315–324.

(237) Fan, Y. A New Family of Fast Ion Conductor-Montmorillonites. *Solid State Ionics* **1997**, *93*, 347–354.

(238) Suzuki, M.; Wada, N.; Hines, D.; Whittingham, M. S. Hydration States and Phase Transitions in Vermiculite Intercalation Compounds. *Phys. Rev. B* **1987**, *36*, 2844–2851.

(239) Ouvrard, G.; Brec, R.; Rouxel, J. Structural Determination of Some MPS3 Layered Phases (M = Mn, Fe, Co, Ni and Cd). *Materials Research Bulletin* **1985**, *20*, 1181–1189.

(240) Shannon, R. D. Revised Effective Ionic Radii and Systematic Studies of Interatomic Distances in Halides and Chalcogenides. *Acta Cryst A* **1976**, *32*, 751–767.

(241) Clement, R.; Leaustic, A.; Marney, K.; Francis, A. Synthesis and Luminescence Properties of CdPS3 Intercalated with Rare Earth Cations. *Journal of Physics and Chemistry of Solids* **1994**, *55*, 9–16.

(242) Coradin, T.; Coupé, A.; Livage, J. Intercalation of Biomolecules in the MnPS3 Layered Phase. *J. Mater. Chem.* **2003**, *13*, 705–707.

(243) Lagadic, I.; Léaustic, A.; Clément, R. Intercalation of Polyethers into the MPS_3 (M = Mn, Cd) Host Lattice. *J. Chem. Soc., Chem. Commun.* **1992**, *0*, 1396–1397.

(244) Oriakhi, C. O.; Nafshun, R. L.; Lerner, M. M. Preparation of Nanocomposites of Linear Poly(Ethylenimine) with Layered Hosts. *Materials Research Bulletin* **1996**, *31*, 1513–1520.

(245) Clement, R.; Lomas, L.; Audiere, J. P. Intercalation Chemistry of Layered Iron Trithiohypophosphate ($FePS_3$). An Approach toward Insulating Magnets below 90 K. *Chem. Mater.* **1990**, *2*, 641–643.

(246) Jeevanandam, P.; Vasudevan, S. Preparation and Characterization of $Cd_{0.75}PS_3A_{0.5}(H_2O)_y$ [A=Na, K and Cs]. *Solid State Ionics* **1997**, *104*, 45–55.

(247) Jeevanandam, P.; Vasudevan, S. Conductivity and Dielectric Response in the Ion-Exchange Intercalated Mono- and Double-Layer Hydrates $Cd_{0.75}PS_3Na_{0.5}(H_2O)_y$, y = 1, 2. *J. Phys. Chem. B* **1998**, *102*, 3082–3089.

(248) Arun, N.; Jeevanandam, P.; Vasudevan, S.; Ramanathan, K. V. Motion of Interlamellar Hydrated Sodium Ions in Layered $Cd_{0.75}PS_3Na_{0.5}\ (H_2O)_2$. *The Journal of Chemical Physics* **1999**, *111*, 1231–1239.

(249) Arun, N.; Vasudevan, S.; Ramanathan, K. V. Orientation and Motion of Interlamellar Water: An Infrared and NMR Investigation of Water in the Galleries of Layered $Cd_{0.75}PS_3K_{0.5}(H_2O)_y$. *J. Am. Chem. Soc.* **2000**, *122*, 6028–6038.

(250) Ruiz-León, D.; Manrıquez, V.; Kasaneva, J.; Avila, R. Insertion of Trivalent Cations in the Layered MPS3 (Mn, Cd) Materials. *Materials Research Bulletin* **2002**, *37*, 981–989.

(251) Yu, X.; Ren, W. 2D $CdPS_3$-Based Versatile Superionic Conductors. *Nat Commun* **2023**, *14*, 3998.

(252) Hou, T.; Xu, W.; Pei, X.; Jiang, L.; Yaghi, O. M.; Persson, K. A. Ionic Conduction Mechanism and Design of Metal–Organic Framework Based Quasi-Solid-State Electrolytes. *J. Am. Chem. Soc.* **2022**, *144*, 13446–13450.

(253) García, N. Conductivity in Na^+- and Li^+-Montmorillonite as a Function of Equilibration Humidity. *Solid State Ionics* **1996**, *92*, 139–143.

(254) Fan, Y. Cation Diffusion and Conduction in Solid Electrolytes Li, Na-montmorillonites. *Solid State Ionics* **1988**, *28–30*, 1596–1601.

(255) Barj, M.; Lucazeau, G. Raman Spectra of Lamellar CdPS3 Intercalated with Alkali Ions. *Solid State Ionics* **1983**, *9–10*, 475–479.

(256) Schöllhorn, R.; Meyer, H. Cathodic Reduction of Layered Transition Metal Chalcogenides. *Materials Research Bulletin* **1974**, *9*, 1237–1245.

(257) Lerf, A.; Schoellhorn, R. Solvation Reactions of Layered Ternary Sulfides A_xTiS_2, A_xNbS_2, and A_xTaS_2. *Inorg. Chem.* **1977**, *16*, 2950–2956.

(258) Whittingham, M. The Hydrated Intercalation Complexes of the Layered Disulfides. *Materials Research Bulletin* **1974**, *9*, 1681–1689.

(259) Ghidiu, M.; Halim, J.; Kota, S.; Bish, D.; Gogotsi, Y.; Barsoum, M. W. Ion-Exchange and Cation Solvation Reactions in Ti_3C_2 MXene. *Chem. Mater.* **2016**, *28*, 3507–3514.

(260) Prouzet; Ouvrard, G.; Brec, R. Structure Determination of $ZnPS_3$. *Materials Research Bulletin* **1986**, *21*, 195–200.

(261) Frenkel, M. Surface Acidity of Montmorillonites. *Clays and Clay Minerals* **1974**, *22*, 435–441.

(262) Volkov, V. I.; Chernyak, A. V.; Slesarenko, N. A.; Avilova, I. A. Ion and Molecular Transport in Solid Electrolytes Studied by NMR. *IJMS* **2022**, *23*, 5011.

(263) Gun'ko, V. M.; Turov, V. V. Structure of Hydrogen Bonds and ^{1} H NMR Spectra of Water at the Interface of Oxides. *Langmuir* **1999**, *15*, 6405–6415.

(264) Hayashi, S.; Mizuno, M. Proton Dynamics in $Cs_2(HSO_4)(H_2PO_4)$ Studied by ^{1}H NMR. *Solid State Ionics* **2005**, *176*, 745–754.

(265) Sanz, J.; Sobrados, I.; Robert, J.-L. Influence of Hydration on ^{23}Na, ^{27}Al, and ^{29}Si MAS-NMR Spectra of Sodium Saponites and Sodium Micas. *American Mineralogist* **2015**, *100*, 1076–1083.

(266) Ohkubo, T.; Saito, K.; Kanehashi, K.; Ikeda, Y. A Study on Hydration Behaviors of Interlayer Cations in Montmorillonite by Solid State NMR. *Science and Technology of Advanced Materials* **2004**, *5*, 693–696.

(267) Malicki, N.; Beccat, P.; Bourges, P.; Fernandez, C.; Quoineaud, A.-A.; Simon, L. J.; Thibault-Starzyk, F. In *Studies in Surface Science and Catalysis*; Elsevier: 2007; Vol. 170, pp 762–770.

(268) Haouas, M.; Taulelle, F.; Martineau, C. Recent Advances in Application of 27Al NMR Spectroscopy to Materials Science. *Progress in Nuclear Magnetic Resonance Spectroscopy* **2016**, *94–95*, 11–36.

(269) Tanner, J. E. Use of the Stimulated Echo in NMR Diffusion Studies. *The Journal of Chemical Physics* **1970**, *52*, 2523–2526.

(270) Stejskal, E. O.; Tanner, J. E. Spin Diffusion Measurements: Spin Echoes in the Presence of a Time-Dependent Field Gradient. *The Journal of Chemical Physics* **1965**, *42*, 288–292.

(271) Manrıquez, V.; Galdámez, A.; Villanueva, A.; Aranda, P.; Galván, J. C.; Ruiz-Hitzky, E. Insertion of In(III) and Ga(III) into MPS_3 (M = Mn, Cd) Layered Materials. *Materials Research Bulletin* **1999**, *34*, 673–683.

(272) Scholz, T.; Schneider, C.; Eger, R.; Duppel, V.; Moudrakovski, I.; Schulz, A.; Nuss, J.; Lotsch, B. V. Phase Formation through Synthetic Control: Polymorphism in the Sodium-Ion Solid Electrolyte $Na_4P_2S_6$. *J. Mater. Chem. A* **2021**, *9*, 8692–8703.

(273) Haber, S.; Leskes, M. What Can We Learn from Solid State NMR on the Electrode–Electrolyte Interface? *Advanced Materials* **2018**, *30*, 1706496.

(274) Ramsey, N. F. Magnetic Shielding of Nuclei in Molecules. *Phys. Rev.* **1950**, *78*, 699–703.

(275) Komoroski, R. A. Applications of ^{7}Li NMR in Biomedicine. *Magnetic Resonance Imaging* **2000**, *18*, 103–116.

(276) Beguin, F.; Setton, R.; Beguin, F.; Setton, R.; Hamwi, A.; Touzain, P. The Reversible Intercalation of Tetrahydrofuran in Some Graphite-Alkali Metal Lamellar Compounds. *Materials Science and Engineering* **1979**, *40*, 167–173.

(277) Miner, E. M.; Dincă, M. Metal- and Covalent-Organic Frameworks as Solid-State Electrolytes for Metal-Ion Batteries. *Phil. Trans. R. Soc. A.* **2019**, *377*, 20180225.

(278) Sinnaeve, D. The Stejskal–Tanner Equation Generalized for Any Gradient Shape—an Overview of Most Pulse Sequences Measuring Free Diffusion. *Concepts Magnetic Resonance* **2012**, *40A*, 39–65.

(279) Kresse, G.; Hafner, J. *Ab Initio* Molecular Dynamics for Liquid Metals. *Phys. Rev. B* **1993**, *47*, 558–561.

(280) Kresse, G.; Furthmüller, J. Efficiency of Ab-Initio Total Energy Calculations for Metals and Semiconductors Using a Plane-Wave Basis Set. *Computational Materials Science* **1996**, *6*, 15–50.

(281) Kresse, G.; Furthmüller, J. Efficient Iterative Schemes for *Ab Initio* Total-Energy Calculations Using a Plane-Wave Basis Set. *Phys. Rev. B* **1996**, *54*, 11169–11186.

(282) Kresse, G.; Joubert, D. From Ultrasoft Pseudopotentials to the Projector Augmented-Wave Method. *Phys. Rev. B* **1999**, *59*, 1758–1775.

(283) Blöchl, P. E. Projector Augmented-Wave Method. *Phys. Rev. B* **1994**, *50*, 17953–17979.

(284) Perdew, J. P.; Burke, K.; Ernzerhof, M. Generalized Gradient Approximation Made Simple. *Phys. Rev. Lett.* **1996**, *77*, 3865–3868.

(285) Grimme, S.; Antony, J.; Ehrlich, S.; Krieg, H. A Consistent and Accurate *Ab Initio* Parametrization of Density Functional Dispersion Correction (DFT-D) for the 94 Elements H-Pu. *The Journal of Chemical Physics* **2010**, *132*, 154104.

(286) Grimme, S.; Ehrlich, S.; Goerigk, L. Effect of the Damping Function in Dispersion Corrected Density Functional Theory. *J Comput Chem* **2011**, *32*, 1456–1465.

(287) Nosé, S. A Unified Formulation of the Constant Temperature Molecular Dynamics Methods. *The Journal of Chemical Physics* **1984**, *81*, 511–519.

(288) Nosé, S. Constant Temperature Molecular Dynamics Methods. *Prog. Theor. Phys. Suppl.* **1991**, *103*, 1–46.

(289) Hoover, W. G. Canonical Dynamics: Equilibrium Phase-Space Distributions. *Phys. Rev. A* **1985**, *31*, 1695–1697.

(290) Frenkel, D.; Smit, B. In *Understanding Molecular Simulation*; Elsevier: 2002, pp 139–163.

(291) Morkhova, E. A.; Kabanov, A. A.; Blatov, V. A. Modeling of Ionic Conductivity in Inorganic Compounds with Multivalent Cations. *Russ J Electrochem* **2019**, *55*, 762–777.

(292) Morkhova, Y. A.; Rothenberger, M.; Leisegang, T.; Adams, S.; Blatov, V. A.; Kabanov, A. A. Computational Search for Novel Zn-Ion Conductors—A Crystallochemical, Bond Valence, and Density Functional Study. *J. Phys. Chem. C* **2021**, *125*, 17590–17599.

(293) Dake, L. S.; Baer, D. R.; Zachara, J. M. Auger Parameter Measurements of Zinc Compounds Relevant to Zinc Transport in the Environment. *Surf. Interface Anal.* **1989**, *14*, 71–75.

(294) Kowalczyk, S. P.; Pollak, R. A.; McFeely, F. R.; Ley, L.; Shirley, D. A. L2,3M45M45 Auger Spectra of Metallic Copper and Zinc: Theory and Experiment. *Phys. Rev. B* **1973**, *8*, 2387–2391.

(295) Biesinger, M. C.; Lau, L. W.; Gerson, A. R.; Smart, R. S. Resolving Surface Chemical States in XPS Analysis of First Row Transition Metals, Oxides and Hydroxides: Sc, Ti, V, Cu and Zn. *Applied Surface Science* **2010**, *257*, 887–898.